On the magnetocaloric properties of Heusler compounds: Reversible, time- and size-dependent effects of the martensitic phase transition

Über die magnetokalorischen Eigenschaften von Heusler-Legierungen: Reversible, zeit- und größenabhängige Effekte der martensitischen Phasenumwandlung

Zur Erlangung des Grades eines Doktors der Naturwissenschaften (Dr. rer. nat.)
genehmigte Dissertation von Dipl.-Phys. Tino Gottschall aus Dessau
Tag der Einreichung: 31 May 2016, Tag der Prüfung: 8 July 2016
Darmstadt 2016 — D 17

1. Gutachten: Prof. Dr. Oliver Gutfleisch
2. Gutachten: Prof. Dr. Heiko Wende

TECHNISCHE
UNIVERSITÄT
DARMSTADT

Fachbereich Material- und
Geowissenschaften
Fachgebiet Funktionale Materialien

On the magnetocaloric properties of Heusler compounds: Reversible, time- and size-dependent effects of the martensitic phase transition

Über die magnetokalorischen Eigenschaften von Heusler-Legierungen: Reversible, zeit- und größenabhängige Effekte der martensitischen Phasenumwandlung

Genehmigte Dissertation von Dipl.-Phys. Tino Gottschall aus Dessau

1. Gutachten: Prof. Dr. Oliver Gutfleisch
2. Gutachten: Prof. Dr. Heiko Wende

Tag der Einreichung: 31 May 2016
Tag der Prüfung: 8 July 2016

Darmstadt 2016 — D 17

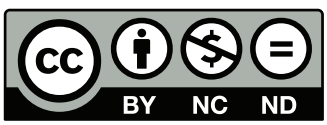

Erklärung zur Dissertation

Hiermit versichere ich, die vorliegende Dissertation ohne Hilfe Dritter nur mit den angegebenen Quellen und Hilfsmitteln angefertigt zu haben. Alle Stellen, die aus Quellen entnommen wurden, sind als solche kenntlich gemacht. Diese Arbeit hat in gleicher oder ähnlicher Form noch keiner Prüfungsbehörde vorgelegen.

Darmstadt, den 31 May 2016

(Tino Gottschall)

Abstract

Large magnetocaloric effects can be obtained in the Heusler alloy systems Ni-Mn-In and Ni-Mn-In-Co during the magnetostructural phase transformation between the low temperature paramagnetic martensite and the high temperature ferromagnetic austenite phase. The martensitic transition takes place by a nucleation and growth process and can be tuned in a wide temperature window by varying the chemical composition. It is furthermore sensitive to a magnetic field but also to hydrostatic pressure. The phase transformation can therefore be induced by those external stimuli, which is investigated in this thesis by means of a phenomenological model. The martensitic transition is related to a significant thermal hysteresis, which limits the reversible adiabatic temperature and isothermal entropy change of the material. However, the magnetocaloric effect under cycling can be enhanced when the material remains all the time in a mixed-phase state, in so-called minor loops of hysteresis. On the contrary, in very high magnetic-field rates as well as in micrometer-sized single particles, the thermal hysteresis increases significantly, which needs to be considered in terms of application. In order to understand the contrasting behavior of small fragments in comparison to their bulk representatives, a finite element model is introduced, from which the importance of mechanical stress during the first-order transition becomes apparent. Furthermore, an attempt is made to improve the sustainability of magnetocaloric Heusler alloys by the substitution of critical elements to move this interesting material class further towards application.

Zusammenfassung

In den beiden Heusler-Verbindungen Ni-Mn-In und Ni-Mn-In-Co lassen sich aufgrund der magnetostrukturellen Umwandlung zwischen der paramagnetischen Tieftemperaturphase, dem Martensit, und der ferromagnetischen Hochtemperaturphase, dem Austenit, große magnetokalorische Effekte erzielen. Die martensitische Umwandlung findet durch Nukleations- und Wachstumsprozesse statt und lässt sich präzise durch die Veränderung der chemischen Zusammensetzung über einen weiten Temperaturbereich einstellen. Ein Magnetfeld oder hydrostatischer Druck verschieben die Umwandlungstemperatur. Aufgrund dieses Effektes kann die Umwandlung induziert werden. In dieser Arbeit wird der Einfluss dieser äußeren Faktoren mit Hilfe eines phänomenologischen Modells definiert untersucht. Die martensitische Umwandlung ist mit einer erheblichen thermischen Hysterese verbunden. Diese beschränkt die Reversibilität der adiabatischen Temperatur- und der isothermen Entropieänderung maßgeblich. Jedoch kann der zyklische magnetokalorische Effekt verbessert werden, wenn das Material stets in einem Zustand der Phasenkoexistenz aus Martensit und Austenit, in sogenannten inneren Hystereseschleifen, festgehalten wird. Im Gegensatz dazu wird die thermische Hysterese durch hohe Magnetfeldraten und in einzelnen, mikrometergroßen Partikeln verbreitert, was für die Anwendung berücksichtigt werden muss. Um das unterschiedliche Verhalten von kleinen Fragmenten bzw. von Volumenmaterialien zu verstehen, wird ein Finite-Elemente-Modell vorgestellt, durch das die Bedeutung mechanischer Spannungen während der Umwandlung ersichtlich wird. Desweiteren wird ein Versuch unternommen, ressourcenkritische Elemente der magnetokalorischen Heusler-Legierungen zu ersetzen, um deren Nachhaltigkeit zu verbessern und diese interessante Materialklasse für die Anwendung weiter zu entwickeln.

Contents

List of Figures

Nomenclature

α	Length change during the transformation
β	Related heating/cooling rate
γ	Coupling force in the stress-coupling model
ΔH	Change of the magnetic field
ΔM	Magnetization change
ΔS_T	Isothermal entropy change
ΔS_t	Entropy change of the complete transition
ΔS_{el}	Entropy change of the electronic system
ΔS_{lat}	Entropy change of the lattice
ΔS_{mag}	Entropy change of the magnetic system
ΔT_t	Shift of the transition temperature
ΔT_{ad}	Adiabatic temperature change
ΔT_{hys}	Width of the thermal hysteresis
ΔV	Volume change during the transition
μ_0	Permeability of the vacuum
μ_B	Bohr magneton
$^{e}/_{a}$	Valence electron concentration per atom
ν	Poisson's ratio
ω	Width of the transition of an individual mesh element
ϕ	Gaussian distribution of the transition temperature
ρ	Density

σ_{xx}	Normal stress along the x direction
σ_{yy}	Normal stress along the y direction
σ_{zz}	Normal stress along the z direction
σ	Standard deviation
A_f	Austenite finish temperature
A_s	Austenite start temperature
C	Curie constant
C_p	Heat capacity at constant pressure
$C_{p,baseline}$	Heat capacity of the baseline
E	Youngs modulus
FWHM	Full width at half maximum
f	Phase fraction of the ensemble
g	Transformation function of a single element
G	Gibbs free energy
H	Magnetic field
h, k, l	Miller indices
H_c	Coercive field
k_B	Boltzmann constant
M	Magnetization
m	Magnetic moment
m_0	Magnetic moment at 0 K
M_f	Martensite finish temperature
M_s	Martensite start temperature
n_W	Molecular field constant
N_{mag}	Number of magnetic degrees of freedom

p	Pressure
Q	Heat per mass
$\dot{Q}$	Heat flow per mass
$\dot{Q}_{baseline}$	Heat flow per mass of the baseline
S	Total entropy
S^h	Entropy of the high temperature phase
S^l	Entropy of the low temperature phase
S_{el}	Entropy of the electronic system
S_{lat}	Entropy of the lattice
S_{mag}	Entropy of the magnetic system
T	Temperature
$\bar{T}_t$	Average transition temperature
T^*	Reference temperature
T_C	Curie temperature
T_C^A	Curie temperature of the austenite phase
T_C^M	Curie temperature of the martensite phase
T_t	Transition temperature
T_{comp}	Compensation temperature
T_{ref}	Temperature of the reference
T_{rev}	Reversal temperature of a minor hysteresis loop
T_{sample}	Temperature of the sample
t	Time
U	Internal energy
V	Volume
x_t	Phase fraction in a single element

1 Introduction

In his book "Anna Karenina", Leo Tolstoi begins his story with the following words: "Happy families are all alike; every unhappy family is unhappy in its own way" [1]. It can be understood in the context that certain conditions like health, love, home, a basic income and many other factors must be fulfilled, which is the case for every happy family. If only one of these conditions is not fulfilled, the family cannot be happy [2]. Jared Diamond used this citation as a metaphor to explain the failure of the domestication of animals in his book "Guns, Germs and Steel" and introduces the Anna Karenina principle [2].

However, this principle is not only useful to understand how human civilization was able to breed livestock. It is also applicable to new evolving technologies on their way to market entry, acceptance and their implementation. There are many factors which need to be addressed in order to make a new technology competitive to others. If only one aspect cannot be fulfilled, the product will fail.

Solid-state magnetic refrigeration near room temperature is a young field of fundamental science [3], material science [4] and engineering [5]. Worldwide, there are many prototypical devices utilizing the magnetocaloric effect in order to obtain a thermal span and cooling power [6]. However, until now there is no mass product available on the market [5]. Prior to the commercialization of the magnetic refrigeration, there are a number of challenges to meet. The conventional gas compression technology for domestic purposes has been available for about 100 years and about one billion refrigerators are in use today [7]. It is predicted that the worldwide energy demand for cooling and air conditioning will multiply during this century, even exceeding the energy consumption for heating [8]. In particular, this is due to the strong growth of the needs in the developing countries India and China. Therefore, the development of new cooling processes has the potential to save large quantities of electric energy. In order to become a "happy" technology, magnetic refrigeration must be more efficient, less costly, environmentally friendly, comparable in weight and volume, and less noisy - just to mention some requirements.

Besides the numerous engineering challenges that need to be addressed [9], magnetocaloric materials with best properties are required. First of all, the adiabatic temperature change ΔT_{ad} should be as large as possible in small magnetic field changes because ΔT_{ad} is related directly to the temperature span of the working device [10]. Equally important is the isothermal entropy change ΔS_T, which defines how much heat can be transferred in one cooling cycle [11].

Since the magnetic field source is the most expensive part of a magnetocaloric cooling device, the volume in which the magnetic field is applied should be utilized as efficiently as possible [12] and an operation at a frequency of several Hz is desirable [13]. Therefore, a good thermal contact between the magnetocaloric material and a heat exchange fluid is the prerequisite [14]. For this reason, the thermal conductivity of the material should be maximized. Another important aspect to enhance the heat exchange is to use fine structures of the magnetocaloric material in order to obtain a large surface area

[15]. Consequently, the magnetocaloric material must be machinable into the desired shape without a reduction of the performance [16]. Furthermore, the magnetocaloric alloy should contain no harmful or critical elements in order to have a low environmental impact [10]. At the same time, the material must be capable to operate for millions of cycles without any fatigue [17]. Since the refrigerant is in permanent contact with the heat exchange fluid, the long-term corrosion resistance must be guaranteed too [18].

Nowadays, there are several material families which have a great potential for application [18, 19]. The benchmark material with outstanding properties is the element Gd, which is used in most magnetocaloric demonstrators [20, 21, 22]. In 1997, Pecharsky and Gschneidner discovered the Gd-based material class $Gd_5(Ge,Si)_4$ [23]. In this system, a comparable ΔT_{ad} to the one of Gd can be achieved, but the isothermal entropy change ΔS_T can be several times larger [24]. This discovery triggered a scientific excitement and enthusiasm about the magnetic refrigeration near room temperature and since then, the number of yearly publications on the topic has grown exponentially [25]. Both Gd and $Gd_5(Ge,Si)_4$ have the drawback that they contain the heavy rare earth Gd, which is among the most critical elements of the periodic table [26]. As an alternative, the material class $La(Fe,Si)_{13}$ was developed [27, 28]. It contains a small amount of the element La, but this light rare earth is much more abundant and less critical than Gd [26]. By compositional variations [29], the addition of Co [30], Mn and interstitial H [31], the transition temperature and the magnetocaloric properties can be tuned precisely to the desired temperature range.

Certain materials show large magnetocaloric effects even though they contain no rare-earth elements. There are numerous Fe_2P-type compounds which are interesting in terms of application [32]. One of the first intensively studied systems was Mn-Fe-P-As [33, 34]. Later, the toxic As was replaced by Si and Ge [35, 36]. The thermal hysteresis can be tuned down to below 5 K by an optimized preparation and compositional variation [37]. Another rare-earth-free material class are Ni-Mn-based Heusler alloys [38, 39]. They undergo a martensitic transformation, whereas the transition temperature can sensitively be tuned in a broad temperature window [40]. Large adiabatic temperature changes can be obtained in these materials near room temperature [19, 41]. This makes these outstanding Heusler alloys very promising and interesting for magnetic refrigeration. However, the large thermal hysteresis of the martensitic transition prevents the utilization of the large ΔT_{ad} under magnetic-field cycling. The focus of this thesis is the study of different application-related properties of Ni-Mn-In and Ni-Mn-In-Co as well as the reduction of the thermal hysteresis.

After the chapter about the fundamentals of the magnetocaloric effect and the martensitic transition, the general magnetic and magnetocaloric properties will be studied. On this basis, the adiabatic temperature change and the isothermal entropy change of certain compounds will be measured under cyclic conditions that are comparable to real working devices. Subsequently, it will be examined how the properties of the martensitic transition change for increasing magnetic-field-sweeping rates and for reduced sample sizes. Both studies are relevant for increasing the operation frequency of the potential magnetic refrigerator. Based on the size-dependent measurements, a finite element model will be introduced, which indicates the importance of mechanical stresses on the magnetostructural transition. Finally, aspects about the substitution of critical elements will be discussed.

2 Fundamentals

2.1 Magnetocaloric effect

In 1905, Langevin predicted theoretically that a paramagnet should change its temperature when being magnetized and demagnetized [42, 43]. This later so-called magnetocaloric effect was first observed experimentally by Weiss and Picard in 1917 in Ni [44]. Subsequently, further predictions have been made by Debye and Giaque to utilize this effect for cooling to low temperatures [45, 46]. Using paramagnetic salts like $Gd_2(SO_4)_3 \cdot 8H_2O$ it was possible to reach temperatures below 1 K in the years to follow [47]. In 1949, Giaque was honored with the Nobel Prize in Chemistry for his studies on the properties of matter at low temperatures [48]. The next milestone for magnetic refrigeration was reached by Brown only in 1976 [49]. He built the first magnetocaloric demonstrator working at room temperature using a heat exchanger of Gd plates and a superconducting magnet with a field of 7 T. With his setup, he could achieve a significant temperature span of 47 K [49]. However, the magnetocaloric material was not used as a regenerator. This means that the temperature of the magnetocaloric material was the same over its whole length and the temperature span was produced only in the fluid. In 1982, Barclay and Steyert introduced the active magnetic regenerator (AMR) [50]. In contrast to the machine of Brown, a temperature gradient in the magnetocaloric material develops during operation, wherefore it is referred to as regenerator. By using a single layer or a stack of different magnetocaloric materials, large temperature spans can be achieved in a rather simple design. Nowadays, nearly every prototypical device uses a variation of the AMR principle [13].

The magnetocaloric cooling cycle is schematically illustrated in Fig. 2.1. The starting point is in the paramagnetic state at a certain temperature in the upper left corner. When a magnetic field is applied adiabatically, the magnetocaloric effect manifests itself in an increase of the temperature of the material. This originates from the partial alignment of the magnetic moments along the magnetic field, which results in a decrease of the entropy of the magnetic system. However, under adiabatic conditions, the total entropy cannot change. For this reason, the decrease of the magnetic entropy is compensated by an increase of the lattice entropy, being nothing else but a heating of the material. By pumping an exchange fluid through the magnetocaloric body, the temperature can be lowered again. Removing the magnetic field results in a disordering of the magnetic moments and an increase of the magnetic entropy. This change is again compensated by the lattice entropy and the material cools down. Via the heat-exchange fluid, the cold magnetocaloric material can be used to absorb heat from the cooling compartment. This leads to an increase of the temperature of the regenerator and the cooling cycle starts over again.

The fundamentals of the magnetocaloric effect as well as the different kinds of transitions will be discussed in the following. In Fig. 2.2(a), a schematic of the magnetic behavior near the Curie temperature T_C of a ferromagnetic material is illustrated. The green curve represents $M(T)$ in zero field. At T_C, the

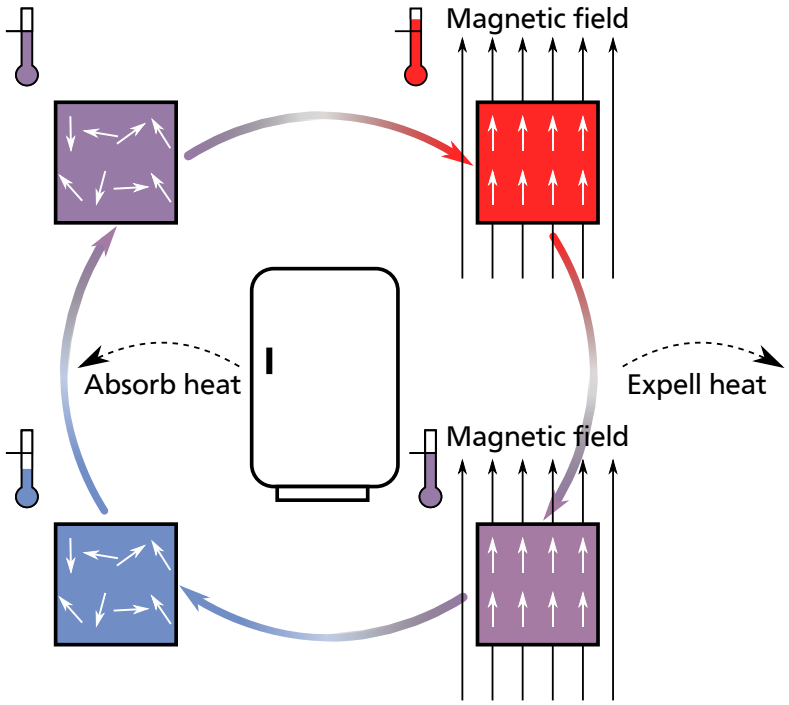

Figure 2.1: Schematic of the magnetic refrigeration cycle. This schematic was adopted from Fig. 1 of [33].

magnetization vanishes and the ferromagnet turns into a paramagnet. This is a pure magnetic-phase transition of second-order type. Elementary Gd is one of the most prominent materials undergoing such a transformation near room temperature [51]. It is worth noting that the zero-field magnetization curve cannot be measured directly due to the formation of magnetic domains, but it can be calculated for instance by Kuz'min's approach [52]. In magnetic fields, a certain magnetization is also observed in the paramagnetic phase due to the partial alignment of the spins (orange curve in Fig. 2.2(a)). The magnetic susceptibility of a paramagnet χ, being the ratio of the magnetization M and the magnetic field H, decreases with temperature, which can be described by the Curie-Weiss law [53]:

$$\chi = \frac{M}{H} = \frac{C}{T - T_C} \tag{2.1}$$

with the Curie constant C and the Curie temperature T_C. In order to describe the magnetocaloric effect, the consideration of the total entropy diagram is useful. Figure 2.2(b) shows the entropy of the material as a function of temperature in the vicinity of the second-order transition. The total entropy is a combination of three terms, namely the contribution of the lattice S_{lat}, of the magnetic moments S_{mag} and the electronic contribution S_{el} resulting in [54]

$$S(T,H) = S_{lat}(T,H) + S_{mag}(T,H) + S_{el}(T,H)\,. \tag{2.2}$$

The temperature dependence of the total entropy without magnetic field is schematically shown as a green curve in Fig. 2.2(b). For isobaric processes, the heat capacity C_p can be written as $C_p = T \cdot \frac{dS}{dT}$.

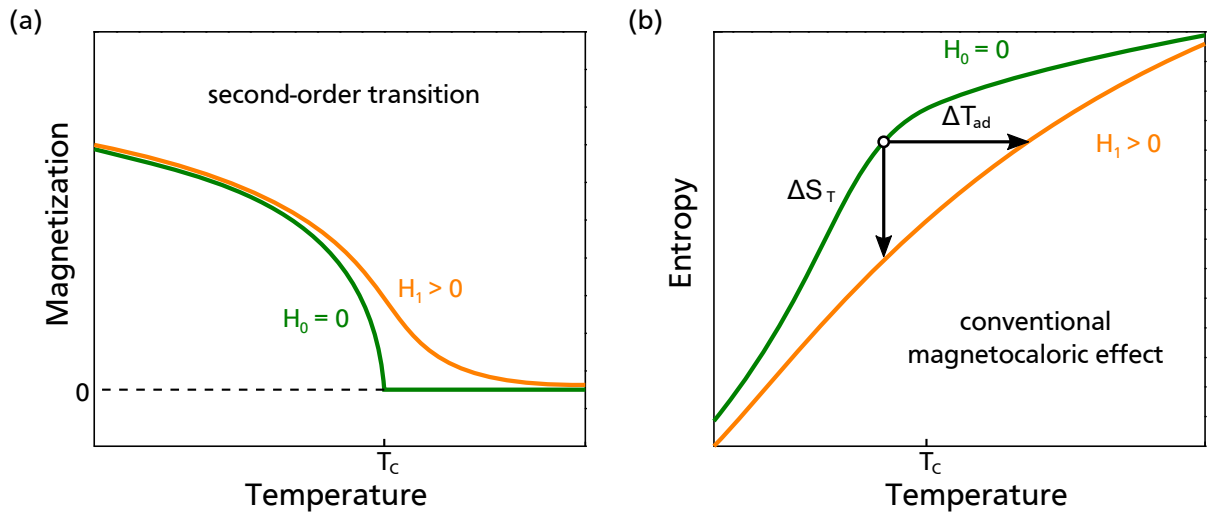

Figure 2.2: Schematic of the conventional second-order transition. (a) Magnetization as a function of temperature with (orange) and without (green) magnetic field. (b) Behavior of the total entropy in different magnetic fields.

Since the measurement of the heat capacity is a well-established technique, the total entropy can be calculated from C_p measurements:

$$S(T) = \int_0^T \frac{C_p}{T} dT \ . \tag{2.3}$$

By applying a magnetic field, the magnetic moments align to some extent. Therefore, the order of the magnetic system increases, which relates to a decrease of the magnetic entropy. For this reason, the external magnetic field lowers the entropy, which is illustrated by the orange curve in Fig. 2.2(b). This decrease in entropy is observed under isothermal conditions. The respective entropy change ΔS_T is plotted as a vertical arrow. Under adiabatic conditions, the total entropy stays constant. In order to compensate the decrease in the magnetic contribution, the lattice entropy increases. For this reason, the application of a magnetic field results in a heating of the material by ΔT_{ad}, which is illustrated as a horizontal arrow.

Both the adiabatic temperature change ΔT_{ad} and the isothermal entropy change ΔS_T can be quantified, which will be derived in the following. The Gibbs free energy G of a magnetic material can be written as

$$G = U - T\,S + p\,V - \mu_0\,m\,H \ . \tag{2.4}$$

The thermodynamic potential $G = G(T,p,H)$ is a function of the intensive variables temperature T, pressure p and the magnetic field H. Those are multiplied by the extensive variables entropy S, volume V and the magnetic moment m. U is the internal energy of the system. The total differential can be derived as

$$dG = V\,dp - S\,dT - \mu_0\,m\,dH \ . \tag{2.5}$$

In the following, only the situation under constant pressure will be discussed. Therefore, the term $V \cdot dp$ is zero. Based on Eq. (2.5), it can be concluded that the entropy is the negative partial derivative of G with respect to temperature in constant magnetic field

$$S(T,H) = -\left(\frac{\partial G}{\partial T}\right)_H . \tag{2.6}$$

The same applies for the magnetic moment m being the partial derivative of the Gibbs free energy with respect to the magnetic field at constant temperature

$$\mu_0\, m(T,H) = -\left(\frac{\partial G}{\partial H}\right)_T . \tag{2.7}$$

In the next step, the partial derivatives of Eq. (2.6) and (2.7), $\left(\frac{\partial S}{\partial H}\right)_T$ and $\left(\frac{\partial m}{\partial T}\right)_H$, are formed with respect to the other intensive variable, which is nothing else but the second mixed partial derivative of G with respect to T and H. Since the order of the partial differentiation is not important, the Maxwell relation can be derived:

$$\left(\frac{\partial S}{\partial H}\right)_T = \mu_0 \left(\frac{\partial m}{\partial T}\right)_H . \tag{2.8}$$

It should be mentioned that in experiment conventionally the specific magnetization M is considered instead of the magnetic moment m. Therefore, the entropy S and also the heat capacity C_p are given per mass in the unit of $\mathrm{J\,kg^{-1}\,K}$. Consequently, they are no longer extensive variables. From now on, only the specific variables will be considered. By integrating Eq. (2.8) over the magnetic field, the integral form of the Maxwell relation can be derived, from which the isothermal entropy change ΔS_T can be calculated for a given magnetic field change from zero to H:

$$\Delta S_T(T,H) = \mu_0 \int_0^H \left(\frac{\partial M}{\partial T}\right)_H dH . \tag{2.9}$$

Under adiabatic conditions, a change of the sample temperature is observed. This can be calculated using Eq. (2.9) and the specific heat capacity C_p [54]

$$\Delta T_{ad}(T,H) = -\mu_0 \int_0^H \frac{T}{C_p} \left(\frac{\partial M}{\partial T}\right)_H dH . \tag{2.10}$$

From Eq. (2.9) and (2.10) it is apparent that the strength of the magnetocaloric effect of a second-order transition, namely ΔS_T and ΔT_{ad}, can be estimated from magnetization measurements as a function of temperature in different magnetic fields.

In contrast to the second-order, a conventional first-order transition is schematically shown in Fig. 2.3. Such a transformation is for instance observed in the material La-Fe-Si for some Si contents [27]. A discontinuity in magnetization is observed in both, the magnetic and total entropy curves due to the

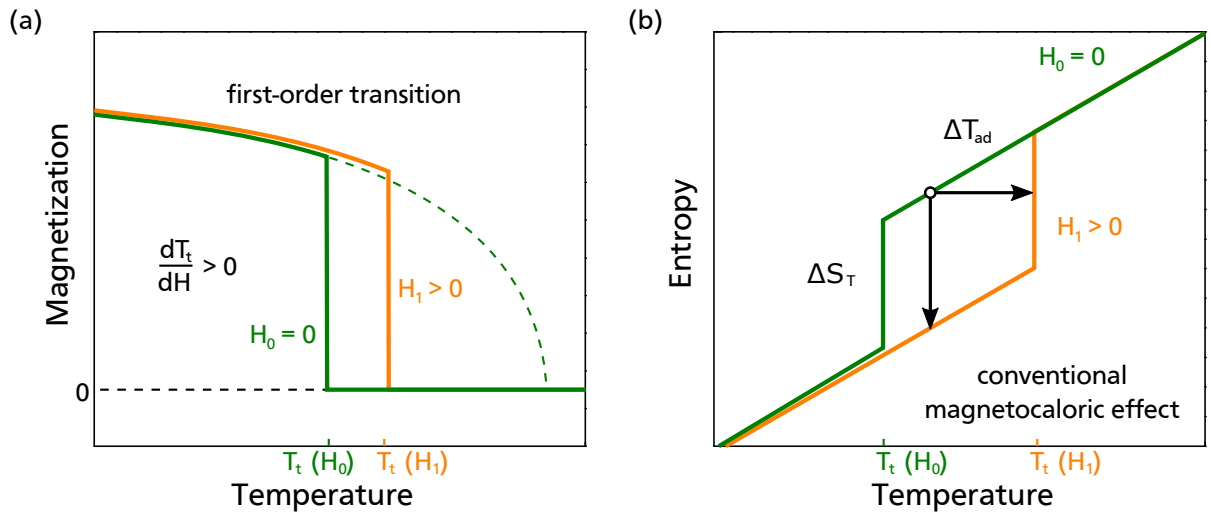

Figure 2.3: Schematic of the conventional first-order transition. (a) Magnetization as a function of temperature with (orange) and without (green) magnetic field. (b) Behavior of the total entropy in different magnetic fields.

transformation between two structurally different phases. In the idealized picture in Fig. 2.3(a), the ferromagnetic phase is stable at low temperatures. At T_t, the material transforms into the high temperature phase with low magnetization. In principle, the low temperature phase would still be ferromagnetic up to its Curie temperature, which is illustrated by the extrapolated magnetization curve (green dashed line). However, this behavior is interrupted by the magnetostructural transition.

The application of a magnetic field results in the shift of the transition temperature T_t. This is happening because the magnetic field stabilizes the phase with higher magnetization, being the low temperature phase [55]. The shift of the transition temperature in magnetic fields $\frac{dT_t}{dH}$, which is positive for a conventional first-order transition, can be understood as the driving force of the magnetocaloric effect in such a material. For instance, if one would stay in the paramagnetic phase at a temperature between $T_t(H_0)$ and $T_t(H_1)$, the application of the magnetic field H_1 would result in the conversion of the material into the low temperature phase. In terms of the magnetocaloric effect, it now depends on whether isothermal or adiabatic conditions are present.

The corresponding total entropy diagram is shown in Fig. 2.3(b). Also the entropy curve has a discontinuity in the ideal case. However, due to the shift of the transition temperature in magnetic fields, the $S(T)$ diagram has the shape of a parallelogram (green and orange curves in Fig. 2.3(b)) [56]. When keeping the temperature constant, the entropy decreases under field application. Therefore, ΔS_T is also negative (vertical arrow in Fig. 2.3(b)), as was the case for the second-order transition above. When a magnetic field is applied adiabatically, the $S(T)$ diagram is crossed horizontally, which results in an increase in the temperature of the material. It is worth noting that in the schematic, the entropy curves do not overlap in the low temperature region of Fig. 2.3. This is because the magnetic field affects the ferromagnetic phase by slightly increasing the ordering of the magnetic moments, counteracting the disorder due to thermal fluctuations. Therefore, the magnetization is slightly increased, as shown by the difference between the green and the orange curves in Fig. 2.3(a). Consequently, the total entropy is slightly

reduced in the ferromagnetic phase under magnetic field application. A similar effect was also observed in Fig. 2.2, which was related to the purely second-order transition. This implies that in Fig. 2.3, both the first- and the second-order transition overlap.

Strictly speaking, the Maxwell relation (Eq. (2.9)) cannot be used for a first-order transition. The problem is that for an ideal transformation, as illustrated in Fig. 2.3, the derivative $\frac{dM}{dT}$ does not exist due to the jump in magnetization at the transition temperature. However, it was shown in literature that the Maxwell relation can also be used for describing a first-order transition, but special attention must be given to the measurement protocol [57]. Another possibility to estimate the magnetocaloric effect is the usage of the Clausius-Clapeyron equation, which will be derived in the following as performed in [58]. For this approach, the Gibbs free energy is considered again (Eq. (2.4)). Under constant pressure, G is only a function of the temperature and the magnetic field. At the transition temperature T_t, the Gibbs free energy of the high (superscript h) and the low temperature phase (superscript l) must coincide

$$G^l(T_t, H) = G^h(T_t, H)\ . \tag{2.11}$$

Changing the magnetic field H will shift the transition temperature T_t, as it was schematically shown in Fig. 2.3. For the two different magnetic field strengths H_1 and H_2, the corresponding Gibbs free energy can be written for the isobaric case as:

$$U^l - T_t(H_1)S^l - \mu_0 M^l H_1 = U^h - T_t(H_1)S^h - \mu_0 M^h H_1 \tag{2.12}$$

$$U^l - T_t(H_2)S^l - \mu_0 M^l H_2 = U^h - T_t(H_2)S^h - \mu_0 M^h H_2\ . \tag{2.13}$$

Here it was assumed that the magnetic field only affects the transition temperature without changing the magnetization M, the internal energy U and the entropy S. With regard to Fig. 2.3, this is only a reasonable assumption if the magnetocaloric effect related to the second-order transition of the ferromagnetic phase is negligible at the transition temperature. Subtracting Eq. (2.13) and (2.12) results in

$$S^l \cdot (T_t(H_2) - T_t(H_1)) + \mu_0 M^l \cdot (H_2 - H_1) = S^h \cdot (T_t(H_2) - T_t(H_1)) + \mu_0 M^h \cdot (H_2 - H_1)\ . \tag{2.14}$$

This equation can be simplified by using $\Delta T_t = T_t(H_2) - T_t(H_1)$ and $\Delta H = H_2 - H_1$. Furthermore, the entropy difference between the high and the low temperature phase $S^h - S^l$ is written as ΔS_t, which is the entropy change of the complete phase transition. The difference in the magnetization between the two phases is simplified to $\Delta M = \left|M^h - M^l\right|$, resulting in the Clausius-Clapeyron equation:

$$\Delta S_t = -\mu_0 \Delta M \frac{\Delta H}{\Delta T_t}\ . \tag{2.15}$$

It relates the entropy change with the shift of the transition temperature in magnetic fields and the difference in the magnetization between the two phases. The assumptions made here imply that if the

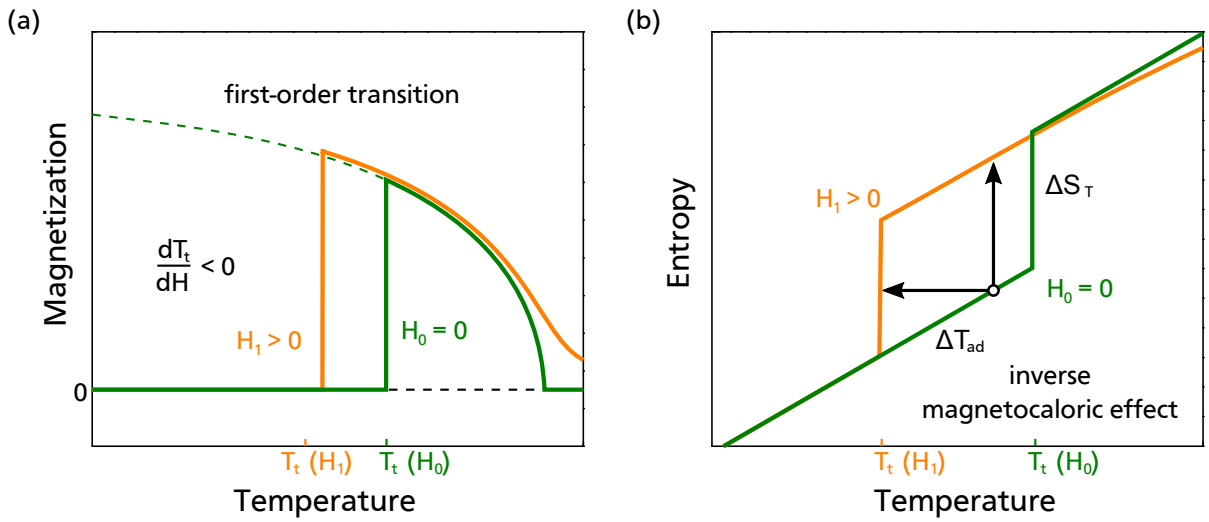

Figure 2.4: Schematic of the inverse first-order transition. (a) Magnetization as a function of temperature with (orange) and without (green) magnetic field. (b) Behavior of the total entropy in different magnetic fields.

transition is rather close to the Curie temperature of the ferromagnetic phase, the Clausius-Clapeyron equation can only give an estimate of the magnetocaloric effect related to the first-order transition.

As a third example, the inverse first-order transformation is schematically illustrated in Fig. 2.4. Such a transition is observed for instance in Ni-Mn-based Heusler alloys [59] or in Fe-Rh [60]. In the inverse case, also a structural phase conversion is taking place. In contrast to Fig. 2.3, the low temperature phase has a low and the high temperature phase has a high magnetization, respectively (see Fig. 2.4(a)). For this reason, a magnetic field shifts the transition to lower temperatures and $\frac{dT_t}{dH}$ is negative. The corresponding total entropy diagram is shown in Fig. 2.4(b). In the ideal case, the $S(T)$ diagram also has the shape of a parallelogram but in comparison to Fig. 2.3(b), the green and the orange curve are exchanged. As a result, the adiabatic temperature change ΔT_{ad} is negative and the isothermal entropy change ΔS_T is positive. Again, the first and the second-order transition are overlapping, which can be seen by the increased magnetization in magnetic fields in Fig. 2.4(a) and by the crossing of the green and the orange $S(T)$ curve in Fig. 2.4(b).

Strictly speaking, a magnetocaloric material with a first-order transition always possesses a certain thermal hysteresis. This means that the back and forth transformation does not take place at the same temperature. In fact, the heating and the cooling branch of the magnetization curve are separated by the thermal hysteresis, which is illustrated for a conventional first-order transition in Fig. 2.5(a). The corresponding $S(T)$ diagram is shown in Fig. 2.5(b). Such a behavior is observed in certain Fe_2P-type materials, but also in La-Fe-Si, a certain thermal hysteresis is observed depending on the composition [61]. Due to the existence of the thermal hysteresis, also the entropy curves under heating and cooling do not coincide. This has far-reaching consequences on the magnetocaloric effect under magnetic-field cycling. If there was no thermal hysteresis related to the transition, then the ΔT_{ad} and ΔS_T as shown in Fig. 2.2, 2.3 and 2.4 would be the same in cyclic operation. But due to the hysteresis, a reversible effect can only be obtained in the highlighted areas of Fig. 2.5(b) and 2.6(b).

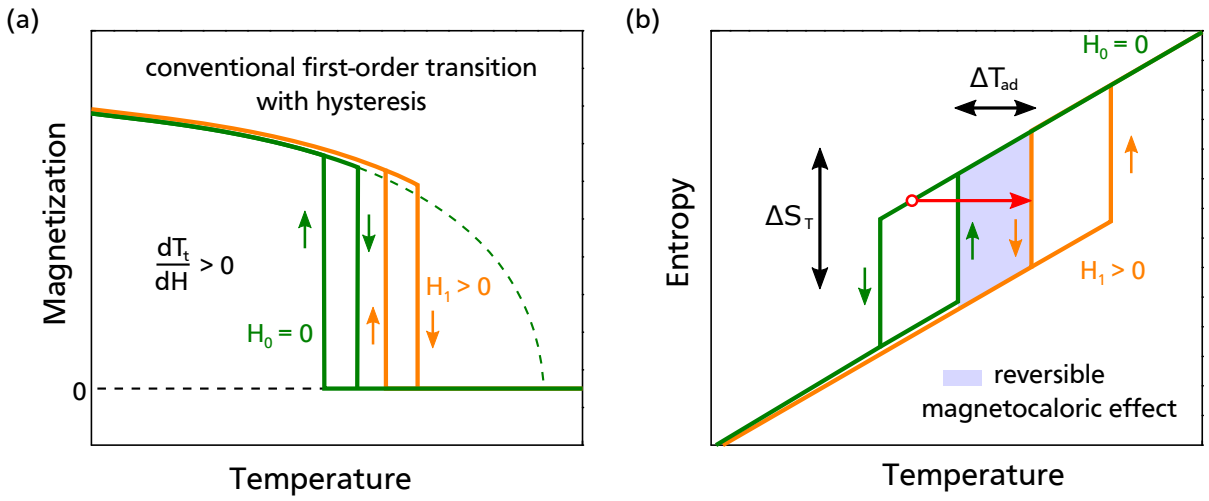

Figure 2.5: Schematic of the conventional first-order transition with thermal hysteresis. (a) Magnetization as a function of temperature with (orange) and without (green) magnetic field under heating and cooling. (b) Behavior of the total entropy in different magnetic fields. The reversibility area is highlighted in blue. The adiabatic heating in the field application is shown as a red arrow.

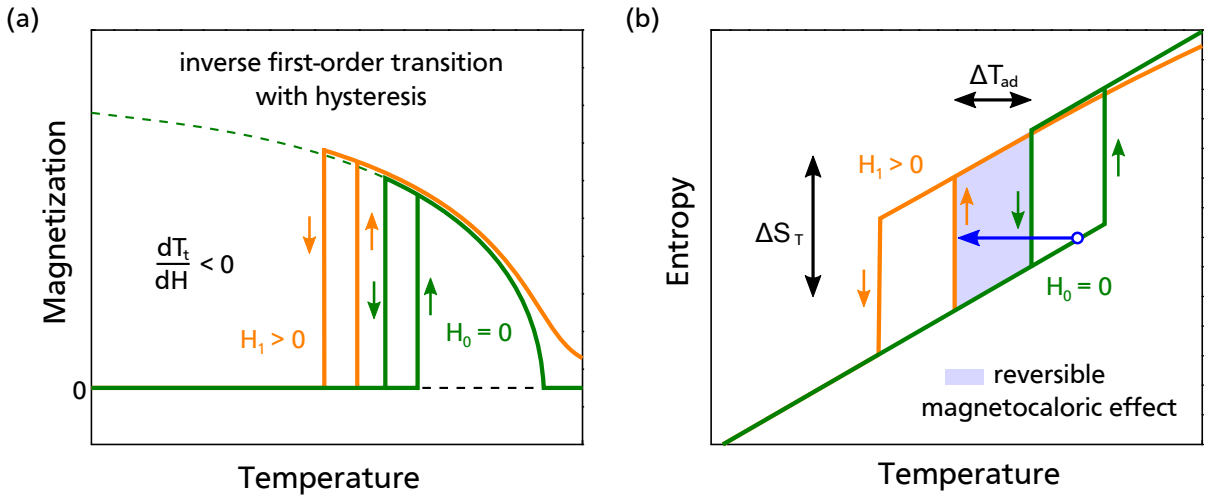

Figure 2.6: Schematic of the inverse first-order transition with thermal hysteresis. (a) Magnetization as a function of temperature with (orange) and without (green) magnetic field under heating and cooling. (b) Behavior of the total entropy in different magnetic fields. The reversibility area is highlighted in blue. The adiabatic cooling in the first field application is shown as a blue arrow.

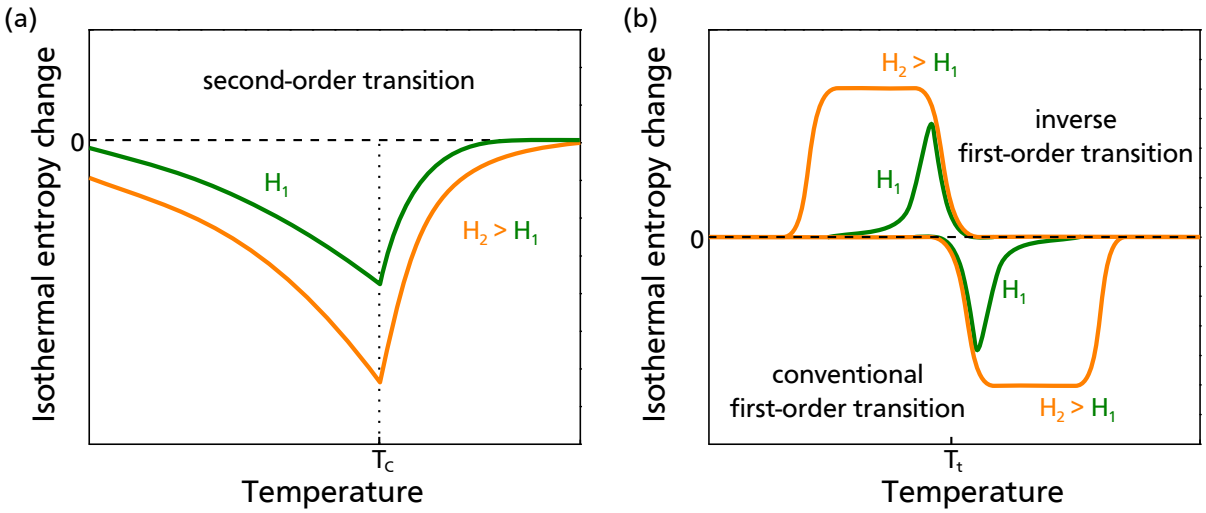

Figure 2.7: Schematic of the isothermal entropy change ΔS_T for a second-order material (a) and for conventional and inverse first-order materials (b).

The red arrow in Fig. 2.5(b) illustrates how the material, being in the high temperature phase, heats when the magnetic field is applied for the first time. About half of the material transforms in this example. However, when the magnetic field is removed again, the initial state cannot be reached. In fact, the adiabatic temperature change under cycling is smaller than indicated by the horizontal double-sided arrow. This description of the thermal hysteresis can be transferred straightforwardly to the first-order transition of inverse magnetocaloric materials, which is shown in Fig. 2.6. The application of a magnetic field transforms the material into the high temperature phase being ferromagnetic. Starting in the paramagnetic phase, a large cooling effect is obtained under field application, as indicated by the blue arrow. In this example, about half of the material transforms. When the magnetic field is removed again, the obtainable temperature change is drastically reduced due to the thermal hysteresis, as illustrated by the double-sided arrow in Fig. 2.6.

The three classes of transitions show very different features in the $S(T)$ diagram. Consequently, also the temperature-dependences of the isothermal entropy change ΔS_T and the adiabatic temperature change ΔT_{ad} in magnetic fields are different for first- and second-order transitions. The schematic in Fig. 2.7 shows ΔS_T for a second-order transformation in the vicinity of T_C in (a) and for a conventional and an inverse first-order transition near T_t in (b). According to Fig. 2.2(b), the entropy change of a second-order transition is negative when a magnetic field is applied. The maximum ΔS_T is always reached at the Curie temperature T_C, even in different magnetic fields. In fact, a significant entropy change is observed in a broad temperature range, which is useful for application. The value of the maximum entropy change scales with the applied magnetic field. This scaling behavior is not linear, because the increase in ΔS_T is weakened in higher magnetic fields [62]. However, the temperature-dependence of the entropy change of a second-order transition can be described in a more universal way with the help of scaling laws [63].

A conventional first-order material also has a negative ΔS_T under field application, which is shown in Fig. 2.7(b). However, the isothermal entropy change saturates at some point and a plateau occurs, which is shown by the orange curve. This is an indication that the transformation is completed in the respective

magnetic field change. The formation of a plateau is originated in the special shape of the $S(T)$ diagram (see Fig. 2.3(b)). In higher magnetic fields, the plateau grows towards higher temperatures, but the left flank always remains at T_t. This behavior is due to the fact that a magnetic field shifts the transition temperature upwards. The higher the field, the broader the temperature window becomes in which the transformation can be induced and completed. If the temperature is too low, the material is already in the ferromagnetic phase and therefore, no transformation can take place. A partial transformation is observed when the magnetic field is not large enough. In this case, the ΔS_T curve has a peak shape at T_t.

For an inverse magnetocaloric material, a similar behavior is observed, which is also illustrated in Fig. 2.7(b). However, as discussed above, the entropy change is negative and the transition temperature is lowered in magnetic fields (see Fig. 2.4). Therefore, the ΔS_T plateau grows towards lower temperatures. It is worth noting that a similar trend is also observed for the adiabatic temperature change ΔT_{ad}.

The temperature-dependences of the magnetocaloric effect of the first- and second-order transformation differ not only in their shape. The width of the ΔS_t plateau of a first-order transition is defined by the shift of the transition temperature in magnetic fields. This value is typically much below $10\,\mathrm{K\,T^{-1}}$. In terms of application, it needs to be considered that the temperature window in which a magnetocaloric effect can be obtained is therefore very small in comparison to a second-order transition. One way to overcome this drawback of first-order materials is the production of stacked heat exchangers [64]. In such a design, layers of materials with slightly different transition temperatures are lined up. Therefore, it is necessary to tune T_t very precisely in fine temperature steps. By this approach it is possible to enhance the temperature span in a magnetic cooling device [50].

There are numerous different materials, with either first-order or second-order transitions, which are interesting for magnetocaloric cooling. Some of them were already mentioned above. Figure 2.8 (taken from [19]) illustrates schematically the adiabatic temperature change ΔT_{ad} in a magnetic field change of 2 T of selected magnetocaloric materials as a function of the Curie temperature T_C and the transition temperature T_t, respectively. Pure Gd undergoes a second-order transition and is the benchmark magnetocaloric material, since it has a T_C of 291 K and shows a very large temperature change of about 5 K in 2 T. For obvious reasons, the Curie temperature of elementary Gd is fixed. However, it is possible to lower T_C for instance by slight additions of the element Y [65]. The opposite effect is observed if a Gd-Pd-based compound is used instead as shown in Fig. 2.8.

Materials with a first-order transformation have the advantage that similar ΔT_{ad} values can be achieved, but the corresponding ΔS_T can be much larger than in Gd. This is due to the coupling of the structural transition and the magnetic transformation. $Gd_5Si_xGe_{4-x}$ undergoes a conventional first-order transition near room temperature, but only in a limited stoichiometry range with $x = 1.98$ to 2.09 (see Fig. 2.8). The transition temperature can be adjusted precisely by varying the ratio between Si and Ge. For higher Si concentrations, the transition turns into a second-order type. However, the amount of the heavy rare-earth Gd is very high. This fact will prevent the utilization of $Gd_5(Si,Ge)_4$ for magnetic refrigeration on a large scale. The material costs would simply too high [66, 8].

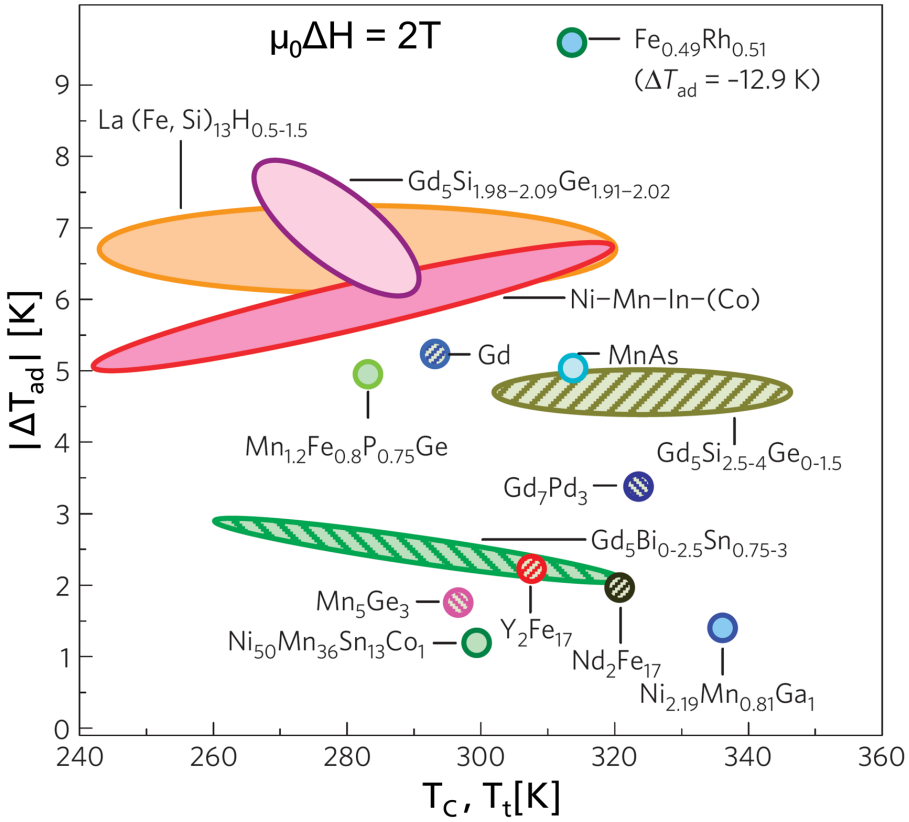

Figure 2.8: Comparison of the adiabatic temperature change in $2\,\mathrm{T}$ of different magnetocaloric materials as a function of the working temperature. Materials with a first-order transition are shown as filled ellipses and second-order materials are plotted with striped filling. This image is taken from Ref. [19].

A much cheaper alternative is partially hydrogenated $La(Fe,Si)_{13}H_x$ [67]. It contains much less rare-earths and in addition, the element La is much less critical than Gd [26]. The H-free material $LaFe_{11.8}Si_{1.2}$ has a conventional first-order transformations at about 200 K. This is much too low for room-temperature application, but by adding H on interstitial lattice sites, T_t can be increased. The amount of H in the compound defines the transition temperature. Fully-hydrogenated $La(Fe,Si)_{13}$ has a T_t around 340 K. This is far too high for the implementation into a household fridge. In order to decrease T_t, less H must be incorporated into the lattice. However, one problem occurs in partially hydrogenated $La(Fe,Si)_{13}H_x$. It is found that the local H concentration in the material is not stable when the high and the low temperature phase coexist. A redistribution of H is observed resulting in an enrichment of H in the phase with a larger unit cell, this being the ferromagnetic phase [68]. Consequently, the single T_t divides into two. Another approach to lower the transition temperature is the partial substitution Fe with Mn. Therefore, the material $La(Fe,Si,Mn)_{13}H_x$ can be fully hydrogenated, which results in a stable transition temperature T_t [69]. However, the hydrogenation process of the base ingot leads to the decrepitation of the material. For this reason, hydrogenated La-Fe-Si is only available in powder form, but it can be bound together for instance using an epoxy [16].

Three different Heusler compounds are shown in Fig. 2.8, namely Ni-Mn-In-(Co), Ni-Mn-Ga and Ni-Mn-Sn-Co. Among them, the In-based alloys are the most promising in terms of magnetic refrigeration. This material undergoes an inverse magnetostructural transition as schematically shown in Fig. 2.4 and 2.6. In fact, a martensitic transformation between the low temperature martensite phase and the high temperature austenite phase is observed. Applying a magnetic field results in a significant cooling of the Heusler alloy and values up to −8 K in 2 T could be achieved [41]. This makes the rare-earth free Ni-Mn-In-(Co) an outstanding magnetocaloric material class. However, these large ΔT_{ad} values cannot be observed in the following field-application cycles due to the large thermal hysteresis in these materials. The mastering of the thermal hysteresis is therefore the central task of this thesis in order to enhance the suitability of Heusler alloys for magnetic refrigeration. Before the special features of the martensitic transition will be introduced, some general rules and characteristics of the interesting material class of Heusler alloys will be discussed in the following section.

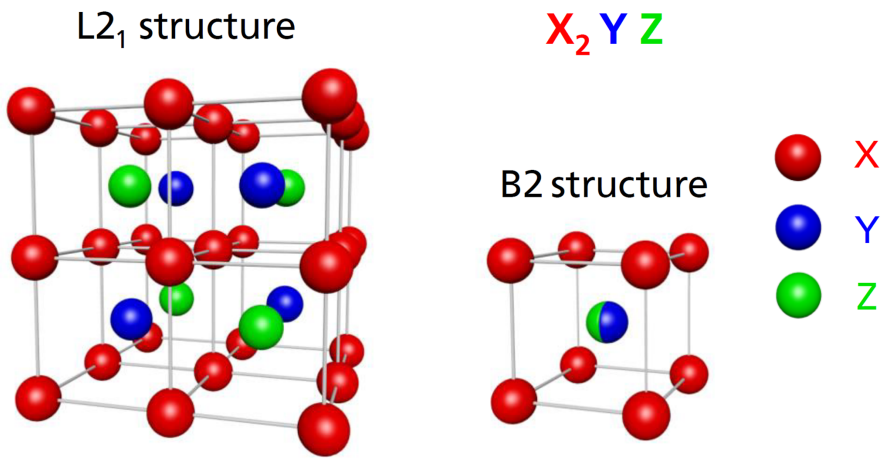

Figure 2.9: Schematic illustration of the $L2_1$ and the B2 structure of a Heusler alloy with the chemical composition X_2YZ. The X, Y and Z atoms, which are shown in red, blue and green respectively, occupy different sublattices.

2.2 Heusler alloys

The material class of Heusler compounds are named after Friedrich Heusler, who discovered in 1903 that an alloy of Cu, Mn and Al is ferromagnetic even though this is not the case for the three base elements [70]. The reason for this originates from the special crystallographic structure of the material. Cu_2MnAl was the first Heusler compound but nowadays there are more than 1000 known Heusler alloys [71]. The typical full Heusler composition is X_2YZ. The crystal structure is schematically illustrated in Fig. 2.9(a). The X, Y and Z elements occupy four different fcc (face centered cubic) lattices, which are shifted along the space diagonal. It is referred to as the $L2_1$ Heusler structure with the space group $Fm\bar{3}m$ [72]. The X atoms are positioned on the (0,0,0) and the $(1/2, 1/2, 1/2)$ lattice whereas the Y and Z atoms occupy the $(1/4, 1/4, 1/4)$ and the $(3/4, 3/4, 3/4)$ lattices, respectively [73]. Mainly 3d and 4d elements are used as X and Y atoms but also rare-earths can be incorporated in the Y lattice. Typically, main group elements are taken as Z atoms [74]. Atomic disorder in the Heusler structure, which can be controlled by heat treatment, plays an essential role [75]. The most important disordered state is the B2 structure, which is shown in Fig. 2.9(b). In this case, the Y and the Z lattices are mixed. Therefore, the unit cell can be described as a bcc (body centered cubic) lattice with X atoms in the corners and Y and Z atoms with 50 % occupancy in the middle position. For instance, in Ni-Mn-based Heusler alloys, the annealing temperature defines which structure is present [76].

From neutron scattering it was found that the magnetic moment in Cu_2MnAl is related to the Mn atoms [78]. This holds true for most of the Mn-based Heusler compounds and the magnetic moment is in the range of $4\mu_B$ [79]. Elementary Mn couples antiferromagnetically. However, the interatomic distance between neighboring Mn atoms is much larger in the $L2_1$ structure. As a consequence, the Mn atoms couple ferromagnetically as for instance in Cu_2MnAl. This behavior can be described in terms of the Bethe-Slater curve which is shown in Fig. 2.10. The exchange energy of the elements Fe, Co and Ni is positive and therefore they are ferromagnetic. Elementary Mn has a negative exchange energy but by

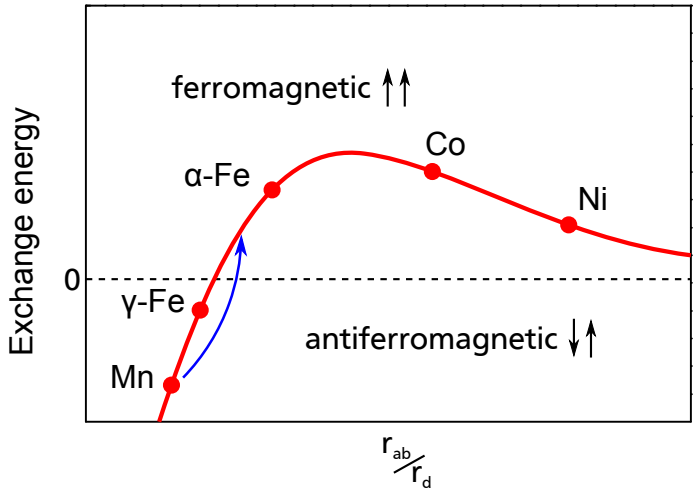

Figure 2.10: Bethe-Slater curve which illustrates the exchange energy as a function of the ratio of the interatomic distance r_{ab} to the radius of the 3d orbital r_d for different elements [77]. The blue arrow indicates how Mn can couple ferromagnetically by expansion of the lattice.

expanding the distance between the Mn atoms, it can be moved to the positive region. The ferromagnetic behavior in Mn-based Heusler alloys is consequently attributed to the magnetic moment of the Mn atoms. An important exception are Co-containing Heusler compounds in which also the Co carries a magnetic moment [73].

Furthermore, it is found that the magnetic moment of the Heusler alloy depends on the number of the valence electrons (N_v), which is defined by the chemical composition of the material [81]. According to the Slater-Pauling rule, the magnetic moment per formula unit can be calculated with $m = (24 - N_v)\,\mu_B$ [81]. Figure 2.11 shows the magnetic moment of several different Heusler alloys as a function of the valence electron number per formula unit showing a linear behavior, taken from Ref. [80]. Only the increasing branch of the Slater-Pauling curve is shown because for Heusler alloys, only the region with a small number of electrons applies. This on the other hand implies that the magnetic moments are localized.

Heusler alloys drew a lot of attention in the last two decades especially due to their suitability for spintronic applications [82]. In spintronics, not only the charge of electrons is used but also their spin [83]. For this kind of technology, a large spin polarization at the Fermi level is needed. In a normal metal, both the spin-up and spin-down bands are equally occupied. However in a ferromagnet, the densities of states are shifted in energy against each other. Therefore, a certain spin polarization is observed in every ferromagnetic material, but for instance in Fe, Ni and Co, the spin polarization accounts for only 40 to 50 % [83]. In half-metallic ferromagnets, the one spin band is partly filled and a metallic behavior is observed. For the other spin states, a band gap occurs at the Fermi energy and therefore these spin electrons show a semiconducting behavior. The resulting spin polarization in these materials can be much higher than for instance in Fe, ideally up to 100 % [84].

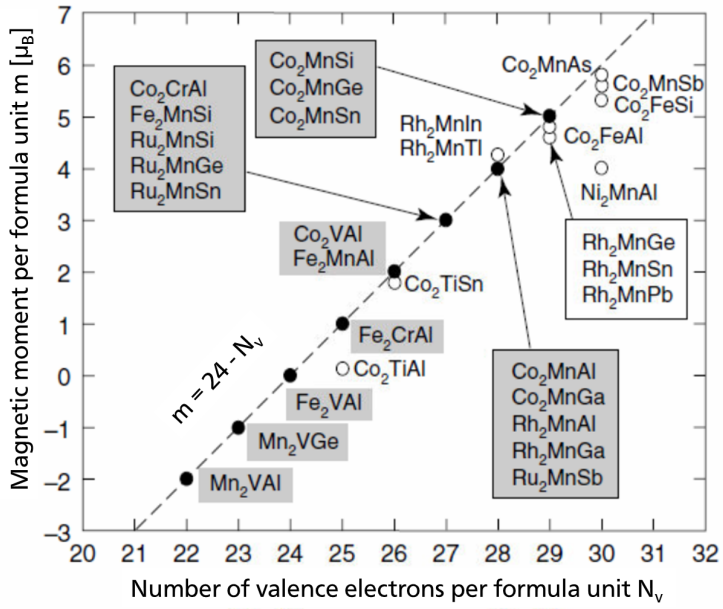

Figure 2.11: Slater-Pauling curve of the low valence electron concentration region (dashed line). The magnetic moment of several Heusler compounds are plotted as points. Figure adapted from Ref. [80], with the axis labels changed according to the notation of this thesis.

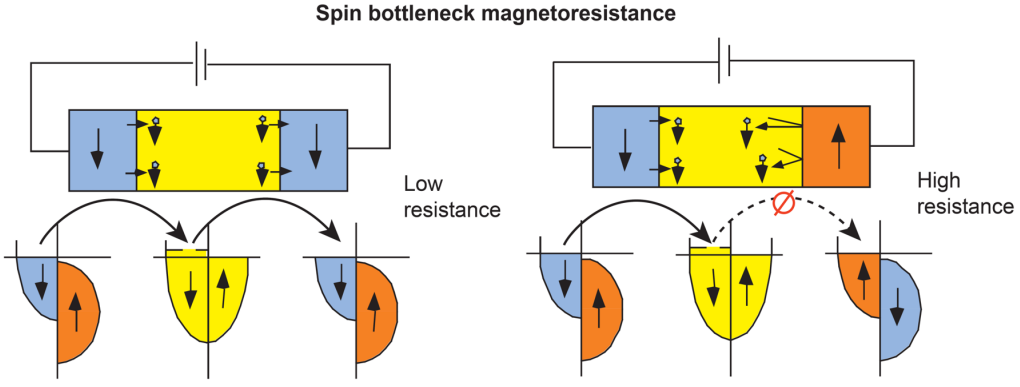

Figure 2.12: Schematic of a spin valve [83]. The low resistance configuration is shown on the left, the high resistance state is shown on the right.

Half metallic Heusler alloys have been widely used for two decades especially for magnetic data storage in hard-disk drives [85]. The commercialization was possible due to the discovery of the giant magnetoresistance effect (GMR effect) in layered magnetic thin-films. A schematic of a so-called spin valve is shown in Fig. 2.12, which is taken from the paper of Prinz [83]. In such a sandwich structure, a voltage is applied between two half-metal layers that are connected with a normal metal. If the magnetization of the two ferromagnetic layers is parallel, the spin-down electrons can travel through and the resistance is low. However, if both layers are aligned antiparallel, the spin-down electrons coming from the left cannot enter the right layer since all spin-down states are occupied. For this reason, a large electrical resistance is observed. This giant magnetoresistance effect is just one of many examples for the multifunctionality of the material class of Heusler compounds; and it is this rich multifunctionality which enables the development of new technologies.

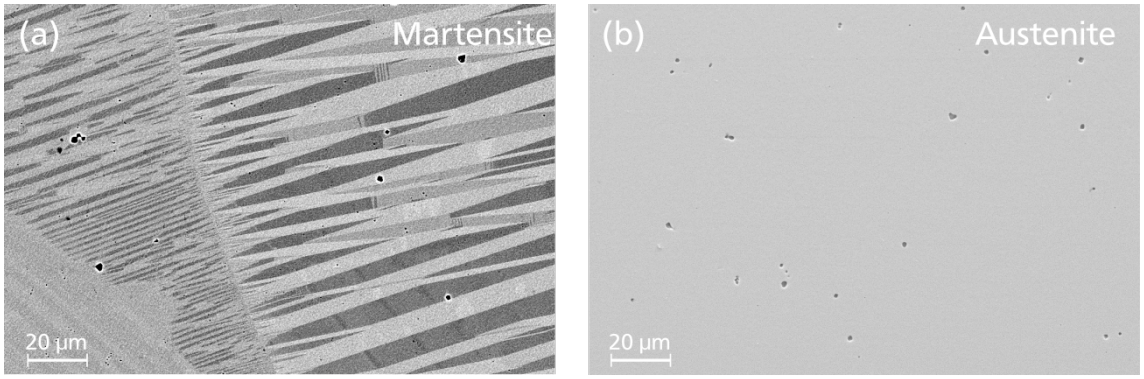

Figure 2.13: Scanning electron microscopy image in backscattered electron contrast of martensite (a) and austenite (b) [91].

2.3 Martensitic transition in Ni-Mn-based Heusler alloys

For the application of magnetic refrigeration, the Ni-Mn-X (X = Ga, In, Sn, Sb, Al) Heusler alloys are interesting because they perform a martensitic transition near room temperature, which is combined with a large change in magnetization [59, 86, 19, 87]. The martensitic transformation between two structurally different phases takes place by a diffusionless rearrangement of atoms of the solid [88]. The cubic austenite phase, which is stable at high temperatures, transforms into the low temperature martensite phase, which is tetragonal and has therefore a lower crystal symmetry [89]. This first-order transition is driven by nucleation and growth of the new phase. Consequently, a phase boundary between martensite and austenite forms, which is called habit plane [89]. Since the lattice parameters of the cubic austenite and the tetragonal martensite are different, a certain lattice mismatch occurs. In order to prevent strong elastic and plastic deformation of the crystal, the martensite forms twin boundaries [90], which results in a complex microstructure in the low temperature phase.

Figure 2.13 shows two electron microscopy images of the martensite (a) and the austenite phase (b) using the backscattered electron contrast. Besides some pores, there is no contrast visible in the austenitic sample. In comparison to that, the martensite shows a really complex structure in the micrometer range and also substructures are visible for instance in the lower right part of Fig. 2.13(a). Certain areas of the sample have different crystallographic orientations, which results in the strong image contrast. These areas are called variants of martensite, which are separated by twin boundaries. The twinning of the material takes place because it is energetically more favorable, since the elastic energy due to the lattice mismatch can be reduced.

Figure 2.14 illustrates the twinning on the nanoscale schematically. It is adopted from Fig. 2.1 of Ref. [92]. In comparison to the cubic austenite, the martensite lattice is distorted tetragonally (Fig. 2.14(a)). In the 2D case, there are two possible variants of martensite, which are shown in green and yellow. During the phase transformation starting from the cubic austenite, a combined structure of the two martensite variants forms. The twin boundary (red line) costs energy due to the lattice deformation in its proximity, but it is more favorable than the transformation from the cubic lattice to the single

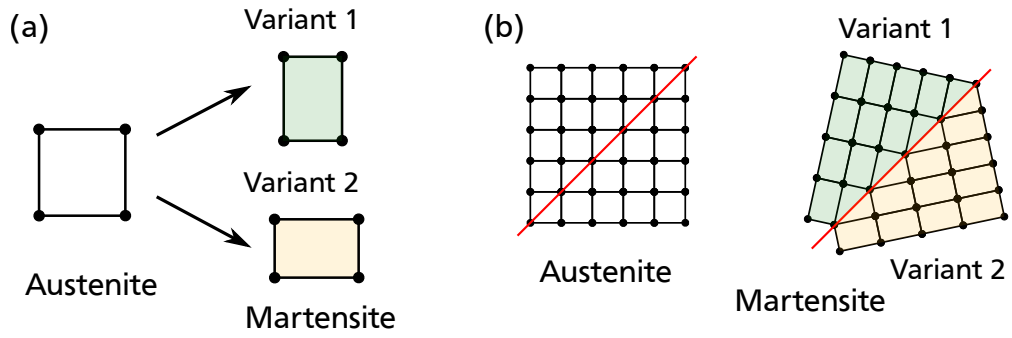

Figure 2.14: Schematic of the formation of nano twins during the martensitic transformation. This image was adapted from Fig. 2.1 of [92].

variant state. The twin boundary between the different variants can be moved for instance by applying a small mechanical stress. As a result, a large change in the volume of the material is observed. This so-called pseudo plasticity can be reverted by transforming the material back to the austenite state. Heusler alloys and especially Ni-Mn-Ga have drawn a lot of attention in the last years due to large obtainable strains up to 12 %, which makes them interesting for shape memory applications [93].

It is worth mentioning that microscopic techniques with high resolution are necessary to image the twinning on the atomic level. However, as shown in Fig. 2.9, martensitic structures, variants and twin boundaries are visible in the micrometer range and even macroscopic objects in the millimeter range can be seen in Fig. 4.26 later in this thesis. The origin of this is the hierarchical nature of the martensite twinning. Therefore, the total energy of the system can only be reduced efficiently if a combined martensite structure on different length scales is formed [94].

As already mentioned, the martensitic transformation is initiated by the formation of nuclei. The Gibbs free energy G of martensite and austenite as a function of temperature is schematically illustrated in Fig. 2.15. At the temperature T_0, the Gibbs free energies of both phases are equal. However, a certain energy barrier must be overcome in order to start the transformation process. For this reason, the material must be cooled below T_0 to start the formation of martensite or it must be heated above T_0 to transform it into austenite. The difference between the Gibbs free energy of martensite and austenite, ΔG_{M-A} and ΔG_{A-M} respectively, acts as the driving force of the transition. It describes how much energy can be gained during the transformation and it increases the stronger the material is undercooled/overheated [95]. At the martensite-start temperature M_s, the gain in energy exceeds the barrier and the formation of martensite is initiated. The same applies for the austenite-start temperature A_s. In the three-dimensional case, this nucleation barrier is determined by the energy of the phase boundary between the first nucleus and the parent phase. The transformation can only be initiated if the energy of the phase-boundary, which is related to the surface of the nucleus, is smaller than the gain due to the phase formation, being proportional to the volume. This is only possible if the nucleus is larger than a certain critical size, which depends on the temperature. However, local defects like grain boundaries or cracks can reduce the energy barrier and support the nucleation process [96]. Once a nucleus of the new phase is existing, it growths further until it hits a barrier like another nucleus or a high angle grain boundary [95].

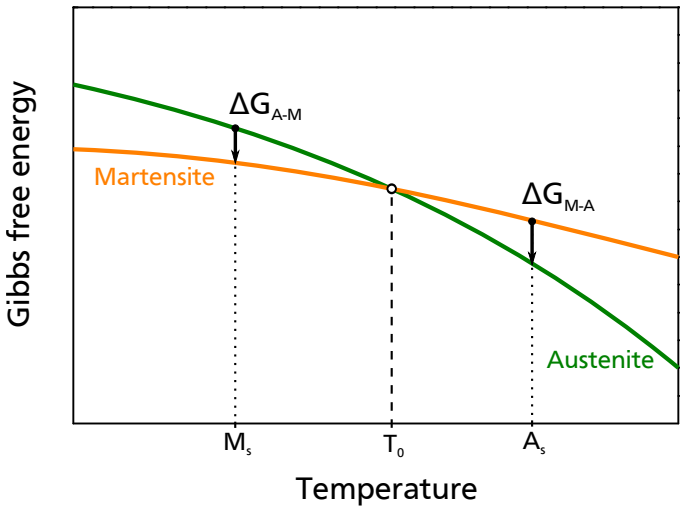

Figure 2.15: Schematic of the Gibbs free energy G as a function of temperature for martensite and austenite. At T_0, the Gibbs free energies of both phases are equal. However, an overheating to A_s or an undercooling to M_s is required in order to initiate the transformation between austenite and martensite. The respective energy differences ΔG_{M-A} and ΔG_{A-M} are marked by arrows.

In Ni-Mn-based Heusler alloys, the martensitic transition is accompanied by a change of the magnetization. Except for certain Ga-based alloys [97], this magnetostructural transition is inverse, as it was illustrated for the ideal case in Fig. 2.4 and 2.6. However, in a real material, the transition is not as sharp as shown in those schematics. Figure 2.16 illustrates what the temperature-dependent magnetization of the magnetostructural transition looks like in reality. The austenite phase is stable at high temperatures and it shows a ferromagnetic behavior below its Curie temperature T_C^A. Under cooling, the first martensite nuclei are formed at a certain temperature. Since the martensitic phase is paramagnetic, the magnetization of the sample decreases. The temperature at which the transformation is initiated is approximated by fitting the magnetization curve linearly before and during the transition (dotted lines in Fig. 2.16). The intersection point of the two lines is furthermore referred to as M_s, the martensite-start temperature.

By further cooling, more and more martensite is formed. At the martensite-finish temperature M_f, the transformation is completed. In the situation illustrated in Fig. 2.16, the magnetization decreases to zero because the martensite is paramagnetic in the temperature range of the transition. However, below the Curie temperature of the martensite T_C^M, a magnetic ordering is observed and the magnetization rises again. Under heating, the backward transition into austenite is initiated at the austenite-start temperature A_s and is finished at A_f. Both the heating and the cooling branch of the magnetization curve do not overlap due to the thermal hysteresis ΔT_{Hys}, which was already discussed in Fig. 2.6. The hysteresis is related to the lattice mismatch between the two phases and the resulting energy barrier, which needs to be overcome by undercooling (austenite to martensite) or overheating (martensite to austenite) [98]. In principle, if the lattice mismatch between martensite and austenite decreases, also the thermal hysteresis would be reduced. This is denoted as the λ_2 criterion, which is the mid-eigenvalue of the transformation matrix and should be as close to 1 as possible [99, 100]. Recently, Song et al. demonstrated that

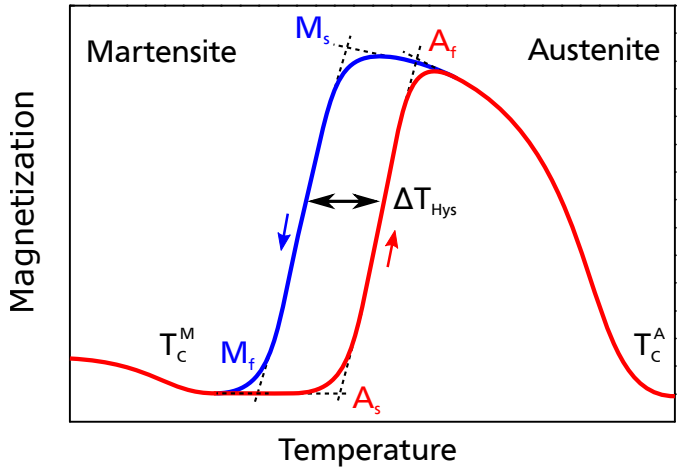

Figure 2.16: Schematic of the martensitic transformation in Ni-Mn-based Heusler alloys which can be described by the respective temperatures austenite start A_s, austenite finish A_f, martensite start M_s and martensite finish M_f. Both martensite and austenite have their own Curie temperature T_C^M and T_C^A.

this condition is close to be fulfilled in the material system Zn-Au-Cu leading to an enhancement of the reversibility of the transition and an unusual microstructure [101].

The transition temperature of a Heusler alloy is subject to its chemical composition. It was discussed above that the magnetic moment of stoichiometric Heusler alloys with a composition X_2YZ is defined by the number of valence electrons per formula unit N_v and can be described by the Slater-Pauling rule. Furthermore, it was found that the transition temperature of Ni-Mn-based Heusler compounds also depends on the number of valence electrons [102]. It is therefore possible to plot the whole phase diagram of off-stoichiometric compounds, which is shown in Fig. 2.17 for Ni-Mn-Sn (a), Ni-Mn-In (b) and Ni-Mn-Ga (c) by changing the ratio between Mn and the Z atoms Sn, In and Ga. This figure is taken from Ref. [40]. It is worth noting that the number of valence electrons is often given per atom, which is represented by the symbol $^{e}/_{a}$. According to Fig. 2.17, the martensitic transition is shifted to higher temperatures almost linearly by increasing the valence electron concentration per atom. This implies that the reduction of the In, Sn and Ga concentration increases the transition temperature, since these elements provide only three and four valence electrons respectively compared to Ni and Mn with a larger number of valence electrons.

The martensite phase can appear in different states. It can be present in the simple tetragonal shape, which is referred to as non-modulated martensite or as $L1_0$. Moreover, modulated structures can form that are repeated in a special stacking order. One distinguishes between the 14M and the 10M martensite depending on the modulation [88]. Furthermore, it is shown in Fig. 2.17 that the Curie temperature of the austenite phase nearly does not change when varing the chemical composition, which is not the case for the magnetic-ordering temperature of the martensite T_C^M.

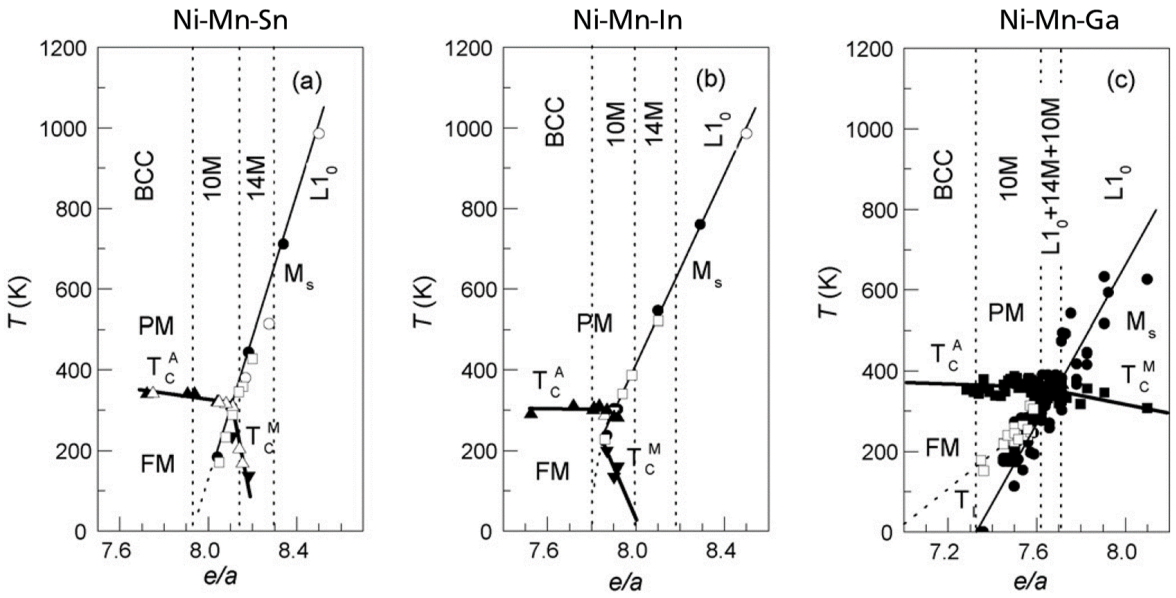

Figure 2.17: Phase diagram of Ni-Mn-X with X = Sn, In and Ga from Ref. [40]. The transition temperature M_s, the Curie temperatures of austenite T_C^A and martensite are plotted as a function of the valence electron concentration per atom $^{e}/_{a}$.

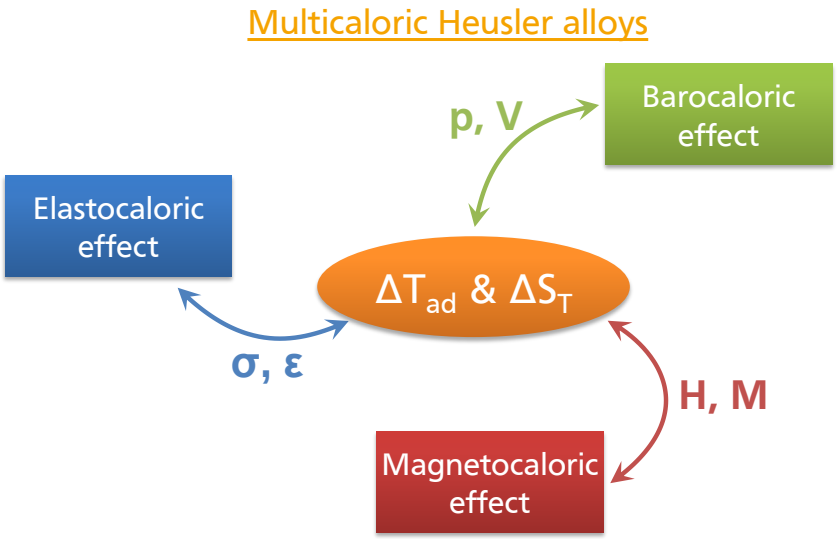

Figure 2.18: Schematic illustration of multicaloric Heusler alloys.

Due to the large diversity of functional properties, Heusler alloys are an important and interesting material class. Especially the Ni-Mn-based systems attracted attention in terms of magnetic shape memory applications, for which a large length change is induced by a magnetic field [55, 103, 104, 105]. The same materials can also be utilized for magnetocaloric cooling applications and large entropy changes of more than $10\,\mathrm{J\,kg^{-1}\,K}$ have been reported in literature [106, 89, 107, 108, 109]. However, direct measurements of the adiabatic temperature change of Ni-Mn-based Heusler alloys are rather scarce and do normally not exceed 2 K in a magnetic field change of less than 2 T [110, 111, 112, 113, 114]. In 2012, Liu et al. [19] reported a ΔT_{ad} of −6.2 K in Ni-Mn-In-Co which set a new record for this material family, but due to the thermal hysteresis, the magnetocaloric effect under cycling is strongly decreased. In addition, mechanical stress and hydrostatic pressure result in a significant cooling and warming as well, which originates from the changing unit-cell volume during the transition. For this reason, Heusler alloys are also suitable as elastocaloric and barocaloric materials [115, 116]. This is summarized schematically in Fig. 2.18. All these caloric effects are related to fascinating features of the first-order martensitic transition, which will be investigated in this thesis.

3 Experimental methods

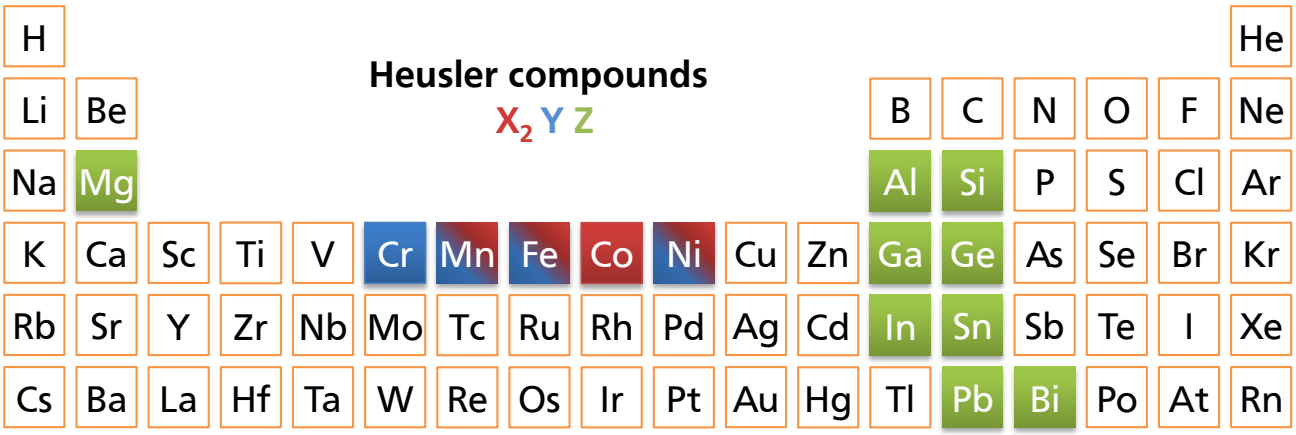

Figure 3.1: Periodic table with highlighted elements which were used for the preparation of Heusler alloys. The type X elements are shown in red, Y in blue and Z elements in green (color scheme adopted from [71]).

3.1 Sample preparation

The different samples were prepared by arc melting technique. Figure 3.1 illustrates which Heusler compounds of the type X_2YZ were produced. Type X elements are shown in red, Y and Z elements in blue and green according to the illustration by Graf et al. [71]. The base elements used for alloying had a high purity of better than 99.95 %. In order to suppress contamination, a special cleaning step was performed to remove the oxide layer from Mn and Fe. Those two elements were molten individually in the arc melter in order to evaporate all oxides from the base material. Subsequently, the different elements were balanced to result in an ingot of 10 g. The preparation of Mn-based alloys required special care during the melting procedure. Due to the rather high vapor pressure of Mn, significant evaporation losses occur (at 1400 °C the vapor pressure of Mn is more than ten times larger than for Ni and Co [117]). In order to keep the final composition as close as possible to the nominal one, an additional amount of 1.5 to 3 % excess Mn was processed based on the experiences in the evaporation behavior of the specific material family. To obtain a high chemical homogeneity, the as-cast ingots were turned and remelted five times. After each melting step, the mass loss was checked. By this procedure it was possible to obtain specimens with a mass very close to the target mass of 10 g.

Subsequently, a heat treatment under protective atmosphere was performed. The ingots were wrapped in Ta or Fe foil to prevent oxidation and placed inside a quartz tube under an Ar pressure of 0.5 bar (the tube was pumped and flushed with Ar several times). The annealing temperature was set between

Table 3.1: Nominal and final compositions of Ni-Mn-In and Ni-Mn-In-Co samples. The valence electron concentration per atom $^{e}/_{a}$ and the austenite-start temperature A_s are presented for selected compounds.

Nominal composition	Chemical analysis	Treatment	e/a	A_s
$Ni_{50.0}Mn_{36.0}In_{14.0}$	$Ni_{49.7}Mn_{36.2}In_{14.1}$	900°C - 24h - wq	7.928	330 K
$Ni_{50.0}Mn_{35.5}In_{14.5}$	-	900°C - 24h - wq	-	320 K
$Ni_{50.0}Mn_{35.0}In_{15.0}$	$Ni_{50.2}Mn_{35.0}In_{14.8}$	900°C - 24h - wq	7.911	305 K
$Ni_{50.0}Mn_{35.3}In_{14.7}$	$Ni_{49.6}Mn_{35.6}In_{14.8}$	900°C - 24h - wq	7.897	305 K
$Ni_{50.0}Mn_{35.0}In_{15.0}$	$Ni_{50.5}Mn_{34.5}In_{15.0}$	900°C - 24h - wq	7.916	270 K
$Ni_{50.0}Mn_{35.0}In_{15.0}$	-	900°C - 24h - wq	-	290 K
$Ni_{50.0}Mn_{34.5}In_{15.5}$	-	900°C - 24h - wq	-	255 K
$Ni_{50.0}Mn_{35.0}In_{15.0}$	$Ni_{49.8}Mn_{35.0}In_{15.2}$	900°C - 24h - wq	7.886	240 K
$Ni_{50.0}Mn_{34.0}In_{16.0}$	$Ni_{50.3}Mn_{33.8}In_{15.9}$	900°C - 24h - wq	7.873	n
$Ni_{50.0}Mn_{34.0}In_{16.0}$	$Ni_{50.0}Mn_{34.0}In_{16.0}$	900°C - 24h - wq	7.856	n
$Ni_{45.0}Mn_{38.6}In_{11.4}Co_{5.0}$	$Ni_{45.9}Mn_{37.8}In_{11.3}Co_{5.0}$	900°C - 24h - wq	8.027	450 K
$Ni_{45.0}Mn_{37.9}In_{12.1}Co_{5.0}$	$Ni_{45.9}Mn_{37.5}In_{11.4}Co_{5.2}$	900°C - 24h - wq	8.021	425 K
$Ni_{45.0}Mn_{37.0}In_{12.5}Co_{5.0}$	-	900°C - 24h - wq	-	390 K
$Ni_{45.0}Mn_{37.0}In_{13.0}Co_{5.0}$	-	900°C - 24h - wq	-	335 K
$Ni_{45.0}Mn_{36.8}In_{13.2}Co_{5.0}$	$Ni_{45.2}Mn_{36.6}In_{13.1}Co_{5.1}$	900°C - 24h - wq	7.936	320 K
$Ni_{45.0}Mn_{36.8}In_{13.2}Co_{5.0}$	$Ni_{45.4}Mn_{36.6}In_{13.1}Co_{4.9}$	900°C - 24h - wq	7.934	310 K
$Ni_{45.0}Mn_{36.8}In_{13.2}Co_{5.0}$	-	900°C - 24h - wq	-	310 K
$Ni_{45.0}Mn_{36.8}In_{13.2}Co_{5.0}$	-	900°C - 24h - wq	-	320 K
$Ni_{45.0}Mn_{36.6}In_{13.4}Co_{5.0}$	$Ni_{45.7}Mn_{36.6}In_{13.5}Co_{4.2}$	900°C - 24h - wq	7.917	280 K
$Ni_{45.0}Mn_{36.6}In_{13.4}Co_{5.0}$	$Ni_{45.1}Mn_{36.5}In_{13.4}Co_{5.0}$	900°C - 24h - wq	7.918	255 K
$Ni_{45.0}Mn_{36.5}In_{13.5}Co_{5.0}$	$Ni_{44.9}Mn_{36.6}In_{13.5}Co_{5.0}$	900°C - 24h - wq	7.905	n
$Ni_{45.0}Mn_{36.4}In_{13.6}Co_{5.0}$	-	900°C - 24h - wq	-	n
$Ni_{45.0}Mn_{35.1}In_{14.9}Co_{5.0}$	$Ni_{45.2}Mn_{34.8}In_{15.0}Co_{5.0}$	900°C - 24h - wq	7.853	n

800 and 1000 °C, depending on the compound. After an annealing time of 24 h, the quartz tube was quenched in water.

The most important alloys of Ni-Mn-In, Ni-Mn-In-Co, Ni-Mn-Sn and Ni-Mn-Sn-Co are listed in Tab. 3.1 and 3.2 (further samples other then the mentioned systems can be found in the appendix). For some selected materials, not only the nominal composition is specified, but also the resulting composition from chemical analysis using inductively coupled plasma optical emission spectrometry (ICP-OES) is presented. For those alloys, the valence electron concentration per atom $^{e}/_{a}$ was calculated. The transition metals Mn, Co and Ni provide 7, 9 and 10 valence electrons, respectively. The main group elements In and Sn have only 3 and 4 valence electrons since the 4d band is completely filled. In Tab. 3.1 and 3.2 also the austenite-start temperature A_s is listed, except for some materials which did not transform at all. From these results, the relation between the transition temperature and the valence electron concentration per atom $^{e}/_{a}$ as discussed in Fig. 2.17 is evident.

Table 3.2: Nominal and final compositions of Ni-Mn-Sn and Ni-Mn-Sn-Co samples. The valence electron concentration per atom $^{e}/_{a}$ and the austenite-start temperature A_s are presented too.

Nominal composition	Chemical analysis	Treatment	e/a	A_s
$Ni_{50.0}Mn_{37.5}Sn_{12.5}$	$Ni_{50.8}Mn_{36.6}Sn_{12.6}$	1000°C - 24h - wq	8.146	340 K
$Ni_{50.0}Mn_{37.0}Sn_{13.0}$	$Ni_{50.5}Mn_{36.4}Sn_{13.1}$	1000°C - 24h - wq	8.125	315 K
$Ni_{50.0}Mn_{36.5}Sn_{13.5}$	$Ni_{51.2}Mn_{35.1}Sn_{13.7}$	1000°C - 24h - wq	8.125	300 K
$Ni_{50.0}Mn_{36.0}Sn_{14.0}$	$Ni_{50.8}Mn_{35.1}Sn_{14.1}$	1000°C - 24h - wq	8.102	260 K
$Ni_{50.0}Mn_{35.5}Sn_{14.5}$	$Ni_{50.8}Mn_{34.6}Sn_{14.6}$	1000°C - 24h - wq	8.087	230 K
$Ni_{50.0}Mn_{35.0}Sn_{15.0}$	$Ni_{50.7}Mn_{34.3}Sn_{15.0}$	1000°C - 24h - wq	8.069	195 K
$Ni_{50.0}Mn_{34.5}Sn_{15.5}$	$Ni_{50.5}Mn_{34.0}Sn_{15.5}$	1000°C - 24h - wq	8.049	145 K
$Ni_{45.0}Mn_{38.8}Sn_{11.2}Co_{5.0}$	$Ni_{45.6}Mn_{38.2}Sn_{11.2}Co_{5.0}$	1000°C - 24h - wq	8.133	350 K
$Ni_{45.0}Mn_{38.6}Sn_{11.4}Co_{5.0}$	$Ni_{45.6}Mn_{38.1}Sn_{11.3}Co_{5.0}$	1000°C - 24h - wq	8.127	340 K
$Ni_{45.0}Mn_{38.4}Sn_{11.6}Co_{5.0}$	$Ni_{45.7}Mn_{37.9}Sn_{11.5}Co_{4.9}$	1000°C - 24h - wq	8.122	330 K
$Ni_{45.0}Mn_{38.2}Sn_{11.8}Co_{5.0}$	$Ni_{47.2}Mn_{35.5}Sn_{12.2}Co_{5.1}$	1000°C - 24h - wq	8.152	295 K
$Ni_{45.0}Mn_{38.0}Sn_{12.0}Co_{5.0}$	$Ni_{46.2}Mn_{36.6}Sn_{12.2}Co_{5.0}$	1000°C - 24h - wq	8.118	225 K

3.2 Crystallographic characterization

The crystal structure was investigated by X-ray powder diffraction (XRD). The X-ray machine STADI P from STOE was used in transmission mode and Bragg-Brentano geometry with a Mo Kα_1 radiation source. θ-2θ scans were performed between 5 and 50° with a step size of 0.01°. For the measurement, the material was crushed to a fine powder with an agate mortar. The indexing of the XRD peaks was done with the help of the software CaRIne Crystallography 3.1. A typical XRD pattern of an austenitic material (green curve) and a sample in a mixed state of martensite and austenite (orange curve) is shown in Fig. 3.2. In the cubic austenite phase, different fundamental peaks like (220) and (400) are always visible - independent of atomic disorder. They are classified by even Miller indices h, k and l, which fulfill the condition $(h+k+l)/2 = 2n$ with the integer n [118]. If $L2_1$ structure is present (see Fig. 2.9(a)), additional peaks appear. Those reflexes have odd Miller indices like (111) and (311). However, if the material is in the B2 structure (see Fig. 2.9(b)) due to atomic disorder, these $L2_1$ peaks are eliminated. Furthermore, in both $L2_1$ and B2 structure, reflexes turn up with even h, k and l which fulfill the condition $(h+k+l)/2 = 2n+1$ [73]. In the martensite state, the cubic lattice is distorted and therefore the peak positions are shifted, as can be seen in the orange curve in Fig. 3.2.

3.3 Microstructural analysis

Before studying the microstructure of the as-cast or as-annealed ingots, the samples were first ground free standing or bond in an epoxy resin with sand paper starting from 320 up to 4000 grain. Subsequently, polishing steps using 3 and 1 µm diamond suspension for approximately 1 min each were performed. The surface finishing was done with water-based neutral oxide polishing agent OP-AN for 1 min, followed by a cleaning step under flowing water.

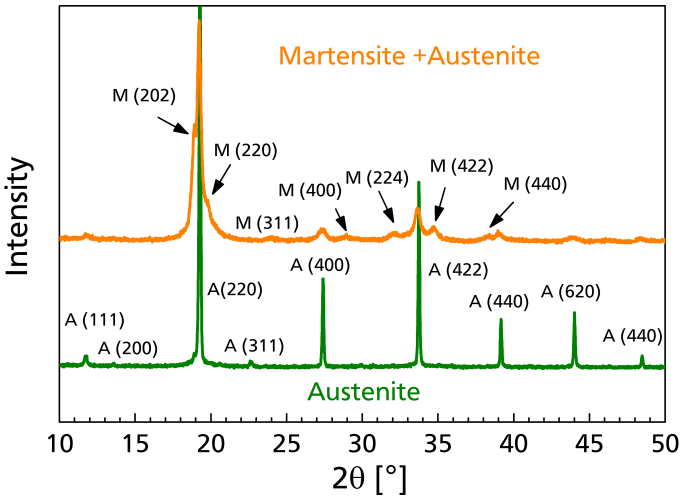

Figure 3.2: Powder diffraction pattern of a Heusler alloy in pure austenite (green curve) and in a mixed state of martensite and austenite (orange curve).

The microstructures of the as-cast and as-annealed compounds were investigated using an optical microscope of the type Axio scope.A1 from Carl Zeiss Microscopy GmbH with polarized light.

Different electron microscopes, namely Philips XL30 FEG, JEOL JSM 7600F and Leo 1530 Gemini were used to study microstructural features with higher resolution. Besides secondary electron (SE) and backscattered electron contrast (BSE) for imaging, also energy dispersive X-ray (EDX) analysis was performed to determine the local composition of different phases.

Temperature and magnetic-field dependent optical microscopy was performed on a magneto-optical Kerr microscope from evico magnetics GmbH. An objective with a low magnification of 2.5x was used in order to investigate a large area of the sample. The flow cryostat from CryoVac GmbH & Co. KG allowed to stabilize at temperatures between 300 K down to the boiling point of N_2 (77 K). The typical heating and cooling rate was set to $3\,\mathrm{K\,min^{-1}}$. For certain experiments the temperature was settled slowly to prevent overshooting. For the temperature-dependent experiments, the polished sample was fixed on a copper plate by Ag paste.

An external magnetic-field source was added to the instrument by using a Halbach setup with a field strength of 1.1 T. It is connected to a step motor which lifts it up and down. In this manner, the magnetic-field strength, which the sample is exposed to, can be varied between 0 and 1.1 T. At the same time it is possible to vary the temperature inside the cryostat. The whole device is illustrated in Fig. 3.3. The magnetic-field-sweeping rate can be tuned up to $1\,\mathrm{T\,s^{-1}}$ by changing the lifting speed. The setup was developed within this thesis together with Bernd Stoll.

Multiple methods have been applied for a quantification of the phase transformation under different stimuli. Binary images were created by difference imaging using the software ImageJ after equalizing the histogram for better contrast. A further refinement of the phase detection was performed manually using Adobe Photoshop. By this approach it was possible to determine the development of the phase

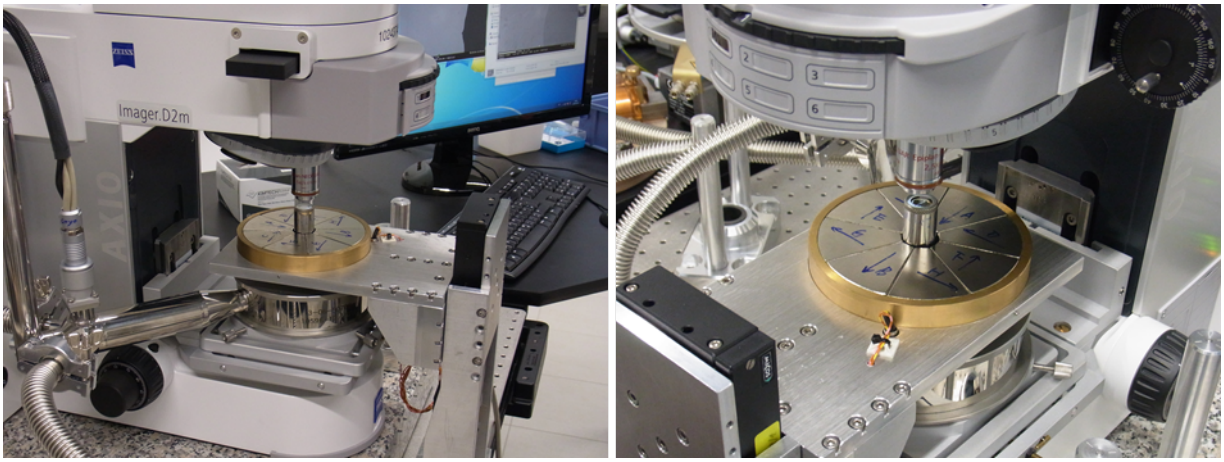

Figure 3.3: Magneto-optical Kerr microscope setup to observe temperature and magnetic-field dependent properties of the martensitic phase transformation. The cold finger of the cryostat is situated in a movable Halbach array creating a magnetic field of 1.1 T.

fraction during heating and cooling as well as in changing magnetic fields. Based on this, a surface map of the local transition temperature was evaluated.

3.4 Magnetic characterization

Magnetic measurements were performed in different setups during the thesis. A SQUID magnetometer (superconducting quantum interference device) of the type MPMS-5S, a PPMS-14 (physical property measurement system) both from Quantum Design and a VSM (vibrating sample magnetometer) from LakeShore were used. For the characterization of the magnetization of bulk pieces, needle-like samples with a mass between 10 and 50 mg (produced by mechanical crushing) were mounted into the sample holder. By sweeping temperature in a constant magnetic field up to 14 T, $M(T)$ curves were measured. Therefore, the sweeping rate was set to $2\,\mathrm{K\,min^{-1}}$ or less to ensure equilibrium conditions.

For the determination of the isothermal entropy change ΔS_T, the isofield curves were obtained in field increments of 0.1 T up to a maximum magnetic-field strength of 2 T. The samples were always heated and cooled to at least 50 K above and below the transition temperature to avoid the transformation in minor loops of hysteresis. From this data set, ΔS_T was calculated by using the Maxwell relation Eq.(2.9). The numerical solution for a magnetic-field change ΔH with n field steps was determined using the trapezoidal rule [119]:

$$\Delta S_T(T, \Delta H) = \frac{\mu_0 dH}{2}\left(\frac{dM_1}{dT} + \sum_{k=2}^{n-1}\frac{dM_k}{dT} + \frac{dM_n}{dT}\right). \tag{3.1}$$

For selected samples also $M(H)$ loops have been measured. For this measurement protocol, a certain temperature was stabilized and the magnetic field was varied. In the vicinity of the martensitic transition,

Figure 3.4: Sequence of the assembly of the pressure cell for magnetization measurements.

the overheating and undercooling of the sample is essential to erase the history and to obtain reasonable measurement results.

Single fragments were characterized with the PPMS. Therefore, small particles of $Ni_{45.7}Mn_{36.6}In_{13.5}Co_{4.2}$, $LaFe_{11.8}Si_{1.2}$ and $Mn_{1.2}Fe_{0.68}P_{0.5}Si_{0.6}$ with a diameter in the micrometer range were selected by using a light microscope and were subsequently mounted into the sample holder with Kapton tape. The sensitivity of the PPMS, namely the oscillation frequency and the amplitude, was increased to the maximum in order to reduce the measurement noise.

Pressure-dependent magnetic measurements were performed using a pressure cell CC-Spr-Φ8.5-MC4 model 1.3 GPa from Quantum Design. An image sequence of the cell which was used for the experiment is shown in Fig. 3.4. The sample was placed inside a plastic tube together with a small piece of Sn which can be seen in the bottom of Fig. 3.4. The tube was filled with oil and sealed subsequently. The specimen was then inserted into the Cu-Be holder and the pistons were connected (second image from the bottom). Different connecting parts, which were also made from Cu-Be were screwed tightly. Finally, the endpieces were connected. Using these screws, the pressure was increased. Magnetization measurements in constant magnetic field were performed by using a heating and cooling rate of 1 K.

The Sn sample was utilized to determine the pressure inside the cell. Therefore, the pressure cell was cooled below liquid He temperature in order to measure the critical temperature of the superconducting phase. This transformation is sensitive to hydrostatic pressure, which is well discussed in literature [120]. By this, the pressure could be measured at low temperatures.

3.5 Calorimetry

3.5.1 Differential scanning calorimeter

A commercial differential scanning calorimeter (DSC) of the type DSC200 F3 Maia from GmbH & Co. Holding KG was used for the calorimetric studies on different specimen. The device was calibrated in the desired temperature range with six different calibration standards (C_6H_{12}, Ga, Hg, In, KNO_3, Sn).

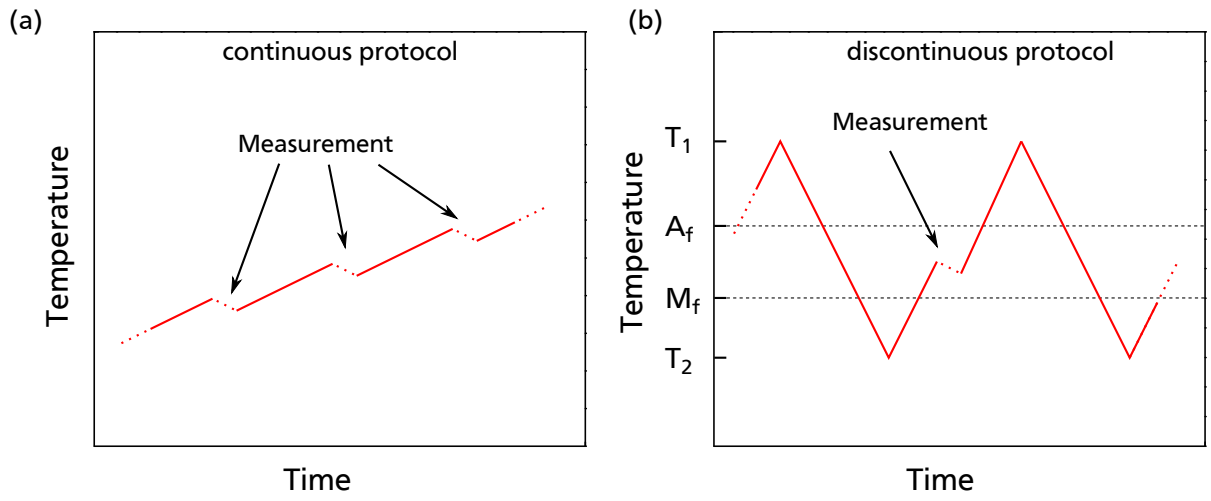

Figure 3.5: Schematic of the continuous (a) and the discontinuous measurement protocols (b). In the discontinuous experiment, the sample is always heated above the A_f to pure austenite and subsequently to it is cooled below M_f to pure martensite before the next measurement.

Furthermore, a baseline correction was performed. The measurement speed was set to $10\,\mathrm{K\,min^{-1}}$. All heating and cooling experiments were repeated three times, whereas only the second and third cycle were utilized for the calculation of the heat flow.

3.5.2 Adiabatic calorimeter

Precise measurements of the heat capacity under heating and cooling in different magnetic fields were performed in an adiabatic calorimeter by the method describe in Ref. [121]. The magnetic field up to 9 T was applied by a superconducting magnet. A slow heating and cooling rate of $0.06\,\mathrm{K\,min^{-1}}$ was used in order to obtain quasistatic conditions. Futhermore, the temperature change ΔT_{ad} was measured inside the calorimeter when applying a magnetic field with a sweeping rate of $1\,\mathrm{T\,min^{-1}}$ under adiabatic conditions. Under isothermal conditions, the entropy change ΔS_T was calculated from the amount of heat $T \cdot \Delta S_T$ which was absorbed by the sample in order to keep the temperature constant [122]. The relative error of the experiments is below 5 %. These measurements were done in collaboration with Ramon Burriel (Universidad de Zaragoza).

3.6 Adiabatic temperature change

The adiabatic temperature change ΔT_{ad} was determined in three facilities with different magnetic-field sources. There are two possible measurement protocols for such an experiment. In the continuous protocol, as illustrated in Fig. 3.5 (a), the sample temperature is being changed with a constant heating and cooling rate without interruption. At certain temperatures, the magnetic field is applied and the adiabatic temperature change is detected. This measurement protocol applies well for second-order materials or for first-order materials with a small thermal hysteresis. However, the hysteresis in Heusler alloys is

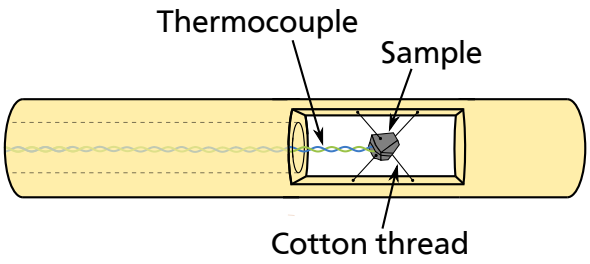

Figure 3.6: Schematic of the sample mounting in the slow ΔT_{ad} measurement.

typically rather large. For this reason, the discontinuous protocol is advantageous (Fig. 3.5(b)). In this measurement, the sample is always heated above the transition temperature and subsequently cooled to low temperatures before stabilizing the target temperature. Utilizing this sequence allows to measure on the same basis of the same initial state. Consequently, all measurements are independent of each other. In comparison, this is not the case in the continuous protocol, where the transformation is partly irreversible during the field application of the adiabatic temperature change measurement of a hysteretic material. In order to exclude effects related to the history of the sample, the discontinuous protocol was used preferably.

Different magnetic-field sources can be utilized in order to measure the adiabatic temperature change ΔT_{ad} directly. One can divide four groups of measurement setups [123]: (1) sweeping of the magnetic field in an electromagnet or a superconducting magnet [124, 125], (2) introducing and extracting the magnetocaloric material from a magnetic field [126, 37], (3) rotating an assembly of nested magnets to change the magnetic field [112, 111, 19] and (4) applying a magnetic-field pulse in a solenoid [127, 128]. Due to the very different magnetic-field generation, the time-scale of those methods varies significantly. Three (1 - 3) of the four above-mentioned techniques have been used within this thesis and are described in more detail in the following.

3.6.1 Superconducting magnet

The slow measurements of the adiabatic temperature change were performed in a device at and in cooperation with the University of Duisburg-Essen [129, 130], Germany. The magnetic field up to 5 T was applied by using a superconducting magnet. The magnetic-field-sweeping rate during the measurements was set to 0.66 T min^{-1}. The sample compartment is schematically illustrated in Fig. 3.6. The temperature of the sample was monitored by a thermocouple placed inside a hole which was drilled into the specimen. In order to provide a good thermal insulation, the sample was suspended by means of thin cotton threads, which were glued to the surface and the holder. The whole sample chamber was evacuated to high vacuum and the temperature was controlled by a surrounding heating unit.

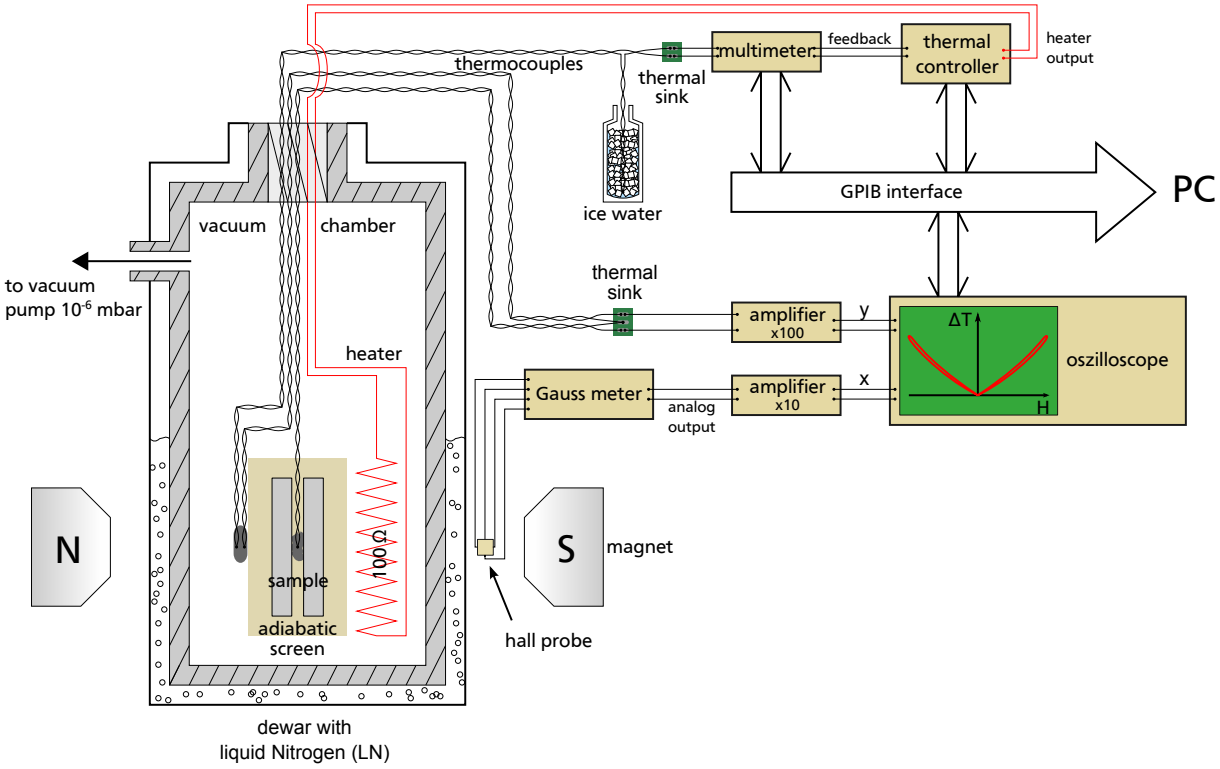

Figure 3.7: Schematic of the entire measurement and data acquisition system in the ΔT_{ad} rig [91].

3.6.2 Halbach setup

Within this thesis, the existing device for the semi-fast measurements of the adiabatic temperature change ΔT_{ad} was further developed and a new user software with enhanced functionality was designed and implemented by using LabView. This work has been down together with Konstantin P. Skokov and Bernd Stoll. The magnetic field source in the ΔT_{ad} rig consisted of two nested Halbach magnets, which rotate against each other. A sinusoidal magnetic-field profile with a maximum of 1.93 T was generated. One full oscillation of the field took about 18 s. The highest magnetic-field-sweeping rate up to $0.7\,\mathrm{T\,s^{-1}}$ was achieved around 0 T.

A schematic of the individual device components is illustrated in Fig. 3.7. The sample temperature was measured with a differential type T thermocouple (Cu and Constantan). One end of the thermocouple was glued between two plates of the sample with an Ag-based epoxy and the reference was fixed to the holder close to the sample. A more detailed drawing of the sample holder is shown in Fig. 3.8. The absolute temperature of the sample holder was measured by a differential thermocouple against ice water. The temperature was controlled by a surrounding resistance heater. The sample holder was mounted inside a vacuum tube with high vacuum, which was placed inside a liquid-nitrogen bath. Furthermore, the sample was wrapped with a thermally insulating wool to improve the adiabaticity of the system. The magnetic field was measured by a Hall probe. Both the magnetic field signal and the thermoelectric voltage between the sample and the reference were amplified and recorded using an oscilloscope. The

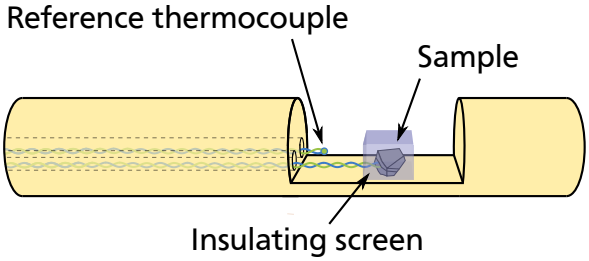

Figure 3.8: Schematic of the sample holder in the semifast ΔT_{ad} measurement.

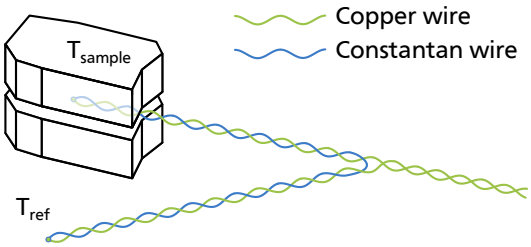

Figure 3.9: Schematic of the fork-like differential thermocouple used for pulsed-field measurements. The temperature difference between the sample and the reference point is evaluated. The length of the constantan wire was kept as short as possible in order to reduce the electrical resistance of the thermocouple.

absolute temperature of the sample holder was measured by a multimeter. A downstream PID controller provided the output power for the resistance heater.

3.6.3 Pulsed magnetic fields

The fast measurements of the adiabatic temperature change were performed in pulsed-magnetic fields inside a solenoid at and in cooperation with the Helmholtz Center Dresden Rossendorf, Germany [128]. Magnetic-field pulses of 2, 5 and 10 T were applied, which resulted in a field rate up to 1500 $\mathrm{T\,s^{-1}}$. The adiabatic temperature was measured via a fine-twisted differential type T thermocouple (Cu and Constantan) with a wire thickness of 25 µm. A fork-like thermocouple was prepared in order to minimize the length of the Constantan wire, which is schematically shown in Fig. 3.9. This was necessary to reduce the electrical resistance of the thermocouple as much as possible. The one end of the fork was glued between two plates of the sample with a small amount of an Ag-based epoxy. The sample itself was glued to the holder with Apiezon. The reference thermocouple was fixed on the other side of the sample holder, as is illustrated in Fig. 3.10. The temperature of the sample holder was measured by means of a PT100 sensor. The temperature was controlled by a resistance heater surrounding the measurement unit.

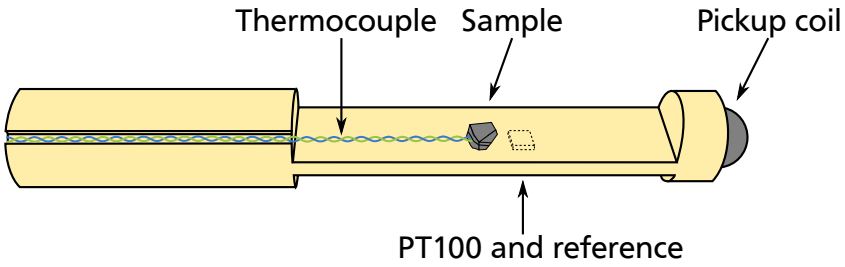

Figure 3.10: Schematic of the sample holder in the semifast ΔT_{ad} measurement.

Table 3.3: Overview of the properties of the artificial magnetocaloric material used in simulations.

Parameter	Symbol	Value
Young's modulus	E	100 GPa
Poisson's ratio	ν	0.3
Isotropic length expansion during transition	α	0.0033
Anisotropic length change during transition	α_1 α_2	0.008 -0.017
Shift of the transition temperature by pressure	$\frac{dT_t}{dp}$	0 ... 50 K GPa^{-1}
Transition width of the individual element	ω	1 ... 2 K
Average transition temperature	$\overline{T_t}$	305 K
Standard deviation of T_t distribution	σ	1 ... 10 K

The field strength of the magnetic-field pulse was determined via a small pick-up coil in proximity to the sample. By integration of the induced voltage in the pick-up coil over time, the magnetic field can be estimated. A small voltage was also induced in the thermocouple wires, which overlapped with the thermoelectric voltage of the thermocouple. This background signal was separated by measurements at low temperatures far away from any magnetocaloric transition and was subsequently removed from the measurement signal of the adiabatic temperature change. Furthermore, a metrological 50 Hz noise was subtracted. The different experiments revealed that eddy-current heating of the sample can be neglected.

Using measurements of the Curie temperature of the austenite phase as a reference point, the absolute temperature measurement of the three devices was compared with magnetization data. The starting temperatures of the different pulsed-field experiments therefore had to be corrected by 3 K in order to coincide the other measurements.

3.7 Modeling

Finite element simulations were performed with the commercial software COMSOL Multiphysics 5.0, using the structural mechanics module. A 3D problem within the solid mechanics interface was utilized. Different mesh sizes from two to 1000 cubic elements were investigated. An artificial magnetocaloric

material with the properties shown in Tab. 3.3 was implemented. The individual transition temperature of each element was set randomly by a Gaussian distribution. A weak contribution with the auxiliary dependent variable x_t was added to the model, which determined the phase fraction of each element according to the actual temperature and the normal components of the stress tensor. The xx, yy, and the zz components of the initial strain tensor were set to $\alpha \cdot x_t$ in order to simulate the volume expansion of the individual mesh elements. A parametric sweep over temperature was performed and a stationary PARDISO solver was utilized. For every temperature step, first the displacement field and subsequently x_t were calculated repeatedly until the termination criteria were fulfilled.

4 Results and discussion

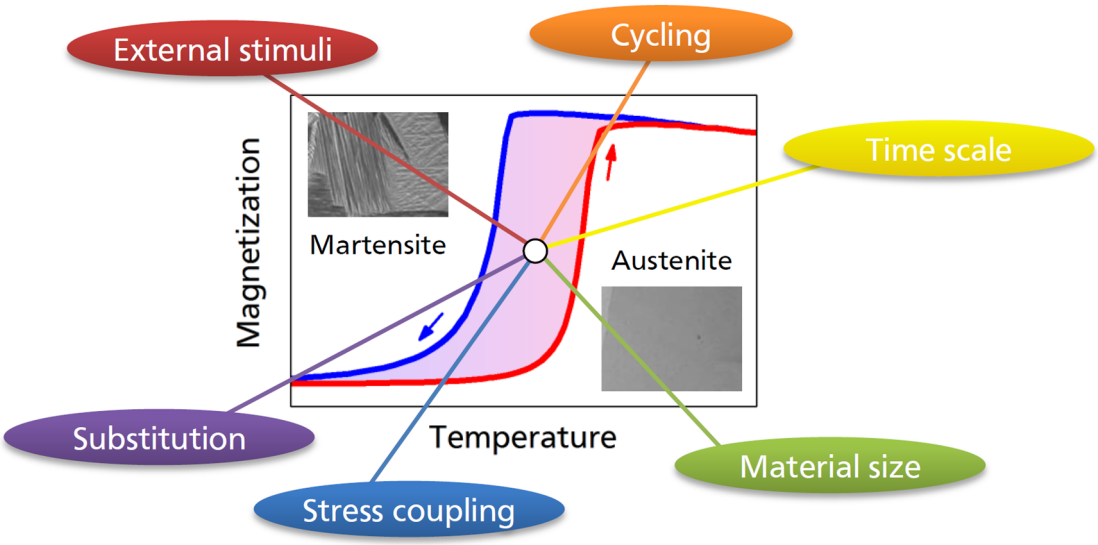

Figure 4.1: Content of the results and discussion chapter: hysteresis in Heusler alloys.

In this thesis, different aspects related to the first-order martensitic transition in Ni-Mn-In and Ni-Mn-In-Co were investigated. Figure 4.1 schematically illustrates the content of the results and discussion part of this work. First, the properties of the magnetostructural transition under different external stimuli, namely a magnetic field and hydrostatic pressure will be studied. In the following section, the adiabatic temperature change ΔT_{ad} and isothermal entropy change ΔS_T under cycling will be examined. The large reversible magnetocaloric effect, which can be obtained, is related to the properties of minor loops of hysteresis. Next, the characteristics of the martensitic transformation will be investigated by direct measurements of the adiabatic temperature change under different time scales. Besides the magnetic-field rate, also the size of the material influences the thermal hysteresis and the width of the transition, which will be studied by magnetic measurements of single particles. This topic is followed by a finite element study, which allows to describe the stress-coupling mechanism in first-order magnetocaloric materials. The focus of the last section is the search for new magnetocaloric Heusler alloys in order to substitute critical elements to enhance the sustainability of Ni-Mn-based Heusler compounds for future applications.

4.1 Magnetic, magnetocaloric and pressure-dependent properties

In the following section, the magnetic and magnetocaloric properties of the Heusler systems Ni-Mn-In and Ni-Mn-In-Co will be investigated as well as the influence of hydrostatic pressure. In the beginning of a comprehensive characterization process, magnetization measurements are of central importance. From this data, the isothermal entropy change ΔS_T can be determined. The quality of the results strongly depends on the utilized measurement protocol. Furthermore, calorimetric techniques are also useful tools in order to characterize the magnetocaloric properties. These are typically used in order to determine the entropy change of the complete transition ΔS_t. This work shows that the magnetic and the magnetocaloric properties can be generalized for both material families under investigation. Based on this finding in connection with a phenomenological description using the Heisenberg model, the different contributions of the total entropy can be estimated. Furthermore, several important consequences arise from this investigation.

4.1.1 Principle characteristics and generalization of the magnetocaloric effect

The martensitic transition in Ni-Mn-based Heusler alloys is a diffusionless transformation between the low temperature tetragonal martensite and the high temperature cubic austenite phase. The transition temperature strongly depends on intrinsic properties like the chemical composition and atomic disorder. Therefore, the material preparation process must be executed in a controlled manner. Especially, evaporation losses of Mn during the melting procedure are a critical issue as the final composition of the alloy is affected. Also local inhomogeneities in stoichiometry arise because the surface of the melt loses most of Mn. In order to contain the compositional spread, the alloys were remolten five times. Furthermore 3 % extra Mn was added. After each melting, the material loss was determined by weight to reach the intended nominal composition. For some samples, the final composition was checked via ICP-OES analysis.

Despite the controlled preparation route, the sample properties are not yet adequate. A proper heat treatment is necessary in order to obtain sharp transitions with small thermal hysteresis. As an example, Fig. 4.2 compares magnetic measurements of a sample before and after annealing. The blue curve shows a very broad and incomplete transition with a huge thermal hysteresis of about 40 K. In great contrast, the annealed material in red shows a very sharp transition, which implies that stoichiometric inhomogeneities were removed by the heat treatment.

It can also be seen that the magnetization curves of both compounds do not overlap above room temperature. This is because both materials have a different Curie point of the high temperature austenite phase, which will be denoted as T_C^A. This effect is related to disorder on the atomic scale since the composition has nearly no influence on the Curie temperature in Ni-Mn-In [131, 76]. A mixture of the different sublattices of the Heusler structure reduces T_C^A. The annealing step provides a better atomic order and therefore enhances the magnetization.

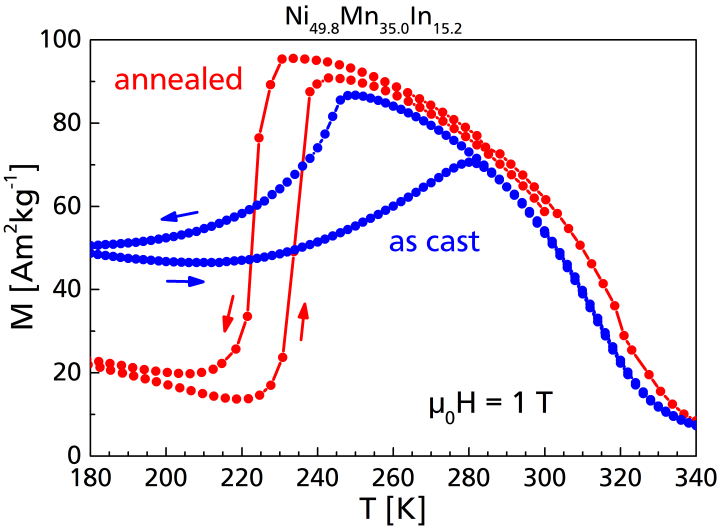

Figure 4.2: Comparison of magnetic measurements of $Ni_{49.8}Mn_{35.0}In_{15.2}$ before and after heat treatment at 900 °C for 24 h.

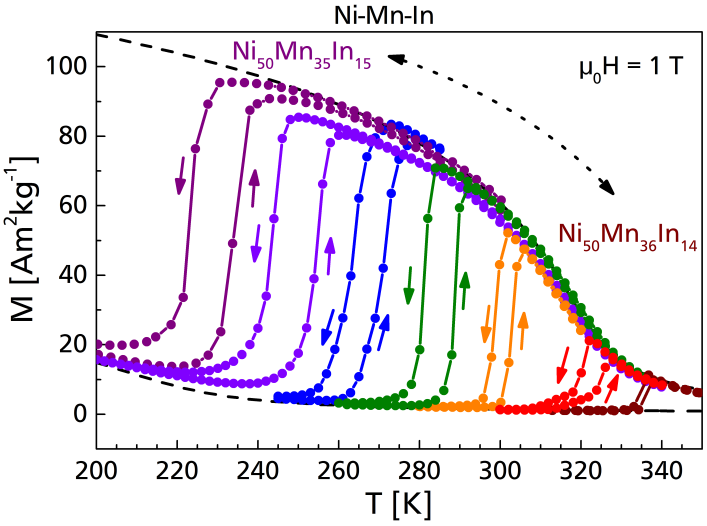

Figure 4.3: Temperature dependence of magnetization for different Ni-Mn-In compounds in a magnetic field of 1 T [132].

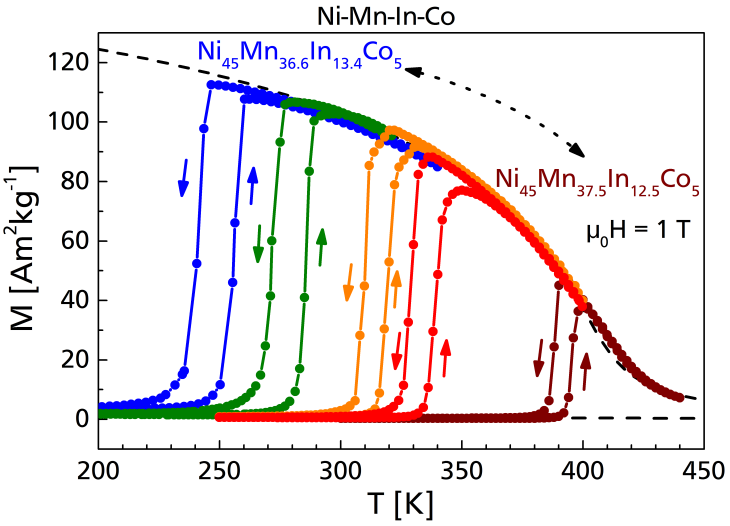

Figure 4.4: Temperature dependence of magnetization of different compounds of Ni-Mn-In-Co in a magnetic field of 1 T [132].

As already discussed in the introduction, the martensitic transition temperature of Heusler alloys is subject to the chemical composition. By changing the Mn to In ratio in $Ni_{50}Mn_{50-x}In_x$, the transition can be adjusted sensitively. In Fig. 4.3, the magnetization curves in 1 T of seven different compounds are plotted. The nominal composition was varied between $Ni_{50}Mn_{36}In_{14}$ with a transition around 335 K and $Ni_{50}Mn_{35}In_{15}$, which transforms at 230 K. Consequently, a change of only 1 at % shifts the transition by about 100 K. This strong relationship between the stoichiometry of the alloy and its transition temperature explains why small chemical inhomogeneities have such a large impact on the transformation properties. It is related to the valence electron concentration per atom $^{e}/_{a}$. The transition temperature linearly depends on $^{e}/_{a}$ with a very steep slope as it is illustrated in Sect. 2.3 in Fig. 2.17. Mn provides seven valence electrons, but In has only three. For this reason, a change in the ratio between Mn and In strongly influences $^{e}/_{a}$.

Besides slight metrological deviations, the statement from literature that the Curie temperature does not depend on the composition [131], mentioned above, can also be confirmed by Fig. 4.3. This circumstance allows to describe the properties of the material family in a more general sense. Figure 4.3 suggests that the magnetization change during the martensitic transition is restricted to take place between the magnetization curves of pure martensite and austenite (black dashed curves). This is an important observation because the magnetization change between the two phases can be predicted for any arbitrary compound and therefore goes beyond characterizing just a single material. Based on this prerequisite, a more general description of the magnetocaloric properties will be derived.

So far, it was discussed how the first-order transition temperature can be adjusted, whereas the Curie point is retained. Since T_C^A is very close to the temperature window of the potential application, also the magnetization change is rather limited. One possibility to increase the magnetization change around room temperature is the partial substitution of Ni by Co. By the substitution of only 5 at %, the Curie temperature can be increased up to 400 K. Therefore, the magnetization change near room temperature can be enhanced effectively.

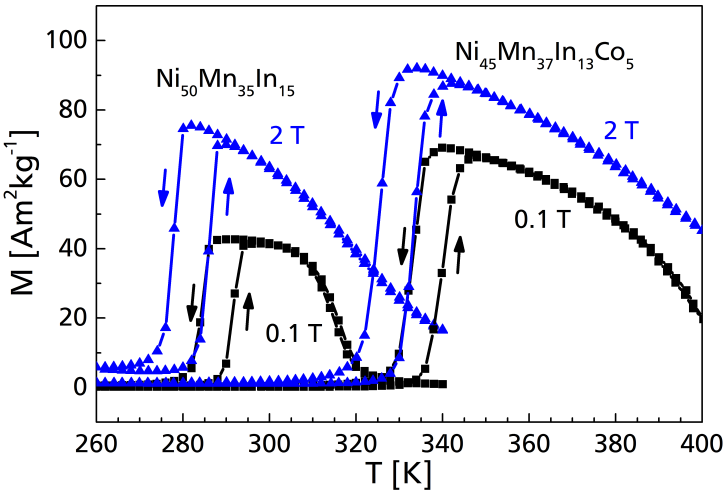

Figure 4.5: Comparison of the magnetization around the first- and second-order transition of a Co-containing and Co-free compound in 0.1 and 2 T.

In Fig. 4.4, a comparison of $M(T)$ curves of different Co-containing compounds in a magnetic field of 1 T is shown (a similar arrangement was done for the Co-free system in Fig. 4.3). It can be seen that also in the system with Co, the transition temperature is adjustable by changing the Mn to In ratio. However, the second material system appears to be more sensitive to compositional changes. In fact, an increase of 0.9 at % of In shifts the transition by about 150 K. Note that in the system without Co, a change of 100 K was achieved for a compositional variation of the In content of 1 at %.

Furthermore, it is evident that for the Co-containing Heusler alloys less In is needed in order to achieve a transition near room temperature ($Ni_{50}Mn_{35.2}In_{14.8}$ in contrast to $Ni_{45}Mn_{36.8}In_{13.2}Co_5$). This means that the partial substitution not only affects the Curie temperature of the austenite but also the transition temperature itself. A third influence of Co in the Heusler structure is obvious in the low temperature range of the martensite phase in Fig. 4.4. It appears that the low temperature martensite phase is paramagnetic even at 200 K. A different behavior was observed in Fig. 4.3, where the magnetization was significant in this temperature range. The reason for this difference is that Co also influences the Curie temperature of the martensite phase T_C^M. It is found that a substitution of 5 at % of Co decreases T_C^M from 200 down to about 50 K. Consequently, due to different reasons, the magnetization change near room temperature can be enhanced by the substitution of Co.

Figure 4.5 shows the magnetic behavior of two exemplary alloys with and without Co in two different magnetic fields. The 2 T curves are shown in blue and the 0.1 T curves in black, respectively. This plot illustrates the driving force of the magnetocaloric effect in these Heusler materials as already discussed in the introduction. The application of a magnetic field affects the transformation and stabilizes the phase with higher magnetization, which is the austenite in these materials. As a consequence, the transition occurs already at lower temperatures when applying a magnetic field. This shift of the transition temperature is the driving force of the magnetocaloric effect in these first-order materials, which will be discussed in more detail in the following section. It was also shown that the magnetic properties of the

transformation can be easily predicted, which will give rise to a more general description of the transition characteristics.

4.1.2 Determination of the isothermal entropy change

In the following, a comprehensive study on three exemplary compounds with different stoichiometry will be performed. Their transition temperatures vary between 240 and 300 K, as plotted in Fig. 4.6. For instance, the first alloy with a composition of $Ni_{49.8}Mn_{35.0}In_{15.2}$ transforms at rather low temperatures (Fig. 4.6(a)). The three magnetization curves were obtained in 0.1, 1 and 2 T respectively. By measuring the $M(T)$ behavior in different magnetic fields, the shift of the transition temperature can be evaluated, which is shown in Fig. 4.6(b). The specific temperatures martensite start M_s, martensite finish M_f, austenite start A_s and austenite finish A_f were determined by fitting the magnetization curve at each field linearly. The magnetic-field dependence of the transition can be summarized by means of a magnetic phase diagram. A linear shift of the transition temperatures in magnetic fields can be observed but the slopes of these fits tend to differ. It can be stated that the shift of M_f ($-7.1\,\mathrm{K\,T^{-1}}$) is larger than for instance for A_f ($-5.7\,\mathrm{K\,T^{-1}}$).

The thermal hysteresis of the first compound is in the range of 16 K, which is large in comparison to the other samples. It becomes smaller for the alloy $Ni_{49.6}Mn_{35.6}In_{14.8}$ in Fig. 4.6(b) and (c). For this material, the thermal hysteresis amounts to only about 8 K. It is worth noting that also the width of the transition is smaller in comparison to the first compound. However, applying a magnetic field shifts the transition temperatures much less. They vary between -4.0 and $-4.4\,\mathrm{K\,T^{-1}}$ only. A further decrease is observed for the third Heusler alloy with the composition $Ni_{50.2}Mn_{35.0}In_{14.8}$, shown in Fig. 4.6(e) and (f).

A straightforward measurement technique to determine the entropy change of the complete transition ΔS_t is the differential scanning calorimetry (DSC). By this method, the heat flow from or into the sample can be determined in comparison to an empty reference holder. The resulting DSC curves of the three specific materials under investigation are shown in Fig. 4.7 (for heating in red and for cooling in blue). For each sample, the heating and cooling curves are separated, which is due to the thermal hysteresis in these materials. The transition entropy ΔS_t can be calculated as follows:

$$\Delta S_t = \int_{A_s}^{A_f} \frac{1}{T}(\dot{Q} - \dot{Q}_{baseline})\left(\frac{\partial T}{\partial t}\right)^{-1} dT \,, \tag{4.1}$$

which is expressed by the integration of the background-corrected heat flow between austenite start A_s and finish A_f. The heating rate during the measurement $\left(\frac{\partial T}{\partial t}\right) = 10\,\mathrm{K\,min^{-1}}$ also needs to be considered. The peak areas of the DSC signal being related to the entropy change of the transition, are highlighted in Fig. 4.7. There is evidence of the trend that ΔS_t decreases with lower transition temperatures. A detailed explanation of this effect will be given later. It is worth noting that for $Ni_{50.2}Mn_{35.0}In_{14.8}$ with the highest transition temperature, the first-order peak is overlapping with the heat flow related to the second-order transition around the austenitic Curie temperature $T_C^A = 314\,\mathrm{K}$. The problem can be illustrated by means of the cooling curve (blue peak). The small hump between 300 and 320 K is the signal of the second-order

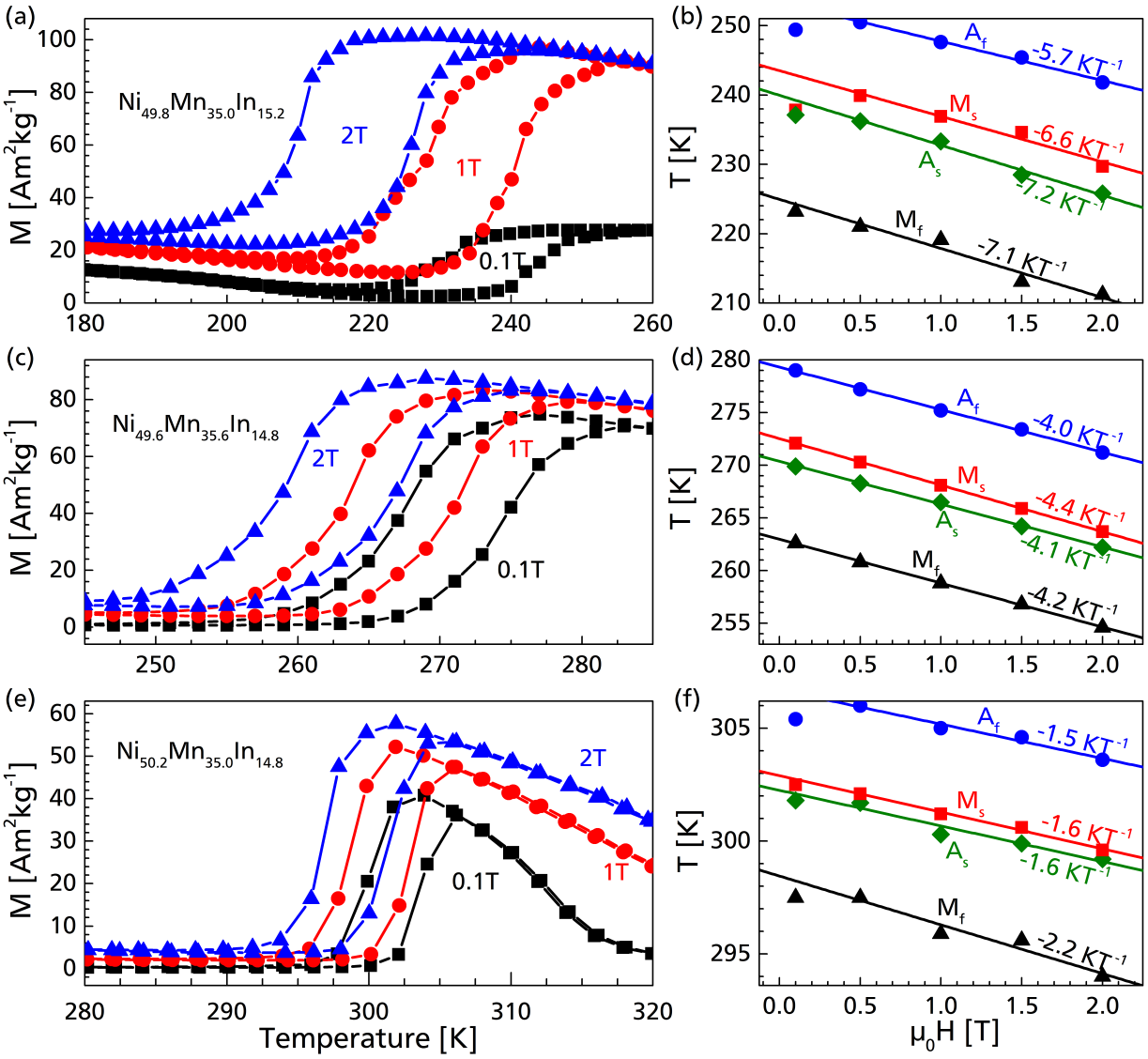

Figure 4.6: Magnetization curves for heating and cooling in 0.1, 1 and $2\,\mathrm{T}$ of (a) $Ni_{49.8}Mn_{35.0}In_{15.2}$, (c) $Ni_{49.6}Mn_{35.6}In_{14.8}$ and (e) $Ni_{50.2}Mn_{35.0}In_{14.8}$. The corresponding magnetic phase diagrams of the temperatures martensite start M_s, martensite finish M_f, austenite start A_s and austenite finish A_f are shown in (b), (d) and (f).

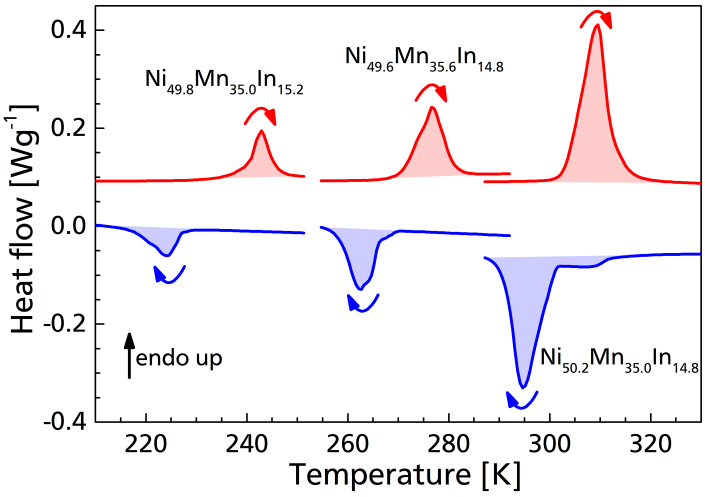

Figure 4.7: Differential scanning calorimetry of the three selected compounds from Fig. 4.6 under heating and cooling.

ferromagnetic-to-paramagnetic transition of the austenite phase. A subtraction of this contribution would be possible by selecting the background curve properly. On the other hand, this is rather complicated for the heating curve since both peaks perfectly overlap. A small overestimation of ΔS_t is therefore to be expected.

The corresponding ΔS_t values determined by DSC are given in Tab. 4.1. Also the transition temperatures, the thermal hysteresis and the transition width are specified. Another approach to determine the transition entropy is the measurement of the heat capacity C_p. These measurements have been performed in collaboration with colleagues from the University of Zaragoza. The C_p results of the three compounds are plotted in Fig. 4.8 under heating and cooling. The separation between these two curves is again related to the thermal hysteresis of the different materials. A reduction of the peak area, as it was apparent from the DSC curves, is also observable in the C_p measurements. The transition entropy can be calculated by using the following equation:

$$\Delta S_t = \int_{A_s}^{A_f} \frac{C_p(T) - C_{p,baseline}(T)}{T} dT \ . \tag{4.2}$$

Also for the heat capacity data, a baseline correction is necessary. The corresponding ΔS_t values under heating are specified in Tab. 4.1 as well. The spikes which are visible in Fig. 4.8 are no measurement errors. They are actually an indication of the high resolution of the setup. Since the martensitic transition is based on a nucleation and growth mechanism, an avalanche-like transformation can be observed in these materials [107]. However, the DSC measurements in Fig. 4.7 show no spikes because the temperature resolution of the signal is much worse. This is also due to the fact that a typical heating rate of $10\,\mathrm{K\,min^{-1}}$ was used in the DSC, whereas the C_p measurement was done under quasistatic conditions. Around 314 K, a small peak of the austenitic Curie temperature is visible in the C_p curves a well, although there is a small deviation in the peak position.

Table 4.1: Transition temperatures austenite start A_s and finish A_f, martensite start M_s and finish M_f in $0.1\,\mathrm{T}$, thermal hysteresis ΔT_{hys} and the width of the transition ($A_f - A_s$) of the three different materials. Also the entropy changes of the complete transition ΔS_t obtained from differential scanning calorimetry (DSC) and C_p measurements as well as the peak values of the magnetic field induced isothermal entropy change ΔS_T in a magnetic field change $\mu_0 \Delta H = 2\,\mathrm{T}$ from C_p and magnetization measurements are shown.

Sample	A_s[K]	A_f [K]	M_s[K]	M_f [K]	ΔT_{hys}[K]	$A_f - A_s$[K]	ΔS_t [J kg^{-1}K^{-1}] DSC	Cp	ΔS_T [J kg^{-1}K^{-1}] Cp	M(T)
$Ni_{49.8}Mn_{35.0}In_{15.2}$	237.9	249.6	238.6	223.7	14.4	11.7	11.6	10.6	8.2	9.3
$Ni_{49.6}Mn_{35.6}In_{14.8}$	269.3	279.4	272.4	262.4	7.9	10.1	18.9	17.1	10.6	13.0
$Ni_{50.2}Mn_{35.0}In_{14.8}$	302.0	306.0	300.9	296.1	3.6	4.0	37.4	36.9	22.1	18.1

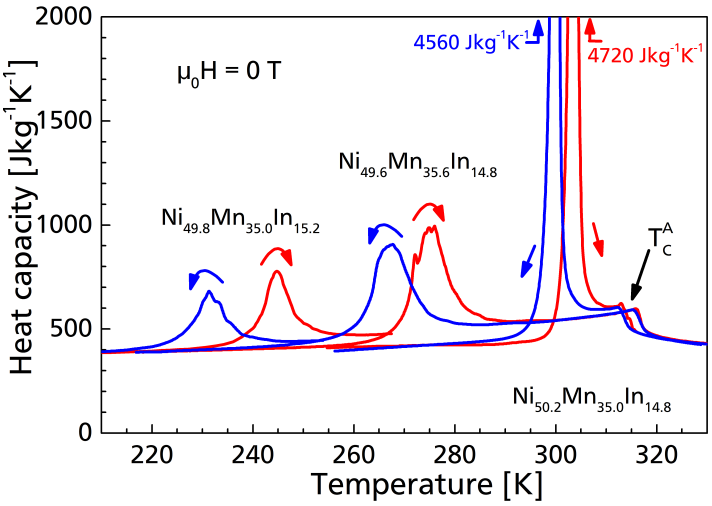

Figure 4.8: Heat capacity measurement for heating and cooling in zero field. Around $314\,\mathrm{K}$ the Curie temperature of the austenite phase T_C^A is visible.

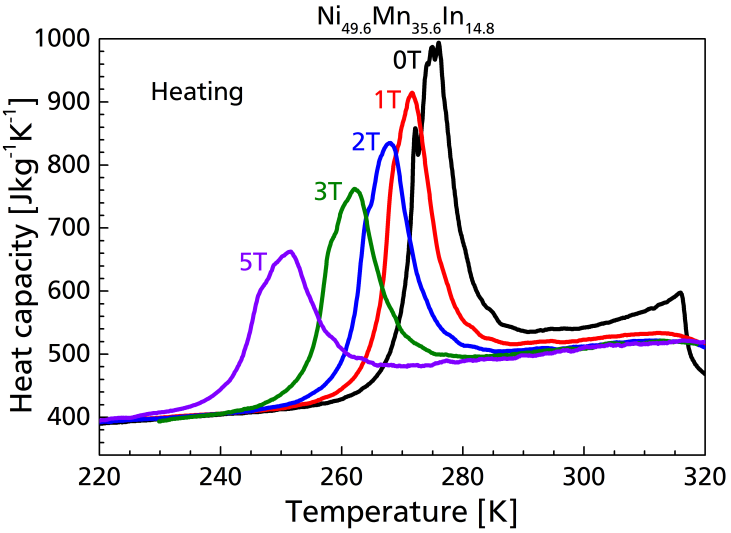

Figure 4.9: Heat capacity measurements under heating protocol in different magnetic fields of the alloy with the composition $Ni_{49.8}Mn_{35.0}In_{15.2}$.

The results of the two utilized methods coincide quite well, as can be confirmed by Tab. 4.1. The entropy change of the transition ΔS_t accounts for about $37\,\mathrm{J\,kg^{-1}\,K^{-1}}$ for the compound transforming close to room temperature and is reduced down to about $11\,\mathrm{J\,kg^{-1}\,K^{-1}}$ for the sample with the lowest transition temperature, which is significant.

So far, the entropy change ΔS_t of the complete transition was determined. This value indicates the ideally achievable entropy change of the compound and sets an upper limit for the magnetocaloric effect induced by the application of a magnetic field. However, the magnetic field induced or isothermal entropy change ΔS_T is strictly to be distinguished from the entropy change of the complete transition ΔS_t. The latter was determined based on zero field data. In order to evaluate ΔS_T, measurements in different magnetic fields need to be considered.

Figure 4.9 shows the heat capacity data in different magnetic fields up to 5 T of the compound $Ni_{49.8}Mn_{35.0}In_{15.2}$, which transforms around 0 °C in zero field. Only the heating protocol is illustrated here. It is clearly visible that the magnetic field has a strong influence. First the transition is shifted to lower temperatures in magnetic fields, which was already discussed several times. Also the peak height and area change drastically. The heat capacity measurement without any magnetic field results in an entropy change of the complete transition of about $17.1\,\mathrm{J\,kg^{-1}\,K^{-1}}$ according to Tab. 4.1. If, for instance, Eq. (4.3) is applied on the C_p data obtained in a magnetic field of 5 T, the ΔS_t value is much smaller and results in only $11.3\,\mathrm{J\,kg^{-1}\,K^{-1}}$. The origin of this reduction will be discussed after some additional investigations have been presented.

The field induced entropy change ΔS_T can be obtained from heat capacity data in different magnetic fields shown in Fig. 4.9. The following equation was applied for this calculation:

$$\Delta S_T(T,H) = \int_0^T \frac{1}{T} \cdot \big(C_p(T,H) - C_p(T,0)\big)\, dT \ . \tag{4.3}$$

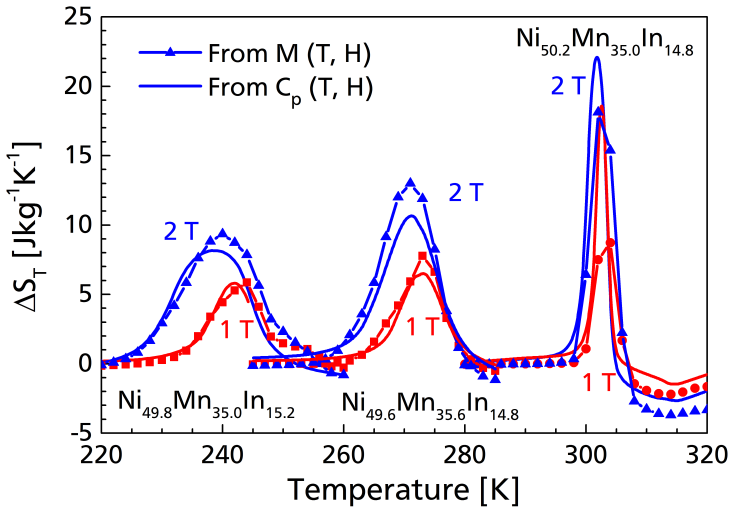

Figure 4.10: Comparison of the isothermal entropy change ΔS_T obtained from isofield magnetization (lines with symbols) and heat capacity measurements (lines without symbols). Red stands for a magnetic field change of 1 T and blue for 2 T respectively.

In contrast to Eq. (4.3), the difference between the heat capacity in field and without field is integrated from zero up to a certain temperature. Obviously this cannot be entirely correct, since it is impossible to measure the heat capacity down to 0 K due to the third law of thermodynamics. A small error will therefore be inevitable. But the difference $C_p(T,H)-C_p(T,0)$ far below the magnetostructural transition is negligibly small. For instance, it can be seen that all five C_p curves come close at 220 K. Therefore, it is reasonable to neglect the integration area below 220 K. However, caution needs to be exercised if the first-order transition is overlapped by a second-order transition.

It is also possible to determine the magnetocaloric effect from magnetization curves using the Maxwell equation (2.9). However, it is to be considered that the quality of the resulting ΔS_T strongly depends on the utilized measurement protocol. For materials with large hysteresis, as for Heusler alloys, the estimation based on $M(H)$ measurements is not recommendable [57]. The problem is that the coexistence of the high and low temperature phase can lead to a critical overestimation of the magnetocaloric effect even though the measurement was done in the discontinuous mode (heating to high temperatures and cooling to low temperatures before each measurement).

On the other hand, when measuring isofield magnetization curves in a broad temperature interval, problems due to phase coexistence are avoided. From this data, the resulting ΔS_T values determined by the Maxwell equation are much more reasonable. Figure 4.10 shows the isothermal entropy change from magnetization data of the three compounds in a magnetic field change of 1 T (red curves with squares) and 2 T (blue curves with triangles). Also ΔS_T curves from C_p are plotted additionally in the same diagram as straight lines without symbols. In general, the coincidence of the two methods is reasonable. Small deviations may occur due to the usage of different sample amounts or imperfect thermal equilibration.

The maximum values of ΔS_T are given in Tab. 4.1. Therefore the compound $Ni_{50.2}Mn_{35.0}In_{14.8}$ with the highest transition temperature shows the highest magnetocaloric effect of about $22\,J\,kg^{-1}\,K^{-1}$ in a magnetic field change of 2 T. Interestingly, this is much lower than one would expect when considering the entropy change of the complete transition ΔS_t. For the other two compounds, a similar effect is observed, but it is less pronounced. This is because the shift of the transition temperature is different, as shown in Fig. 4.6. For the above-mentioned alloy, a magnetic field of 2 T is not sufficient to completely transform the material from martensite into austenite. Consequently, the corresponding ΔS_T will be very much reduced.

4.1.3 The dilemma of inverse magnetocaloric materials

In the previous section, the differences between the entropy change of the complete transition ΔS_t and the isothermal entropy change ΔS_T were explained. Results of several different measurement techniques regarding these two quantities have been evaluated and compared. Based on this data, a more general description of the magnetocaloric properties can be developed. This concept will be introduced next.

Figure 4.11(a) summarizes ΔS_t and ΔS_T of the three materials which were discussed in detail in the previous section. Furthermore, the study is extended to the Co-containing Heusler system as well, which is shown in Fig. 4.11(b). The solid symbols refer to the entropy change of the complete transition obtained from DSC measurements of the different compounds. On the other hand, the isothermal entropy change, which is induced by a magnetic field, is shown as blue lines for a field change of 2 T and in green lines for $\mu_0 \Delta H = 1\,T$. For the compounds with the lowest transition temperature, ΔS_T in 2 T nearly reaches the measurement points from DSC (results for ΔS_t). This means that the transition can be completed in 2 T and the full potential is exploited. For compounds transforming around room temperature, the magnetic field-induced entropy change strongly falls short as the transition is not yet completed in 2 T.

In Fig. 4.11(a) and (b), further DSC results from literature are plotted as hollow symbols in order to obtain a complete picture of the entropy change of the whole material system [127, 133, 115, 134, 114]. The dashed line corresponds to the fitted temperature dependence of the transition entropy change ΔS_t. How this curve was obtained will be deduced in the following. As discussed in the introduction, the total entropy change of the transition consists of three different contributions, the lattice part ΔS_{lat}, the electronic part ΔS_{el} and the contribution of the magnetic system ΔS_{mag}. Kihara et al. [127] found that the electronic contribution is negligibly small in a Ni-Mn-In-Co sample. Therefore, the entropy change of the magnetostructural transition is mainly due to changes in the magnetic system and the structural transformation of the lattice. In the Heusler compounds under investigation, the low temperature martensite phase is paramagnetic, at least above 200 K. On the contrary, the high temperature austenite phase is ferromagnetic and has a high magnetization as for instance shown in Fig. 4.6. It implies that the magnetic ordering increases under heating. Therefore, the entropy change ΔS_{mag} of the transition must be negative. This is a somewhat uncommon behavior because the entropy of the magnetic system decreases when the sample is heated.

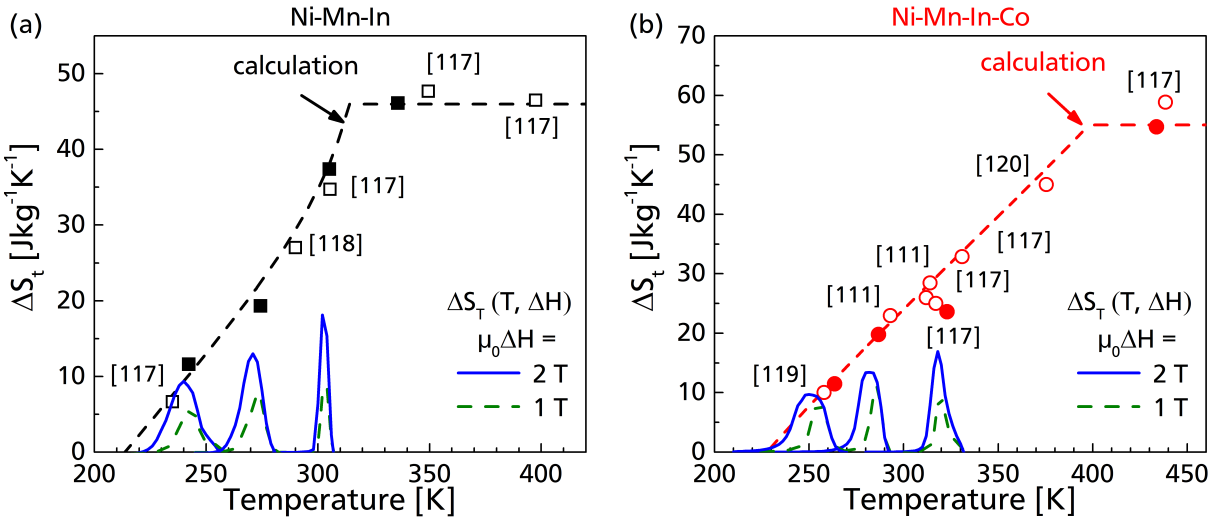

Figure 4.11: Entropy change of the complete transition (solid symbols) obtained from calorimetry for different compounds of Ni-Mn-In (a) and Ni-Mn-In-Co (b). For selected alloys also the isothermal entropy change for different magnetic field changes is plotted (blue and green curves). Additional data from literature is included (hollow symbols) [127, 133, 115, 134, 114].

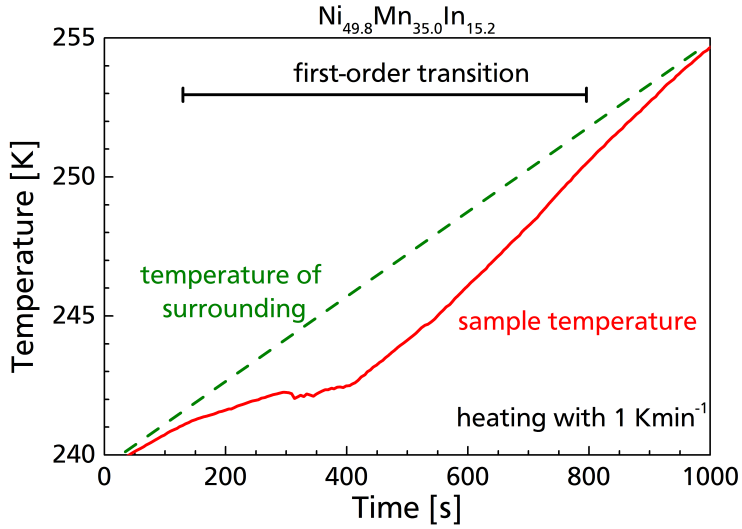

Figure 4.12: Temperature profile of the alloy $Ni_{49.8}Mn_{35.0}In_{15.2}$ under heating with $1\,\mathrm{K\,min^{-1}}$.

The entropy change related to the pure structural martensitic transition of the crystal lattice ΔS_{lat} under heating is positive. For $Ni_{49.8}Mn_{35.0}In_{15.2}$, the sample temperature profile under heating with a sweeping rate of $1\,K\,min^{-1}$ in the absence of a magnetic field is illustrated in Fig. 4.12. It can be seen that the sample temperature comes to a standstill at about 242 K, which is described by the concept of latent heat being a typical feature of first-order transitions. In the further course of the experiment, the sample approaches the temperature of the surroundings again. Two important issues must be considered at this point. First, the transformation under heating is not ideal. This is because the martensitic transition temperature of the material is distributed over a range of more than 10 K (see Fig. 4.6). Therefore, the heating profile is smoothed out; note that the spikes appearing around 242 K are due to the avalanche-like transformation character [107].

Secondly, it should be mentioned that the contribution of the magnetic system ΔS_{mag} is active despite being in zero-field. What is observed is the superposition of both ΔS_{mag} and ΔS_{lat} but the latter is dominant here. Now the focus will be again on the results presented in Fig. 4.11. It is discussed above that the variation of the chemical composition between the different alloys under investigation is only very small. For instance for increasing the transition temperature by 100 K, only a change of 1 at % of In and Mn is necessary. In the phenomenological model it is therefore assumed that the lattice part of the entropy change ΔS_{lat} does not change in the temperature interval of interest between 200 and 400 K. Above the austenitic Curie temperature T_C^A, the magnetic contribution to the entropy change is zero. Furthermore it can be seen in Fig. 4.11(a) for the three Co-free alloys transforming above the austenitic Curie temperature T_C^A that the entropy change of the transition is rather constant, from which the structural entropy change ΔS_{lat} was determined to be constant with values of $46\,J\,kg^{-1}\,K^{-1}$ in the Ni-Mn-In and $55\,J\,kg^{-1}\,K^{-1}$ in the Ni-Mn-In-Co system.

Based on the assumption that ΔS_{lat} is constant, it can be concluded that the temperature dependence of ΔS_t is related to the contribution of the magnetic system ΔS_{mag}. In order to calculate the magnetic entropy of martensite and austenite, a simple Heisenberg model description was used [54]:

$$S_{mag} = N_{mag}\, k_B \left[\ln\left(4\pi \frac{\sinh(x)}{x}\right) - x\, \coth(x) + 1 \right] \tag{4.4}$$

$$\text{with } x = \frac{\mu_0\, m_0\, (\rho\, n_W\, M + H)}{k_B\, T}.$$

The parameter N_{mag} is the number of magnetic degrees of freedom. The In atoms carry only a small induced magnetic moment and do not contribute to the magnetic entropy. In Ni_2MnGa it was furthermore demonstrated that the magnetic moment of Ni is induced too [135]. Consequently, only the Mn and the Co moments were considered as magnetic degrees of freedom. In Eq. (4.4), m_0 is the effective magnetic moment per magnetic degree of freedom. This is calculated from the saturation magnetization at $T = 0\,K$, determined from $M(T)$ measurement at low temperature. In Ni-Mn-In and Ni-Mn-In-Co, m_0 turns out to be $4.38\,\mu_B$ and $4.02\,\mu_B$ respectively by distributing the saturation magnetization to all magnetic degrees of freedom. The molecular field constant n_W is the only fitting parameter in the model. It is fitted to a value of 260 in both systems. Based on magnetization measurements of martensitic and austenitic

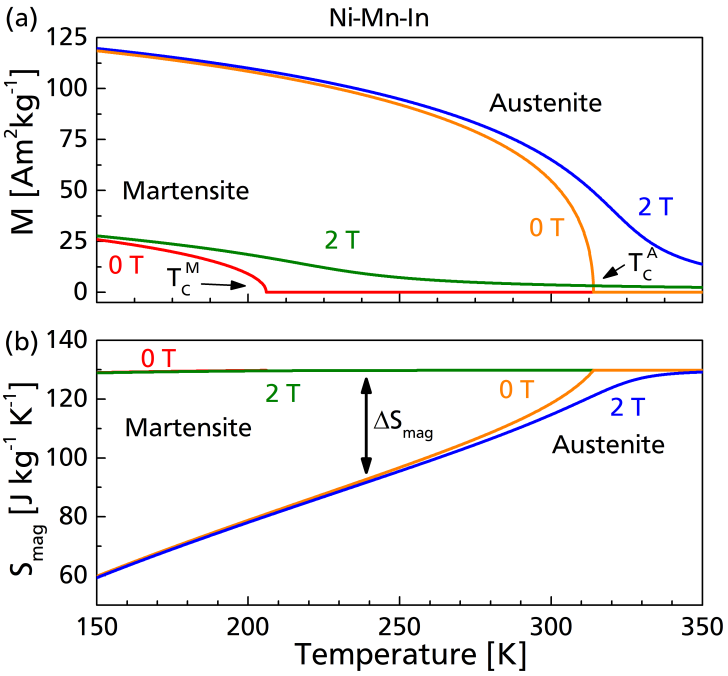

Figure 4.13: (a) Calculated magnetization of martensite and austenite in 0 and 2 T based on experimental data. (b) Magnetic entropy of the two phases as a function of temperature.

samples in different magnetic fields H, $M(T)$ was estimated by using the approach from Kuz'min [52], which is illustrated in Fig. 4.13(a) for 0 and 2 T for the Co-free system.

Figure 4.13(b) shows the magnetic entropy of both phases in 0 and 2 T, which is calculated by using the Heisenberg model (Eq. (4.4)). The small magnetization of the martensite and especially its low Curie temperature T_C^M imply that the magnetic entropy of martensite is already maximal above 200 K. This fact simplifies the determination of the magnetic contribution, which is the difference of the magnetic entropy of the two phases. For this reason and the assumption that the lattice contribution is constant, the temperature dependence of the entropy change of the transition is only related to the magnetization of the austenite phase:

$$\Delta S_t(T) = \Delta S_{lat} + \Delta S_{mag} = \Delta S_{lat} + S^A_{mag}(T) - S^M_{mag} \,. \tag{4.5}$$

In Fig. 4.11(a) and (b), the resulting ΔS_t dependence in zero-field is shown as a dashed line. The correlation between the calculated and the measured ΔS_t is reasonable. At the Curie temperatures of the two Heusler systems a pronounced kink is visible. This is the point at which the magnetization vanishes and therefore the magnetic contribution vanishes too. However, when applying a magnetic field, the entropy change curve would be smoothed out at T_C^A, as can be seen in the magnetic entropy of the austenite in 2 T in Fig. 4.13(b). For higher temperatures, the entropy change remains constant as implemented in the model. With decreasing transition temperature, the magnetization of austenite increases significantly, as was shown in Fig. 4.6. Therefore the magnetic contribution ΔS_{mag} gains more importance, which reduces ΔS_t according to Eq. (4.5). At a certain temperature, both the magnetic

and the lattice contribution compensate each other and ΔS_t goes to zero. This point is denoted as the compensation temperature T_{comp}, which is 214 K for the Co-free and 228 K for the Co-containing system in $H = 0$. When the temperature is decreased further, the entropy change of the transition would in principle change sign. But this would mean that the inverse magnetocaloric transition would change into a conventional one. Such a behavior is not observed in Heusler alloys. However, the transition does not take place any more. In literature this effect is typically referred to as the kinetic arrest phenomenon [136, 137, 138, 139, 140].

Many far-reaching consequences result from Eq. (4.5). On the one hand, a large magnetization change is deplets the available entropy change of the structural transition and is therefore parasitic. This increases until both contributions are equal and a transformation is no longer possible. It is most contradictory that on the other hand a large magnetization change is essential in order to drive the magnetocaloric effect. This is because large isothermal entropy changes are only observable if the transition temperature can be shifted efficiently. But for this, the difference in the magnetization must be as large as possible. The contradiction that the change in magnetization is at the same time necessary and undesirable can be denoted as the dilemma of inverse magnetocaloric materials. This result allows to explain the effects of the heat capacity measurements in different magnetic fields in Sect. 4.1.2. In Fig. 4.9 in Sect. 4.1.2 it was obvious that the area of the heat capacity peak related to the first-order transition was decreasing when shifting the transition to lower temperatures by applying a magnetic field. The reason for this is the enhanced influence of the magnetic contribution, which reduces the entropy change of the transition.

In the following, the shift of the transition temperature in magnetic fields will be discussed in more detail. In Fig. 4.14, the magnetization curves for heating and cooling of the Co-containing alloy $Ni_{45.7}Mn_{36.6}In_{13.5}Co_{4.2}$ in magnetic fields up to 14 T is shown. A number of important observations arise from this investigation. In a small magnetic field of 0.1 T (black curve), the material transforms around room temperature. The transition itself is very sharp and the thermal hysteresis of 10 K is significant but not too large. For 2 T (red curve) and 4 T (blue curve), the shape of the $M(T)$ curve does not change much but a strong shift of the loop down to lower temperatures can be observed. It is worth noting again that for the Co-containing Heusler system, the magnetization of the martensite has only a very limited influence because its Curie temperature T_C^M is around 50 K and therefore very low. Also the saturation magnetization at 0 K is small. Consequently, the magnetic contribution of the martensite is negligible.

When increasing the magnetic field further to 6 T (green curve), the transition becomes broader and also the thermal hysteresis increases. Interestingly, the magnetization at low temperatures is much higher than in the 4 T experiment. It may be speculated that the martensite is not saturated in smaller fields and therefore the $M(T)$ curve in 6 T shows a higher magnetization. However, this explanation is not correct, which will be more obvious when considering the ΔS_t contribution separation model from above.

In this section, the compensation temperature T_{comp} was introduced. It describes the temperature at which the magnetic and the lattice part of the entropy change cancel each other out. For Ni-Mn-In-Co T_{comp} in zero-field is about 228 K. If this concept is valid, the transition will be suppressed below that temperature. This is exactly what happens when measuring the 6 T magnetization curve. Some residual

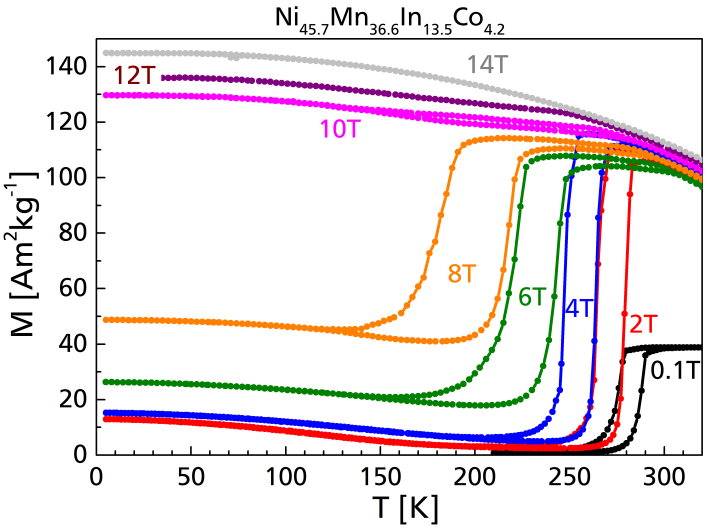

Figure 4.14: Magnetization as a function of temperature under heating and cooling in different magnetic fields.

austenite remains in the material and this is the reason why the magnetization at low temperatures is about twice as large as in smaller fields. When increasing the magnetic field further, the transition becomes more and more suppressed. Finally, in a magnetic field of 14 T (grey curve) the sample does not transform at all and remains in the pure austenitic state.

In conclusion, important observations can be made:
(1) The transition temperature shifts in magnetic fields. In literature it is often assumed that this shift is linear [141]. In small magnetic fields, this is a reasonable approximation, but it is apparent from Fig. 4.14 that this is not a good description in high magnetic fields. Here, the shift is far from being linear.
(2) An efficient transformation is only observed for temperatures above 200 K. When the magnetic field becomes stronger, more and more parts of the material remain in the austenite phase.
(3) The thermal hysteresis increases when the transition temperature is significantly lowered by an external magnetic field.
(4) The width of the transition increases in higher magnetic fields.

An attempt is made in order to explain all these effects in the context of the phenomenological model. For this purpose it is necessary to utilize the Clausius-Clapeyron equation (Eq. (2.15)), which is derived above. It relates the entropy change ΔS_t with the magnetization change ΔM and the shift of the transition temperature $\frac{dT_t}{dH}$. Since the Heisenberg model (Eq. (4.4)) and Eq. (4.5) provide a comprehensive description of the ΔS_t of the whole material family, it is obvious to combine this with the Clausius-Clapeyron equation in order to get an extended picture of the shift of transition temperature. Therefore, the following equation can be derived:

$$\frac{1}{\mu_0} \cdot \frac{dT_t}{dH} = -\frac{\Delta M(T)}{\Delta S_t(T)} = -\frac{\Delta M(T)}{\Delta S_{lat} + S^A_{mag}(T) - S^M_{mag}} \,. \tag{4.6}$$

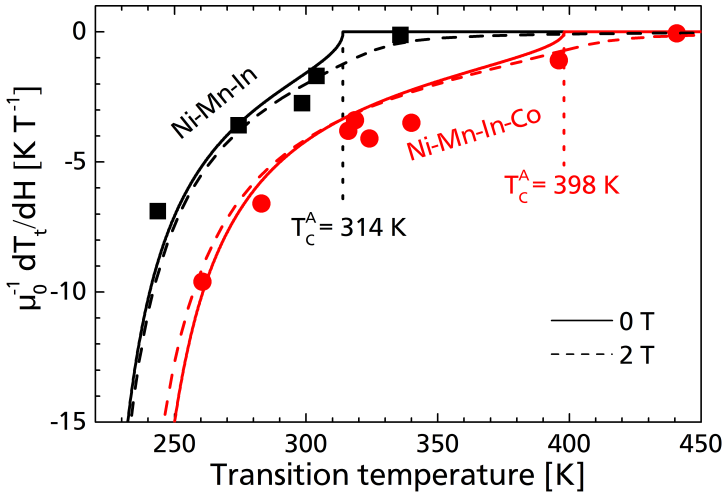

Figure 4.15: Shift of transition temperature $\frac{dT_t}{dH}$ as a function of the transition temperature T_t. The Heusler system without Co is drawn in black and the system with Co in red respectively. For selected compounds, the shift of the transition temperature was determined in small magnetic field changes (black and red symbols). The solid and the dashed curves are trend lines for 0 and 2 T calculated from Eq. (4.6).

Based on this equation, the temperature profile of $\frac{dT_t}{dH}$ was determined and is plotted in Fig. 4.15 for Ni-Mn-In and Ni-Mn-In-Co in a magnetic field of 0 and 2 T. For several different alloys the shift of the transition temperature is determined in rather small fields, which is also shown in the diagram. The magnetization vanishes above T_C^A, at least in the absence of a magnetic field, and therefore the shift of the transition temperature goes to zero as well. By applying a magnetic field, the magnetic moments of the paramagnetic austenite are partly aligned, which results in a small magnetization change and therefore the transition temperature can also be shifted to some extent, even above T_C^A. Below the Curie temperature, $\frac{dT_t}{dH}$ varies significantly for the different materials. The calculated curves for 0 T (solid line) and for 2 T (dashed line) can give a reasonable description of this behavior. The origin for the divergence of $\frac{dT_t}{dH}$ at lower temperatures is again the competition between the entropy change of the structural transformation and the contribution of the magnetic system. At the compensation point T_{comp}, the total entropy change ΔS_t is zero and therefore Eq. (4.6) has a pole at this temperature.

What does this mean for the previously discussed effects? Without a magnetic field, the material $Ni_{45.7}Mn_{36.6}In_{13.5}Co_{4.2}$ shown in Fig. 4.14 transforms around room temperature. At this temperature, the difference in the magnetization between the two phases is very large and consequently the transition shifts with approximately $-7\,\mathrm{K\,T^{-1}}$ in small fields. Applying a certain magnetic field will consequently lower the transition temperature. But at the same time, the magnetic contribution to the entropy change increases and therefore the shift of the transition temperature grows. For instance for the 6 T curve in Fig. 4.14 under heating, half of the sample transformed at about 240 K. Comparing this with the 8 T measurement in Fig. 4.14, the according $\frac{dT_t}{dH}$ would be about $-15\,\mathrm{K\,T^{-1}}$.

Observation (1) from above can therefore be explained. The shift of the transition temperature in magnetic fields appears not to be linear. It is found by the help of the model that it is strongly divergent. The

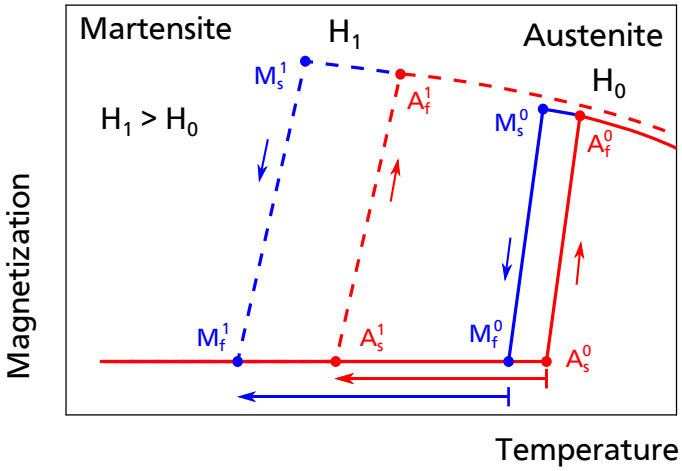

Figure 4.16: Idealized martensitic transformation. Both the hysteresis and the transition width change when applying a magnetic field.

origin is the depletion of the structural entropy change by the increased magnetic contribution. When both are equal, the martensitic transition is no longer possible. Therefore, some amount of the sample stays in the austenitic phase. As a consequence of this incomplete transformation, the magnetization below T_t is higher (see Fig. 4.14). Therefore, observation (2) can also be understood by the description from above. So far, it is not clear how the incomplete transformation further influences the $\frac{dT_t}{dH}$ behavior. In principle, the magnetization change reduces due to the incomplete transition, but a quantitative description of this issue is difficult. It should also be mentioned that the assumption of a constant lattice contribution to the entropy change ΔS_{lat} is no longer valid for lower temperatures. In order to give a better description for temperatures below 200 K, a different model would need to be introduced, which takes the temperature dependence of the structural entropy change into consideration as well.

The remaining points (3) and (4) will be addressed with the help of the schematic in Fig. 4.16. An idealized transition is illustrated, showing a rather small thermal hysteresis in the field H_0 (solid lines) being $A_s^0 - M_f^0$. Consider that the shift of the transition temperature would be constant for all temperatures. In this case the shape of the hysteresis curve would be always the same when applying different magnetic fields. But from Eq. (4.6) it follows that $\frac{dT_t}{dH}$ strongly deviates with temperature. What does this mean for the idealized transition in Fig. 4.16? Due to the thermal hysteresis, the point M_f^0 is situated at a slightly lower temperature than A_s^0. Looking at Fig. 4.15, it implies that the martensite finish temperature would shift slightly more in magnetic fields than the austenite start temperature. Consequently, the thermal hysteresis increases the stronger the deviation between these two points becomes.

The same approach can be utilized in order to explain the increasing transition width in magnetic fields observed in Fig. 4.14. As previously discussed, it is inevitable to have some chemical variations in the material. For this reason, the transition temperature locally scatters and the transformation of the whole sample has a certain distribution. This is schematically shown in Fig. 4.16. The points A_s^0 and A_f^0 are separated to some extent. Therefore, the latter point should have a slightly lower $\frac{dT_t}{dH}$. An incremental increase of the external magnetic field will consequently intensify the difference between A_s^0 and A_f^0. This

is nothing else but a broadening of the transition in magnetic fields. Supporting this argumentation, the described characteristics are observed in real measurements of $M(T)$, as shown in Fig. 4.6. There, the trend is visible that the shift of the transition temperature increases from A_f to M_f.

In this section, the dilemma of inverse magnetocaloric materials was introduced. It describes the conflict between the magnetic system and the structural transition. Of course, these two contributions are coupled, since this kind of transition is a magnetostructural one. Nevertheless, it could be demonstrated that the entropy change of the transition ΔS_t can be separated into the lattice entropy change ΔS_{lat} and the entropy change related to the magnetic moments ΔS_{mag}. Based on experimental and literature data, a phenomenological description using the Heisenberg model was developed, in which it is assumed that the lattice contribution is constant. It turned out that both contributions act against each other and therefore the available entropy change decreases when the magnetization of the austenite phase gets stronger. This effect progresses until the lattice and the magnetic contribution cancel each other out. The great contradiction for inverse magnetocaloric materials like Ni-Mn-based Heusler alloys is that a large magnetization is parasitic, since it reduces the lattice entropy change, but at the same time a large magnetization change is essential in order to drive the transition by applying a magnetic field.

This description turned out to be very useful in order to explain the transition behavior of the different compounds under investigation. The separation approach could also be extended using the Clausius-Clapeyron equation. By this it was possible to predict the temperature profile of the driving force of the magnetocaloric effect, namely $\frac{dT_t}{dH}$. Due to the special features of the total entropy change, $\frac{dT_t}{dH}$ strongly deviates with temperature. Several important consequences were derived from this behavior. Therefore, the shift of the transition accelerates and both the thermal hysteresis and the transition width increase when a sample is exposed to high magnetic fields.

With the help of the ΔS_t separation, it was possible to understand the observed effects of the transformation when being shifted by an external magnetic field. In principle, this concept is also applicable when the transition temperature is changing because of the chemical composition. In Sect. 4.1.1 it was discussed that the width of the transition and the thermal hysteresis is larger for compounds with lower transition temperature. There are many similarities between the above-mentioned effects and the shift of the transition temperature induced by compositional changes. For a "base" alloy transforming near the Curie temperature with a relatively sharp transition and small hysteresis, the influence of the magnetic system is weak. If the transition temperature is "incrementally" lowered by small chemical variations, the magnetic system gains importance, which results in the broadening of the transition and the hysteresis.

4.1.4 Influence of hydrostatic pressure

In this section, the influence of hydrostatic pressure on the martensitic transformation will be investigated. Therefore, magnetic measurements of the compound $Ni_{45.7}Mn_{36.6}In_{13.5}Co_{4.2}$ were performed using a pressure cell. Figure 4.17 shows the magnetic behavior of this sample in a magnetic field of 1 T without pressure, in 4.5 and 8.4 kbar. One can clearly see how strong the martensitic transition is shifted to higher temperatures in the presence of hydrostatic pressure. The corresponding $\frac{dT_t}{dp}$ is in the

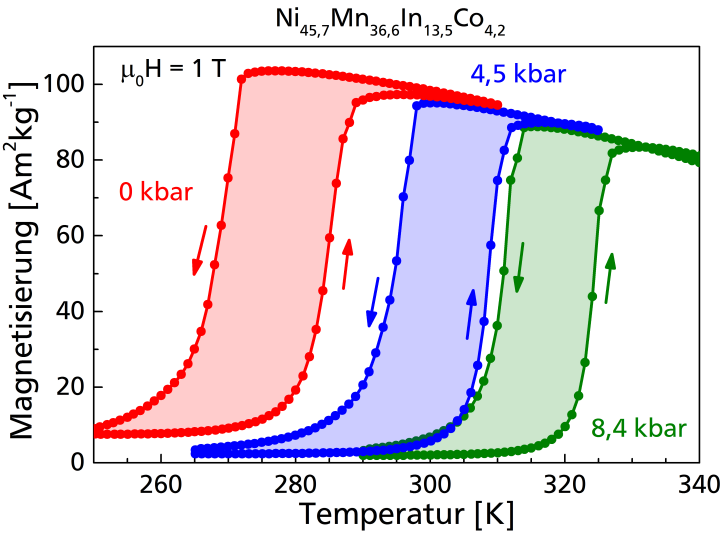

Figure 4.17: Magnetization as a function of temperature of $Ni_{45.7}Mn_{36.6}In_{13.5}Co_{4.2}$ in a magnetic field of 1 T in different pressures of 0, 4.5 and 8.4 kbar.

range of $5\,\mathrm{K\,kbar^{-1}}$ or $50\,\mathrm{K\,GPa^{-1}}$. The magnetization of the austenite decreases under pressure but this is in agreement with the temperature dependence of the pure austenitic phase, since the three curves in Fig. 4.17 follow the same trend in the high temperature region. This means that the influence of hydrostatic pressure on the Curie temperature of austenite T_C^A is not pronounced.

In comparison to the magnetization measurements in different magnetic fields up to 14 T in Fig. 4.14, the transition is slightly broader and has a bigger thermal hysteresis too. This can be related to the different measurement conditions that were used. For simple magnetization measurements without pressure, the sample is fixed on the sample holder and it is heated and cooled by a gas stream. However, the measurements under pressure were performed with the sample placed inside the pressure cell shown in Fig. 3.4 (note that also the 0 kbar measurement was done using the pressure cell). The mass of the cell is significant. Consequently, it is more complicated to change the sample temperature precisely. Even though the heating and cooling rate was only $1\,\mathrm{K\,min^{-1}}$, the sample temperature slightly lacked behind. For this reason, the thermal hysteresis is increased by the measurement setup to some extent but generally speaking, the results are reasonable.

In the three different hydrostatic pressures, $M(T)$ curves in magnetic fields from 0.2 to 2 T in steps of 0.2 T were measured in order to calculate the isothermal entropy change ΔS_T. The results are shown in Fig. 4.18 for a magnetic field change of 1 (circles) and 2 T (triangles). It can be seen that the isothermal entropy change increases under pressure. It should also be pointed out that the ΔS_T peak is sharper in higher pressures. This behavior is in perfect agreement with the results discussed above (see Fig. 4.11). It turns out that the same trend is visible when the transition temperature is changed by means of hydrostatic pressure instead of a compositional variation. This suggests that the concept of the dilemma of inverse magnetocaloric materials also applies under the influence of pressure.

It is worth focusing more on this point. For this reason, the magnetization curves in 0.2 and 2 T in 0 and 8.4 kbar are plotted in Fig. 4.19. From this comparison, it is apparent that the thermal hysteresis

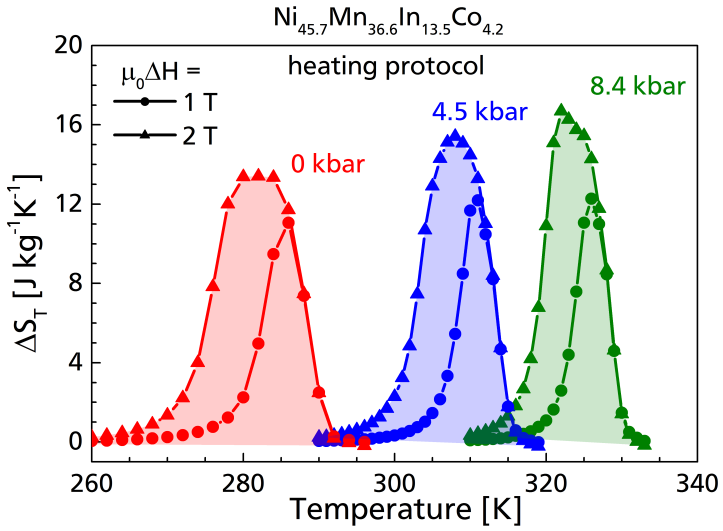

Figure 4.18: Isothermal entropy change ΔS_T as a function of temperature in a magnetic field change of 1 (circles) and $2\,\mathrm{T}$ (triangles) under different pressure.

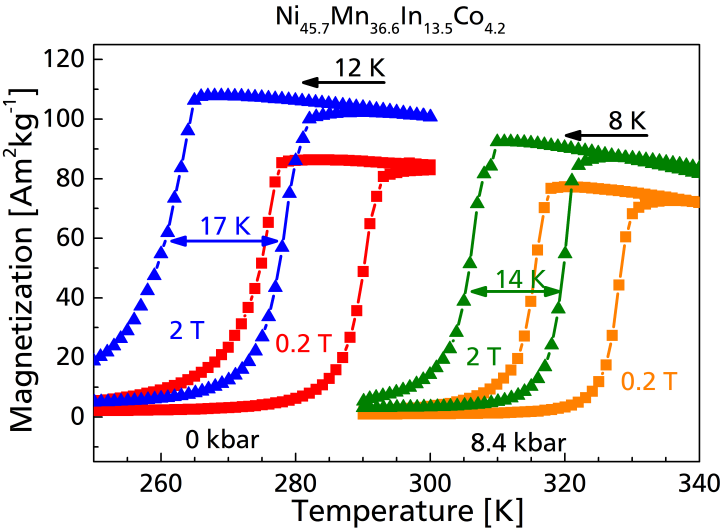

Figure 4.19: Magnetization as a function of temperature of $Ni_{45.7}Mn_{36.6}In_{13.5}Co_{4.2}$ in a magnetic field of 0.2 and $2\,\mathrm{T}$, in zero-pressure and in $8.4\,\mathrm{kbar}$.

is reduced under pressure by about 3 K. Furthermore, it can also be seen that the shift of the transition temperature in magnetic fields decreases from approximately $-7\,\mathrm{K\,T^{-1}}$ in $p = 0\,\mathrm{kbar}$ down to $-4.5\,\mathrm{K\,T^{-1}}$ in $p = 8.4\,\mathrm{kbar}$. The transformation also appears to be sharper under the influence of pressure. All these findings explain why the shape of the $\Delta S_T(T)$ curves in Fig. 4.18 changes.

Under hydrostatic pressure, the same conclusions can be made as in the previous section. By shifting the transition temperature about 40 K to higher temperatures simply by applying 8.4 kbar, the magnetization of the austenite phase and consequently the magnetic contribution to the entropy change decreases. This means that a larger ΔS_T can be obtained, as it illustrated in Fig. 4.11. At the same time, the shift of the transition temperature is reduced, which is shown in Fig. 4.15. The change in $\frac{dT_t}{\mu_0 dH}$ from -7 to $-4.5\,\mathrm{K\,T^{-1}}$ by a pressure of 8.4 kbar together with the sharpening of the transition and the reduction of the thermal hysteresis fits nicely into the derived concept, which demonstrates the universality of the dilemma of inverse magnetocaloric materials.

4.2 Reversibility of the magnetocaloric effect

The problem of thermal hysteresis in first-order materials was already pointed out. In this section the topic will be discussed in a more detailed way. In terms of applications, it is necessary to utilize the magnetocaloric effect related to a magnetostructural transition in a reversible manner. The presence of thermal hysteresis makes this more difficult because for instance higher magnetic field changes would be necessary in order to achieve a reversible transition. When speaking about the magnetocaloric properties, often only the isothermal entropy change ΔS_T is presented in literature and sometimes unrealistically high values are reported, which is attributed to an inappropriate use of the Maxwell Eq. (2.9) [108]. Certainly, the determination of the reversibility of the magnetocaloric effect is even more complex [142].

In addition to the isothermal entropy change ΔS_T, the adiabatic temperature change ΔT_{ad} is equally important. In the following, the focus will be on direct measurements of this parameter. It appears that significant temperature changes can be achieved in Ni-Mn-In-Co when applying a reasonable magnetic field to a fresh sample, but also under cycling of the magnetic field. This is originated in the special properties of so-called minor loops of hysteresis, which enhance the reversibility of the adiabatic temperature change ΔT_{ad} [41].

Finally, the reversible isothermal entropy change ΔS_T will be addressed. Therefore, it is necessary to investigate the total entropy diagram $S(T)$ of the martensitic transition, which can be determined by calorimetric methods. A comparison of both the $S(T)$ and direct ΔT_{ad} measurements reveals that the methods do not always match. The reason for this discrepancy will be investigated, from which it will be apparent that the reversible ΔS_T of minor loops is not easily accessible. However, a method will be proposed enabling the determination of the magnetocaloric effect under cycling [143].

4.2.1 Reversible adiabatic temperature change

So far, the isothermal entropy change ΔS_T was characterized when applying an external magnetic field. However, the adiabatic temperature change ΔT_{ad} is an equally important manifestation of the magnetocaloric effect. Both quantities are in principle identical from a thermodynamic point of view, it just depends on the thermodynamic condition which facet of the effect will be observed. In the case of a thermally insulated material, or in other words, under adiabatic conditions, the temperature will change when applying a magnetic field. Consequently, the measurement of ΔT_{ad} gives important insights into the properties of the magnetostructural transition.

In this section, the discussion of the results of direct ΔT_{ad} measurements will be performed on the alloy $Ni_{45.7}Mn_{36.6}In_{13.5}Co_{4.2}$ with outstanding magnetocaloric properties [41]. The magnetization curves in different magnetic fields of this material are shown in Fig. 4.20 (same sample as shown in Fig. 4.14 and 4.17). In small fields, the transition takes place near room temperature, but by applying only 2 T, the transition is shifted to about 0 °C. It was already shown in this work that the shift of the transition temperature does not follow a linear magnetic field relationship. In fact, the real correlation is much

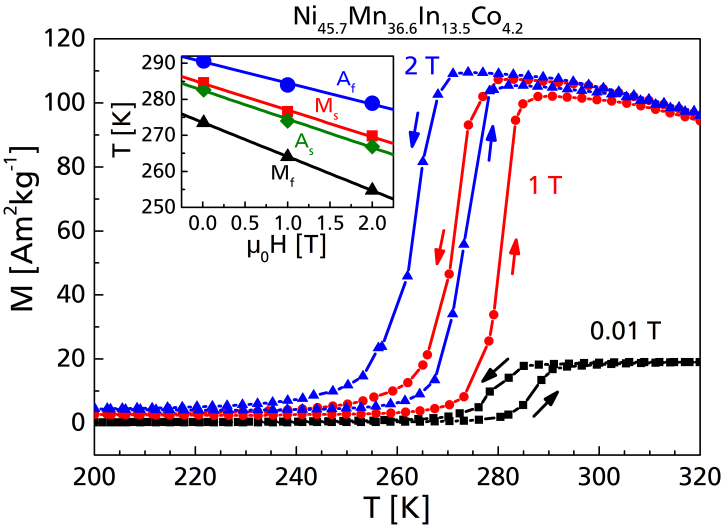

Figure 4.20: Magnetization as a function of temperature in different magnetic fields of the compound $Ni_{45.7}Mn_{36.6}In_{13.5}Co_{4.2}$. The inset illustrates the magnetic phase diagram.

more complicated. At least for the compound under investigation, it can be stated that between 1 and 2 T the transition is shifted by approximately 8 K to lower temperatures. This strong influence causes a complete transformation by applying a magnetic field of only 2 T under isothermal conditions, for example at 280 K.

The thermal hysteresis accounts for 10 K, which is rather large in comparison to other first-order magnetocaloric materials like La-Fe-Si [144]. It implies that under isothermal conditions at 280 K, the transition cannot be completely transformed back to the pure martensite phase when decreasing the field back to zero. Still half of the sample would probably be in the austenite state.

Under isothermal conditions, the transformation behavior can principally be described in a simple manner, as done above. In contrast to that, adiabatic conditions make this description much more complicated because the temperature is changing. However, from direct ΔT_{ad} measurements clear statements can be made. Figure 4.21 shows the temperature profile of the sample starting from a certain temperature when a magnetic field is applied. Depending on the starting condition, a different temperature profile is observed. Therefore, three exemplary starting temperatures were selected in order to elaborate this further. It is worth noting that the measurements were performed in the discontinuous protocol. This means that the sample was heated to the pure austenite and subsequently cooled down into the pure martensite state before approaching towards the target temperature. In this measurement protocol it is guaranteed that all individual experiments are independent from each other. This would not be the case if the sample is just simply heated continuously between the measurements.

The magnetic field profile is plotted linearly in Fig. 4.21, even though the magnetic field is in fact changing in a sinusoidal way. The chosen presentation form allows to separate the contributions of the first- and second-order transition to the ΔT_{ad} curve. The green curve starting at 292 K in Fig. 4.21 describes a zic-zac behavior. It is related to the conventional magnetocaloric effect of the pure austenite phase. In this case, the temperature changes almost linearly with the external magnetic field. It is worth

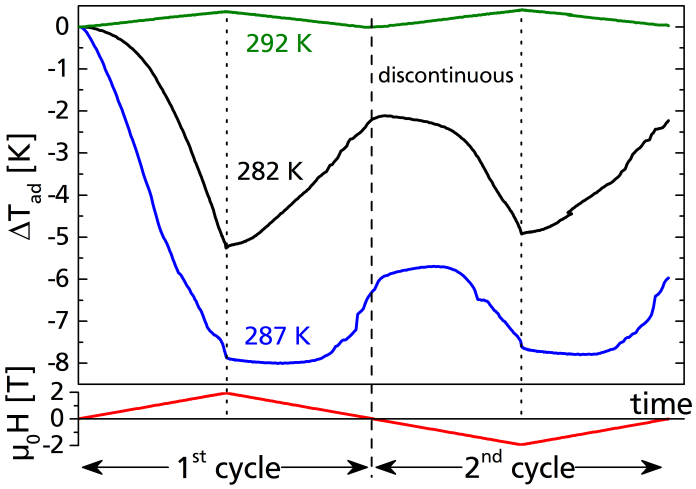

Figure 4.21: Adiabatic temperature change ΔT_{ad} of $Ni_{45.7}Mn_{36.6}In_{13.5}Co_{4.2}$ in a magnetic field change of 1.93 T. The data was modified to reflect a linear magnetic field profile.

noting that the sample heats up when being magnetized. However, the magnetocaloric effect is rather small for this room temperature measurement because this is very far away from the austenitic Curie temperature T_C^A at 398 K.

At a slightly lower starting temperature of 287 K, the sample cools down drastically by about −8 K when applying a magnetic field of 1.93 T. In this particular measurement, the first-order transition from martensite to austenite is close to completion, which will be discussed in more detail later. When removing the magnetic field again, the sample continues to cool a bit more. This is again due to the conventional magnetocaloric effect of the new created austenite phase. The magnetic field needs to be decreased to about 0.25 T to overcome hysteresis until the backward transition into martensite takes place. As a consequence, the material heats up by about 2 K. In the second field application cycle, the ΔT_{ad} profile does not change anymore. It should be mentioned that the magnetic field becomes negative in the second cycle. But since the materials under investigation are soft magnets and magnetocrystalline anisotropy is not an issue in the temperature range of interest, only the value of the magnetic field is important. Therefore, the negative field sequence can truly be considered as a second magnetic field cycle.

The black curve in Fig. 4.21 shows the cooling behavior when the experiment was initiated at an even lower temperature of 282 K. In this example, the temperature is far from changing linearly with field and a ΔT_{ad} of −5.2 K can be obtained in $\mu_0 \Delta H = 1.93$ T. In contrast to the blue curve, the sample starts heating immediately after decreasing the external magnetic field. After the intense initial cooling effect in the first magnetization step, the ΔT_{ad} profile remains the same in the second cycle also in this experiment. In fact, a reversible adiabatic temperature change of 3 K can be obtained in a magnetic field change of 1.93 T in this particular compound. This is a remarkably large reversible magnetocaloric effect, and comparable with the ΔT_{ad} of $La(Fe,Si,Co)_{13}$ showing a transition in the same temperature window and in the same magnetic field change [145].

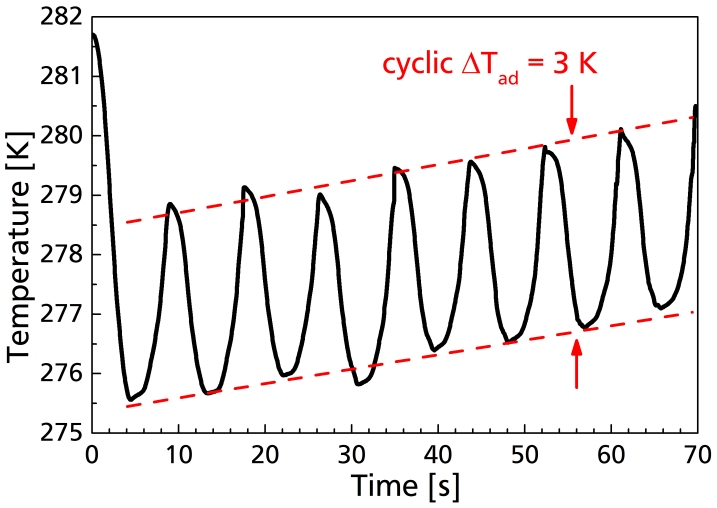

Figure 4.22: Cyclic response of the sample temperature in magnetic fields up to 1.93 T. After the first field application, a reversible adiabatic temperature change of 3 K can be obtained.

In a second experiment, the ΔT_{ad} measurement was repeated at this specific starting temperature in order to check the reliability of the results. The sample was therefore overheated to austenite, undercooled to martensite and then set to 282 K. Subsequently, the magnetic field was applied and removed 16 times in order to study the cyclic behavior of the material. As can be seen from Fig. 4.22, the large reversible adiabatic temperature change of 3 K is retained during the whole experiment. However, a temperature drift is present during the long measurement time of more than one minute. This heating of the sample is not surprising considering the fact that the initial ΔT_{ad} of −6.1 K drastically moved the sample temperature away from the equilibrium state at 282 K. Unless the sample is situated in a high vacuum and is well insulated with a special glass wool, the material drifts back to the equilibrium temperature. Due to the limitations of the adiabaticity in the setup, this drift in temperature cannot be avoided during the long measurement times. Nevertheless, the reversibility of the magnetocaloric effect remains unaffected in the cycling experiment.

Figure 4.23 compares the ΔT_{ad} values in the maximum field measured at different starting temperatures. The red curve illustrates the temperature change in the first field application, whereas the green curve is related to the temperature change of the second cycle. As mentioned above, an adiabatic temperature change up to −8 K could be achieved in the first field application. This is observable at 286 and 287 K, indicating that the transformation is completed. For just slightly higher starting temperatures, the adiabatic temperature change of the first-order transition vanishes and the overlapping second-order contribution becomes visible. Therefore a slight heating is observed above 290 K.

The first magnetization process of the discontinuously treated sample leads to significant ΔT_{ad} values over a temperature window of about 15 K. The reason for this is the strong shift of the transition temperature in magnetic fields, as illustrated in Fig. 4.20. The maximum ΔT_{ad} values represented by the red curve in Fig. 4.23 grow monotonously with increasing starting temperature because more and more martensite can be transformed into austenite when approaching the transition temperature in zero field.

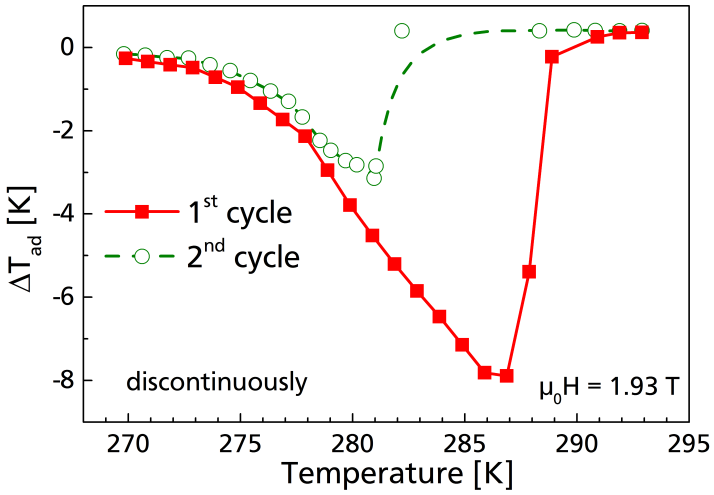

Figure 4.23: Adiabatic temperature change ΔT_{ad} after the first (red) and second field application of 1.93 T. The positions of the green data points are adjusted in respect to the absolute temperature at which the second magnetization sequence was initiated.

The reversible adiabatic temperature change is also plotted in Fig. 4.23 as a green line. The position of the data points is different in comparison to the first cycle ΔT_{ad} because the reference temperature was adjusted. Looking at Fig. 4.21, the starting temperature of the second field application was changed to the absolute temperature reached after the first field sequence was completed and the magnetic field went to zero. One can see that both, the first and second cycle ΔT_{ad} are comparable for temperatures below 280 K. However, for higher temperatures, the reversible adiabatic temperature change vanishes.

Figure 4.24 shows the magnetic phase diagram of the Heusler alloy $Ni_{45.7}Mn_{36.6}In_{13.5}Co_{4.2}$. The dashed lines indicate how the temperatures austenite start A_s, austenite finish A_f, martensite start M_s and martensite finish M_f change with increasing magnetic fields whereas M_f would only be visible at lower temperatures. These lines were determined from the magnetization measurements shown in Fig. 4.20.

The black and the blue curves in Fig. 4.24 reflect the temperature change of the sample in absolute values in the first field cycle. This data is taken from the same measurement as in Fig. 4.21 as ΔT_{ad} versus time. In zero magnetic field at 287 K, the sample is in a mixed phase region since this point is between A_s (green dashed line) and A_f (blue dashed line). The cool down starts immediately after increasing the magnetic field and continues monotonically. In the maximum field of 1.93 T, the austenite-finish line is breached. This means that the sample should be in the more or less pure austenite state. When decreasing the magnetic field again, the sample temperature does not change until the martensite-start line M_s is passed and the backward transition into martensite leads to a heating.

In contrast to this, the black curve starting at 282 K is almost completely in the martensite state before the field experiment, since this point is below A_s. The further cooling of the sample results in a lowering of the temperature down to 277 K in 1.93 T. In the maximum field, the sample is in a mixed phase region since the A_f line has not been reached yet. Decreasing the magnetic field again leads to an instantaneous heating of the material. For this particular case, a large reversible magnetocaloric effect is observed. This

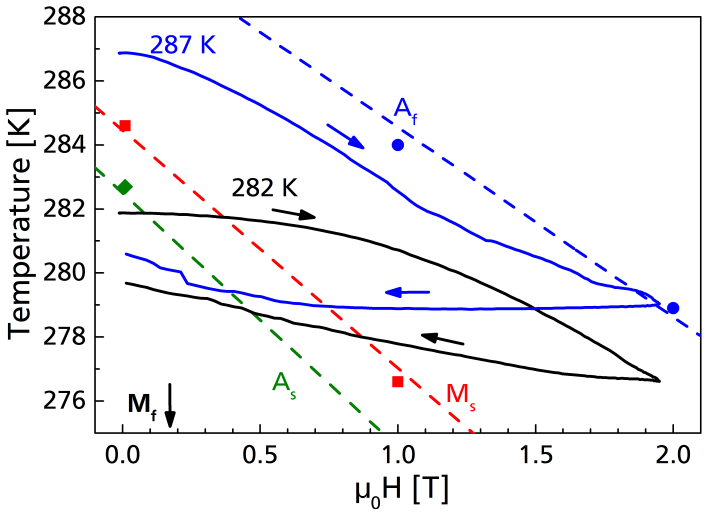

Figure 4.24: Magnetic phase diagram of $Ni_{45.7}Mn_{36.6}In_{13.5}Co_{4.2}$. The dashed lines represent the austenite-start A_s, austenite-finish A_f, martensite-start M_s and martensite-finish M_f temperatures in magnetic fields. Two adiabatic temperature change experiments are plotted in absolute temperatures for the first field cycle.

cannot be explained in terms of the magnetic phase diagram because in principle the backward transition should start only after overcoming the hysteresis of the transition or, in other words, by crossing the martensite-start line. The reason for this special behavior is that the transformation character is very different in so-called minor loops of hysteresis [107, 146], which will be further discussed in the next section.

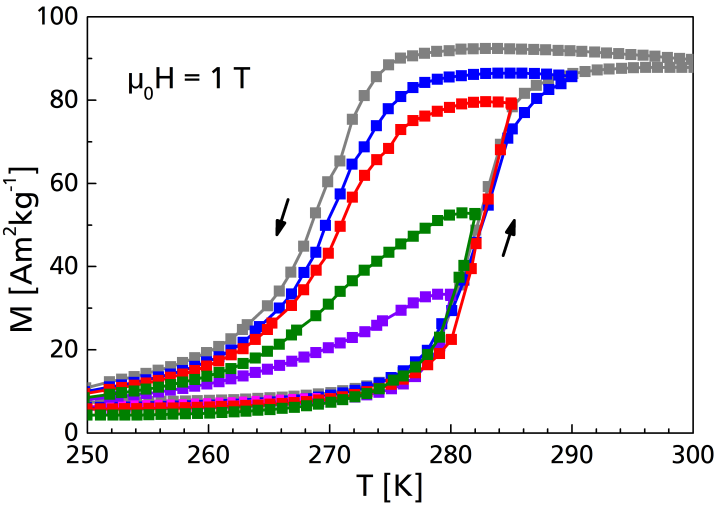

Figure 4.25: Magnetization measurements in a constant magnetic field of 1 T under heating and cooling in major and minor loops of hysteresis.

4.2.2 Minor loops of hysteresis

The reversibility study points to the fact that the transformation character in minor hysteresis loops is very different to that of a complete transition from martensite to austenite and vice versa. In order to further investigate this behavior, comprehensive magnetization measurements were performed on the compound $Ni_{45.7}Mn_{36.6}In_{13.5}Co_{4.2}$. This is of good use because the magnetization is directly linked to the phase fraction of the high and low temperature phase. In Fig. 4.25, the magnetization is plotted versus temperature in a constant magnetic field of 1 T. The grey curve shows the magnetization loop of the complete phase transition. This is similar to the results shown in Fig. 4.20 (red curve).

For measuring minor loops of hysteresis, the experiment was started at low temperatures and the heating branch was recorded. For this reason, the magnetization curves upon heating overlap in all measurements. At a certain reversal temperature, the heating was stopped, followed by the measurement of the cooling branch. Finally, the sample was cooled to low temperatures again to erase the memory of the material. Four different magnetization curves of minor hysteresis loops are shown in Fig. 4.25. The blue curve with the highest reversal temperature of $T_{rev} = 290\,\mathrm{K}$ looks very similar to the major loop (grey curve). However, for lower reversal temperatures, the backward transition is significantly different.

Especially for the green curve with $T_{rev} = 282\,\mathrm{K}$, the reduction of the thermal hysteresis is apparent. After entering the minor loop in the mixed phase region with about 50 % of austenite and martensite, cooling the sample by only 2 K is enough to initiate the transition back to martensite. In comparison to that, the decrease in magnetization starts just below 276 K in the major hysteresis loop. Even though the magnetization decreases less strongly in the cooling branch of the green minor loop, a significant phase fraction change can be initiated in a rather small temperature interval. Consequently, the thermal hysteresis is reduced when entering minor hysteresis loops.

The martensitic transition in Heusler compounds is driven by nucleation and growth of the new-forming phase. This process must therefore be the origin for the reduction of the thermal hysteresis in minor loops. An effective tool for the in-situ observation of the martensitic transition is optical microscopy. It allows to investigate the phase transition of a large surface area of the sample in the millimeter range under different stimuli. A sequence of four microscopy images at different temperatures is shown in Fig. 4.26. The first image (Fig. 4.26(a)) was taken at room temperature in the pure austenite state. There is not much contrast visible, only two grains separated by a grain boundary can be seen. When cooling the sample inside the cryostat of the microscope, the nucleation of martensite starts at a certain temperature. Figure 4.26(b) is taken at 283.5 K, shortly after the first martensite nuclei turn up. Typical needle-like structures of the martensite phase are visible, which grow further through the whole sample, ending up in a high contrast image at low temperatures (Fig. 4.26(c)). This contrast is due to the topology of the sample surface, since the different variants of martensite lead to a deformation of the surface. Depending on the orientation of the variant, more or less light is reflected, which allows to optically distinguish between austenite and martensite.

After heating the material back to room temperature, as shown in Fig. 4.26(d), two observations can be made. The sample is again in the pure austenite state, but some cracks are visible (highlighted areas). Interestingly, both cracks are located near the nucleation sites of the first martensite nuclei, which becomes apparent when comparing Fig. 4.26(b) and (d). The crack at the bottom of the image was formed along the grain boundary, but the second crack appeared inside the left grain. The reason for this is the large volume change during the transition and the resulting formation of high mechanical stress. Furthermore, some surface relief is visible in the pure austenite state after the first cool-down. This might be a modification of the sample surface induced by the martensite structure.

A series of further cooling experiments was performed. Microscopic images of the martensite phase at low temperature are presented in Fig. 4.27 after the second (a) and third (b) cool-down. By comparing those two images with Fig. 4.26(c) it becomes obvious that the microstructure of the martensite phase is always different or even unique. This is an important observation because it implies that the nucleation process takes place in an arbitrary manner. The first nuclei form with a certain randomness in location and orientation. These first events strongly influence the transformation of neighboring parts. As will be discussed in more detail later in this thesis, this is mainly triggered by local stress created during the transformation.

Mechanical stress has a strong influence on the formation of martensite [96]. In order to point out this effect even more, a map of the local transition temperature T_t is generated from the image sequences taken with the microscope. Therefore, the martensite phase is marked in selected images. Those are related to the actual temperature of the sample at which the images were taken. From this analysis, a 3D map of the local transition temperature on the surface can be created, which is shown for the first (see Fig. 4.26) and the second cooling experiment (see Fig. 4.27(a)) in Fig. 4.28. The local transition temperature is illustrated by both height and color. It is apparent that the two profiles differ significantly. This means that not only the martensite structure changes when the sample is heated through the transition completely. Also the local transition temperature is varied by 5 K and more. Since the chemical

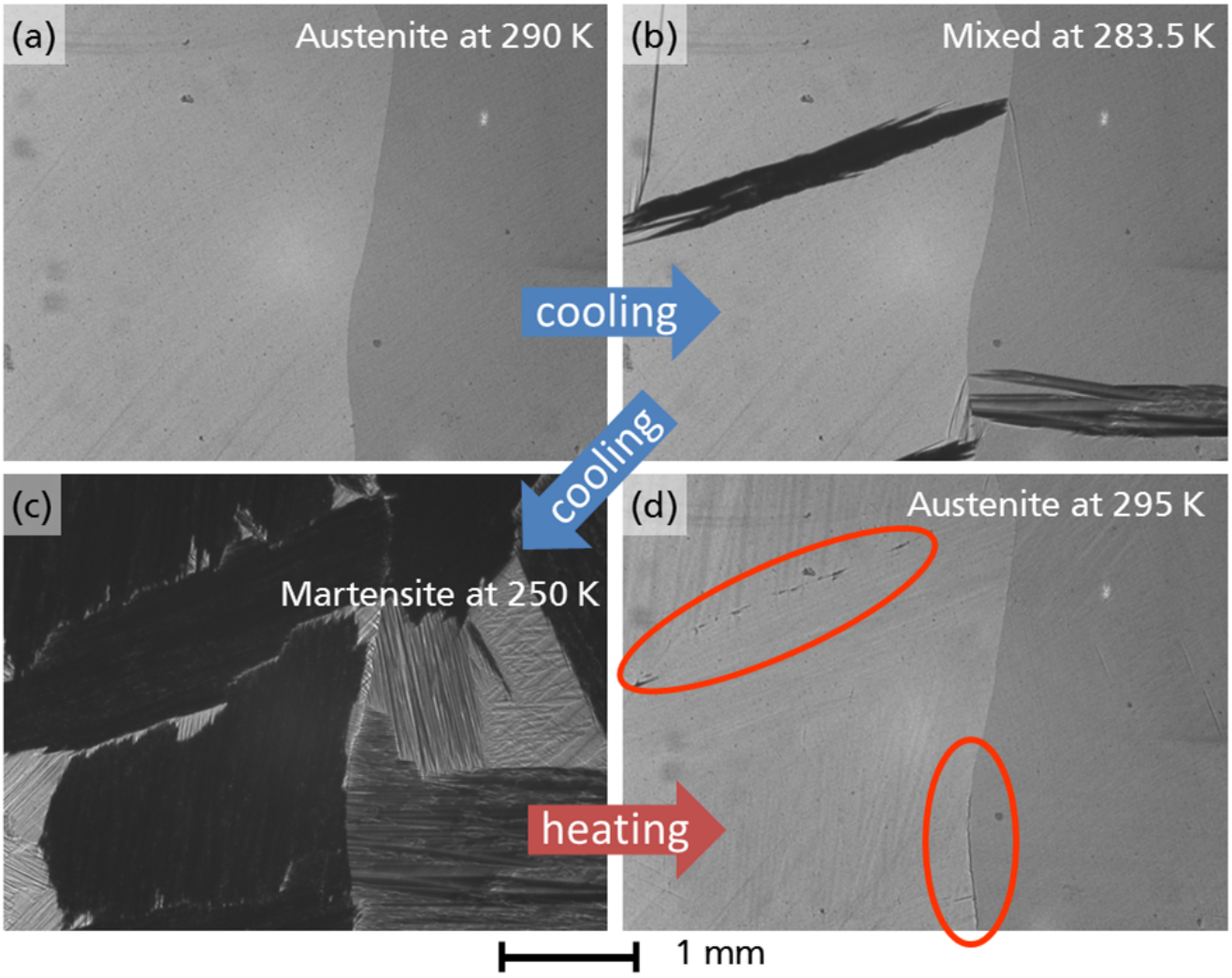

Figure 4.26: Optical microscopy images of the sample in the austenite state at room temperature (a), at 283.5 K in a mixed state (b), in pure martensite at low temperature (c) and after heating back to room temperature again (d). Cracks inside the grain and along the grain boundary are highlighted. After the cooling and heating sequence, a surface relief remains.

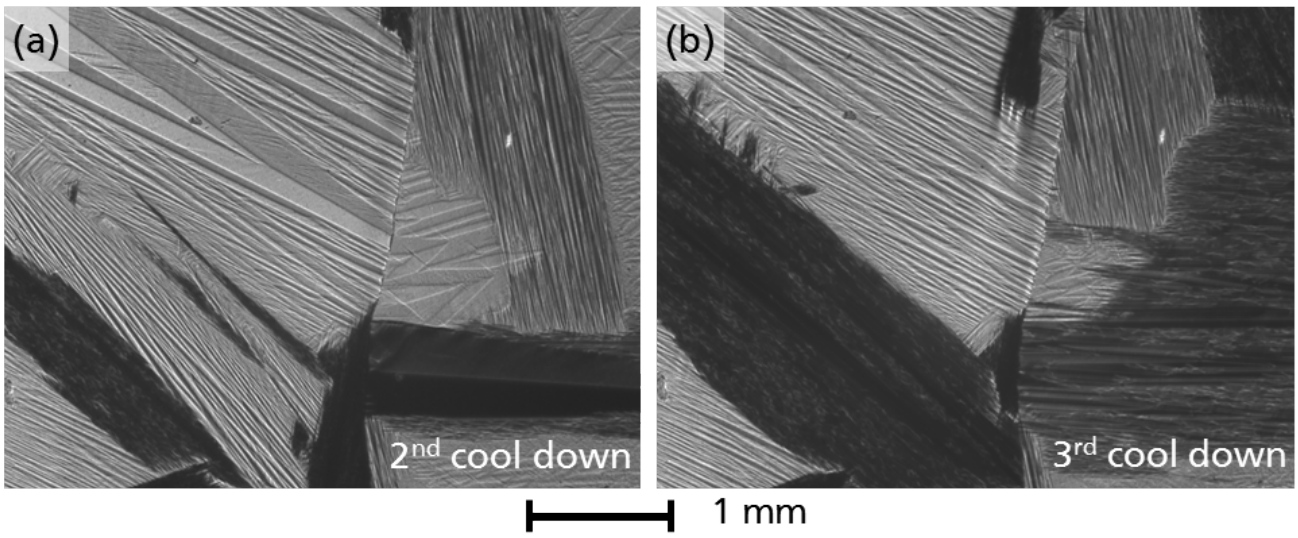

Figure 4.27: Optical microscopy images of the martensite structure of the sample from Fig. 4.26 after the second (a) and the third cool down (b) showing entirely different martensite structures.

composition does not change, this strong shift of T_t must be related to the formation of stress during the martensitic transition.

In the following, minor loops of hysteresis will be studied by in-situ microscopy. Figure 4.29 shows a series of microscopic images of one minor loop with a reversal temperature of 290 K. This T_{rev} seems to be rather high in comparison to the values used in Fig. 4.25, but one needs to consider that the magnetic measurements were performed in a magnetic field of 1 T. In contrast to that, the microscopic study was done in zero magnetic field. For this reason, the sample transforms at about 8 K lower in the magnetization measurements. Figure 4.29(f) schematically illustrates the phase fraction of the path followed in the minor loop experiment in zero magnetic field.

The first image, Fig. 4.29(a), was taken at 290 K. Some martensite needles are already visible at this temperature. At first, the sample was cooled down to 260 K into the pure martensite state, following the blue path in the schematic (Fig. 4.29(f)). About 30 % martensite is visible at a temperature of 281 K. Further cooling of the material leads to a complete transformation to martensite, as shown in Fig. 4.29(c). It is worth mentioning that this is the same picture as in Fig 4.27(a). In the next step, the sample was heated to the reversal temperature T_{rev} without overshooting, following the red path and then immediately cooling down again. Image (d) was obtained exactly at the reversal point. The two Figs. 4.29(b) and (d) look rather similar, but there are significant differences in the contrast, especially in the mid-region to the right of the grain boundary. For instance a big vertical martensite needle can be seen in (b) but nearly disappeared in (d).

The final cooling step, following the green path, results in the microstructure shown in Fig. 4.29(e). This martensite state looks very much the same as the one after the initial cool-down in Fig. 4.29(c). Slight differences can be seen in the highlighted areas in (e), but in general it is rather surprising that a comparable martensite structure could be obtained even though about 70 % of the low temperature

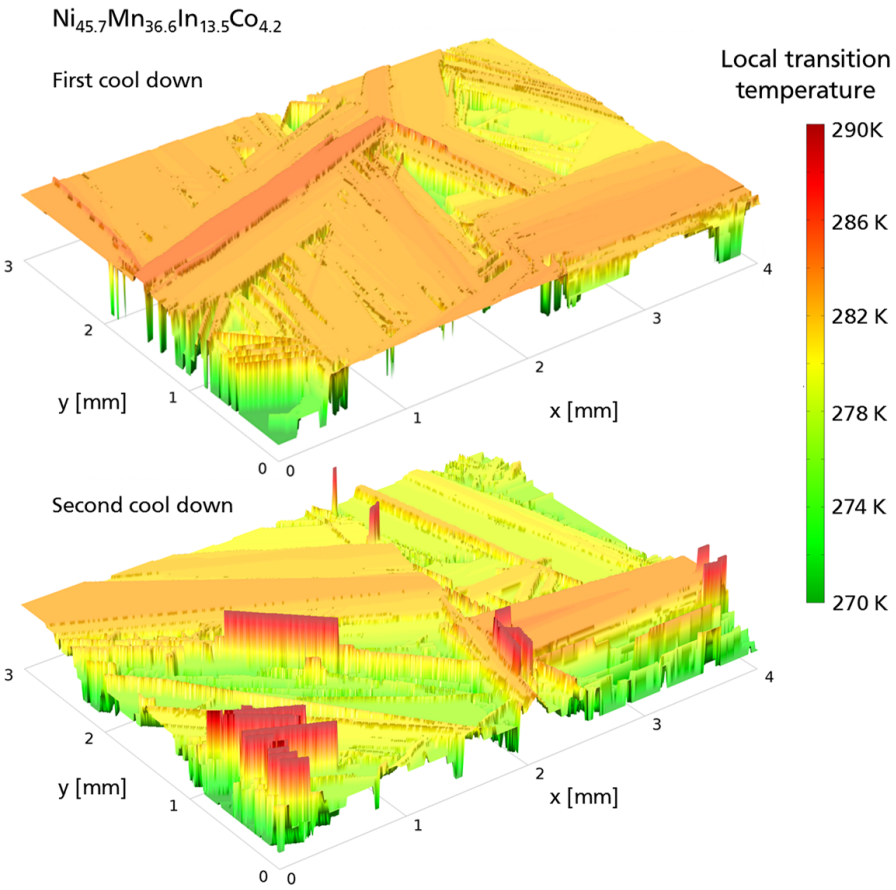

Figure 4.28: Map of the local transition temperature during first and second cooling obtained from image analysis of in-situ optical microscopy.

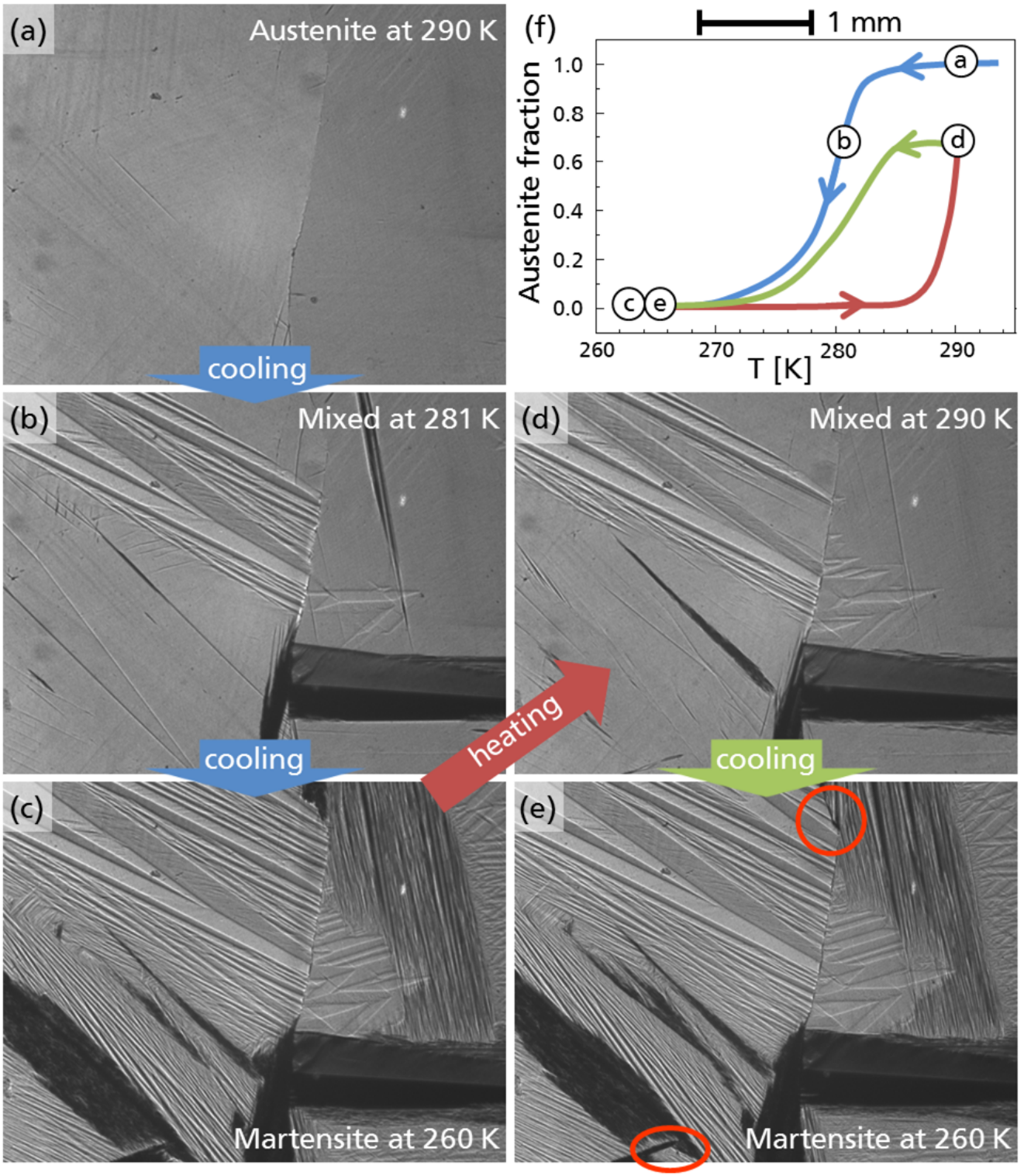

Figure 4.29: Optical microscopy images following a minor loop of hysteresis after the initial cool down from the pure austenite phase (a) via the mixed state (b) to the low temperature martensite state (c). Subsequently a minor loop was performed by heating to $290\,\mathrm{K}$ (d) and cooling to the low temperature again (e). Changes in the martensitic configuration can only be found in the highlighted areas. (f) Schematic illustration of the experiment.

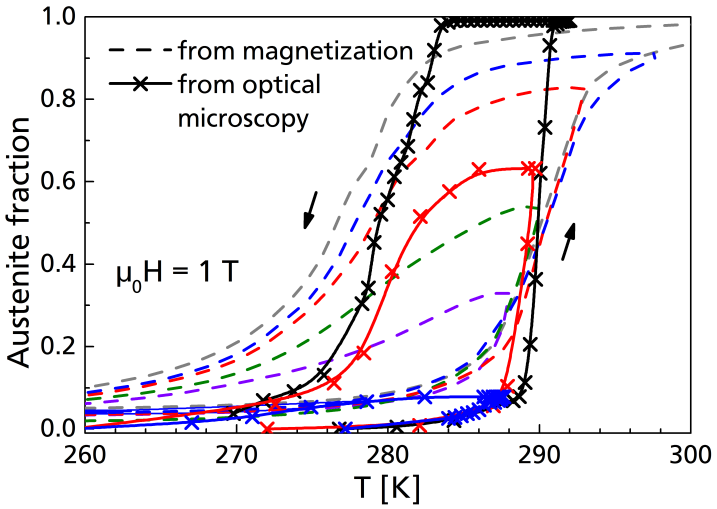

Figure 4.30: Comparison of the phase fraction of austenite determined from magnetization measurements (dashed curves) and image analysis of in-situ optical microscopy (crosses and solid curves) in full and in minor loops of hysteresis.

phase has been turned into austenite before. This observation is in contrast to the findings from above when transforming the sample completely.

From the images obtained by in-situ microscopy, also a quantitative analysis is feasible. Therefore, the microscopic images taken at certain temperatures were transformed into binary data. By this approach, the phase fraction between martensite and austenite can be determined as a function of temperature. The major hysteresis loop of the material $Ni_{45.7}Mn_{36.6}In_{13.5}Co_{4.2}$, based on optical microscopy, is plotted as black crosses in Fig. 4.30. Also two minor loops of hysteresis are shown (red and blue crosses). In order to compare the results from microscopy in zero field with magnetization measurements in a magnetic field of 1 T (see Fig. 4.25), the data points were shifted to lower temperatures by 8 K. Even though the optical microscopy study only provides information about the transformation behavior on the surface of the sample, in contrast to the magnetic measurements being sensitive to the whole volume of the material, the agreement of the two methods appears to be reasonable.

Comparing the solid black and red curve in Fig. 4.30 reveals that in the minor hysteresis loop, the backward transition into martensite starts already at 286 K, in contrast to 283.5 K in the major loop. When starting from the pure high temperature austenite phase, nuclei of martensite need to be created in order to initiate the transformation, which costs energy. On the other hand, when starting from a mixed phase state with both martensite and austenite as in the minor loop, the martensite nuclei already exist. Consequently, there is no need to form new nuclei of martensite, at least to a certain extent. A significant transformation of the material can occur simply by moving the phase boundary between martensite and austenite. This is energetically more favorable and therefore the thermal hysteresis is smaller in the minor loop of hysteresis. Dominated by the local stress field, the martensite converts back to its original structure by cooling further.

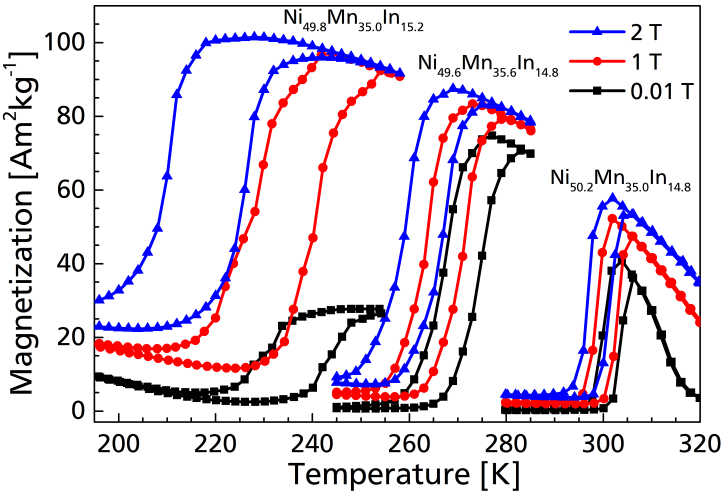

Figure 4.31: Magnetic behavior of $Ni_{49.8}Mn_{35.0}In_{15.2}$, $Ni_{49.6}Mn_{35.6}In_{14.8}$ and $Ni_{50.2}Mn_{35.0}In_{14.8}$ as a function of temperature in three different fields.

Thus, it is apparent that partly avoiding the nucleation of martensite reduces the thermal hysteresis. In other words, the hysteresis of the nucleation process is a bit larger than that of the relatively easy phase boundary movement. This explains the large reversible adiabatic temperature change shown above in Fig. 4.22, even though now a smaller amount of the Heusler sample contributes to the ΔT_{ad}. However, a certain mixture is necessary in order to efficiently avoid the formation of new nuclei. One possible attempt is to pin the martensite to some extent, for instance by introducing defects like microscopic precipitates of a different phase or microcracks [96]. This issue deserves further investigation.

4.2.3 Reversible entropy change

The focus of this section is on the determination of the reversible isothermal entropy change. How the ΔS_T can be calculated from magnetization data was already discussed in Sect. 4.1.2. In order to study the entropy change under cycling, a new approach will be introduced, which utilizes the combination of the $S(T)$ diagram and direct ΔT_{ad} measurements. For this calorimetric investigation, the three compounds $Ni_{49.8}Mn_{35.0}In_{15.2}$, $Ni_{49.6}Mn_{35.6}In_{14.8}$ and $Ni_{50.2}Mn_{35.0}In_{14.8}$ from above will be characterized. Their magnetization as a function of temperature in 0.1, 1 and 2 T is again summarized in Fig. 4.31.

As already mentioned in the introduction, from the $S(T)$ diagram in two different magnetic fields both the adiabatic temperature change and the isothermal entropy change are well-defined. For this reason, plotting the total entropy without a magnetic field and in 2 T together with the adiabatic temperature change from the ΔT_{ad} rig should lead to a perfect coincidence.

Figure 4.32 shows such a comparison for the specimen with the chemical composition $Ni_{50.2}Mn_{35.0}In_{14.8}$ and the highest transition temperature. All data is plotted for the heating protocol, which means that only the transition from martensite into austenite is considered. The total entropy (green and red curves in Fig. 4.32) was calculated from heat capacity measurements. Corresponding to Eq. (2.3), the integral

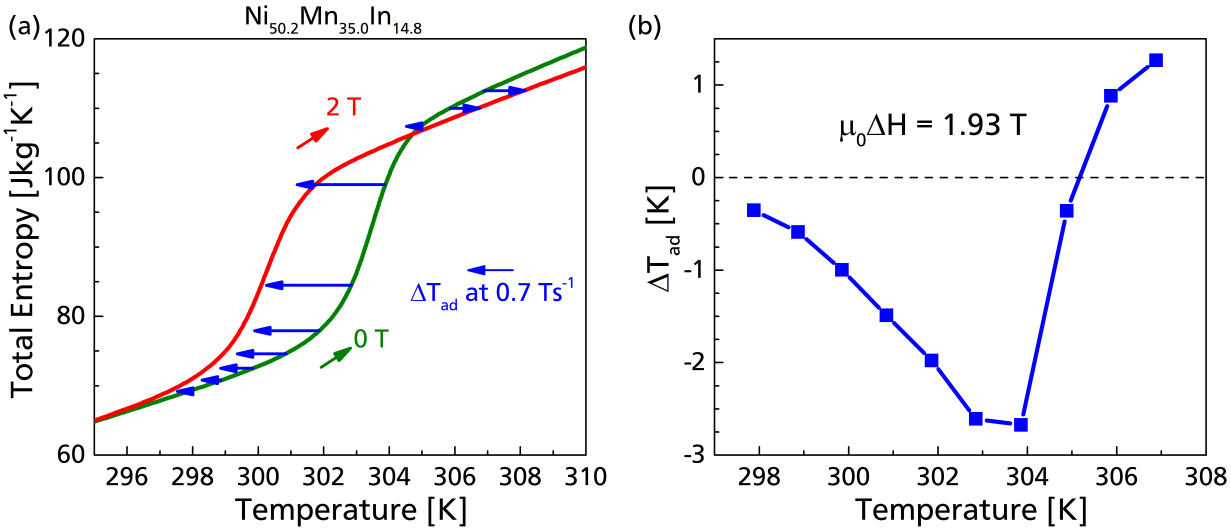

Figure 4.32: (a) $S(T)$ diagram of $Ni_{50.2}Mn_{35.0}In_{14.8}$ in 0 (green curve) and 2 T (red curve) under heating protocol. The adiabatic temperature change is plotted as blue horizontal arrows. (b) Corresponding ΔT_{ad} values in the maximum magnetic field of 1.93 T.

over $\frac{C_p}{T}$ from 0 K up to a certain T results in the total entropy $S(T)$ at this specific temperature. Due to the third law of thermodynamics, it is not possible to measure the heat capacity down to absolute zero. But for the characterization of the martensitic transition, this is not needed anyway. For this reason, Eq. (2.3) is simplified

$$S(T,H) = \int_{T^*}^{T} \frac{C_p(T,H)}{T} dT + \int_{0}^{T^*} \frac{C_p(T,H)}{T} dT = \int_{T^*}^{T} \frac{C_p(T,H)}{T} dT + S_0(T^*) \tag{4.7}$$

with the reference temperature T^*. This reference point is to be selected far below the martensitic transition up to which the heat capacity with and without magnetic field are approximately the same. Therefore, only the first term in Eq. (4.7) is considered. This is not exactly the total entropy of the material, but it gives the entropy in relation to the reference temperature T^*. This is a reasonable approach because mainly the entropy change during the first-order transition is of interest. In addition, it reduces the tremendous measurement time of the precise heat capacity experiment significantly.

The adiabatic temperature change of the Heusler alloy $Ni_{50.2}Mn_{35.0}In_{14.8}$ after the first field application of 1.93 T is plotted in Fig. 4.32(b). The ΔT_{ad} measurements were obtained in discontinuous protocol to ensure independent single measurements. This data is used and plotted as horizontal arrows in Fig. 4.32(a). The entropy level of the arrows in Fig. 4.32 was fitted to the values of the zero-field entropy at the starting temperature of the specific ΔT_{ad} experiment. It can be seen that the agreement between both methods is reasonable. All arrows end near the red curve, the entropy in a magnetic field of 2 T.

The shape of the $S(T)$ is nearly rectangular and the transition from martensite into austenite takes place in a rather small temperature window, which was also apparent from the heat capacity data in Fig. 4.8. The shift of the transition temperature in magnetic fields, which defines the width of the rectangle, accounts for about 3 K in 2 T. At a temperature of about 305 K, the red and the green curves cross each

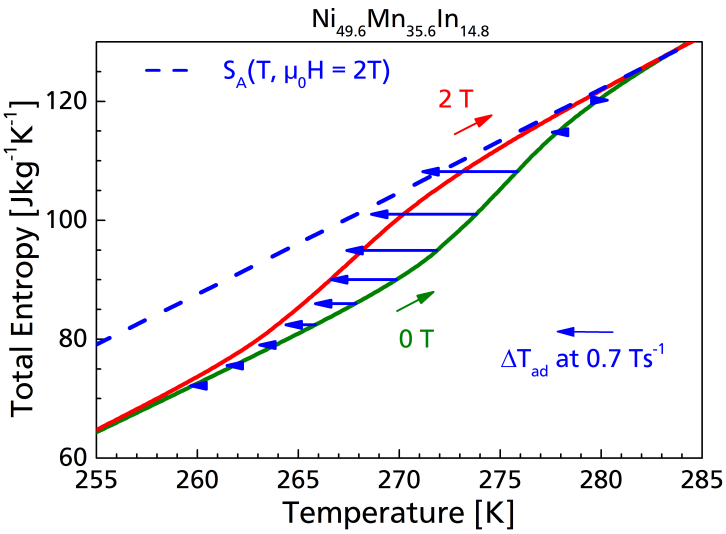

Figure 4.33: $S(T)$ diagram of $Ni_{49.6}Mn_{35.6}In_{14.8}$ in 0 (green curve) and 2 T (red curve) under heating protocol. The adiabatic temperature change is plotted as blue horizontal arrows.

other. This is due to the second-order transition in the vicinity of the Curie temperature of the austenite phase at 314 K. The isothermal entropy change ΔS_T of the second-order transition is negative (vertical distance between the zero-field and in-field entropy) and the temperature increases under adiabatic conditions.

The second compound under investigation has the chemical composition $Ni_{49.6}Mn_{35.6}In_{14.8}$ and its $S(T)$ diagram is plotted in Fig. 4.33. It has a transition below room temperature, slightly lower than the previous alloy. First of all, the rectangular shape of the $S(T)$ diagram is not so pronounced as for the other compound. This is because the transition is much broader, but also the shift of the transition in magnetic fields is enhanced. Furthermore, the agreement between the ΔT_{ad} results and the $S(T)$ is not as good as in Fig. 4.32, especially around 270 K. In this area, an overshooting of the ΔT_{ad} is observed.

The blue dashed line in Fig. 4.33 illustrates the total entropy of the austenite in a magnetic field of 2 T. It was approximated by shifting the red curve (in 2 T) along the green curve (in 0 T) to lower temperatures. Subsequently, the vertical position of the red curve was adjusted in such a way that the red and green curves overlap in the martensitic region. It can be seen that the two ΔT_{ad} arrows with the largest mismatch end near the dashed line, which implies that the sample should be in the pure high temperature phase after the magnetic field application and the cooling of the material. On the other hand, this means that the sample transformed completely, even though the $S(T)$ diagram does not predict this.

The time scale of the calorimetric study and the direct ΔT_{ad} measurements is rather different. In order to exclude that time-dependent effects of the martensitic transition are the origin for the mismatch, further measurements of the adiabatic temperature change were performed using different magnetic field sweep rates. In Fig. 4.34(a), the cooling curves under three different sweeping rates are plotted. Since the magnetic-field profile over time has a sinusoidal shape, the values of 0.7, 2.1 and 2.7 $\mathrm{T\,s^{-1}}$ relate to the sweeping rate in the beginning of the experiment in zero field. One can see that the cooling

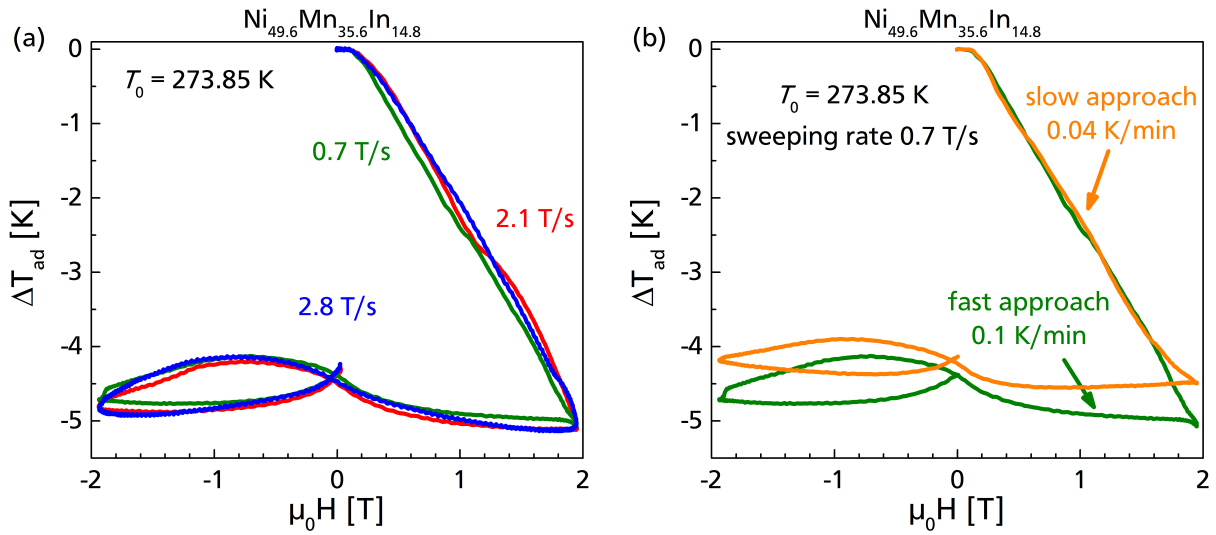

Figure 4.34: Adiabatic temperature change ΔT_{ad} for a starting temperature of 273.85 K of $Ni_{49.6}Mn_{35.6}In_{14.8}$ in (a) different magnetic-field-sweep rates and (b) heating rates.

behavior of the material $Ni_{49.6}Mn_{35.6}In_{14.8}$ is nearly the same, even though the duration of the experiment was accelerated by a factor of four in comparison to the standard speed of $0.7\,\mathrm{T\,s^{-1}}$. This means that the sweeping rate of the direct ΔT_{ad} measurement is not the origin for the observed deviation in the $S(T)$ diagram. However, it turned out that the heating rate before the ΔT_{ad} measurement strongly influences the obtainable cooling effect. Figure 4.34(b) illustrates that a slightly higher ΔT_{ad} value is reached when the sample was heated with $0.1\,\mathrm{K\,min^{-1}}$ (green curve) instead of $0.04\,\mathrm{K\,min^{-1}}$ (orange curve). The magnetic-field-sweeping rate was set to $0.7\,\mathrm{T\,s^{-1}}$.

An even larger discrepancy between the $S(T)$ diagram and the adiabatic temperature change can be found in the third compound $Ni_{49.8}Mn_{35.0}In_{15.2}$ with the lowest transition temperature. The corresponding $S(T)$ diagram is shown in Fig. 4.35. It has a long-stretched shape because it has a strong shift of the transition temperature in magnetic fields, a large transition width and a rather modest entropy difference between martensite and austenite. The results of two ΔT_{ad} experiments with different approaching speeds are plotted as arrows in Fig. 4.35. Especially between 228 and 235 K, the mismatch between those two measurements is significant. The blue arrows measured after heating with $0.2\,\mathrm{K\,min^{-1}}$ overshoot the total entropy curve in 2 T a lot.

For instance at a starting temperature of 234 K, the fast approach experiment results in a twice as large adiabatic temperature change as predicted by the $S(T)$ diagram. Furthermore, the blue arrows end close to the dashed blue line approximating the total entropy of the pure austenite phase in magnetic fields. However, by reducing the approaching speed down to $0.05\,\mathrm{K\,min^{-1}}$, the coincidence between the direct ΔT_{ad} and the calorimetric methods becomes reasonable.

For a small number of starting temperatures, the adiabatic temperature change of the sample was measured inside the calorimeter. Since it is using a superconducting magnet, the magnetic-field-sweeping rate accounts for only $0.24\,\mathrm{T\,min^{-1}}$. The measurement temperature was set in a quasistatic mode. In this case, the agreement of the $S(T)$ diagram is convincing, as shown in Fig. 4.36. Also the isothermal

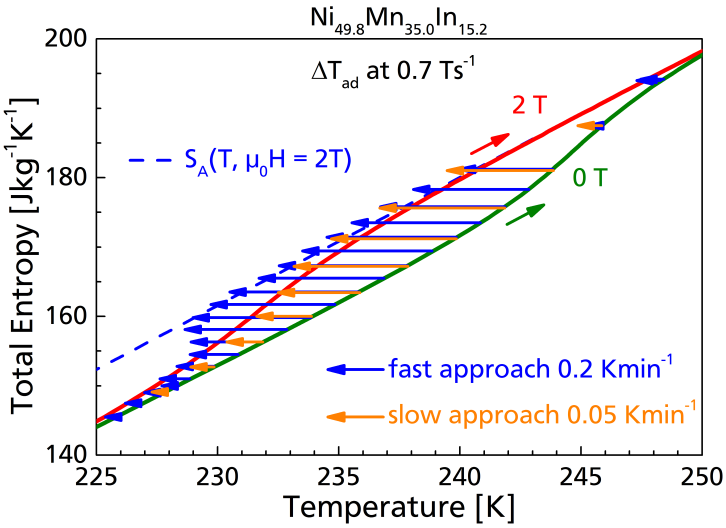

Figure 4.35: Total entropy diagram of $Ni_{49.8}Mn_{35.0}In_{15.2}$ combined with ΔT_{ad} measurements using two different heating rates to reach the target temperature of the experiment.

entropy change ΔS_T obtained from magnetization data is plotted as vertical arrows leading to a good agreement. This is an important finding because the heating rate during the measurement of the $M(T)$ curves used for the calculation was about $1\,\mathrm{K\,min^{-1}}$ and therefore much higher than in all direct ΔT_{ad} measurements.

It is worth mentioning that the sample was under isothermal conditions in the VSM, meaning that there is obviously a good thermal contact between the material and the surroundings. The thermal equilibrium can therefore be reached in a rather fast manner. However, in the ΔT_{ad} rig the sample is thermally insulated very well to ensure good adiabaticity. It seems that under these conditions, the sample is not in equilibrium when using a heating rate of only $0.2\,\mathrm{K\,min^{-1}}$. This effect must be related to the properties of the martensite phase, since the mismatch in Fig. 4.35 occurs for starting temperatures at which there is nearly no austenite present in the material (the austenite start temperature A_s is about 238 K in zero field). It should also be pointed out again that the temperature was measured directly using a thermocouple placed inside the sample. Therefore, the suspicion that the sample temperature was probably lacking behind in the fast approach experiment cannot be correct.

A more detailed study on the heating rate is shown in Fig. 4.37. The cooling curves after the fast and slow approach at the starting temperature of 233.85 K, at which the largest discrepancy was observed, are shown in Fig. 4.37(a). When heating the sample with $0.05\,\mathrm{K\,min^{-1}}$ (orange curve), the maximum ΔT_{ad} is about −2.5 K. However, the green curve showing the result after heating with $0.2\,\mathrm{K\,min^{-1}}$, provides a much higher adiabatic temperature change of −5.0 K in the maximum magnetic field of 1.93 T. From the profile of the fast approach curve it is also apparent that the transition was indeed completed because the cooling saturates in the high magnetic-field region. The adiabatic temperature change in 1.93 T as a function of the starting temperature is plotted in Fig. 4.37(b). Above 240 K, both experiments coincide very well. However, for lower temperatures the difference is very significant.

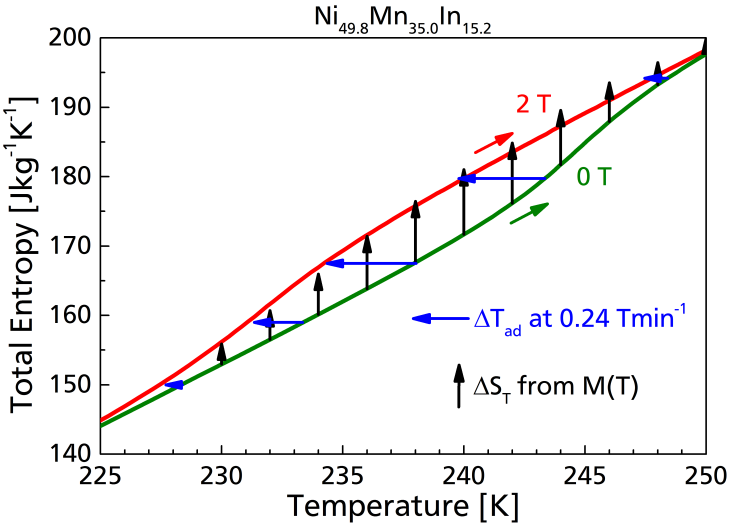

Figure 4.36: Total entropy diagram of $Ni_{49.8}Mn_{35.0}In_{15.2}$ combined with ΔT_{ad} measurements from the calorimeter (horizontal arrows) and the isothermal entropy change ΔS_T from magnetic measurements using the Maxwell equation (vertical arrows).

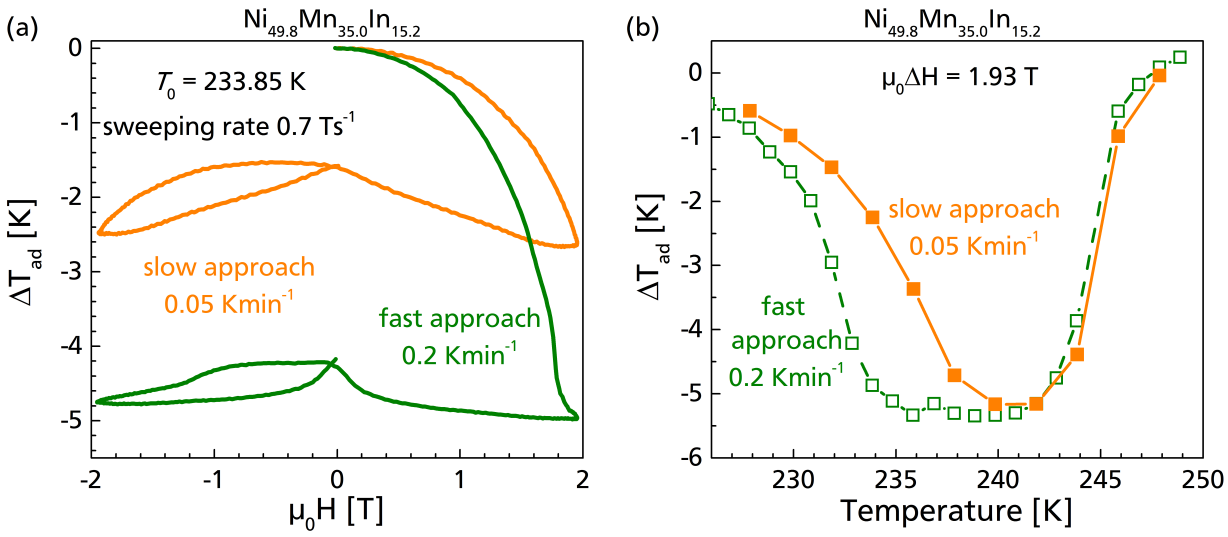

Figure 4.37: Adiabatic temperature change ΔT_{ad} of $Ni_{49.8}Mn_{35.0}In_{15.2}$ after slow and fast heating to the target temperature as a function of (a) magnetic field and (b) the starting temperature.

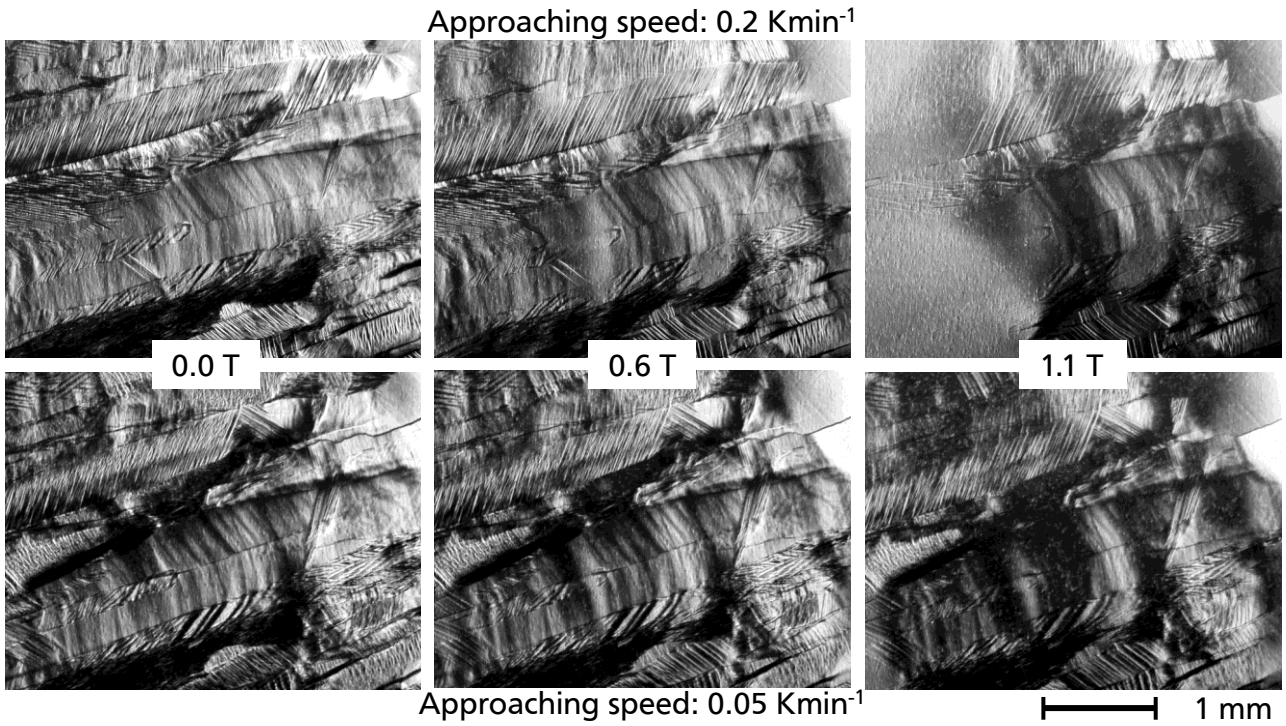

Figure 4.38: In-situ optical microscopy of the compound $Ni_{49.8}Mn_{35.0}In_{15.2}$ when applying a magnetic field up to 1.1 T. The upper and the lower image sequence illustrate the transformation behavior of the sample after heating with 0.2 and 0.05 K min^{-1} respectively.

In order to further study the influence of the approaching speed on the adiabatic temperature change, in-situ optical microscopy was performed. In this experiment, the sample was heated with either 0.2 or 0.05 K min^{-1} to the target temperature. Subsequently, a magnetic field up to 1.1 T was applied with a magnetic-field sweeping rate of about 0.2 T s^{-1}. The upper three images in Fig. 4.38 in zero field, in 0.6 and 1.1 T show the transition behavior of the material after the fast approach. Approximately half of the sample transformed from martensite into austenite and the high contrast of the martensite disappears. Subsequently, the sample was heated to turn the sample completely into austenite and then cooled to low temperatures before the slow approach experiment. For this reason, the martensite structure is certainly different in the lower images in Fig. 4.38, as can be for instance seen in upper right corner of the 0 T pictures.

Direct measurements of the adiabatic temperature change and in-situ microscopy show that a larger amount of the sample transforms when the heating to the target temperature is accelerated. It is apparent that this effect originates from a process in the pure martensite state. It is probable that a reorientation of the martensite variants is happening prior to the transformation into austenite. This is suppressed when heated with a rather fast speed under thermally isolated conditions. However, no clear mechanism can be identified from the low magnification microscopy study. For this, a higher lateral resolution might be necessary. At least, one can state that for the compound $Ni_{49.8}Mn_{35.0}In_{15.2}$ a heating rate of 0.05 K min^{-1} or less is necessary to ensure coincidence between the ΔT_{ad} measurements and the $S(T)$ diagram obtained from quasistatic calorimetry. For the other two alloys, the mismatch in the $S(T)$ diagram is less and less pronounced. The reason for this could be the increased transition temperature

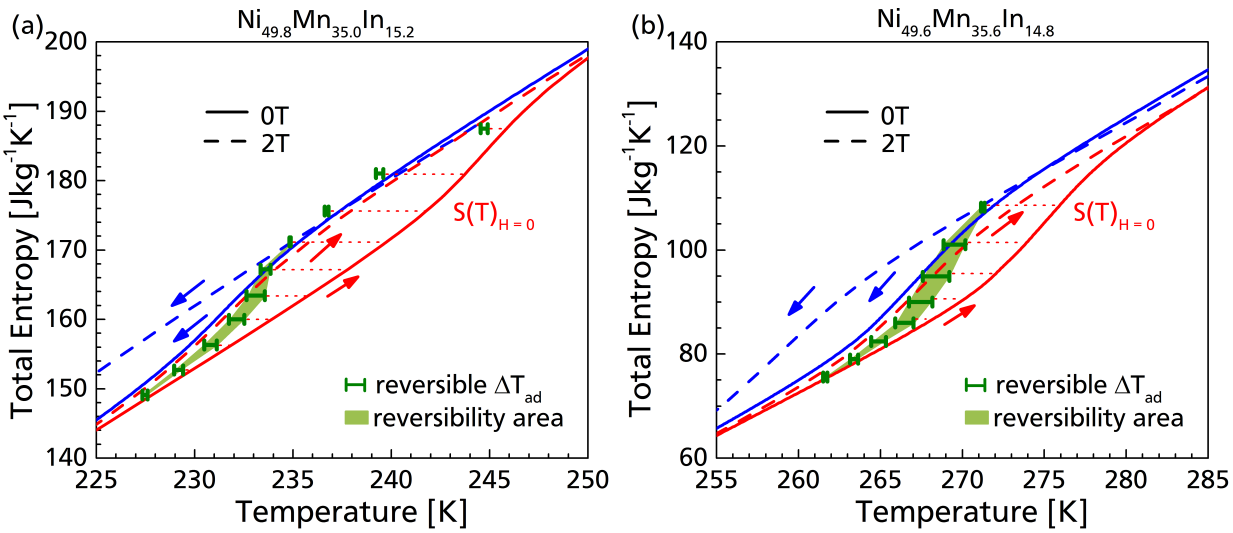

Figure 4.39: $S(T)$ diagram of $Ni_{49.8}Mn_{35.0}In_{15.2}$ (a) and $Ni_{49.6}Mn_{35.6}In_{14.8}$ (b) for heating and cooling in 0 and in 2 T. The reversible adiabatic temperature change is plotted as green bars.

of the compounds $Ni_{49.6}Mn_{35.6}In_{14.8}$ and $Ni_{50.2}Mn_{35.0}In_{14.8}$. At higher temperatures, there is also more thermal energy in the system which allows for a faster reaching of the equilibrium state.

It remains to study the reversibility of the magnetocaloric effect under cycling in terms of the $S(T)$ diagram. Therefore, the heat capacity was measured also under cooling with and without magnetic field in order to consider the thermal hysteresis of the transition. The respective $S(T)$ diagrams for the two compounds $Ni_{49.8}Mn_{35.0}In_{15.2}$ and $Ni_{49.6}Mn_{35.6}In_{14.8}$ are plotted in Fig. 4.39. As discussed in the beginning of this thesis, the prerequisite for being able to observe a reversible magnetocaloric effect is a sufficiently strong shift of the transition to lower temperatures in magnetic fields. In order to overcome the thermal hysteresis, the heating curve in the magnetic field needs to be moved beyond the cooling curve without field.

For a magnetic field of only 2 T, this is not the case in both compounds shown in Fig. 4.39. Consequently, there should be no cyclic ΔT_{ad}. However, significant reversible adiabatic temperature changes were observed in direct measurements. The ΔT_{ad} under cycling is plotted in Fig. 4.39 as green bars. The entropy level is adopted to the values used in Fig. 4.33 and 4.35. The green bars span a polygon which describes the reversibility area of the $S(T)$ diagram. This is not represented at all by the total entropy curves determined from calorimetry. The reason for this is that the strong reversibility is related to minor loops of hysteresis as discussed above. However, the heat capacity measurements were performed under continuous heating and cooling in a major hysteresis loop instead. This is why the $S(T)$ diagram fails to predict the cyclic magnetocaloric properties.

In principle it is also possible to characterize minor loops of hysteresis by calorimetric methods, but precise C_p measurements are typically very slow in order to ensure quasistatic conditions. On the other hand, it is very simple and fast to determine the cyclic ΔT_{ad} in direct measurements. The combination of both, the adiabatic temperature change under cycling and quasistatic calorimetry is a powerful tool in order to determine the reversible isothermal entropy change.

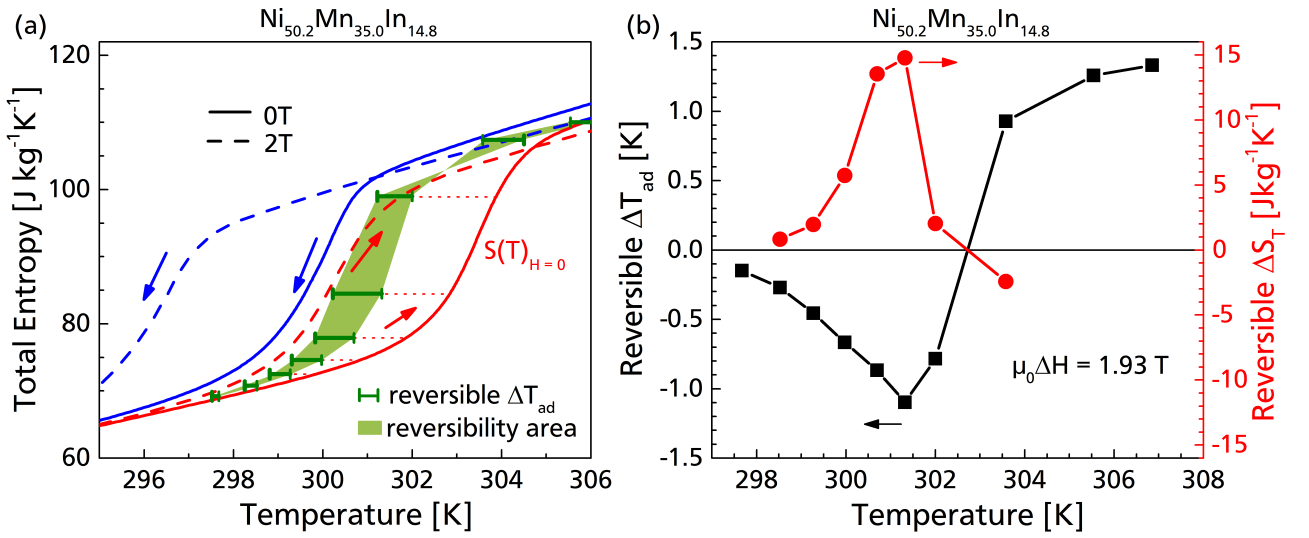

Figure 4.40: (a) $S(T)$ diagram of $Ni_{50.2}Mn_{35.0}In_{14.8}$ under heating and cooling in 0 and in 2 T. The reversible adiabatic temperature change is plotted as green bars. (b) The reversible magnetocaloric properties in a magnetic field change of 2 T.

Figure 4.40(a) shows the $S(T)$ diagram of the sample $Ni_{50.2}Mn_{35.0}In_{14.8}$ for heating and cooling. The reversible adiabatic temperature change is again shown as green bars. In contrast to the other two compounds in Fig. 4.39, the reversibility area is very large. The reversible entropy change can be obtained by measuring the vertical height of the polygonal face. Both the reversible ΔT_{ad} and ΔS_T are summarized in Fig. 4.40. Therefore only a modest temperature change of 1.2 K (left axis in Fig. 4.40(b)) can be reached in $Ni_{50.2}Mn_{35.0}In_{14.8}$ in a magnetic field change of 1.93 T, but the resulting entropy change amounts to 15 J kg^{-1} K (right axis in Fig. 4.40(b)). This value is a bit smaller than the ΔS_T observed in Fig. 4.10 from magnetization and heat capacity measurements. Nevertheless, the reversible entropy change is about three times larger than in the benchmark material Gd in the same magnetic field change [119].

Minor loops of the martensitic transition enhance the cyclability. The thermal hysteresis can be reduced significantly and therefore large reversible adiabatic temperature and isothermal entropy changes can be generated. In this case, only a certain percentage of the material transforms instead of switching the whole material between martensite and austenite. Due to the coexistence of the two phases in minor loops of hysteresis, the nucleation of the new phase is partly prevented. Instead, the material transforms by moving the phase boundary, which costs less energy than the formation of nuclei. Consequently, the thermal hysteresis is reduced, which promotes the cyclability of the magnetostructural transition.

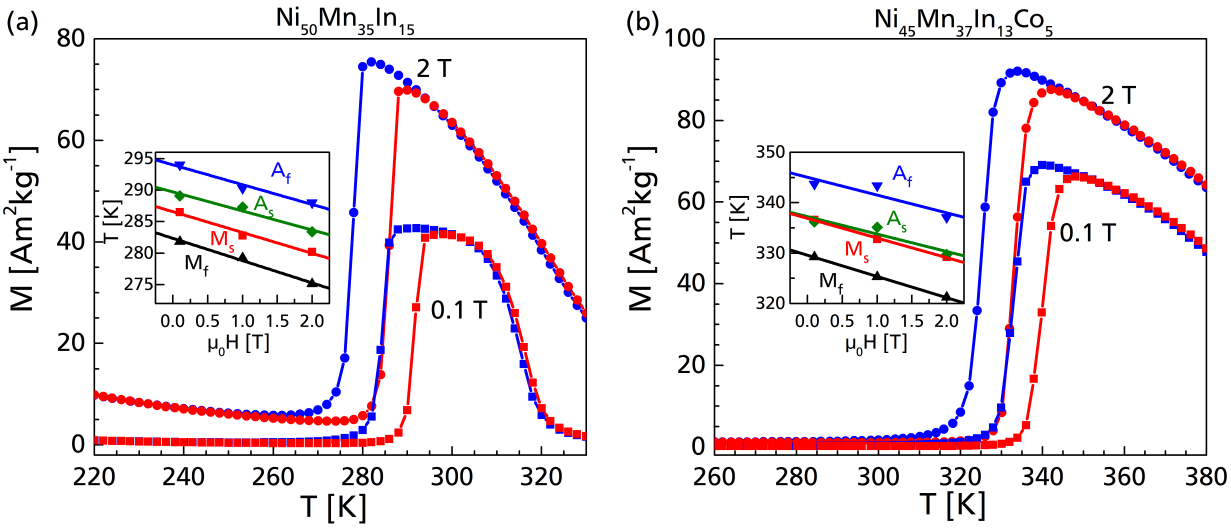

Figure 4.41: Magnetization as a function of temperature of $Ni_{50}Mn_{35}In_{15}$ (a) and $Ni_{45}Mn_{37}In_{13}Co_5$ (b). The insets show the respective magnetic phase diagram.

4.3 Martensitic transition under different time scales

In the previous section, it was demonstrated that the measurement conditions can have a great influence on the magnetocaloric properties. For instance, the usage of a slightly different heating rate before the ΔT_{ad} experiment resulted in a considerable change of the temperature profile during field application. Consequently, the results from quasistatic methods do not necessarily coincide with fast experiments. In terms of the application of magnetic refrigeration, it would be favorable to operate the AMR (active magnetic regenerator) with frequencies up to 10 Hz [64]. This means that the magnetocaloric material has to transform several times each second. For second-order materials like Gd with a purely magnetic transition, this is not an issue because the spin alignment in magnetic fields is extremely fast in comparison to the operation frequency of a magnetic-cooling machine.

First-order materials, however, transform via a nucleation and growth process [147]. The kinetics of a magnetostructural transition may be significantly slower. Problems arise when the transformation speed is in the same order of magnitude as the magnetic-field rate. In the following, the question will therefore be addressed to what extent the magnetic-field-sweeping rate influences the martensitic transformation. For this study, three different ΔT_{ad} measurement setups have been utilized, which allow to compare the temperature change in field rates from 0.01 up to 1500 T s^{-1} [123].

Two Heusler alloys with the nominal compositions $Ni_{50}Mn_{35}In_{15}$ and $Ni_{45}Mn_{37}In_{13}Co_5$ have been selected. Their magnetization curves in a small field of 0.1 and in 2 T are shown in Fig. 4.41. The heating and the cooling branches are plotted in red and blue respectively. The thermal hysteresis amounts to about 8 K in both materials. According to the magnetic phase diagram shown in the insets of Fig. 4.41, the transition temperature is lowered by approximately −3.5 K T^{-1} in magnetic fields up to 2 T.

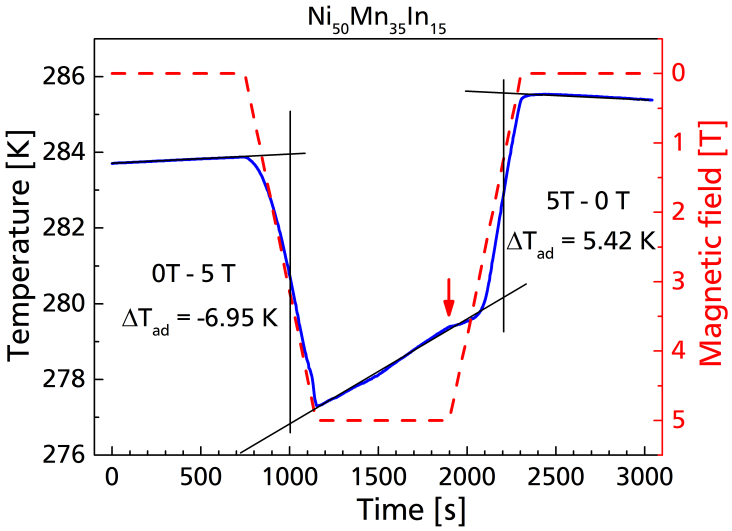

Figure 4.42: Absolute temperature of $Ni_{50}Mn_{35}In_{15}$ in the slow ΔT_{ad} experiment. The arrow points to the time at which the magnetic-field removal was initiated.

4.3.1 Slow ΔT_{ad} experiment

In the first measurement setup, a superconducting magnet generated the magnetic field. Therefore the magnetic-field rate was limited to approximately $0.01\,\mathrm{T\,s^{-1}}$ and about 400 s were needed in order to ramp the field up to the maximum of 5 T. It is very challenging to ensure a good adiabaticity during such a long measurement time. A certain drift of the sample temperature cannot be avoided completely. The temperature development of the compound $Ni_{50}Mn_{35}In_{15}$ during the slow measurement is plotted in Fig. 4.42. Before the experiment, the sample temperature was stabilized at 284 K. According to the magnetization data in Fig. 4.41(a), mainly martensite should be present at this temperature.

The magnetic-field profile is plotted as a red dashed line in Fig. 4.42 (right axis). After about 750 s, the magnetic-field sweeping was initiated. The sample starts to cool down momentarily and in the maximum field, a temperature of 277.3 K can be reached. Keeping the magnetic field constant for a certain time enables an estimation of the temperature drift. As a result, the sample heats up by about $0.16\,\mathrm{K\,min^{-1}}$. The reason for this is the strong deflection from the equilibrium temperature due to the large ΔT_{ad}. The imperfect adiabatic conditions in the setup cause the sample to move back to the initial temperature. This drifting process is already present during the magnetic-field sweeping. The drift rate is proportional to the temperature difference in comparison to the initial state. Consequently, the observed ΔT_{ad} is reduced by the temperature drift to some extent, which is most pronounced in the high magnetic-field range.

One can approximately correct the temperature evolution in order to obtain a more reasonable ΔT_{ad} value. This is done by linear extrapolation of the temperature profile before and after the field application. Furthermore, a vertical line at the mid point of the cooling curve is added. The temperature difference between the two intersection points is considered as the real adiabatic temperature change, accounting for −6.95 T. This is slightly higher than the temperature difference between the sample temperature before and after the field sweeping.

After a certain waiting time, the magnetic field is removed again. The small hump marked by the red arrow is no anomaly. At this point mainly austenite is present. Due to the conventional magnetocaloric effect of the austenite, the material starts to cool in decreasing field. This competes with the heating effect of the material when the backward transition into martensite takes place. Shortly after, the first-order transition gains the upper hand, a strong heating is observed. Due to the significant drift in temperature during the long measurement time, the field-decreasing branch cannot be considered as the reversible ΔT_{ad} because the temperature changed too much.

4.3.2 Semifast ΔT_{ad} experiment

In the semifast experiment, two nested Halbach magnets were used to create a magnetic field up to 1.93 T. By rotating the two magnets against each other, the magnetic field could be varied following a sinusoidal shape. The typical measurement time was about 18 s. This results in a magnetic-field rate of about $0.7\,\mathrm{T\,s^{-1}}$ in the zero-field region. For higher magnetic fields, the sweeping rate decreases respectively. Figure 4.43 shows the adiabatic temperature change ΔT_{ad} as a function of time of the two compounds under consideration. Such a plot was already presented in Fig. 4.21 for a different compound. For simplicity reasons, the ΔT_{ad} curves there were normalized to a linear magnetic-field profile. In Fig. 4.43, the data is plotted as a function of the real time. The magnetic-field profile is shown as a red dashed curve.

The temperature evolution of the Co-free alloy is plotted for different starting temperatures in Fig. 4.43(a). A large adiabatic temperature change of −4 K is observed in the 290 K experiment (blue curve). At this temperature, a small amount of austenite is already present in low magnetic fields according to the increased magnetization in the heating branch of Fig. 4.41(a). Due to the thermal hysteresis of about 8 K, the reversible ΔT_{ad} is reduced, but it still accounts for 1.5 K. For the lower initial temperature of 286 K, the resulting temperature change is significantly smaller, because the shift of the transition temperature in magnetic fields is not sufficiently large. For this reason, the cooling starts only after the magnetic field already exceeds 1 T, which is needed to lower the transition temperature to the critical point. At even lower starting temperatures, nearly no adiabatic temperature change is observed anymore.

A very similar behavior is also observed in the Co-containing alloy in Fig. 4.43(b). Starting at 336 K results in a temperature change of about −5 K in the maximum magnetic field of 1.93 T. At higher temperatures, the conventional magnetocaloric effect of the austenite phase is dominant, leading to a heating of the material when applying a magnetic field. Even though the magnetic-field-sweeping rate was about 60 times faster in the Halbach setup in comparison to the experiment using the superconducting magnet source, the sample temperature immediately follows the magnetic field.

4.3.3 Fast ΔT_{ad} experiment

The fast ΔT_{ad} measurements were performed in a pulsed-field solenoid. Therefore, magnetic-field pulses of 2, 5 and 10 T were applied and the temperature was measured using a thermocouple. Figure 4.44

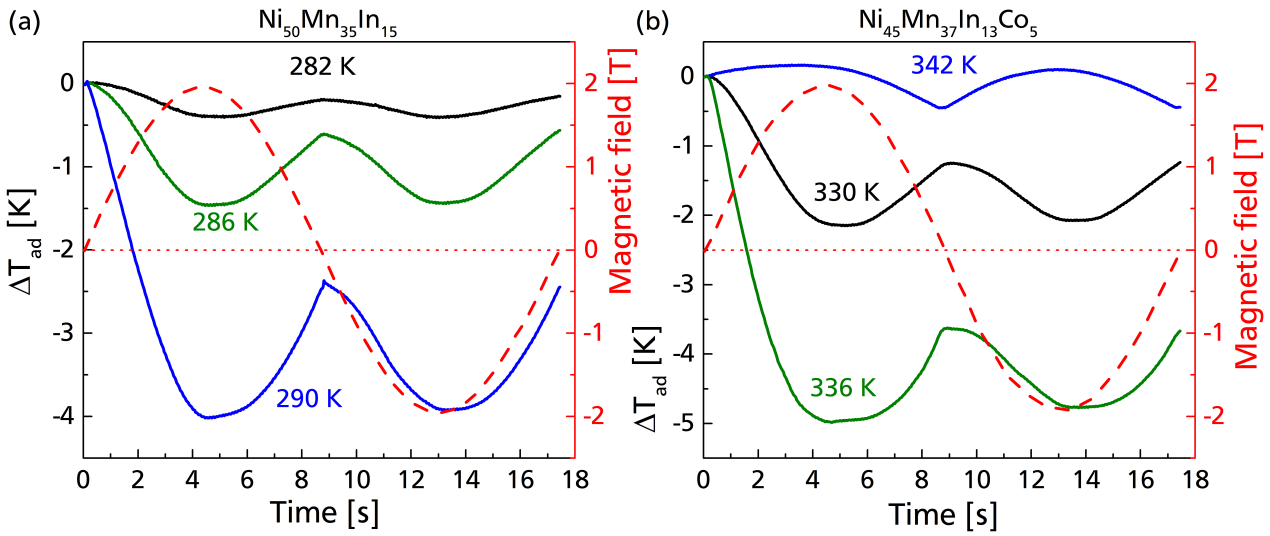

Figure 4.43: Adiabatic temperature change ΔT_{ad} in the semifast experiment of $Ni_{50}Mn_{35}In_{15}$ (a) and $Ni_{45}Mn_{37}In_{13}Co_5$ (b). The magnetic field profile is plotted as a red dashed curve (right axis).

shows several 10 T experiments at different starting temperatures. The magnetic-field profile plotted as a red dashed curve is characterized by a steep and fast field increasing branch followed by a slower decay of the magnetic field in the decreasing branch. After only 13 ms, the maximum magnetic field is reached, which relates to a magnetic-field-sweeping rate of 1500 T s^{-1} in the beginning of the field application.

This measurement is orders of magnitudes faster than the Halbach and the superconducting magnet experiments. Nevertheless, great temperature changes up to −9.5 K can be reached at a starting temperature of 286.6 K. The phase transformation is mostly reversible in the 276.0 and 280.3 K measurement. This becomes apparent when checking the cooling branch (blue curve) of the magnetization curve in 0.1 T in Fig. 4.41(a) again. At 276.0 K, the backward transition is already finished. For this reason, the sample will go back to the pure martensite state when the field is removed. This is also true for the experiment which was started at 280.3 K (see Fig. 4.44). However, this temperature is already very close to the raising edge of the blue curve in Fig. 4.41, meaning that not all of the material can be transformed back. This is even more pronounced for the starting temperature of 286.6 K.

Larger adiabatic temperature changes can be obtained in the alloy with the composition $Ni_{50}Mn_{37}In_{13}Co_5$ shown in Fig. 4.45. When the sample is heated to 328.5 K before the 10 T pulse, a magnetocaloric effect of −13 K can be observed (blue curve). However, the nature of the kink at around 30 ms cannot be resolved by plotting the temperature versus time. Therefore, the magnetic-field dependences of the adiabatic temperature change are necessary, which will be introduced in the following.

4.3.4 Magnetic-field dependence of the adiabatic temperature change

When plotting the adiabatic temperature change as a function of the magnetic field, the characteristics of the first-order martensitic transition can be understood much better. In Fig. 4.46, the temperature evolution of the Co-free material is plotted. The same curves as shown in Fig. 4.44 versus time are plotted

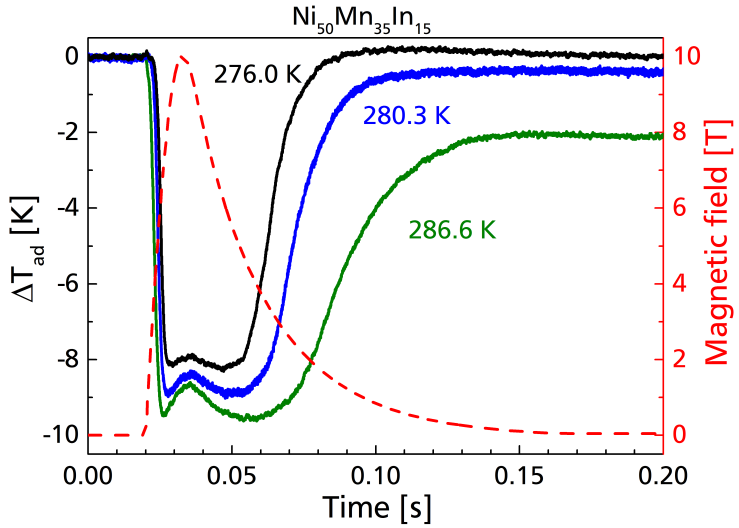

Figure 4.44: Adiabatic temperature change ΔT_{ad} of $Ni_{50}Mn_{35}In_{15}$ in pulsed-magnetic fields up to $10\,\mathrm{T}$. The magnetic field profile is illustrated as a red dashed curve.

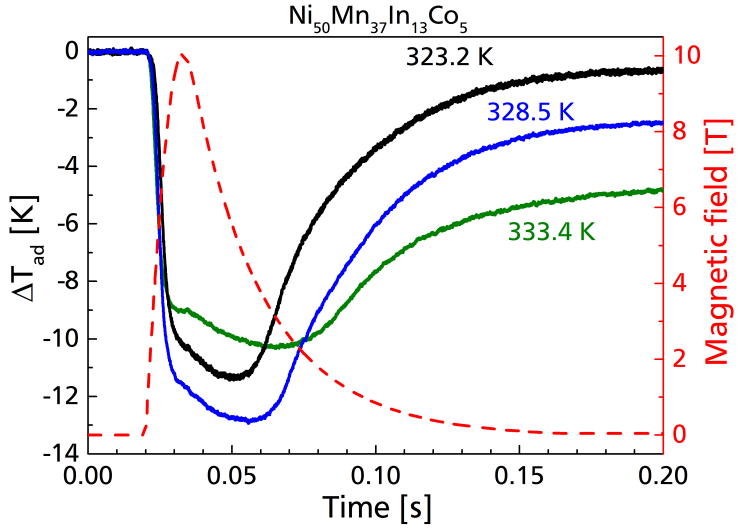

Figure 4.45: Adiabatic temperature change ΔT_{ad} of $Ni_{50}Mn_{37}In_{13}Co_5$ in pulsed-magnetic fields up to $10\,\mathrm{T}$. The magnetic field profile is illustrated as a red dashed curve.

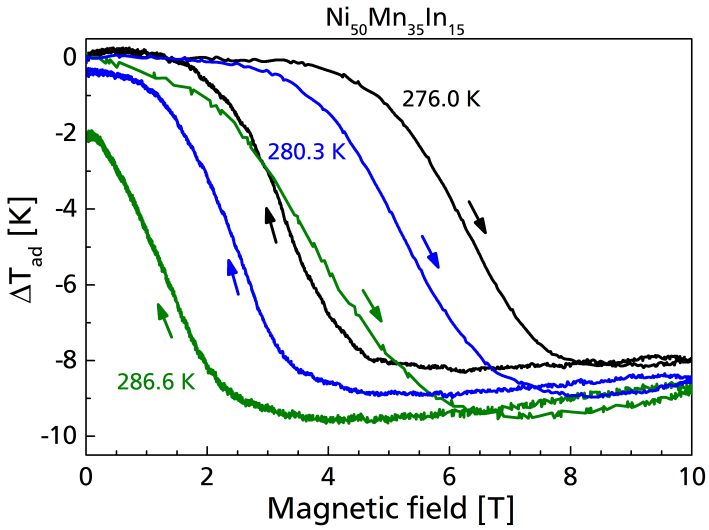

Figure 4.46: Magnetic-field dependence of the adiabatic temperature change ΔT_{ad} of $Ni_{50}Mn_{35}In_{15}$ in 10 T pulses started at different temperatures.

as a function of the magnetic field, leading to major hysteresis loops. Now also the kink in the temperature profile in Fig. 4.44 can be understood, which was most pronounced for the initial temperature of 286.6 K. A magnetic field of 6 T is enough to completely transform the sample into austenite. Increasing the field further leads to a heating of the material by about 1 K due to the second-order magnetocaloric effect of the high temperature phase. After passing the maximum field, the sample cools down, following the same line until the transformation into martensite starts at around 3 T.

For the two other measurements at lower temperatures, the ΔT_{ad} loops seem to be shifted to higher fields. For instance, in order to initiate the transition at 280.3 K, the magnetic field must be increased to about 3 T. Considering that the shift of the transition temperature is about $-3.2\,\mathrm{K\,T^{-1}}$, this implies that the transition temperature was lowered by approximately 10 K in a magnetic field of 3 T. This is reasonable when comparing this with the austenite start temperature A_s in 0.1 T in Fig. 4.41(a), which is about 290 K. It is worth noting that the magnetic-field hysteresis in the ΔT_{ad} plot is about 3 T, which translates into a thermal hysteresis of about 10 K by multiplying the field with the shift of the transition temperature. This value is larger in comparison to the thermal hysteresis, which was determined by magnetization measurements to be 8 K. The question is, whether this increase in the hysteresis is due to measurement errors or due to kinetic effects of the martensitic transition.

In order to answer this question, the adiabatic temperature change was measured in magnetic-field pulses of 2, 5 and 10 T to compare the results with the cooling characteristics in the slow and semifast experiments. Therefore, the starting temperature was set to the same value after discontinuous heating and cooling to erase the memory of the material. The comparison of the three different pulse experiments is illustrated in Fig. 4.47. A significant difference between the red (5 T pulse) and the blue curve (10 T pulse) exists during the magnetization branch between 4 and 6 T. In this region, the sample cools down much more slowly in the 10 T pulse experiment in contrast to the 5 T measurement. Anyhow, the maximum adiabatic temperature change is the same, leading to a cooling to 277 K. This implies that the same phase fraction is transformed during field application and that the transition is completed. In the

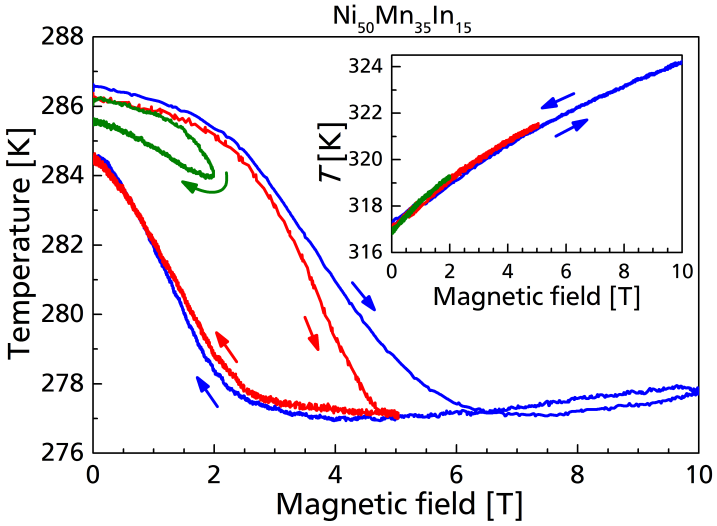

Figure 4.47: Magnetic-field dependence of the sample temperature of $Ni_{50}Mn_{35}In_{15}$ in a 2, 5 and 10 T pulse. The inset shows the magnetocaloric effect of the conventional second-order transition near the Curie temperature.

high-field regime, the conventional magnetocaloric effect is visible by a slight heating of the sample with increasing magnetic field.

By decreasing the magnetic field again, the blue curve follows more or less the same path until the sample starts to heat around 3 T, when the backward transition into martensite is initiated. In zero magnetic field, the temperature stabilizes at about 284.5 K, since the transition is not fully reversible at this particular starting temperature of 286.6 K. Interestingly, the heating branch of the red and the blue curves coincide very well. After the transition into austenite is finished in the 5 T pulse measurement, which is characterized by the saturation of the cooling effect, the temperature dependence of the sample in decreasing magnetic field follows the blue curve. In great contrast to this, the 2 T measurement looks very different. First, the cooling of the material starts already in lower magnetic fields and secondly also the hysteresis is reduced. A magnetic field change of only 2 T is not sufficient to completely transform the material. Consequently, the sample undergoes a minor hysteresis loop, which could also be seen in Fig. 4.43 for the ΔT_{ad} measurement using the Halbach magnet. However, the delay of the transition in higher magnetic-field pulses cannot be explained in this context.

In order to verify that the observed effects are really related to the martensitic transformation and not due to measurement errors, the second-order transition around the austenitic Curie temperature T_C^A was investigated. The nature of this purely magnetic transition is that there is no thermal hysteresis. However, the measurement of the adiabatic temperature change in pulsed-magnetic fields is obviously not trivial due to the short duration. A very quick response of the thermocouple is necessary in order to ensure a proper detection. The time constant of a temperature measurement using a thermocouple is related to the electrical resistance but also to the mass of the spot weld. Furthermore, the induction of a voltage in the thermocouple due to the changing magnetic field is a critical issue since this signal can easily be much larger than the thermosignal, which is in the range of mV. For this reason, very thin wires (diameter of 25 µm) with a thin insulation layer were twisted with highest quality to minimize the distance between

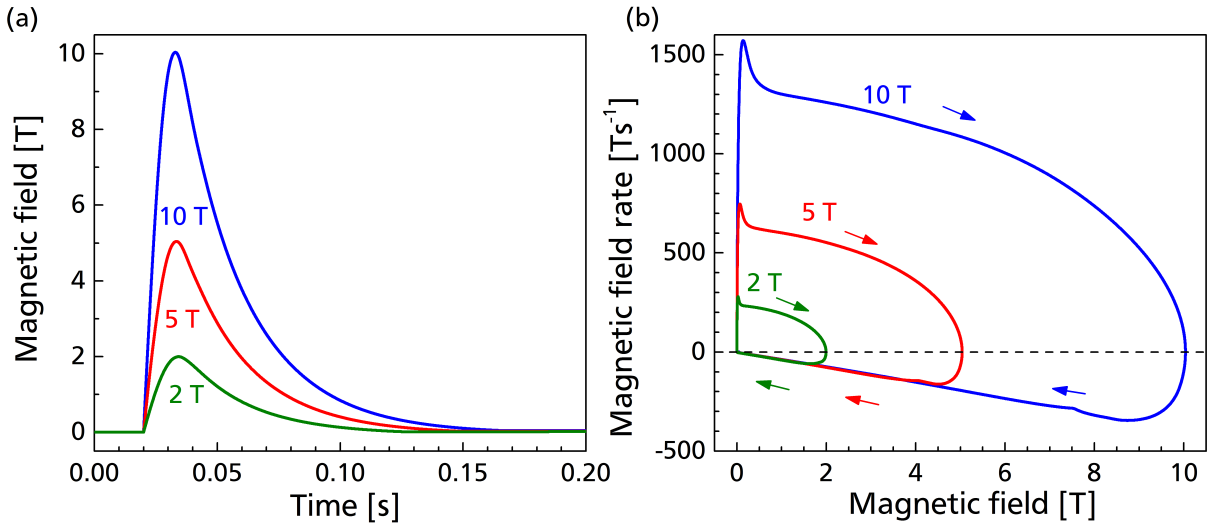

Figure 4.48: (a) Magnetic-field profile of the 2, 5 and 10 T pulse experiment as a function of time. (b) Magnetic-field-sweeping rate as a function of the magnetic field itself.

the two wires. Unfortunately, the resistance of an electrical conductor increases with decreasing cross section. For the Cu wire of the type-T thermocouple this is not a big issue, but the specific resistance of the thin Constantan wire is very large. Therefore the length of the Constantan wire was kept as short as possible (≈ 10 cm). The welding spot was prepared was about twice the wire thickness of 25 µm.

The inset of Fig. 4.47 shows the temperature profile of the sample in the vicinity of the second-order transition. One can see that no hysteresis is visible in the temperature curves between the magnetization and the demagnetization branch. All three curves overlap reasonably even though the pulse strength was very different. At a starting temperature of 317 K, a large magnetocaloric effect is obtainable, which amounts to about 7 K in a magnetic field change of 10 T, but still the magnetocaloric effect of the first-order transition is larger in this field range. The flattening of the temperature profile in higher magnetic fields is a typical feature of the second-order magnetocaloric effect, which was described by [148]. This experiment demonstrates that the measurement quality of the adiabatic temperature change in pulsed fields is reasonable. If the response time of the thermocouple were too long, an artificial hysteresis in the ΔT_{ad} measurement would be the consequence. Since this was not observed in the characterization of the second-order transition, the hysteresis which is visible in Fig. 4.47 must be related to the martensitic transformation alone.

In order to reveal the origin of the difference in the pulse experiments, Fig. 4.48 needs to be considered. The magnetic field of the three pulses is plotted in Fig. 4.48(a) versus time. It is apparent that the field maximum is reached at the same time, in fact 13 ms after the pulse is launched. This implies that the magnetic-field-sweeping rate must be much higher in the 10 T experiment in comparison to the 2 T pulse. However, the decreasing field branch is much slower. For instance for the blue curve, the field decay takes about ten times longer than the field increase. This great deviation in the field sweeping is illustrated in Fig. 4.48(b) in a different form. It shows the magnetic-field rate as a function of the respective magnetic field. As expected, the sweeping rate is largest in the 10 T pulse, reaching a value of more than 1500 T s^{-1}

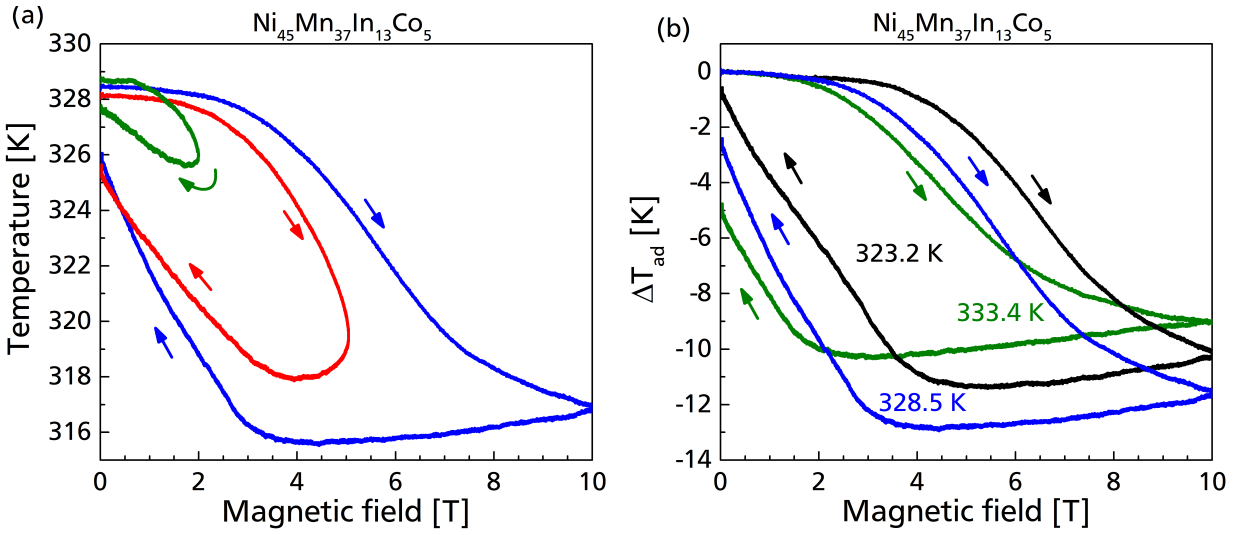

Figure 4.49: (a) Magnetic-field dependence of the sample temperature of $Ni_{50}Mn_{37}In_{13}Co_5$ in a 2, 5 and 10 T pulse. (b) Cooling behavior of the sample in 10 T for different starting temperatures.

in the small field range. Even up to 6 T, the field rate is larger than 1000 T s^{-1}. The sweeping rate is much smaller for the other two curves.

For the field-decreasing branch, meaning for negative sweeping rates, the situation changes drastically. Even for the 10 T pulse, the absolute magnetic-field sweeping rate is below 350 T s^{-1}. The field rate decreases more or less linearly with decreasing magnetic field. Furthermore, all three curves come together, describing the same field decay. Now the origin of the cooling behavior of the sample in the 5 and in the 10 T pulse measurement shown in Fig. 4.47 becomes obvious. For the magnetization process, the difference in the field rate was significant. The blue curve is lacking behind the red curve because the martensitic transition cannot follow the magnetic field momentarily. Consequently, the hysteresis increases. For the demagnetization, the sweeping rate is much smaller and even more importantly, the sweeping rates of the 5 and 10 T pulses are identical in relation to the magnetic field. This is why the red and the blue curve coincide for the heating branch in Fig. 4.47. It can be summarized that by direct measurements of the adiabatic temperature change of $Ni_{50}Mn_{35}In_{15}$ in pulsed-magnetic fields, the dynamics of the martensitic transition can be investigated. It turned out that for high sweeping rates above 1000 T s^{-1} an additional hysteresis is the consequence.

A similar result was obtained for the Co-containing sample as well, which is plotted in Fig. 4.49. Even though the hysteresis is larger in the ΔT_{ad} measurements of $Ni_{50}Mn_{37}In_{13}Co_5$, the broadening of the transition and therefore the increase of the hysteresis is evident. Especially the blue curve of Fig. 4.49(a) is smeared out significantly in the high-field range of the magnetization branch in comparison to the relatively sharp demagnetization branch (note that the width of the martensitic transition is a bit larger in the Co-containing sample - see Fig. 4.41). A magnetic field of 5 T is not sufficient to completely transform the material and therefore a comparison of the red and the blue curve is only of limited benefit. However, a delayed initiation of the transition is observed with increasing field rate.

4.3.5 Comparison of slow, semifast and fast ΔT_{ad} measurements

The results of the three different facilities measuring the adiabatic temperature change ΔT_{ad} of the Co-free compound are compared in Fig. 4.50. The starting temperature was set close to 290 K in discontinuous protocol. From the magnetization curves in Fig. 4.41 it can be derived that mainly martensite is present at this temperature. In the ΔT_{ad} measurement using the Halbach magnet, a typical minor loop behavior is observed, leading to a modest reversibility (blue curve in Fig. 4.43(a)). In contrast to this, in the slow experiment with the superconducting magnet already a magnetic field of 5 T is more than sufficient to complete the transition. This is visible by the flattening of the cooling curve above 3.5 T. As already mentioned, the demagnetization branch is only of limited benefit due to the unavoidable drift of the sample temperature during the holding time in the maximum magnetic field. For this reason, the temperature profile in decreasing field is plotted as a blue dashed curve in Fig. 4.50.

Even though the time scale of the two measurements is very different, the similarities during the cooling branch are evident. One can translate the magnetic-field-sweeping rate into a related cooling/heating rate β by forming the product of the sweep rate and the shift of the transition temperature in magnetic fields:

$$\beta = \frac{dH}{dt} \cdot \left| \frac{dT_t}{dH} \right| . \tag{4.8}$$

The parameter β gives an impression of how fast the sample would need to be heated in a purely temperature-driven transformation in order to achieve comparable conditions. In $Ni_{50}Mn_{35}In_{15}$, the shift of the transition temperature $\frac{dT_t}{\mu_0 dH}$ was found to be $-3.2\,\mathrm{K\,T^{-1}}$. For the superconducting magnet, β results in about $2.3\,\mathrm{K\,min^{-1}}$. This related heating rate is typical for magnetic measurements and in the order of magnitude of differential scanning calorimetry (DSC). However, β equals $135\,\mathrm{K\,min^{-1}}$ in the beginning of the field application for the semifast experiment using the Halbach magnet field source. This value is far too large for any standard characterization method. Nevertheless, the phase transformation is fast enough to follow the magnetic field.

For the 5 T magnetic-field pulse, the related heating rate results in about $150\,000\,\mathrm{K\,min^{-1}}$ at maximum. Obviously, the sample is subject to extreme condition. Such high rates can, for instance, be reached by rapid quenching techniques, but this is far from any characterization method. Even under these extreme conditions, the sample transforms and a complete transition can be obtained in a magnetic field change of 5 T. However, there are certain peculiarities in the temperature profile of the fast measurement in comparison to the other two. First, the initialization of the phase transition seems to be hindered to some extent. Furthermore, a higher magnetic-field change is necessary in order to completely transform the material. In the fast measurement, the transition is almost finished in a magnetic field of 5 T, as indicated by the flattening of the red curve, which was observed already in 3.5 T in the slow experiment (blue curve). The slight difference in the temperature in the high field range between the red and the blue curve, accounting for about 0.5 K, is due to the temperature drift in the slow measurements, as already discussed above. However, a third observation can be made by comparing the graphs in Fig. 4.50. The

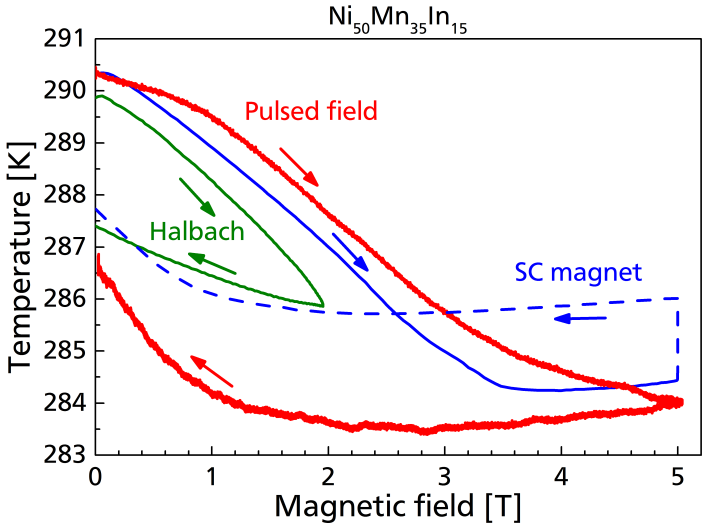

Figure 4.50: Comparison of the temperature change of $Ni_{50}Mn_{35}In_{15}$ in pulsed-magnetic fields (red), in the setup using a superconducting magnet (blue) and a Halbach magnet (green).

slope of the cooling behavior of the sample in the mid region is rather similar in all three measurements. By linear fitting, the cooling rate was determined to be $-1.9\,\mathrm{K\,T^{-1}}$.

Recently, Xu et al. [149] showed for a comparable Heusler compound an increasing hysteresis in magnetization measurements if faster sweeping rates are applied. This is consistent with the results obtained from Fig. 4.50, even though it is questionable whether isothermal conditions can be guaranteed in pulsed-field magnetization measurements in the vicinity of large magnetocaloric effects. The martensitic transition is driven by nucleation and growth. This process was already discussed in Sect. 4.2 in terms of in-situ optical microscopy. For this study it was derived that the two processes are related to a different thermal hysteresis due to energetic reasons. The comparison of ΔT_{ad} measurements under different magnetic-field-sweeping rates now reveals that also the kinetics of the nucleation process and the phase boundary motion act on different time scales. Starting in the more or less pure low temperature phase, the transformation is not fast enough to follow the magnetic field applied with $750\,\mathrm{T\,s^{-1}}$, which suggests that the nucleation process is a rather slow process. In contrast to that, in the mixed phase region, the phase boundary motion becomes dominant. The cooling rate in this region was the same in all three ΔT_{ad} measurements, which implies that the movement of the phase boundary between martensite and austenite is a much faster process. The flattening of the temperature profile in Fig. 4.50 can be attributed to the removal of lasting martensite nuclei, which requires a longer time again and the cooling of the sample is lacking behind.

In terms of application, it can be concluded that the martensitic transformation around room temperature is fast enough for typical operation frequencies up to 10 Hz, as utilized in an AMR device. However, when aiming for high frequency applications beyond 100 Hz, for instance in thin-film based cooling machines, it must be considered that the hysteresis increases due to the limited transformation speed. Because of this additional kinetic hysteresis, higher magnetic fields would need to be applied in order to completely transform the material between martensite and austenite. One possible attempt could be to move in minor loops of hysteresis to suppress the slower nucleation process, transforming always in a

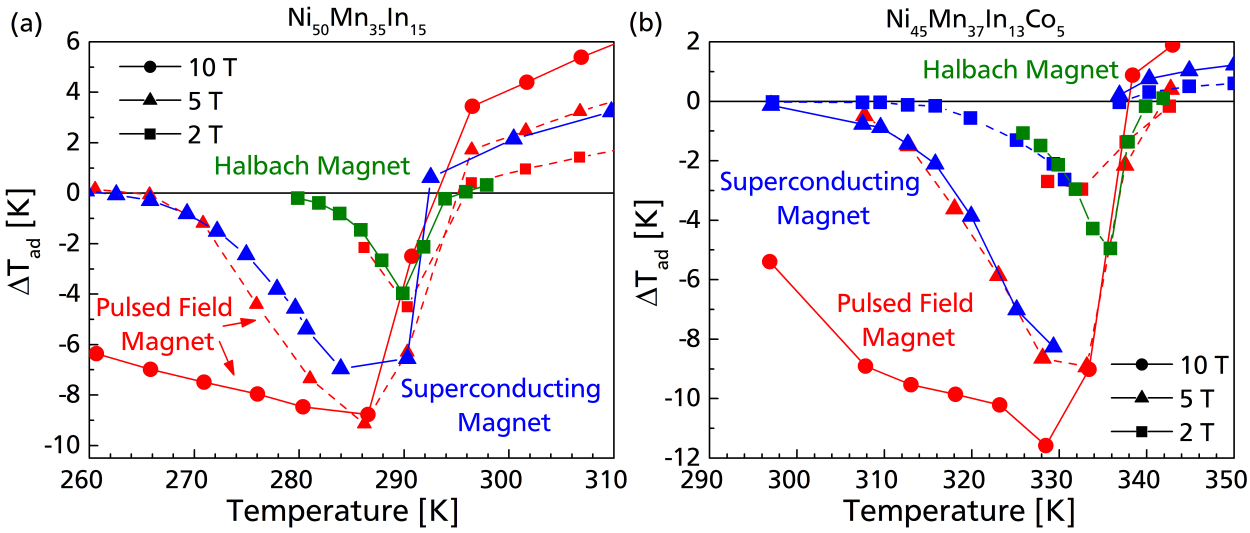

Figure 4.51: Adiabatic temperature change ΔT_{ad} of (a) $Ni_{50}Mn_{35}In_{15}$ and (b) $Ni_{45}Mn_{37}In_{13}Co_5$ in magnetic field changes of 2 (squares), 5 (triangles) and 10 T (circles). The different magnetic field sources are illustrated in green (Halbach magnet), blue (superconducting magnet) and red (pulse-field magnet).

mixed phase region. But the ΔT_{ad} measurements in 10 T pulses (see Fig. 4.46 and 4.47) suggest that in sweeping rates of 1500 T s^{-1} also the phase boundary motion reaches its limits.

4.3.6 Comparison of the maximum magnetocaloric effect

Finally, the results of the maximum adiabatic temperature change will be discussed. In Fig. 4.51, the ΔT_{ad} values for certain starting temperatures are shown for the Co-free sample in (a) and for the Co-containing sample in (b) respectively. The slow measurements using a superconducting magnet source are plotted in blue, the Halbach magnet results in green and the pulsed-field experiments are illustrated in red. Different magnetic fields have been applied in the direct ΔT_{ad} measurements, namely 2 T plotted as squares, 5 T as triangles and 10 T as circles.

In a magnetic field change of 2 T, an adiabatic temperature change of −4 and −5 K can be achieved in $Ni_{50}Mn_{35}In_{15}$ and $Ni_{45}Mn_{37}In_{13}Co_5$ respectively. The ΔT_{ad} curve has a peak shape and therefore the temperature window is rather limited. At higher temperatures, the second-order transition of the austenite phase leads to a heating of the samples when a magnetic field is applied. By increasing the magnetic field to 5 T, both the maximum temperature change and the operation window can be much enhanced. For the Co-free alloy shown in Fig. 4.51(a), a large $\Delta T_{ad} = -9.2$ K can be achieved. This value is very similar to the maximum obtained in 10 T pulses, but still the $\Delta T_{ad}(T)$ curve (red triangles) follows a peak shape in contrast to the evolving plateau in the 10 T measurements (red circles). This plateau implies that the transformation from martensite to austenite could be completed. The upper limit of the plateau is the austenite start temperature A_s in zero field, which is about 289 K. At higher starting temperatures, the transition might still be completed, but less material was transformed during

field application because some austenite already existed before. However, increasing the magnetic field allows to completely transform the sample over a large temperature range even below 260 K.

The decreasing plateau height is due to the enhanced magnetization of the austenite phase and therefore the magnetic entropy contribution gains importance, leading to the reduction of the entropy change of the transition. Since ΔS_t is related to the adiabatic temperature change, the reduction of ΔT_{ad} can be understood. Besides the strong widening of the temperature window of the first-order transition, also the reversibility is significantly enhanced in high magnetic-field changes. From the diagrams showing the field-dependent ΔT_{ad} (see Fig. 4.46), it can be stated that a fully reversible transformation takes place for starting temperatures below 280 K. A similar analysis can also be done for the Co-containing material plotted in Fig. 4.51(b). In general, the coincidence between the different measurement setups is reasonable, even though slight changes can be identified, but the principle behavior is reasonably monitored.

In conclusion, it could be demonstrated that direct measurements of the adiabatic temperature change using different magnetic-field-sweeping rates from 0.01 up to 1500 T s^{-1} allow to study the kinetics of the martensitic transformation. Based on these experiments, it is evident that the nucleation of the new phase is much slower than the simple phase boundary movement. However, limitations due to kinetics of the martensitic transformation might only play a role for high frequency applications beyond 100 Hz [9], leading to an increased hysteresis. At least for typical operation frequencies as used in an active magnetic regenerator, no kinetic restrictions were identified.

4.4 Size-dependent effects of magnetostructural transitions

The focus of this section is the question whether the magnetostructural transition depends on the size of the material. This is an essential issue in terms of the application of magnetic refrigeration. In order to provide an efficient magnetocaloric regenerator operating at several Hertz, the surface of the material needs to be very large in such a way that a good heat transfer between the material and the exchange fluid is possible. This can be achieved by creating fine structures with well-organized micro channels, for instance by selective laser melting [150]. It is also possible to build a regenerator from magnetocaloric plates. These plates should have a thickness of no more than 300 µm, otherwise the heat transfer would not be efficient [15]. They can be produced by cutting plates from a bulk block or by bonding a magnetocaloric powder with an epoxy or metal in the desired shape [151, 152]. The most straightforward way to obtain a good magnetocaloric heat exchanger is the use of a powder bed. However, it has the drawback that the pressure drop can be significantly higher in a powder-based regenerator in comparison to a plate geometry, which becomes relevant especially at higher operation frequencies [153].

For both the bonded plates and the powder bed, a base material with a particle size of less than 300 µm is required. For this reason, it is a crucial question how the magnetostructural transition takes place in small particles. Therefore, magnetic measurements of single fragments of the Heusler compound $Ni_{45.7}Mn_{36.6}In_{13.5}Co_{4.2}$ with different sizes were performed. Due to the relevance of this study for application, the analysis was extended to the two materials $LaFe_{11.8}Si_{1.2}$ and $Mn_{1.2}Fe_{0.68}P_{0.5}Si_{0.6}$. The samples were provided by Konstantin P. Skokov (TU Darmstadt) and Maximilian Fries (TU Darmstadt).

4.4.1 Single-particle measurements in Heusler alloys

The bulk properties of the selected Heusler alloy $Ni_{45.7}Mn_{36.6}In_{13.5}Co_{4.2}$ were already studied intensively above. The martensitic transition takes place near room temperature (see Fig. 4.20) and significant adiabatic temperature changes ΔT_{ad} are related to this transition when applying a magnetic field (see Fig. 4.23). The corresponding magnetization curve of the bulk sample in a magnetic field of 1 T is shown in black in Fig. 4.52(a) (upper curve). As already mentioned above, the thermal hysteresis is in the range of 10 K and the transformation takes place in a rather narrow temperature window.

In order to characterize the transformation properties of micrometer-sized particles, small fragments of the material were isolated under a light microscope and subsequently fixed to the sample holder with Kapton tape. Since the magnetic signals of the small samples were in the µemu range, it was essential to avoid any contamination by other magnetic materials. Since mechanical stresses can significantly influence the martensitic transition, the material was not actively crushed. Instead, only pieces were selected which were separated during the sample preparation for different experiments. In order to get the optimal signal to noise ratio, the frequency and the amplitude of the VSM head of the PPMS were maximized. A single fragment with a size of approximately 250 µm is plotted in red in Fig. 4.52(a). A light microscopy image of this particular particle is shown on the left side of Fig. 4.52(b). The diameter was determined by relating the change of the magnetic moment during the transformation to the one of

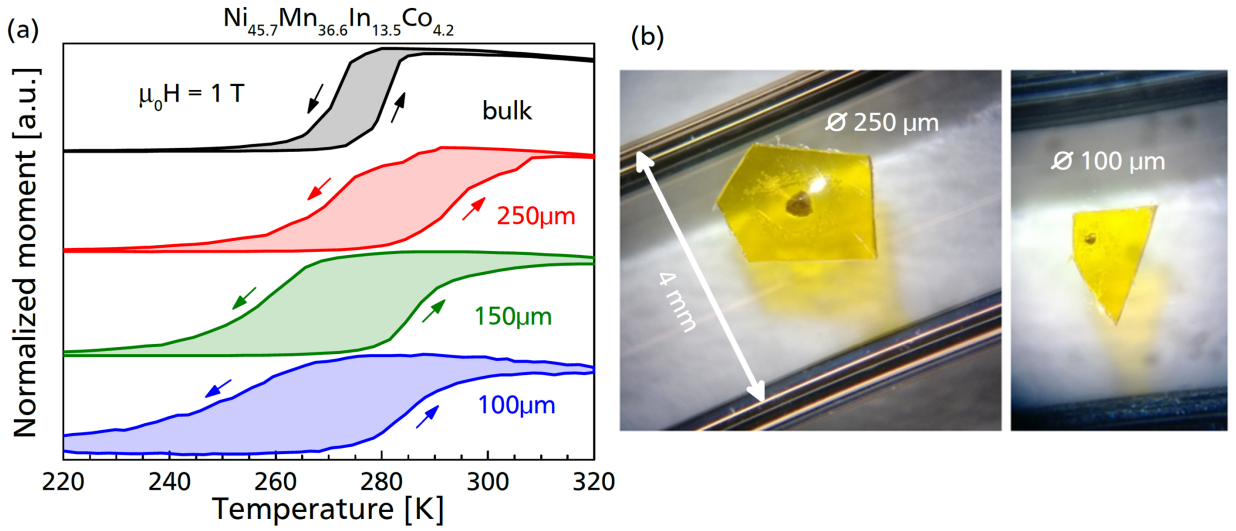

Figure 4.52: (a) Comparison of the magnetic behavior of a bulk sample and differently sized fragments of $Ni_{45.7}Mn_{36.6}In_{13.5}Co_{4.2}$ in a magnetic field of 1 T. (b) Light microscopy images of two single particles glued to the sample holder with Kapton tape.

the bulk sample in order to obtain the mass of the fragment. Via the density of $8\,g\,cm^{-3}$, the volume can be approximated and transferred to the diameter of a sphere-like particle. Obviously, this can only be a rough estimation since the single particles are no ideal spheres. Furthermore, also the measurement error of the magnetic moment becomes larger when reducing the particle size due to the limited sensitivity of the device.

As it can be seen in Fig. 4.52(a), the transition of the 250 µm particle is several times broader than the one of the bulk sample. Also the thermal hysteresis is about twice as large. Furthermore, it turns out that the transformation from martensite to austenite starts at about 285 K, which is 10 K higher than in the bulk material. This size-dependent behavior becomes even more pronounced for smaller particles. For instance, the particle with a diameter of approximately 100 µm shows a tremendously increased transition from austenite to martensite, spanning over more than 50 K. In Fig. 4.52(a), only three exemplary particles are illustrated, but in total more than ten single fragments have been studied, which reveals that the transition is scattered. In order to quantify this distribution of the transition temperature, a much higher number of single particle measurements would be required, which is simply not feasible.

The observed variation is in fact not surprising, since the chemical composition of the alloy strongly influences the transition temperature, as discussed above by means of Fig. 4.3 and 4.4. From this it was pointed out that already a change of only 0.1 at % shifts the transition by about 10 K. During the melting and heat treatment of the alloy, a good homogeneity might be obtainable, but it is never perfect. Slight changes of the local composition are therefore not avoidable and they affect the transition temperature of the single particles. However, the origin for the broadening of the transition and the increase in hysteresis is not straightforward and could not be definitively identified. As a fact, the martensite structures in millimeter-sized samples, as observed by optical microscopy for instance in Fig. 4.26, are also in the millimeter range. However in thin films, the martensite features are much smaller [154]. This is due to

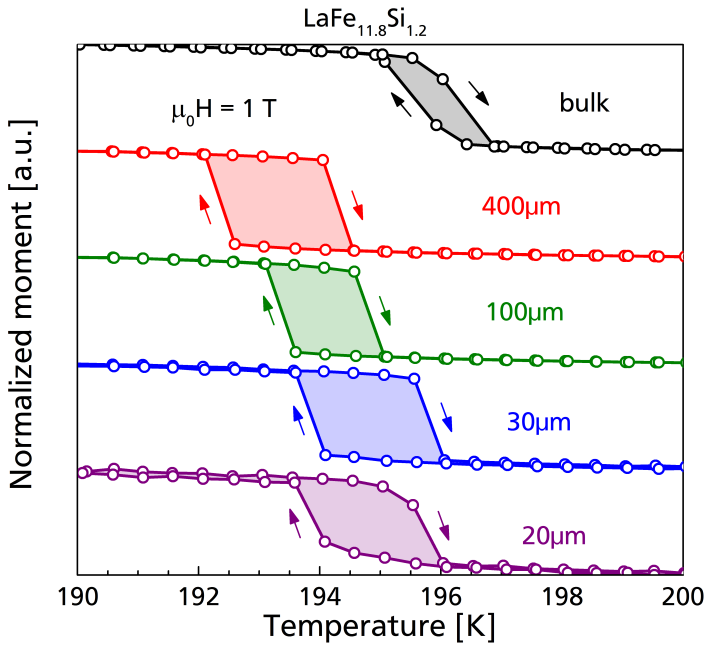

Figure 4.53: Comparison of the magnetic behavior of a bulk sample and differently sized fragments of $LaFe_{11.8}Si_{1.2}$ in a magnetic field of 1 T. The material was provided by Konstantin P. Skokov (TU Darmstadt).

the formation of martensite nuclei which have an uneven aspect ratio [92]. These needle-like structures somehow must fit into the small fragments, which becomes more and more difficult the smaller the samples get. Also the role of defects and the increasing importance of the surface which creates stresses could be related to the observed size effects, but this can not be clarified within this thesis.

4.4.2 Single-particle measurements in La-Fe-Si

The situation is completely different in the second material example. Magnetic measurements of bulk $LaFe_{11.8}Si_{1.2}$ and of small single particles are shown in Fig. 4.53. In this compound, the sharp first-order transition takes place below 200 K. The thermal hysteresis of the bulk sample is very narrow, as can be seen by the black curve in Fig. 4.53. Four different particles with a size of 400 down to 20 µm are plotted in Fig. 4.53 as well. It can be seen that the transformation of small fragments is always jump-like, at least within the measurement resolution. For this reason, the determination of the particle size based on the change in the magnetic moment during the transition is much more reliable in $LaFe_{11.8}Si_{1.2}$ than in the Heusler sample. Furthermore, one can see that the thermal hysteresis also increases in comparison to the bulk material.

Also in this material, a distribution of the transition temperature is visible, but it is not so pronounced. This could be related to the fact that the 1:13 stoichiometry between La and (Fe,Si) is fixed so that in principle only the Fe-to-Si ratio can change locally. In contrast to that, in the Ni-Mn-In-based Heusler sample all elements are mixable in a large composition range of the Heusler phase without the formation of secondary phases [155]. The reduced variation of the transition temperature could also originates from in the typically much longer heat treatment of La-Fe-Si compounds. This is required because the

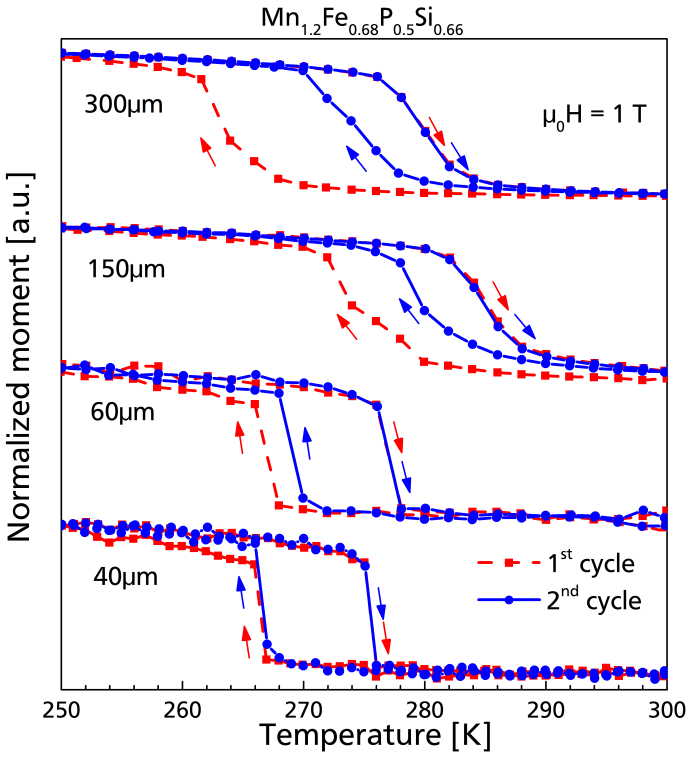

Figure 4.54: Comparison of the magnetic behavior of differently sized fragments of $Mn_{1.2}Fe_{0.68}P_{0.5}Si_{0.6}$ in a magnetic field of 1 T. The first and the second cooling and heating cycle is plotted in red and blue respectively. The material was provided by Maximilian Fries (TU Darmstadt).

1:13 phase forms in a peritectic reaction [156]. It is probable that the local chemical composition does not change much because of the special formation character of the magnetocaloric phase.

4.4.3 Single-particle measurements in Fe_2P-type materials

As a third material example, the results for the Fe_2P-type compound $Mn_{1.2}Fe_{0.68}P_{0.5}Si_{0.6}$ are plotted in Fig. 4.54. This particular alloy transforms near room temperature. The illustration is different in comparison to Fig. 4.52 and 4.53 because one aspect of the single-particle measurements here is the study of the so-called virgin effect [32]. Starting at 300 K, two cooling and heating sequences have been performed. The largest particle with a size of approximately 300 µm shows an increasing magnetization just below 270 K in the first cooling of the fresh material. However, when repeating the sequence, the transition takes place about 10 K above. Interestingly, the virgin effect vanishes for single particles with a size below 60 µm. It will be discussed in the following section that stresses appear during the transformation, which result in the formation of cracks, which is the explanation of the virgin effect. However, the single-particle measurements suggest that crack formation is not required for small fragments which have a size of less than 60 µm. As it was also observed in the La-Fe-Si sample, the transformation of small fragments turns to a jump-like transition and also a slight increase of the thermal hysteresis is observed as well as a distribution of the transition temperature. However neither in the La-Fe-Si nor in the Heusler sample, such behavior between the first and second measurement cycle could be identified.

It can be concluded that interesting effects of the magnetostructural transition in a Heusler, a La-Fe-Si and a Fe_2P-type sample can be identified by magnetic measurements of single particles. From this study it became obvious that a reduction of the size can lead to a significant obstruction of the martensitic transition in the Heusler alloy. This implies that Heusler compounds might not be used as a powder bed magnetocaloric regenerator with a particle size in the sub-micrometer range because both the transition width and the thermal hysteresis would increase. However for plate geometries cut from bulk material, this is probably not so critical, since also in thin films it is possible to obtain relatively sharp transitions with modest thermal hysteresis [90].

For the other two materials, such a broadening of the transition was not observed in small fragments in the size range relevant for application. Consequently, it is safe to use $LaFe_{11.8}Si_{1.2}$ and $Mn_{1.2}Fe_{0.68}P_{0.5}Si_{0.6}$ also in form of a fine powder for magnetic refrigeration. However, a distribution of the transition temperature was observed in all three materials, being stronger than the transition width of the bulk sample. This raises the question how the transformation can be sharper in a big material considering the fact that it is built from particles with a larger spread in their transition temperature. This issue will be discussed in the following section.

4.5 Modeling of magnetostructural transitions

It was shown above that the magnetostructural transition in Heusler alloys can be influenced by the application of hydrostatic pressure. The reason for this behavior is the volume change of the unit cell, which is related to the martensitic transformation. For Heusler alloys, the transition is shifted to higher temperatures because pressure stabilizes the phase with smaller volume, which is the martensite phase (conventional barocaloric effect). From XRD measurements, the volume change during the transition was determined to be in the range of 1 %. This value is also in the order of magnitude reported in literature [157]. For La-Fe-Si, similar volume changes were observed [145]. However, the substitution of Fe by Co leads to an increase of the transition temperature and a reduction of ΔV. This is accompanied by a change of the transition type from a first to second-order transformation [145].

It was demonstrated in literature that the size of the magnetocaloric material has an influence on the magnetocaloric properties. For instance in $LaFe_{11.8}Si_{1.2}$, a rather big sample of 0.12 mm^3 has a sharp transition based on magnetization measurements [158]. In great contrast, after separating this big particle into smaller fragments, the transformation of the resulting powder is significantly broader [158]. This behavior is in agreement with the results from the single-particle measurements in the previous section. Due to inevitable chemical inhomogeneities, the transition temperature of each fragment varies to some extent. However, when those fragments are connected, the transition is much sharper than the average of the particle ensemble. The question is which mechanism is responsible for the sharpening of the transition. In order to answer this question, finite element simulations were performed, which suggest that the coupling of individual fragments by mechanical stress together with the sensitivity of the transition temperature to stress and pressure is the origin for this effect.

4.5.1 Stress coupling in the two-cube problem

In this section, the finite element analysis will be applied to the most simple problem - the two-cube scenario. For the simulation, an artificial material with the following properties is postulated. The material is constructed from two individual cubic elements, as illustrated in Fig. 4.55(a). The two elements have slightly different fictitious transition temperatures and their transformation starts at 300 and 305 K respectively. During the transformation from the low to the high temperature phase, the individual blocks expand. The length change is 0.33 %, which results in a volume change of approximately 1 %. It is assumed that the transition takes place continuously over a certain temperature interval of 15 K in this example. The high-temperature-phase fraction of the individual elements is illustrated in Fig. 4.55(b). It is furthermore assumed that the elastic properties, the Young's modulus $E = 100$ GPa and the Poisson's ration $\nu = 0.3$ do not change during the transition.

If there was no coupling by stress, the transition of the two-block ensemble would just be the average of the two individuals. This transformation behavior is shown as a blue line in Fig. 4.55(c). Three different segments can be identified in this diagram. Between 300 and 305 K only cube 1 transforms, but for higher

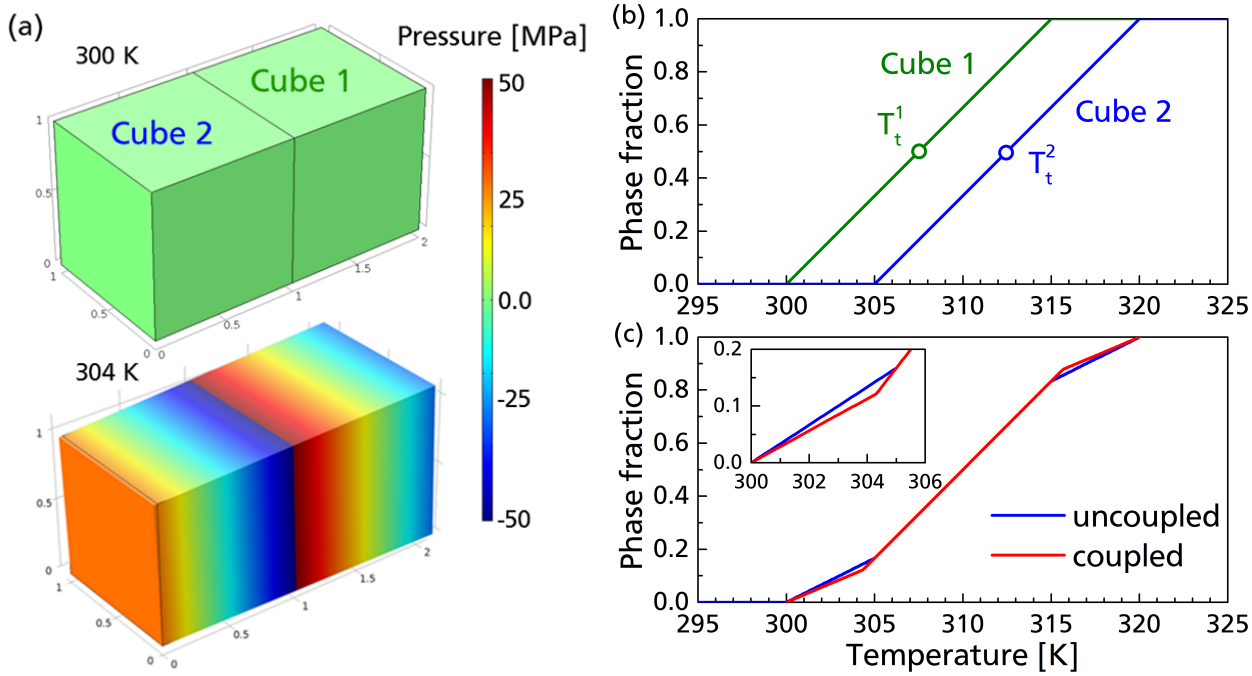

Figure 4.55: (a) Stress evolution in the two-cube problem. (b) Individual transition temperature of the two cubes. (c) Coupled (red) and uncoupled (blue) situation of the two-cube problem. The inset shows a zoomed in view of the critical region.

temperature, both elements transform and a larger slope is observed. Above 315 K, cube 1 is already in the pure high temperature phase, but cube 2 transforms further.

The situation changes when the coupling by stress is considered (blue line in Fig. 4.55(c)). At 300 K, the ensemble is in the stress free state as can be seen in Fig. 4.55(a). However, increasing the temperature leads to an expansion of cube 1. Since it is connected to the second element, both elements are deformed and a stress field evolves. These stresses can be significant, as for instance shown for the state at 304 K reaching values up to 50 MPa. Therefore, a compressive stress acts on cube 1, which shifts the transition temperature upwards. This coupling to stress is considered in the simulation by the following equation:

$$x_t = \left(T - T_t + \frac{(\sigma_{xx} + \sigma_{yy} + \sigma_{zz})}{3} \cdot \frac{dT_t}{dp} \right) \frac{1}{\omega} + 0.5 \quad \text{with} \quad x_t \in [0,1] \,. \tag{4.9}$$

The parameter x_t describes the phase fraction of the individual element. It depends on the elemental transition temperature T_t, defined by the middle position of the transformation, the transition width ω, the coupling constant $\frac{dT_t}{dp}$ and the normal stresses σ_{xx}, σ_{yy} and σ_{zz}. It is worth noting that it was assumed that shearing stresses do not shift the transition temperature because the volume does not change under shearing - at least for the first approximation. The shift of the transition temperature by stress $\frac{dT_t}{dp}$ was selected to be 50 K GPa^{-1} according to pressure-dependent magnetization measurements from above (see Fig. 4.17) and from literature [19, 159].

In the stress-free case, Eq. (4.9) simply results in a linear transformation shape of the individual element. However, in order to quantify the stress coupling, the local stress field must be calculated. The difficulty in the simulation is the interlink between the elemental phase fraction and the resulting stresses. Therefore, an iterative approach is necessary in order to find the global minimum in solution space. For instance, by increasing the temperature from 300 to 301 K in the two-cube problem, cube 1 will transform to some extent. But the related expansion creates net compressive stresses to cube 1. Considering these stresses in Eq. (4.9) will lead to a much smaller $x_t(T = 301\,\mathrm{K})$. But this will on the other hand result in less stresses and so on and so forth. This problem is manageable when only two cubes are involved. However, when considering larger problems, this optimization procedure can be very time-consuming and even lead to the instability of the code.

The solution of the stress-coupled problem is shown in Fig. 4.55(c) as a red curve. In fact, there is no big difference between the coupled and the uncoupled situation, but in the temperature range from 300 to 305 K one can clearly see that the transformation of cube 1 is suppressed, which is indicated by a smaller slope. At about 304.3 K, also cube 2 starts to transform and both elements continue together. This result is nothing else than a sharpening of the ensemble transition even though it is not very pronounced. In the simulation, cube 1 is hindered by the neighboring block leading to a suppression of the transition. On the other hand, cube 2 is under tension caused by cube 1 and a lowering of the transition temperature of cube 2 is observed. For obvious reasons, the two-cube scenario is too simple in order to describe a real magnetocaloric material. Therefore, larger meshes need to be considered, which will be discussed in the following.

4.5.2 Stress coupling in the 1000-cube problem

The finite element mesh which was used for the study is illustrated in Fig. 4.56(a). The artificial first-order magnetocaloric material consists of 1000 individual blocks with randomly distributed transition temperatures. In order to simulate a certain variation of the local transition temperature due to chemical inhomogeneities, a Gaussian distribution with a standard deviation of 2 K or a full width at half maximum FWHM = 4.3 K was used. The peak position of the distribution was set to a fictitious temperature of 305 K. It can be seen in Fig. 4.56(a) that there is a certain discrepancy between the calculated Gaussian function, plotted as a red curve, and the histogram of the elemental transition temperature. It should be mentioned that the resulting diagram strongly depends on the selection of the class width of the histogram, but it is also important to note that a number of 1000 elements does not perfectly mimic a Gaussian distribution. Nevertheless, the statistics of the transition distribution is reasonably good.

First, the uncoupled situation will be discussed. The transformation of the ensemble should therefore be similar to the transition of a loose powder of the different fragments. In this case, there is no connection between neighboring particles. Consequently, each element transforms without being influenced by the others. An image sequence of this transition is illustrated in Fig. 4.57. In the pictures, only elements which are at least half transformed are visible. For x_t between 0.5 and 1, a color legend from blue to red is used. From the frozen pictures of the simulation in Fig. 4.57 at certain temperatures, the arbitrary nature of the uncoupled transformation is obvious.

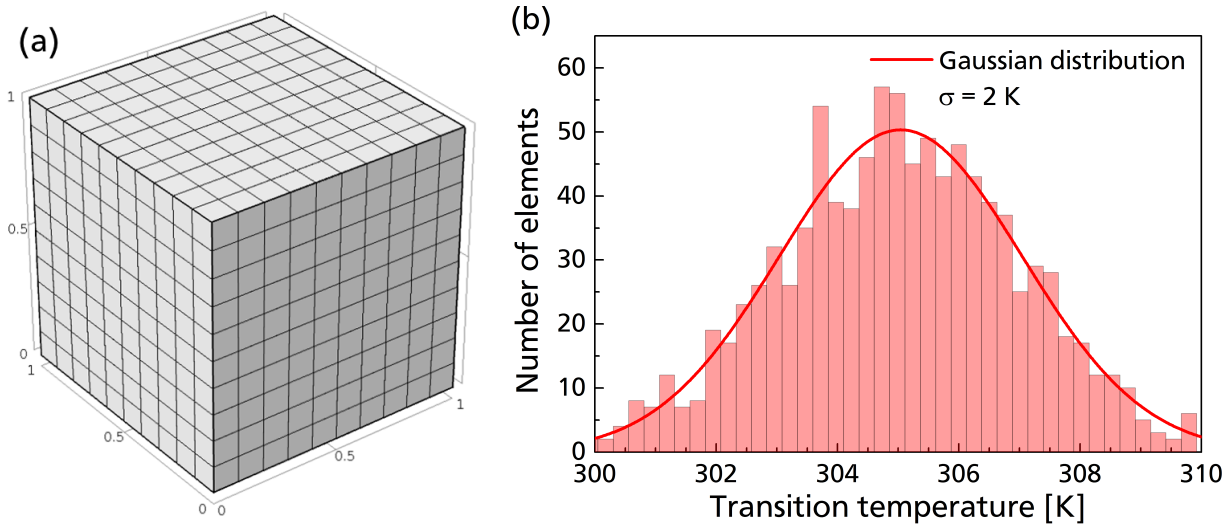

Figure 4.56: (a) 1000-element mesh used for the simulation study. (b) The individual transition temperature is distributed randomly by means of a Gaussian distribution.

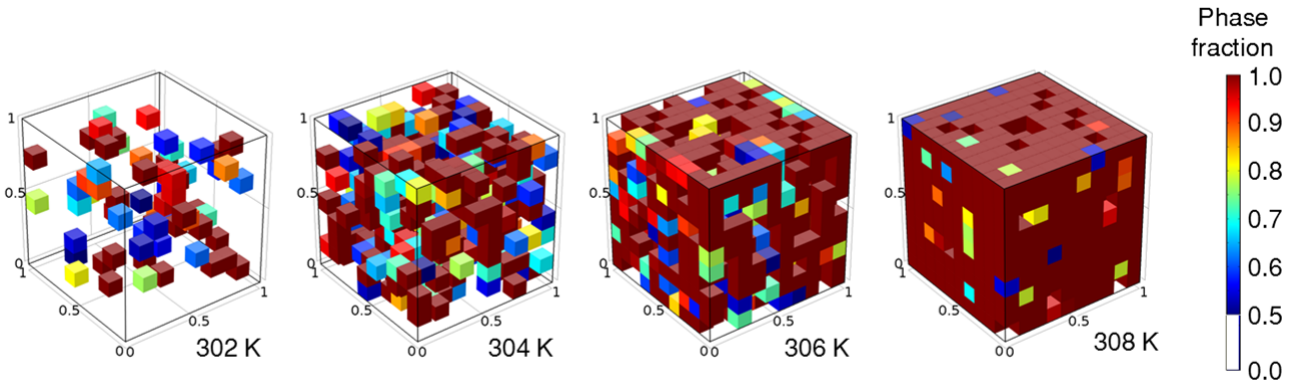

Figure 4.57: Image sequence of the transformation of an ensemble of 1000 elements without any coupling by stress. The transition width of the individual elements is $\omega = 1\,\mathrm{K}$. The elemental transition temperature is randomly distributed by means of a Gaussian distribution with a standard deviation $\sigma = 2\,\mathrm{K}$ and the peak transition temperature of $305\,\mathrm{K}$.

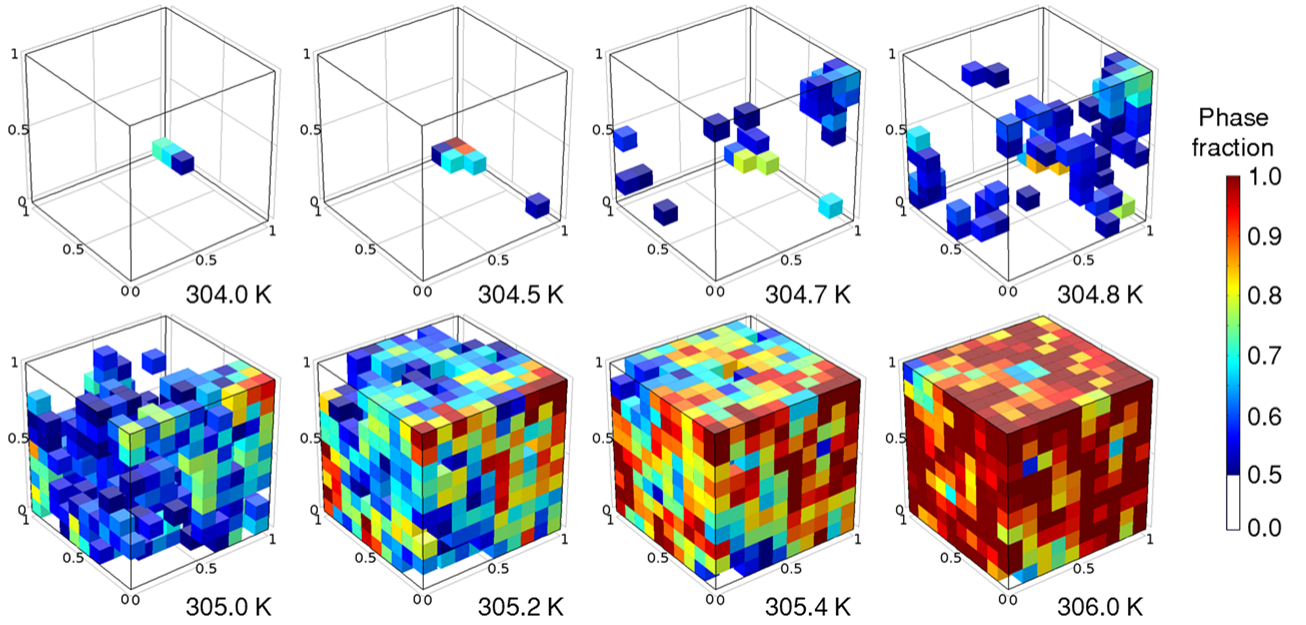

Figure 4.58: Image sequence of the transformation of an ensemble of 1000 elements coupled by stress with $\frac{dT_t}{dp} = 50\,\mathrm{K\,GPa^{-1}}$. The transition width of the individual elements is $\omega = 1\,\mathrm{K}$. The elemental transition temperature is randomly distributed by means of a Gaussian distribution with a standard deviation $\sigma = 2\,\mathrm{K}$ and the peak transition temperature of $305\,\mathrm{K}$.

The situation changes drastically when the stress-coupling mechanism is active. One can see that the transformation is preferentially initiated in the corners of the finite element mesh. This is intuitive because elements on the surface are not as restricted as elements inside the body. Surface blocks and especially blocks in the corners can expand more easily. Once initiated, the furthest transformed elements apply tensile stresses to their neighbors, which lowers their transition temperature and forces them to convert as well. As a consequence, an avalanche progresses through the mesh and the material transforms together. This result is rather surprising, since this transformation behavior can somewhat be understood as a nucleation and growth process, even though no such feature was implemented in the FEM study. The only mechanism which drives this combined ensemble transition is the stress coupling of neighboring blocks due to the volume change during the first-order transition and the sensitivity of the transition to external pressure and stress.

The sharpening of the transition can already be seen by comparing the image sequences of the coupled and the uncoupled solution (see Fig. 4.57 and 4.58). A more quantitative analysis is possible by plotting the phase fraction of the whole body as a function of temperature. This is illustrated in Fig. 4.59 for different coupling constants $\frac{dT_t}{dp}$. The individual transition of each element has a width of 1 K, which is illustrated in the inset of Fig 4.59. Also the transition temperature of the single block T_t^i is marked, being measured in the mid point of the transformation. In the uncoupled case (black curve), the ensemble transition is simply the average of the individual transition temperatures, which is similar to an error function of the Gaussian distribution that was shown in Fig. 4.56. Without coupling, the transition takes place within approximately 10 K.

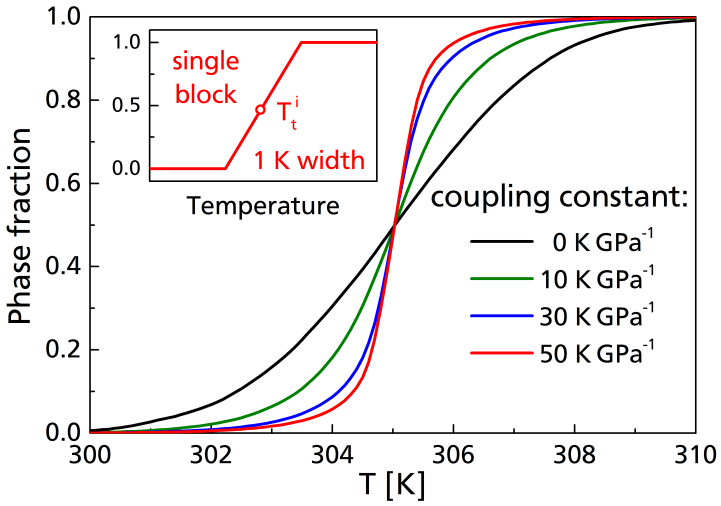

Figure 4.59: Transformation of an ensemble of 1000 elements for different coupling constants $\frac{dT_t}{dp}$. The standard deviation σ of the Gaussian distribution is 2 K and the individual transition width $\omega = 1$ K. The inset schematically illustrates the transformation of an individual block.

Already a small coupling constant of only 10 K GPa^{-1} has an extreme influence on the properties of the ensemble. The transformation is completed in a much smaller temperature window of only 6 K. This trend continues for higher values of $\frac{dT_t}{dp}$. In real materials, a coupling constant in the range of 50 K GPa^{-1} was measured (see Sect. 4.1.4. For this strong coupling, the ensemble transition becomes even sharper. In fact, the transition approaches the transition width of a single block ($\omega = 1$ K) or in other words, the ensemble behaves as one. This behavior can be approximated by a folding integral:

$$f(T) = \int_{-\infty}^{\infty} g(T' - T) \cdot \phi(T', \gamma) dT' \,. \tag{4.10}$$

The function f stands for the transition of the ensemble as a function of temperature T. It is calculated by integrating the product $g \cdot \phi$ over T' from 0 up to infinity, whereas g describes the transformation of a single element. The function ϕ is the Gaussian distribution of the transition temperature:

$$\phi(T, \gamma) = \frac{1}{\gamma\sigma\sqrt{2\pi}} \cdot \mathrm{e}^{-\frac{\left(T - T_t^0\right)^2}{2(\gamma\sigma)^2}} \tag{4.11}$$

In order to simulate the transformation behavior in Fig. 4.58, the factor γ is needed. For $\gamma = 1$, there would be no stress coupling, as in loose powder. By reducing γ, the coupling force increases and for $\gamma \to 0$, the ensemble transition would transform as a single element at the average transition temperature. Figure 4.60 illustrates how the calculation of the function $f(T)$ takes place. The Gaussian distribution $\phi(T', \gamma)$ is plotted as a red curve in Fig. 4.60(a) for $\gamma = 1$ and $\sigma = 2$ K, which corresponds to the uncoupled case (see black curve in Fig. 4.58). The function $g(T' - T)$ is shown in blue. It describes the single element transformation with a transition temperature $T = 303$ K. As a result, $g(T' - T)$ is mirrored at the y-axis. Therefore, the product $g(T' - T) \cdot \phi(T', \gamma)$ equals the Gaussian distribution for lower

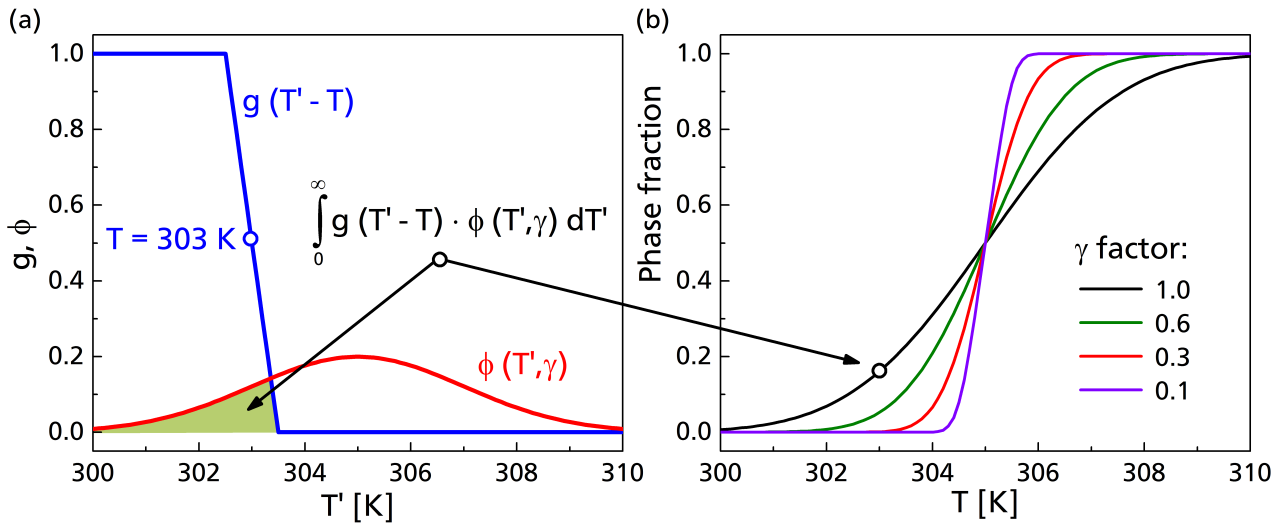

Figure 4.60: (a) Illustration of the concept of the folding integral. g is the transition of the individual element and ϕ is the Gaussian distribution of the transition temperature extended by the factor γ. (b) Ensemble transformation results for different γ values.

temperatures T' and is zero for higher values. The folding integral in Eq. (4.10) would approximately result in the highlighted green area in Fig. 4.60(a) for the temperature $T = 303\,\mathrm{K}$, which is also marked by the black circle in Fig. 4.60(b). Repeating the integration for different T and γ values results in the transformation behavior shown in Fig. 4.66. For $\gamma \to 0$ and 1, the ensemble transition is identical with the results from the finite element simulation shown in Fig. 4.59. However, for modest stress coupling, the different results do not coincide perfectly. For this reason, so far no correlation between the factor γ and the coupling constant $\frac{dT_t}{dp}$ could be derived.

In Fig. 4.61 the phase fraction of the ensemble is plotted for Gaussian distributions with different standard deviations σ. The coupling constant $\frac{dT_t}{dp}$ is set to $50\,\mathrm{K\,GPa^{-1}}$. The red curve is the same as already shown in Fig. 4.59. Using a much sharper transition temperature distribution continues the trend which was discussed in terms of the folding integral Eq. (4.10). However, for a broad transition temperature distribution with $\sigma = 10\,\mathrm{K}$, the transformation of the ensemble is smeared out significantly. It should also be mentioned that the first-order nature of the macroscopic object is not clearly obvious when the spread of the transition temperature over the material is large. On the microscopic scale, the transition of the constituent parts was always first-order, but this can be easily overseen if only the sharpness of the bulk transition is considered. For instance, a material with a first-order transition and a small thermal hysteresis as for La-Fe-Si could look like a second-order material if the spreading of the local chemical composition is large.

In the case of a broad transition distribution, a certain fraction of the elements transforms far from the average transformation. Such a behavior is for instance observed in Heusler alloys. Even though the major transformation is happening in a rather small temperature interval, an infinitesimal transition can always be observed far from this temperature (see for instance Fig. 4.3). This means that the "real" chemical transition temperature distribution is much broader, as one would expect from magnetization measurements of a bulk piece. This finding is also in agreement with the single particle measurements of

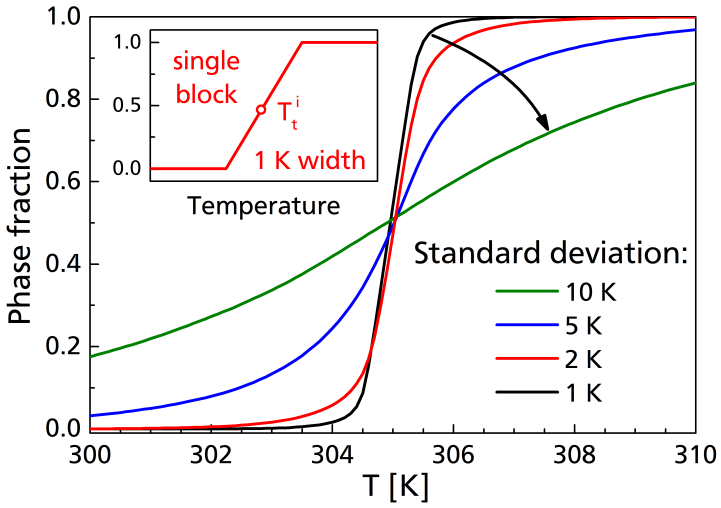

Figure 4.61: Transformation of an ensemble of 1000 elements for different values of the standard deviation σ. The coupling constant is $\frac{dT_t}{dp} = 50\,\mathrm{K\,GPa^{-1}}$ and the individual transition width is $\omega = 1\,\mathrm{K}$.

the Heusler compound showing a large scattering of the transition in different fragments. Although the results from the stress-coupling simulations are promising, one needs to consider that a real material is much more complicated than can be described by the simulations scheme.

For La-Fe-Si, the single particle measurements also suggested a distribution of the transition temperature, but it is much less pronounced than in the Heusler sample. In the magnetization data of small fragments, the transition is always jump-like, at least within the resolution of the measurement. A drawback of the finite element simulation is the unstable optimization routine for a single element width ω much below 1 K. A discontinuous transformation of the individual elements cannot be described because a continuous transition is always required. Nevertheless, the derived transformation behavior can also be applied to La-Fe-Si-based compounds. For this reason, the stress-coupling mechanism can give an insight into the nature of the magnetostructural transition in general.

4.5.3 Stress coupling under different boundary conditions

So far, the artificial material was free to expand, meaning that no special boundary condition was used. However, the finite element model provides a rigorous tool for studying the influence of different stimuli on the magnetostructural transition. Due to the application of hydrostatic pressure, the transition should shift to higher temperature in the model, since the low temperature phase with smaller volume is stabilized. Such a computer experiment also allows to check the robustness of the simulation scheme. In Fig. 4.62, the transition of the free mesh with a coupling of $\frac{dT_t}{dp} = 50\,\mathrm{K\,GPa^{-1}}$, a standard deviation of $\sigma = 2\,\mathrm{K}$ and a transition width of the single element $\omega = 1\,\mathrm{K}$ is shown. The volume change during the transition $\frac{\Delta V}{V}$ is still 1 % as in the simulations above.

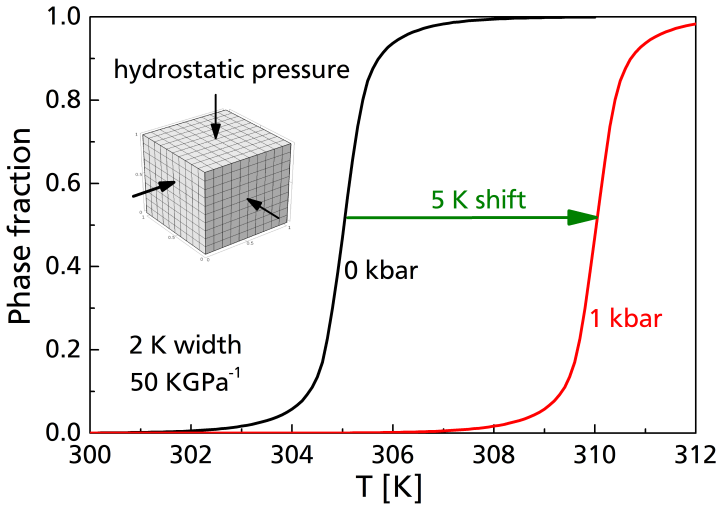

Figure 4.62: Comparison of the ensemble transition of a mesh without restrictions (black) and under a boundary load of 1 kbar (red). The Gaussian distribution has a standard deviation of 2 K. The stress-coupling constant is $\frac{dT_t}{dp} = 50\,\mathrm{K\,GPa^{-1}}$ and the transition width of the individual element is 1 K.

The red curve in Fig. 4.62 shows the transformation character of the material in the presence of a hydrostatic pressure of 1 kbar or 0.1 GPa. Indeed, the transition is shifted to higher temperatures. This shift accounts for 5 K. The result of the simulation is exactly as it would be expected, since a shift of the transition temperature by pressure of $50\,\mathrm{K\,GPa^{-1}}$ was selected. It can be also seen that the shape of the transition does not change by simply applying hydrostatic pressure. The Heusler sample in Fig. 4.17 showed a slightly sharper transition under pressure, but it should also be mentioned that in real materials, other factors influence the transition width (see Sect. 4.1.3).

Another important result evolves when considering fixed boundary conditions instead of hydrostatic pressure. In Fig. 4.63 again the transformation of the free mesh is plotted in black, only the temperature scale is different. The blue curve represents the transition of the material when the expansion along the z-axis is restricted by a solid boundary. In the low temperature region, both curves grow in a more or less similar way. However, at higher temperatures, a large deviation can be observed. For instance at 310 K, only half of the material has been able to transform. It is interesting to note that a similar shift is obtained in Fig. 4.62 by applying a hydrostatic pressure of 1 kbar. This gives an impression of the strong influence a solid boundary can create.

The reason for this great deceleration of the transition is illustrated by the picture pointing to the blue curve in Fig. 4.63 (note that all elements are shown). At low temperatures, some of the elements transform similarly to the stress-coupled but not restricted case. However, these pioneer elements expand the whole mesh to some extent. This applies a significant pressure to the elements near the fixed boundary at the base plane and the upper surface. This compression results in a huge shift of the transition to higher temperature, hindering these elements to transform. Elements which do not directly border the solid walls suffer less by the evolving stresses. In fact, the stress partly relaxes in the middle of the mesh

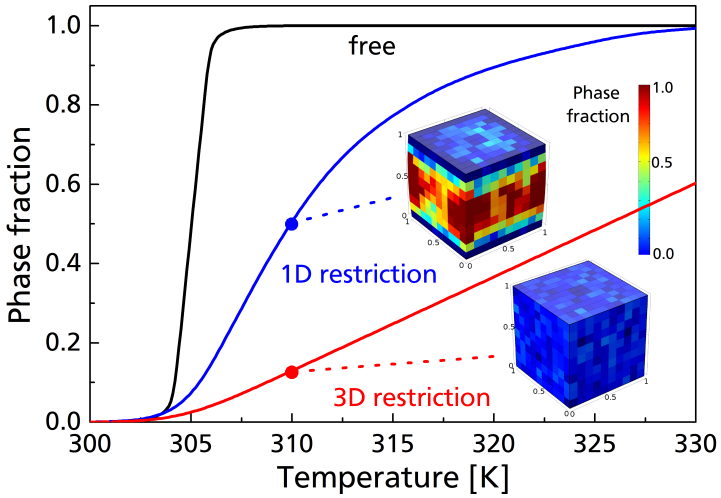

Figure 4.63: Comparison of the ensemble transition in the free case (black curve), under fixed constraint along the z-axis (blue curve) and under full restriction along all directions. The Gaussian distribution has a standard deviation of 2 K. The stress-coupling constant is $\frac{dT_t}{dp} = 50\,\mathrm{K\,GPa^{-1}}$ and the transition width of the individual element is 1 K.

because those elements can at least expand along the x-y plane. Especially elements near the edges can transform more easily, since they are less restricted by neighbors.

In order to completely transform the (simulated) material, the temperature must be increased up to 330 K. At this high temperature, the suppressing pressure and the resulting shift of the transition can be compensated and most of the material transforms, though the fixed boundary is still there. It can be seen that the temperature dependence of the phase fraction of the high temperature phase is very asymmetric. This effect is only due to the volume expansion of the material itself. By clamping the magnetocaloric material between solid boundaries, the transformation can be broadened many times over without applying pressure actively.

This situation is even more pronounced when a constraint along all three space directions is realized. This means that the material cannot expand at all. Consequently, the transition is restricted much more in contrast to the one-dimensional constraint. The red curve in Fig. 4.63 shows how the ensemble reacts to this special condition. It can be seen that the transformation is extremely hindered. Even at 330 K, only 60 % of the material could transform so far. Looking at the image taken at 310 K, one can see that the transition character is completely different. The ensemble transition is rather homogeneous in comparison to the free case shown in Fig. 4.58. This means that the coupling of the elements is even more pronounced under fixed boundary conditions.

An interesting implication evolves from this study. When the material is fixed along one direction in the low temperature phase, large stresses will be created under heating the ensemble for instance up to 310 K. Consequently, only 50 % of the elements have transformed at this temperature. If the fixed constraint was released suddenly, the material would transform momentarily into the high temperature phase. By this, a phase fraction change of 50 % could be achieved in a very sharp transformation and

a large caloric effect would be the consequence. This stress-release caloric effect is originated in the volume change during the first-order transition. The fixed boundary only provides the condition for the self pressurization of the material. This effect is even larger when a restriction along all three directions is applied. In the current example, heating the material to 310 K and subsequently releasing the constraint would lead to a transformation of more than 85 % of the elements.

So far, only the temperature-driven transition was considered in order to bring the material in a critical state in the way that a complete conversion is enabled during stress-release. However, for magnetocaloric materials this critical state can also be set by a magnetic field or by changing both magnetic field and temperature. In terms of application, a restriction along three dimensions is rather complicated. In fact, a fixed boundary only along one direction is sufficient to obtain significant phase-change rates during stress-release, depending on the specific properties of the material.

This study underlines the fundamental role of mechanical stresses for a first-order magnetostructural transformation. This correlation can be utilized for instance in order to achieve a stress-release caloric effect, as mentioned above. In contrast, the relation between the transition properties and stress can also be obstructive. Embedding a magnetocaloric material in a polymer matrix is an accepted preparation technique in order to produce heat exchangers in certain geometries like plates [16]. However, using a polymer with a rather high stiffness will affect the transition of the individual particles in an unwanted way due to the restriction of the volume change during the transition [160]. On the other hand, a not fully densely compacted magnetocaloric powder with or without binder additions contains pores, which could damp the volume expansion to some extent. Therefore, the stress-coupling mechanism cannot sharpen the transition efficiently.

4.5.4 Modeling an anisotropic expansion transformation

In the following, the manifestation of the stress-release caloric effect will be discussed by means of a real material. The so-called virgin effect was already discussed in terms of the single particle magnetic measurements of the Fe_2P-type material $Mn_{1.2}Fe_{0.68}P_{0.5}Si_{0.66}$. With the help of simulations, it will be pointed out that this first cycle behavior is due to the release of stress. This is realized in the material by the formation of cracks. In the finite element simulation, an artificial material with a cubic-cubic transition with a volume expansion of 1 % has been considered so far. This is a suitable model for instance for La-Fe-Si, leading to a sharpening of the transition due to the stress-coupling mechanism. However, for Fe_2P-type materials, this is not a useful description. In this material family, an isostructural hexagonal-hexagonal transformation is observed. The change in the lattice parameters is highly anisotropic since the crystal is shrinking along the c-direction but expanding along the a-axis. This change of the lattice parameters does not necessarily lead to a net volume change. It can be compensated, as for instance reported by Guillou et al. [161]. It is worth noting that even in the case of $\frac{\Delta V}{V} = 0$, large stresses evolve during the transformation, which will be further investigated.

In order to model such an anisotropic behavior, the individual mesh elements are assumed to be a cubic cutout of the hexagonal cell. The high temperature phase is considered as the stress-free state.

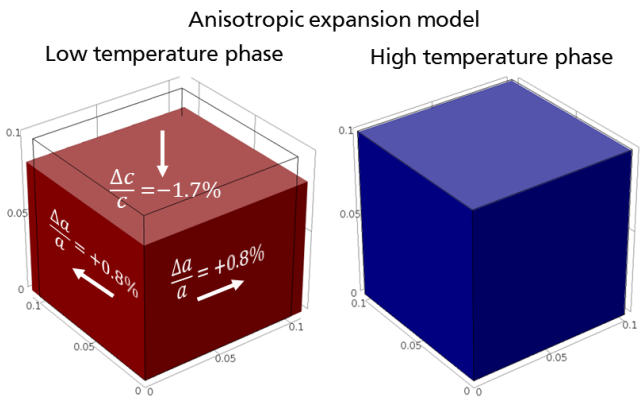

Figure 4.64: Schematic of the anisotropic volume change as in Fe_2P-type materials of a single mesh element. In the high temperature phase, the element is cubic, but in the low temperature phase it is tetragonally distorted.

Therefore, at high temperature the mesh consists of individual cubic blocks, as illustrated in Fig. 4.56(a). By cooling the material to the low temperature phase, the single blocks are distorted tetragonally. This behavior is schematically shown in Fig. 4.64. The specific values of the changing lattice parameters of $\left|\frac{\Delta c}{c}\right| = -1.7\,\%$ and $\left|\frac{\Delta a}{a}\right| = 0.8\,\%$ were selected according to literature [162, 163]. Even though the lattice changes drastically, the volume change is only about 0.1 %. In order to obtain reasonable results in the simulations, it has to be considered that the coupling constant is not equal along the different crystallographic directions. This idea is put across by imagining the application of pressure along the c-axis. Since the lattice is expanding in c-direction under heating, the low temperature phase should be stabilized, which shifts the transition upwards. On the contrary, applying pressure along the a-axis will lower the transition temperature. Therefore, each individual finite element needs to possess an orientation-dependent set of coupling constants $\frac{dT_t}{dp}$.

Unfortunately, a single-crystal calorimetric or magnetic study of Fe_2P under uniaxial pressure would be required in order to measure these parameters. However, no such work could be found in the literature. For this reason, similar values of the coupling constant $\frac{dT_t}{dp}$ of 50 K GPa^{-1} were assumed. The only difference is that $\frac{dT_t}{dp}$ is positive in c but negative in a-direction. In Fig. 4.65, the corresponding transformation behavior in the anisotropic case is shown. For the simulation, a standard deviation of the transition temperature σ of 2 K and a transition width of the individual element $\omega = 1$ K was used. The transformation of loose powder is shown in black. It should be pointed out that the high temperature phase was considered as the stress-free starting state. Therefore, all curves in Fig. 4.65 start at a phase fraction of 0 above 310 K. By cooling the material, the transformation into the low temperature phase takes place. For the loose powder case, this transition is completed within 10 K.

As a first stress-coupled example, a perfectly textured material will be considered. This means that the c-axis of all elements points along the z-direction. The corresponding transition is plotted as a red curve in Fig. 4.65. It can be seen that the transformation under cooling is rather sharp. In fact, the textured problem gives a similar result as the cubic-cubic transition shown in Fig. 4.58. Only the length changes of the elements are different in the other model. Therefore, the sharpening of the transition can again

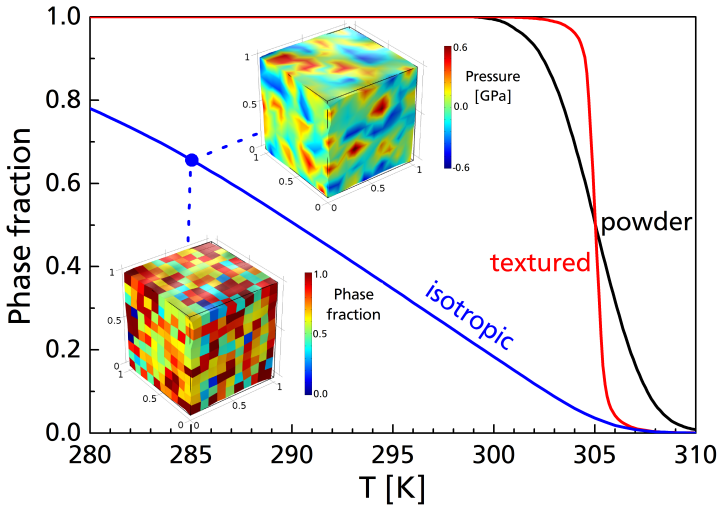

Figure 4.65: Phase fraction simulation as a function of temperature of an anisotropic material in powder (black), in textured (red) and in isotropic form (blue). The two images pointing to the blue curve illustrate the evolving stresses and the elemental phase fraction. The Gaussian distribution has a standard deviation of 2 K. The stress-coupling constant $\frac{dT_t}{dp}$ is $50\,\mathrm{K\,GPa^{-1}}$ along the crystallographic c- and $-50\,\mathrm{K\,GPa^{-1}}$ along the a-axis. The transition width of the individual element is 1 K.

be explained by the stress-coupling mechanism. There is no reason for any unexpected behavior because all elements push or pull in the same direction.

The situation changes drastically when considering an isotropic material. In order to simulate such a problem, the crystallographic directions of each mesh element were distributed randomly. For reasons of simplicity, only three cases were distinguished in the way that the c-axis points in the x-, y- or z-direction. As a consequence, the transition of the ensemble is extremely hindered by itself, as plotted in blue in Fig. 4.65. The two small images pointing at 285 K nicely illustrate the result of the anisotropic expansion. Neighboring elements which are aligned differently disturb each other massively. Therefore, the mesh is deformed quite impressively, which can be seen by the wavy surface. The evolving stresses are locally very different, as shown in the second image reaching values up to 0.6 GPa. This has a significant influence on the transformation of the ensemble. The system is also coupled by stress in the isotropic case but it cannot act in a beneficial way. Actually, the transformation behavior in the isotropic case looks comparable to the situation under external restrictions by solid boundaries (see Fig. 4.63).

For the anisotropic expansion, the local stress field is so large that a real material cannot bear them and forms cracks. This is currently not implemented in the simulation scheme but would in principle be possible. The simulation results suggest that the virgin effect in Fe_2P-type materials is due to crack formation in the vicinity of large stresses evolving during the anisotropic expansion in an untextured material. However, this process can be denoted as the previously introduced stress-release caloric effect. In Fig. 4.66, magnetization and direct measurements of ΔT_{ad} in the first (red) and in the second cycle (blue) are shown. This data was provided by Maximilian Fries within the framework of a doctoral thesis at TU Darmstadt. The magnetic behavior of this sample is comparable to the one of the bulk sample

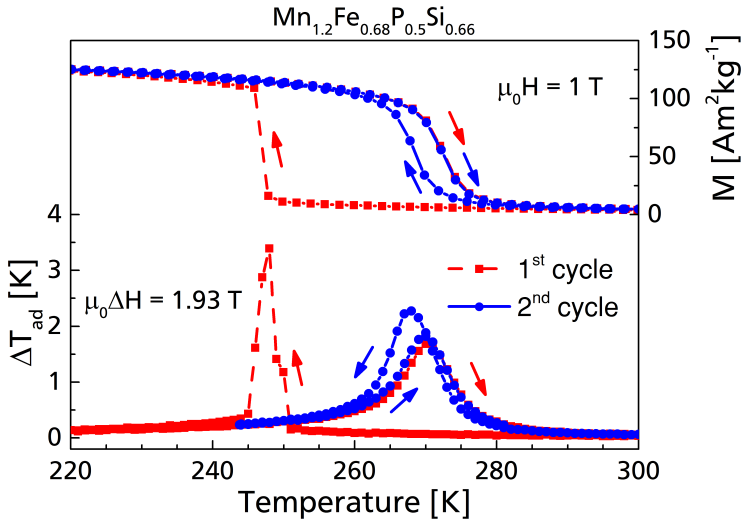

Figure 4.66: Magnetization and ΔT_{ad} of $Mn_{1.2}Fe_{0.68}P_{0.5}Si_{0.66}$ as a function of temperature in the first (red) and in the second (blue) cooling and heating cycle. This data was provided by Maximilian Fries within the framework of a doctoral thesis at TU Darmstadt.

and bigger particles shown in Fig. 4.54. Between 245 and 250 K a sharp jump in the magnetization can be seen in the first cooling of the fresh material. In the same temperature range, a large adiabatic temperature change of up to 3.5 K is visible. It should be mentioned that two different pieces of the sample were measured to be able to observe the virgin effect in both experiments. In the following heating and cooling cycles, the shape of the transformation does not change anymore and it is worth noting that the ΔT_{ad} is much smaller in operation. In the first cycle, the stresses can be released by the formation of cracks, which takes place severely in a rather short time. Consequently, a large volume fraction of the material transforms in this process, leading to a significant adiabatic temperature change.

The virgin effect in the material $Mn_{1.2}Fe_{0.68}P_{0.5}Si_{0.66}$ is a nice example for the stress-release caloric effect, which is originated in the coupling of neighboring grains through the stresses evolving during the first-order transition. The finite-element-based simulation scheme turned out to be a useful tool in order to deepen the understanding of the interplay between connected fragments of a magnetocaloric material. For cubic-cubic transformations the sharpening of the transition could clearly be demonstrated, which explains the observations obtained in the measurements of single particles in comparison to the bulk material. Also the more complicated transition in Fe_2P-type materials could partly be reproduced. However, the martensitic transformation in Heusler alloys cannot be modeled in a satisfying way. The big problem is the symmetry breaking during the transformation [89]. The lattice mismatch in the tetragonally distorted martensite is compensated by the formation of twin boundaries. For energetic reasons, different variants of martensite evolve during the transition. However, their orientation strongly depends on the local stresses. For these reasons, the finite element model cannot be applied to the martensitic transition in Heusler alloys because it is far too complicated. It should also be mentioned that thermal hysteresis has not been implemented so far. This is an important future goal in order to understand the effects related to hysteresis.

4.6 Search for new materials

In this thesis, the outstanding magnetocaloric properties of the two Heusler systems Ni-Mn-In and Ni-Mn-In-Co could be demonstrated in different prospects. However, there is one important aspect which makes these materials less attractive for the application of magnetic refrigeration. According to [164], Co and In are among the most critical elements of the periodic table. Therefore, the complete substitution or at least the reduction of those critical elements is a desirable objective. There are different main group elements which can be used instead of In. The most intensively studied magnetocaloric Heusler system is Ni-Mn-Ga [38]. However, also Ga is a critical element and is therefore unfavorable in terms of resource efficiency and sustainability. Another potential candidate is the Ni-Mn-Al system [87]. Unfortunately, the obtainable magnetocaloric effects are rather small [165]. Similar to the In-based material family shown above, the partial substitution of Ni by Co can enhance the magnetocaloric properties significantly [166]. In this way, at least the critical In can be substituted completely.

Also the main group element Sn is suitable for replacing In [167, 168]. The magnetic behavior of four different compounds of Ni-Mn-Sn are shown in Fig. 4.67(a), measured in a magnetic field of 1 T. The magnetization curves of this set of alloys look different in comparison to Ni-Mn-In shown in Fig. 4.3. It turns out that the low temperature martensite phase has both, a higher saturation magnetization and a higher Curie temperature T_C^M. For this reason, but also because of the smaller saturation magnetization of the austenite phase, the magnetization change between martensite and austenite is only modest over the whole temperature range. However, the transformation in the Ni-Mn-Sn samples is much sharper in comparison to the Ni-Mn-In system. The thermal hysteresis accounts for about 12 K. It seems that the compensation temperature T_{comp} is lower in this system because a transformation is visible at about 150 K. There is one problem which arises from the small magnetization change during the transition. The shift of the transition temperature in magnetic fields is rather small and for this reason also the magnetocaloric effect is not that large [111, 107].

The partial substitution of Ni by Co increases the Curie temperature of the austenite T_C^A, but decreases T_C^M as shown in Fig. 4.67(b). Consequently, the higher magnetization change also results in a better magnetocaloric performance of the material. As a side effect, the thermal hysteresis can be decreased down to less than 10 K. Still, the magnetocaloric properties are not comparable to the In-based system. The amount of Co can in principle be increased up to 10 at % [168]. By further decreasing the Sn content, the magnetostructural transition can be shifted to temperatures above 400 K and still a significant magnetization change is obtainable [168]. This could make Ni-Mn-Sn-Co an interesting material for the application of thermomagnetic power generation from waste heat [169, 170, 171]. This technology requires materials with a large and sharp change in magnetization, small thermal hysteresis and tunable transition temperature. The Ni-Mn-Sn-Co family provides these requirements and therefore appears to be very interesting for this kind of application [170]. However, one challenge is to reduce the demand for the critical element Co as much as possible.

Besides the well-known Ni-Mn-based systems, the search for new Heusler materials for magnetic refrigeration is interesting, keeping in mind the large variety of element combinations which are in principle

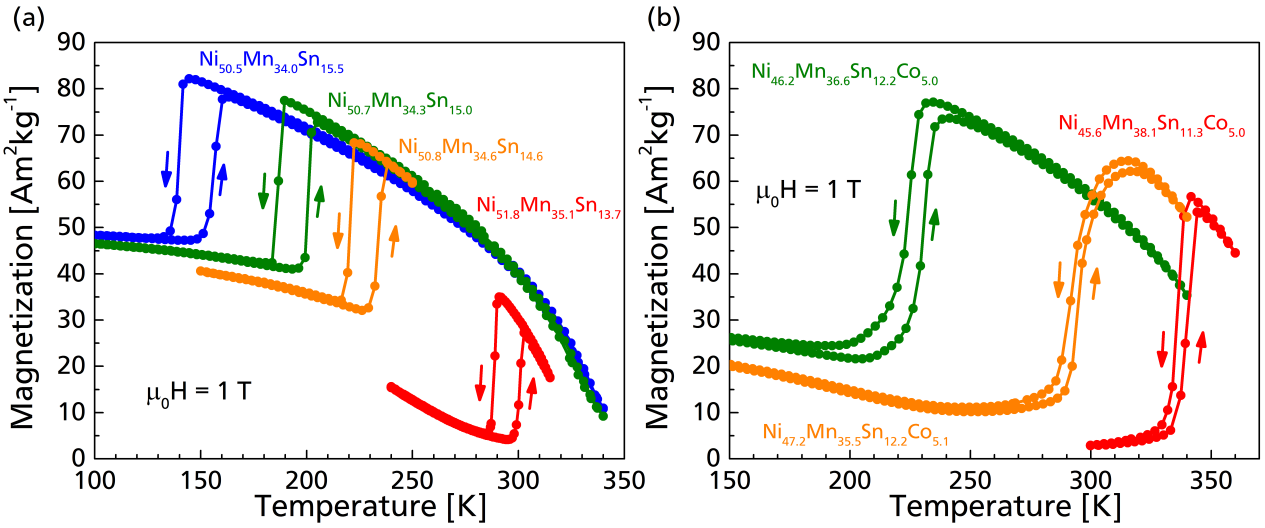

Figure 4.67: Temperature dependence of magnetization in a magnetic field of 1 T of Ni-Mn-Sn (a) and Ni-Mn-Sn-Co (b).

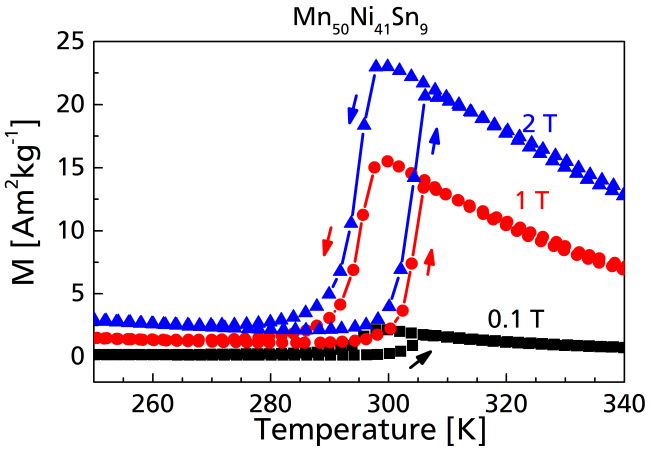

Figure 4.68: Temperature dependence of magnetization in 0.1, 1 and 2 T of the material $Mn_{50}Ni_{41}Sn_9$.

possible [71]. For stoichiometric compositions X_2YZ, magnetic and other functional properties are reported in literature frequently [73, 172]. The challenge is to identify potential material families with a magnetostructural transition. For instance, the composition Ni_2MnGa (or $Ni_{50}Mn_{25}Ga_{25}$) undergoes a martensitic transition near room temperature [173]. On the contrary, the stoichiometric $Ni_{50}Mn_{25}In_{25}$ shows no transition. One needs to vary the composition in order to obtain a magnetostructural transformation.

Another example is the recently reported Mn-rich Heusler family Mn-Ni-Sn [174]. A list of the prepared samples can be found in the appendix. In this system, the Sn content must be reduced to about 10 at % to the composition $Mn_{50}Ni_{40}Sn_{10}$ in order to achieve a first-order transition near room temperature. The magnetic behavior of this material is plotted in Fig. 4.68. It can be seen that the properties of the transition are promising. The transformation is rather sharp and the thermal hysteresis is below 10 K. However, the magnetization change and the shift of the transition temperature in magnetic fields are not large enough in order to provide high magnetocaloric effects. Also, the partial substitution of Co

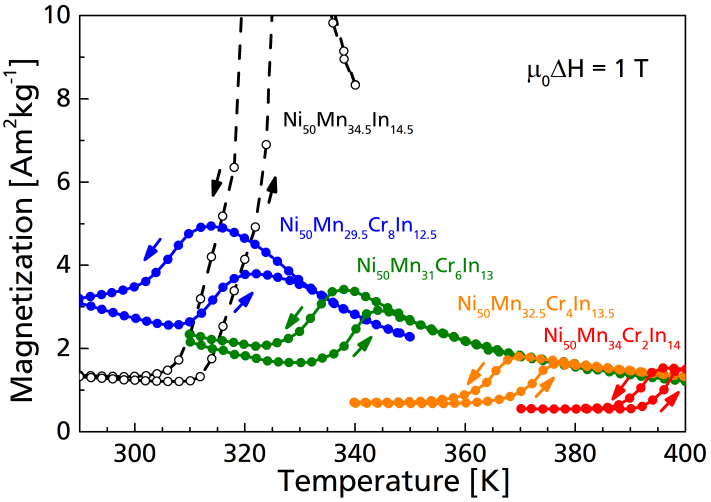

Figure 4.69: Magnetization as a function of temperature of Cr-substituted Ni-Mn-In measured in a magnetic field of 1 T.

affects the Curie temperature of the high temperature phase, as was demonstrated for Ni-Mn-In-Co and Ni-Mn-Sn-Co [175]. It is worth noting that a Ni-Mn-Sn sample with a Sn content of about 14 at % shows a martensitic transition near room temperature (see Fig. 4.67(a)), but only 9 at % are needed in Mn-Ni-Sn to reach a comparable transition temperature. This is also a possible way to reduce the amount of critical In in Ni-Mn-In by changing the composition to Mn-Ni-In [176, 177].

A substitutional sequence starting from a known material is a useful approach in order to find new Heusler materials with a martensitic transformation near room temperature [125]. As an example for this approach, the substitution of Mn by Cr will be discussed. Recently, it was reported that Cr in the Heusler structure enhances the magnetic and the magnetocaloric properties [178, 179]. For this reason, a series of samples with a Cr concentration from 0 to 10 at % was produced. According to the results from Khan et al. [180], showing a significant reduction of the transition temperature due to the substitution of Cr in the comparable system Ni-Mn-Sb, the amount of In was reduced in parallel in order to keep the transition in the desired temperature window.

Figure 4.69 shows the magnetization curves of the different Cr-substituted compounds. It is apparent that the martensitic transition temperature decreases with increasing Cr content even though the In concentration was adjusted in order to prevent this effect. The reference material is plotted in black in Fig. 4.68. In comparison to the reference, the Cr-substituted alloys have a significantly lower magnetization. Furthermore, an unexpected behavior can be observed when comparing $Ni_{50}Mn_{35.5}In_{14.5}$ and $Ni_{50}Mn_{36}In_{14}Cr_2$. By adding 2 at % of Cr, the transition temperature increases by about 80 K. For higher Cr contents, the transition temperature decreases again. Naively one would expect a continuous change of the transition temperature with advancing substitution, which is however not the case.

Images of the microstructure reveal the origin for the discontinuous change of the transition temperature by Cr substitution. Based on light microscopy, the material $Ni_{50}Mn_{36}In_{14}Cr_2$ is single-phase. However, for Cr concentrations of more than 2 at %, a large quantity of a secondary phase is visible even after

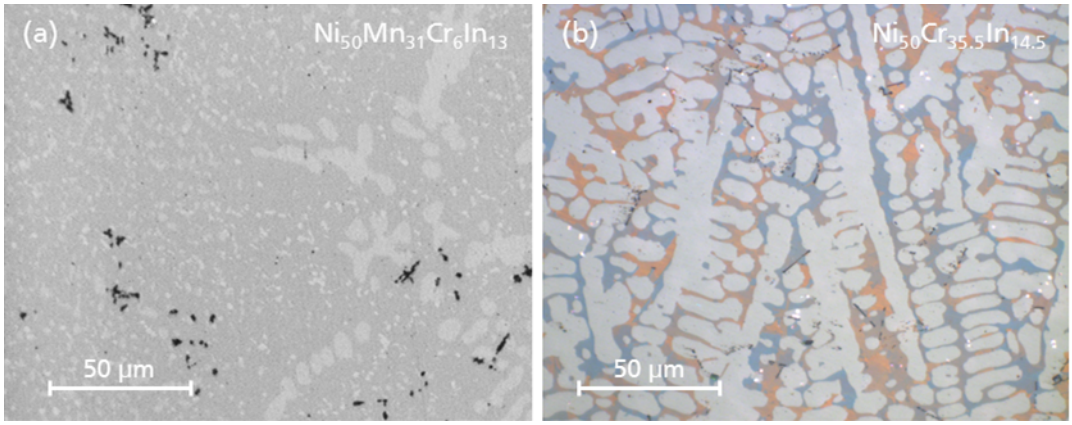

Figure 4.70: Light microscopy of $Ni_{50}Mn_{31}In_{13}Cr_6$ (a) and $Ni_{50}Cr_{35.5}In_{14.5}$ (b)

heat treatment, as shown in Fig. 4.70(a). This suggests that the observed effects are not due to the incorporation of Cr into the Heusler structure as stated in literature [179]. In fact, secondary phases are formed which slightly change the composition of the matrix Heusler phase. As was already mentioned above, only very small changes of the composition can affect the transition temperature significantly. Only up to a Cr concentration of 2 % it can be assumed that Cr could really be incooperated in the Heusler structure. The strong increase of the transition temperature as well as the decrease of the austenitic Curie temperature by substituting only 2 at % can indeed be the nature of Cr.

It is obvious that the existence of larger amounts of secondary phases are not affordable in order to achieve large magnetocaloric effects and a high performance. In fact, the secondary phase acts as a heat load, which reduces the adiabatic temperature change. Furthermore, the mechanical properties of a two-phase material will be different and stresses within the material could influence the transformation. In principle, inclusions could also favor the martensitic transition and reduce the hysteresis, as was demonstrated for an elastocaloric Ni-Ti-based alloy [181]. However, the magnetocaloric properties of the Cr-substituted Heusler alloy could not be enhanced. In addition, a sample with the composition $Ni_{50}Cr_{35.5}In_{14.5}$ was produced. The fine microstructure of this material is shown in Fig. 4.67. This light microscopy image shows that the Heusler phase is not stable, which is completely different in comparison to Ni-Mn-based families, which are single phase in a large composition range.

The precepitation of secondary phases was also observed in many Fe-based Heusler alloys. The partial substitution of Mn by Fe in Ni-Mn-In resulted in Fe-rich inclusions already for very low Fe contents. Also for Fe-Mn-Ga, a phase-pure material could not be synthesized. On the other hand, a martenstic transition could be achieved in the material $Ni_{52}Fe_{20}Ga_{23}Al_3Co_2$ even though the sample was not phase-pure. In principle, the complete substitution of Mn by Fe is advantageous because of the higher magnetic moment of the Fe atom. It is also worth noting that evaporation losses during production and heat treatment are no issue in Fe-based Heusler alloys, which is in great contrast to Mn-based systems. Although the loss of Mn can be controlled, a certain degree of chemical inhomogeneities cannot be avoided due to the evaporation of Mn at the surface.

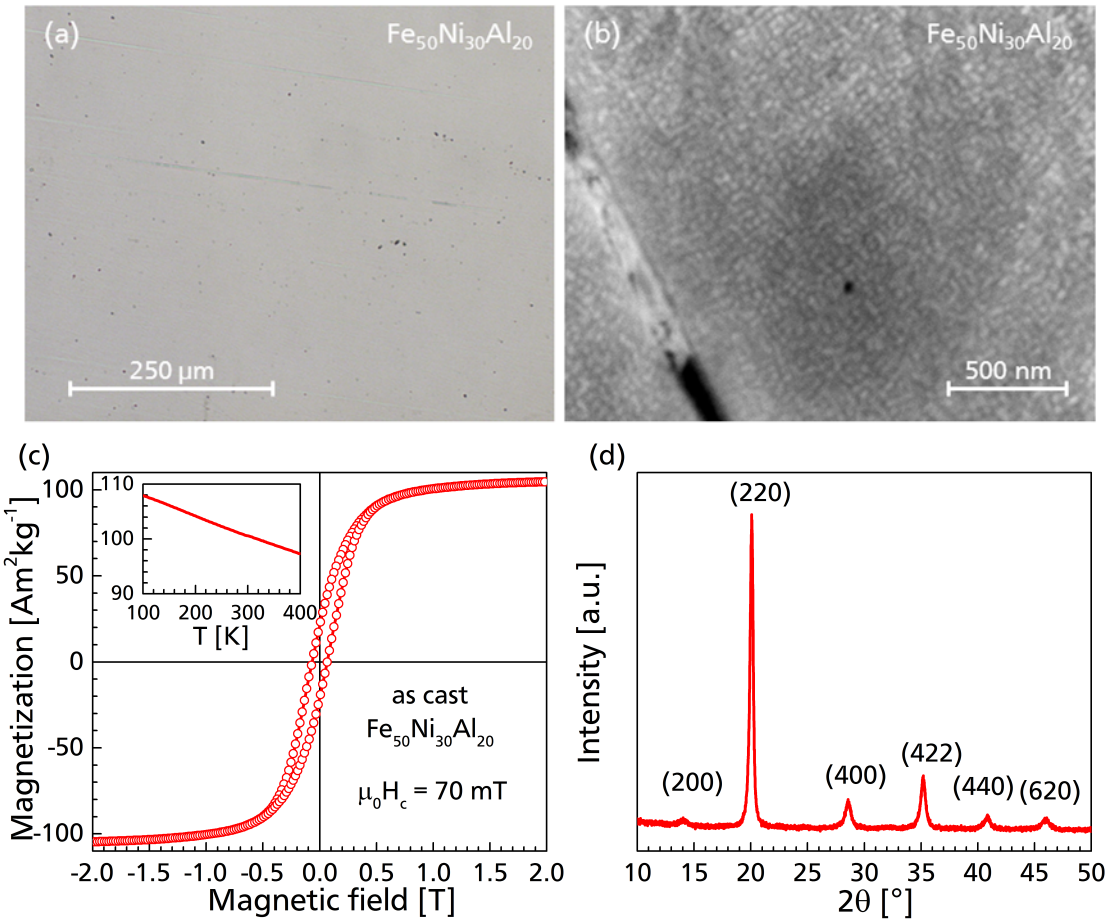

Figure 4.71: Light (a) and electron microscopy with BSE contrast (b) of as-cast $Fe_{50}Ni_{30}Al_{20}$. The SEM image was taken by Konrad Löwe (TU Darmstadt). (c) Magnetization as a function of magnetic field. The inset shows the magnetization as a function of temperature. (d) Podwer diffraction pattern of $Fe_{50}Ni_{30}Al_{20}$.

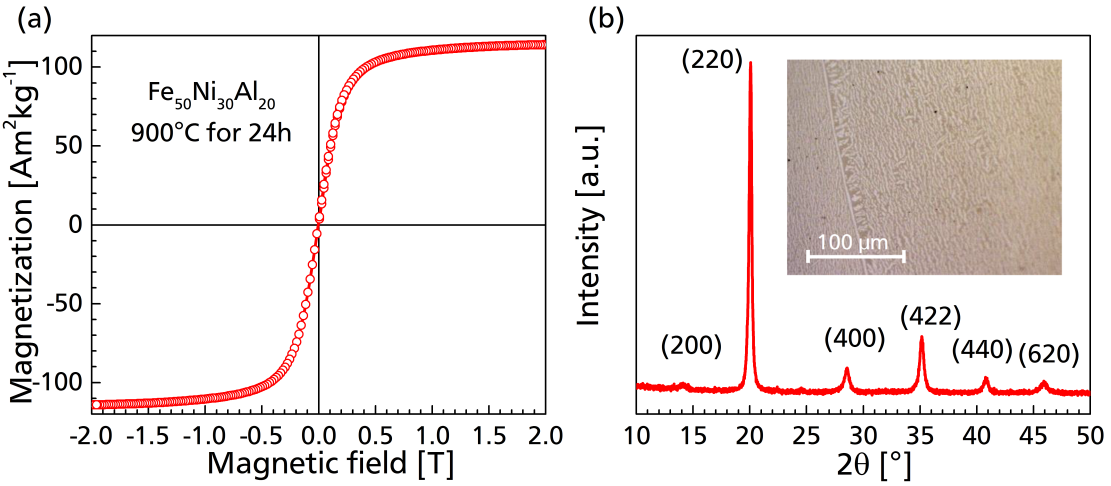

Figure 4.72: Magnetization measurements (a) and powder diffraction of as-annealed $Fe_{50}Ni_{30}Al_{20}$ (b). The inset in (b) shows a light-microscopy image.

The Fe-rich material $Fe_{50}Ni_{30}Al_{20}$ could be produced as single phase already in the as-cast state based on light microscopy, as can be seen in Fig. 4.71(a). Interestingly, the material shows a small coercivity of 70 mT, as illustrated by the $M(H)$ loop in Fig. 4.71(c), even though no martensitic transition can be identified, as shown in the inset of Fig. 4.71(b). The small coercive field is quite surprising for a cubic material, which is evident from the X-ray pattern. The origin for the obtained coercivity can only be revealed by high resolution electron microscopy, which is shown in Fig. 4.71(b). In this picture, fine structures are visible on the nanoscale. It is probable that the coercivity is related to the shape anisotropy of small grains like in Alnico magnets [53]. After a heat treatment at 900 °C for 24 h, followed by water quenching, the coercivity disappears, as shown in Fig. 4.72(a). The phase decomposition in the annealed sample can be seen even using light microscopy (inset in Fig. 4.72(b)). The reduction of the coercivity could be attributed to the much coarser structure in comparison to the as-cast material. However, the XRD pattern in Fig. 4.72(b) shows no peaks which could be related to a secondary phase and furthermore in, there is no difference compared to Fig. 4.71(d). It is probable that the two phases present in the material are both cubic and have similar lattice parameters. In fact, the compound $Fe_{50}Ni_{25}Al_{25}$ is described as a Heusler material in literature [182, 183, 184] but this is questionable in view of the measurement results.

In conclusion, a number of different, potentially interesting Heusler alloys have been produced and characterized, but no material with comparable magnetocaloric properties like in Ni-Mn-In could be identified yet. The chemical stability of the Heusler phase can be a critical issue when partially or completely substituting an element from the reference material Ni-Mn-In. However, the search for new Heusler compounds is a field of great potential, which deserves an intensive research in order to reduce the amount of critical elements in the material.

5 Conclusion and outlook

In this work, the martensitic transition of Ni-Mn-based Heusler compounds was investigated with regard to the magnetocaloric properties. Among the large variety of Heusler alloys, especially the materials Ni-Mn-In and Ni-Mn-In-Co show outstanding magnetocaloric effects as could be shown in Ref. [19]. Building on this work, it was demonstrated that the transition can be tuned precisely to the desired temperature window by changing the chemical composition of the alloy. During the phase transformation between martensite and austenite, which was induced by a magnetic field change of about 2 T, large isothermal entropy changes and adiabatic temperature changes up to $22\,\mathrm{J\,kg^{-1}\,K^{-1}}$ and −8 K could be achieved. There are manifold reasons for this. The large difference in the magnetization of martensite and austenite is one cause, which is related to the strong sensitivity of the transition temperature to an external magnetic field. Even though the high magnetization change is required in order to obtain a significant magnetocaloric effect in small magnetic fields, it could be pointed out that it is parasitic at the same time. In fact, the entropy contributions of the structural transition and of the magnetic system counteract. This can even go so far that both contributions cancel each other out. The contradicting role of the magnetization change was denoted as the dilemma of inverse magnetocaloric materials, Gottschall et al. [132].

Based on a phenomenological model, the sum of the two contributions could be calculated for both material families Ni-Mn-In and Ni-Mn-In-Co. It resulted in a reduction of the entropy change of the complete transition when decreasing the transformation temperature either by applying a magnetic field or by changing the chemical composition. Also the increasing thermal hysteresis and transition width at lower temperatures could be traced back to the dilemma. In accordance with this, the application of hydrostatic pressure leads to exactly the opposite effect, making the transformation sharper and reducing the thermal hysteresis due to the shift of the transition to higher temperatures.

The size of the thermal hysteresis decisively determines the cyclability of the magnetocaloric material in a magnetic field. Even though the hysteresis in the compounds under investigation is significant, large reversible adiabatic temperature changes of 3 K in 2 T were measured. The origin for this lies in the special transformation characteristics in minor loops of hysteresis in which only a certain percentage of the material transforms instead of turning it completely from one phase to the other. It was found by in-situ optical microscopy that the nucleation process is partly avoided and the phase boundary movement is enhanced, which efficiently reduces the thermal hysteresis, Gottschall et al. [41].

A comprehensive study of the $S(T)$ diagram and the adiabatic temperature change revealed that both methods do not necessarily coincide. This was, for instance, observed for a compound with a transition at low temperatures. A slightly higher heating rate prior to the ΔT_{ad} measurement resulted in an adiabatic temperature change which strongly exceeded the predictions of the $S(T)$ diagram because the equilibrium state was not reached yet. Especially for minor hysteresis loops, the $S(T)$ diagram

failed to predict the large reversible magnetocaloric effects under cycling. However, by combining the temperature-dependent total entropy from quasistatic calorimetry and direct measurements of the adiabatic temperature change under cycling, the reversibility area of the transformation was determined for a given magnetic field change, which also allowed the determination of the reversible isothermal entropy change, Gottschall et al. [143].

Based on the finding that the magnetocaloric properties strongly depend on the measurement conditions, the martensitic transition was studied under different magnetic-field-sweeping rates spanning over five orders of magnitude. From direct ΔT_{ad} measurements in three different facilities it could be concluded that the thermal hysteresis increases when the magnetic field changes too fast. In addition, it turned out that the nucleation process is much slower than the movement of the phase boundary between martensite and austenite. However, in terms of application, limitations due to the kinetics of the martensitic transition are only expected for operation frequencies of a machine beyond 100 Hz, Gottschall et al. [123].

The thermal hysteresis as well as the width of the transition are also influenced by the size of the material. Magnetic measurements of single particles of Ni-Mn-In-Co were performed, which suggested that the transition becomes more and more disabled when reducing the size of the fragment. This investigation was extended to a sample of La-Fe-Si and Mn-Fe-P-Si showing also size-dependent effects. All three materials had in common that the transition temperatures of the different particles were largely scattered. In order to explain the transformation character of single particles on the one hand and of the bulk material on the other hand, a finite element model was introduced. In the simulation scheme, the volume change during the magnetostructural transition was taken into consideration, which resulted in the evolution of high mechanical stresses. Since the transition temperature is sensitive to stress and pressure, an ensemble of connected elements showed a sharper transition in comparison to the average transformation of individual fragments. This effect was denoted as the stress-coupling mechanism.

Even though the Heusler compounds under investigation showed outstanding reversible magnetocaloric effects, the suitability of those materials for the application on a large scale is questionable. The problem is that these alloys contain considerable amounts of the critical elements In and Co. For this reason, alternative magnetocaloric Heusler compounds were studied. It was, for instance, shown that In can be replaced by Sn, but unfortunately, the shift of the transition temperature in magnetic fields is too small in order to enable large magnetocaloric effects. There are many possibilities to form a magnetic Heusler alloy. But this does not necessarily imply that they undergo a magnetostructural transformation near room temperature. Also, the formation of secondary phases can occur when substituting different elements, which sensitively influences the Heusler phase. So far, Ni-Mn-In-Co is still the best known magnetocaloric Heusler material. However, the screening by high-troughput methods in combination with phase stability calculations could be a promising approach in order to identify new potential Heusler materials in future, not only for magnetic refrigeration.

In this thesis, it was demonstrated how the martensitic transformation and the thermal hysteresis can be manipulated via the chemical composition, by a magnetic field, stress or pressure, by the time and length scale in order to improve the reversibility of the magnetocaloric effect but also to diminish it. However,

a distinct thermal hysteresis is not necessarily always disadvantageous. In fact, it can be utilized also for magnetic refrigeration. A fully reversible material heats and cools as the magnetic field is applied and removed. This implies that the magnetic field cannot be changed until the heat is expelled to the environment or taken from the cooling compartment. For this reason, the amount of permanent magnets which are needed in a magnetic refrigerator is significant.

This situation could be changed by using inverse magnetocaloric Heusler alloys with a tuned thermal hysteresis. It was shown in this work for different samples of Ni-Mn-In-Co that under certain conditions, a significant cooling effect can be obtained when increasing the magnetic field up to 2 T. But when decreasing the field again, the temperature of the sample does not change anymore due to the thermal hysteresis. This means that the magnetic field does not need to be retained in order to transfer the heat. For this reason, the amount of permanent magnets could be extremely reduced in a cyclic operating cooling device by utilizing the thermal hysteresis, because the magnetic field is only needed in a very small volume. However, in order to bring the material back to the initial state, an additional stimulus is required. The application of a small pressure would be sufficient to transform the magnetocaloric material back to its initial state and the cycle can start over again. This conceptual new cooling cycle illustrates how the thermal hysteresis in magnetocaloric materials can be utilized in order to reduce the necessary amount of permanent magnets, which could enhance the sustainability and reduce the costs of a magnetic refrigerator in future.

Bibliography

[1] L. Tolstoy, *Anna Karenina*, Original 1901 English Translation ed. (Mermaids Classics, 2013), p. 1, translated by Constance Garnett.

[2] J. Diamond, *Guns, Germs, and Steel: The Fates of Human Societies* (W. W. Norton & Company, 1997), chapter 9.

[3] D. Comtesse, M. E. Gruner, M. Ogura, V. V. Sokolovskiy, V. D. Buchelnikov, A. Grünebohm, R. Arróyave, N. Singh, T. Gottschall, O. Gutfleisch, V. A. Chernenko, F. Albertini, S. Fähler, and P. Entel, Phys. Rev. B **89**, 184403 (2014).

[4] O. Gutfleisch, M. A. Willard, E. Brück, C. H. Chen, S. G. Sankar, and J. P. Liu, Adv. Mater. **23**, 821 (2011).

[5] A. Kitanovski, U. Plaznik, U. Tomc, and A. Poredoš, Int. J. Refrig. **57**, 288 (2015).

[6] F. Scarpa, G. Tagliafico, and L. A. Tagliafico, Renew. and Sust. Energ. Rev. **50**, 497 (2015).

[7] J. M. Belman-Flores, J. M. Barroso-Maldonado, A. P. Rodríguez-Muñoz, and G. Camacho-Vázquez, Renew. and Sust. Energ. Rev. **51**, 955 (2015).

[8] R. Gauß, G. Homm, and O. Gutfleisch, in *Magnetic cooling: from fundamentals to high efficiency refrigeration*, edited by K. Sandeman and O. Gutfleisch (Wiley-VCH, 2016).

[9] A. Kitanovski and P. W. Egolf, Int. J. Refrig. **33**, 449 (2010).

[10] J. R. Gómez, R. F. Garcia, A. D. M. Catoira, and M. R. Gómez, Renew. and Sust. Energ. Rev. **17**, 74 (2013).

[11] K. P. Skokov, A. Y. Karpenkov, D. Y. Karpenkov, and O. Gutfleisch, J. Appl. Phys. **113**, 17A945 (2013).

[12] R. Bjørk, C. Bahl, and K. Nielsen, Int. J. Refrig. **63**, 48 (2016).

[13] B. Yu, M. Liu, P. W. Egolf, and A. Kitanovski, Int. J. Refrig. **33**, 1029 (2010).

[14] A. Smith, C. R. Bahl, R. Bjørk, K. Engelbrecht, K. K. Nielsen, and N. Pryds, Adv. Eng. Mater. **2**, 1288 (2012).

[15] K. P. Skokov, D. Y. Karpenkov, M. D. Kuz'min, I. A. Radulov, T. Gottschall, B. Kaeswurm, M. Fries, and O. Gutfleisch, J. Appl. Phys. **115**, 17A941 (2014).

[16] I. A. Radulov, K. P. Skokov, D. Y. Karpenkov, T. Gottschall, and O. Gutfleisch, J. Mag. Mag. Mater. **396**, 228 (2015).

[17] J. Lyubina, R. Schäfer, N. Martin, L. Schultz, and O. Gutfleisch, Adv. Mater. **22**, 3735 (2010).

[18] V. Franco, J. Blázquez, B. Ingale, and A. Conde, Annu. Rev. Mater. Sci. **42**, 305 (2012).

[19] J. Liu, T. Gottschall, K. P. Skokov, J. D. Moore, and O. Gutfleisch, Nat. Mater. **11**, 620 (2012).

[20] C. Zimm, A. Boeder, J. Chell, A. Sternberg, A. Fujita, S. Fujieda, and K. Fukamichi, Int. J. Refrig. **29**, 1302 (2006).

[21] M. Balli, O. Sari, C. Mahmed, C. Besson, P. Bonhote, D. Duc, and J. Forchelet, Appl. Energy **98**, 556 (2012).

[22] K. Engelbrecht, D. Eriksen, C. Bahl, R. Bjørk, J. Geyti, J. Lozano, K. Nielsen, F. Saxild, A. Smith, and N. Pryds, Int. J. Refrig. **35**, 1498 (2012).

[23] V. K. Pecharsky and K. A. Gschneidner, Appl. Phys. Lett. **70**, 3299 (1997).

[24] V. K. Pecharsky and K. A. Gschneidner, Phys. Rev. Lett. **78**, 4494 (1997).

[25] A. Kitanovski and P. W. Egolf, Int. J. Refrig. **29**, 3 (2006).

[26] J. Kynicky, M. Smith, and X. Cheng, Elements **8**, 361 (2012).

[27] A. Fujita, Y. Akamatsu, and K. Fukamichi, J. Appl. Phys. **85**, 4756 (1999).

[28] S. Fujieda, A. Fujita, and K. Fukamichi, Appl. Phys. Lett. **81**, 1276 (2002).

[29] O. Gutfleisch, A. Yan, and K.-H. Müller, J. Appl. Phys. **97**, 10M305 (2005).

[30] X. B. Liu and Z. Altounian, J. Mag. Mag. Mater. **264**, 209 (2003).

[31] M. Krautz, K. Skokov, T. Gottschall, C. S. Teixeira, A. Waske, J. Liu, L. Schultz, and O. Gutfleisch, J. Alloys Compd. **598**, 27 (2014).

[32] D. T. Cam Thanh, E. Brück, O. Tegus, J. C. P. Klaasse, T. J. Gortenmulder, and K. H. J. Buschow, J. Appl. Phys. **99**, 08Q107 (2006).

[33] O. Tegus, E. Brück, K. H. J. Buschow, and F. R. de Boer, Nature **415**, 150 (2002).

[34] E. Brück, J. Phys. D: Appl. Phys. **38**, R381 (2005).

[35] W. Dagula, O. Tegus, X. W. Li, L. Song, E. Brück, D. T. Cam Thanh, F. R. de Boer, and K. H. J. Buschow, J. Appl. Phys. **99**, 08Q105 (2006).

[36] A. Yan, K.-H. Müller, L. Schultz, and O. Gutfleisch, J. Appl. Phys. **99**, 08K903 (2006).

[37] H. Yibole, F. Guillou, L. Zhang, N. H. van Dijk, and E. Brück, J. Phys. D: Appl. Phys. **47**, 075002 (2014).

[38] F.-x. Hu, B.-g. Shen, and J.-r. Sun, Appl. Phys. Lett. **76**, 3460 (2000).

[39] Z. D. Han, D. H. Wang, C. L. Zhang, S. L. Tang, B. X. Gu, and Y. W. Du, Appl. Phys. Lett. **89**, 182507 (2006).

[40] X. Moya, L. Mañosa, A. Planes, T. Krenke, M. Acet, and E. F. Wassermann, Mater. Sci. Eng., A **438-440**, 911 (2006).

[41] T. Gottschall, K. P. Skokov, B. Frincu, and O. Gutfleisch, Appl. Phys. Lett. **106**, 021901 (2015).

[42] M. Langevin, Ann. Chim. Phys. **5**, 70 (1905).

[43] A. Smith, Eur. Phys. J. H **38**, 507 (2013).

[44] A. Weiss, Pierre; Piccard, J. Phys. (Paris) **5**, 103 (1917).

[45] P. Debye, Ann. Phys. **386**, 1154 (1926).

[46] W. F. Giauque, J. Am. Chem. Soc. **49**, 1864 (1927).

[47] W. F. Giauque and D. P. MacDougall, Phys. Rev. **43**, 768 (1933).

[48] Nobelprize.org, The Nobel Prize in Chemistry 1949, 29 Mar 2016.

[49] G. V. Brown, Journal of Applied Physics **47**, 3673 (1976).

[50] J. Barclay and W. Steyert, Active magnetic regenerator, 1982, US Patent 4,332,135.

[51] S. Y. Dan'kov, A. M. Tishin, V. K. Pecharsky, and K. A. Gschneidner, Phys. Rev. B **57**, 3478 (1998).

[52] M. D. Kuz'min, Phys. Rev. B **77**, 184431 (2008).

[53] J. M. D. Coey, *Magnetism and Magnetic Materials* (Cambridge University Press, 2010).

[54] A. Tishin and Y. Spichkin, *The Magnetocaloric Effect and Its Applications* (Institute of Physics, 2003), pp. 69 – 95.

[55] H. E. Karaca, I. Karaman, B. Basaran, Y. Ren, Y. I. Chumlyakov, and H. J. Maier, Adv. Funct. Mater. **19**, 983 (2009).

[56] K. G. Sandeman, Scripta Mater. **67**, 566 (2012).

[57] L. Caron, Z. Q. Ou, T. T. Nguyen, D. T. C. Thanh, O. Tegus, and E. Brück, J. Mag. Mag. Mater. **321**, 3559 (2009).

[58] A. Giguère, M. Foldeaki, B. Ravi Gopal, R. Chahine, T. K. Bose, A. Frydman, and J. A. Barclay, Phys. Rev. Lett. **83**, 2262 (1999).

[59] Y. Sutou, Y. Imano, N. Koeda, T. Omori, R. Kainuma, K. Ishida, and K. Oikawa, Appl. Phys. Lett. **85**, 4358 (2004).

[60] S. Nikitin, G. Myalikgulyev, A. Tishin, M. Annaorazov, K. Asatryan, and A. Tyurin, Phys. Lett. A **148**, 363 (1990).

[61] K. P. Skokov, V. V. Khovaylo, K.-H. Müller, J. D. Moore, J. Liu, and O. Gutfleisch, J. Appl. Phys. **111**, 07A910 (2012).

[62] V. K. Pecharsky and K. A. Gschneidner, Material Matters **2**, 4 (2007).

[63] V. Franco and A. Conde, Int. J. Refrig. **33**, 465 (2010).

[64] A. Kitanovski, J. Tušek, U. Tomc, U. Plaznik, M. Ozbolt, and A. Poredoš, *Magnetocaloric Energy Conversion: From Theory to Applications*, *Green Energy and Technology* (Springer International Publishing, 2014).

[65] S. Taskaev, K. Skokov, D. Karpenkov, V. Khovaylo, V. Buchelnikov, D. Zherebtsov, M. Ulyanov, D. Bataev, M. Drobosyuk, and A. Pellenen, Acta Phys. Pol. A **127**, 641 (2015).

[66] E. Commission, Report on Critical Raw Materials for the EU - Critical Raw Materials Profiles, 2014.

[67] K. Mandal, O. Gutfleisch, A. Yan, A. Handstein, and K.-H. Müller, J. Magn. Magn. Mater. **290-291**, 673 (2005).

[68] M. Krautz, J. D. Moore, K. P. Skokov, J. Liu, C. S. Teixeira, R. Schäfer, L. Schultz, and O. Gutfleisch, J. Appl. Phys. **112**, 083918 (2012).

[69] M. Krautz, Ph.D. thesis, TU Dresden, 2015.

[70] F. Heusler, Verh. Dtsch. Phys. Ges. **5**, 219 (1903).

[71] T. Graf, C. Felser, and S. S. Parkin, Prog. Solid State Chem. **39**, 1 (2011).

[72] F. Liu, Q. Wang, W. Ao, Y. Yu, L. Pan, and J. Li, J. Magn. Magn. Mater. **324**, 514 (2012).

[73] P. J. Webster, Contemp. Phys. **10**, 559 (1969).

[74] T. Krenke, Ph.D. thesis, Universität Duisburg-Essen, Fachbereich Physik, 2007.

[75] T. Miyamoto, W. Ito, R. Y. Umetsu, T. Kanomata, K. Ishida, and R. Kainuma, Materials Transactions **52**, 1836 (2011).

[76] W. Ito, M. Nagasako, R. Y. Umetsu, R. Kainuma, T. Kanomata, and K. Ishida, Appl. Phys. Lett. **93**, 232503 (2008).

[77] J. C. Slater, Phys. Rev. **35**, 509 (1930).

[78] G. Felcher, J. Cable, and M. Wilkinson, J. Phys. Chem. Solids **24**, 1663 (1963).

[79] P. J. Webster and R. S. Tebble, Philos. Mag. **16**, 347 (1967).

[80] M. Venkatesan, in *Handbook of magnetism and advanced magnetic materials*, edited by H. Kronmüller and S. S. P. Parkin (John Wiley and Sons, 2007), Vol. 3, Half-metals.

[81] T. Graf, J. Winterlik, L. Müchler, G. H. Fecher, C. Felser, and S. S. Parkin, in *Handbook of Magnetic Materials*, Vol. 21 of *Handbook of Magnetic Materials*, edited by K. Buschow (Elsevier, 2013), pp. 1 – 75.

[82] W. E. Pickett and J. S. Moodera, Phys. Today **54**, 39 (2001).

[83] G. A. Prinz, Science **282**, 1660 (1998).

[84] T. Hesjedal and K. H. Ploog, in *Handbook of magnetism and advanced magnetic materials*, edited by H. Kronmüller and S. S. P. Parkin (John Wiley and Sons, 2007), Vol. 3, Epitaxial Heusler Alloys on III-V Semiconductors.

[85] B. Dieny, V. S. Speriosu, S. S. P. Parkin, B. A. Gurney, D. R. Wilhoit, and D. Mauri, Phys. Rev. B **43**, 1297 (1991).

[86] I. Dubenko, M. Khan, A. K. Pathak, B. R. Gautam, S. Stadler, and N. Ali, J. Magn. Magn. Mater. **321**, 754 (2009).

[87] R. Kainuma, W. Ito, R. Y. Umetsu, K. Oikawa, and K. Ishida, Appl. Phys. Lett. **93**, 091906 (2008).

[88] T. Krenke, M. Acet, E. F. Wassermann, X. Moya, L. Mañosa, and A. Planes, Phys. Rev. B **72**, 014412 (2005).

[89] S. Fähler, U. K. Rößler, O. Kastner, J. Eckert, G. Eggeler, H. Emmerich, P. Entel, S. Müller, E. Quandt, and K. Albe, Adv. Eng. Mater. **14**, 10 (2012).

[90] A. Diestel, R. Niemann, B. Schleicher, S. Schwabe, L. Schultz, and S. Fähler, J. Appl. Phys. **118**, 023908 (2015).

[91] T. Gottschall, Master's thesis, TU Dresden, Fachbereich Physik, 2012.

[92] R. Niemann, Ph.D. thesis, TU Dresden, Fachbereich Physik, 2015.

[93] A. Sozinov, N. Lanska, A. Soroka, and W. Zou, Appl. Phys. Lett. **102**, 021902 (2013).

[94] A. L. Roytburd, Phase Transitions **45**, 1 (1993).

[95] D. A. Porter and K. E. Easterling, *Phase Transformations in Metals and Alloys, Second Edition* (CRC Press, 1992), pp. 382–416.

[96] R. Niemann, S. Hahn, A. Diestel, A. Backen, L. Schultz, K. Nielsch, M. F.-X. Wagner, and S. Fähler, APL Mater. **4**, 064101 (2016).

[97] L. Pareti, M. Solzi, F. Albertini, and A. Paoluzi, Eur. Phys. J. B **32**, 303 (2003).

[98] E. Hornbogen, Phys. Status Solidi B **172**, 161 (1992).

[99] J. M. Ball and R. D. James, in *Analysis and Continuum Mechanics: A Collection of Papers Dedicated to J. Serrin on His Sixtieth Birthday* (Springer Berlin Heidelberg, 1989), Chap. Fine Phase Mixtures as Minimizers of Energy, pp. 647–686.

[100] I. Takeuchi and K. Sandeman, Phys. Today **68**, 48 (2015).

[101] Y. Song, X. Chen, V. Dabade, T. W. Shield, and R. D. James, Nature **502**, 85 (2013).

[102] P. Entel, V. D. Buchelnikov, V. V. Khovailo, A. T. Zayak, W. A. Adeagbo, M. E. Gruner, H. C. Herper, and E. F. Wassermann, J. Phys. D: Appl. Phys. **39**, 865 (2006).

[103] J. Liu, S. Aksoy, N. Scheerbaum, M. Acet, and O. Gutfleisch, Appl. Phys. Lett. **95**, 232515 (2009).

[104] M. Acet and E. F. Wassermann, Adv. Eng. Mater. **14**, 523 (2012).

[105] B. Holz, L. Riccardi, H. Janocha, and D. Naso, Adv. Eng. Mater. **14**, 668 (2012).

[106] P. A. Bhobe, K. R. Priolkar, and A. K. Nigam, Appl. Phys. Lett. **91**, 242503 (2007).

[107] V. Basso, C. P. Sasso, K. P. Skokov, O. Gutfleisch, and V. V. Khovaylo, Phys. Rev. B **85**, 014430 (2012).

[108] V. Khovaylo, J. Alloys Compd. **577**, S362 (2012).

[109] E. Stern-Taulats, P. O. Castillo-Villa, L. Mañosa, C. Frontera, S. Pramanick, S. Majumdar, and A. Planes, J. Appl. Phys. **115**, 173907 (2014).

[110] X. Moya, L. Mañosa, A. Planes, S. Aksoy, M. Acet, E. F. Wassermann, and T. Krenke, Phys. Rev. B **75**, 184412 (2007).

[111] V. V. Khovaylo, K. P. Skokov, O. Gutfleisch, H. Miki, R. Kainuma, and T. Kanomata, Appl. Phys. Lett. **97**, 052503 (2010).

[112] A. P. Kazakov, V. N. Prudnikov, A. B. Granovsky, A. P. Zhukov, J. Gonzalez, I. Dubenko, A. K. Pathak, S. Stadler, and N. Ali, Appl. Phys. Lett. **98**, 131911 (2011).

[113] G. Porcari, S. Fabbrici, C. Pernechele, F. Albertini, M. Buzzi, A. Paoluzi, J. Kamarad, Z. Arnold, and M. Solzi, Phys. Rev. B **85**, 024414 (2012).

[114] F. Guillou, P. Courtois, L. Porcar, P. Plaindoux, D. Bourgault, and V. Hardy, J. Phys. D: Appl. Phys. **45**, 255001 (2012).

[115] L. Mañosa, D. González-Alonso, A. Planes, E. Bonnot, M. Barrio, J.-L. Tamarit, S. Aksoy, and M. Acet, Nat. Mater. **9**, 478 (2010).

[116] E. Stern-Taulats, A. Planes, P. Lloveras, M. Barrio, J.-L. Tamarit, S. Pramanick, S. Majumdar, S. Yüce, B. Emre, C. Frontera, and L. Mañosa, Acta Mater. **96**, 324 (2015).

[117] C. L. Yaws, *Handbook of vapor pressure* (Gulf Publishing Company, 1995), Vol. 4.

[118] Y. Takamura, R. Nakane, and S. Sugahara, J. Appl. Phys. **105**, 07B109 (2009).

[119] V. K. Pecharsky and K. A. Gschneidner, J. Appl. Phys. **86**, 565 (1999).

[120] D. H. Bowen and G. O. Jones, Proceedings of the Royal Society of London. Series A, Mathematical and Physical Sciences **254**, 522 (1960).

[121] L. Tocado, E. Palacios, and R. Burriel, J. Therm. Anal. Calorim. **84**, 213 (2006).

[122] E. Palacios, G. F. Wang, R. Burriel, V. Provenzano, and R. D. Shull, J. Phys. Conf. Ser. **200**, 092011 (2010).

[123] T. Gottschall, K. P. Skokov, F. Scheibel, M. Acet, M. G. Zavareh, Y. Skourski, J. Wosnitza, M. Farle, and O. Gutfleisch, Phys. Rev. Applied **5**, 024013 (2016).

[124] L. Tocado, E. Palacios, and R. Burriel, J. Magn. Magn. Mater. **290-291**, 719 (2005).

[125] S. Aksoy, T. Krenke, M. Acet, E. F. Wassermann, X. Moya, L. Mañosa, and A. Planes, Appl. Phys. Lett. **91**, 241916 (2007).

[126] M. Katter, V. Zellmann, G. Reppel, and K. Uestuener, IEEE Trans. Magn. **44**, 3044 (2008).

[127] T. Kihara, X. Xu, W. Ito, R. Kainuma, and M. Tokunaga, Phys. Rev. B **90**, 214409 (2014).

[128] M. Ghorbani Zavareh, C. Salazar Mejía, A. K. Nayak, Y. Skourski, J. Wosnitza, C. Felser, and M. Nicklas, Appl. Phys. Lett. **106**, 071904 (2015).

[129] O. Cakir and M. Acet, Appl. Phys. Lett. **100**, 202404 (2012).

[130] F. Scheibel, T. Gottschall, K. Skokov, O. Gutfleisch, M. Ghorbani-Zavareh, Y. Skourski, J. Wosnitza, O. Cakir, M. Farle, and M. Acet, J. Appl. Phys. **117**, 233902 (2015).

[131] T. Krenke, M. Acet, E. F. Wassermann, X. Moya, L. Mañosa, and A. Planes, Phys. Rev. B **73**, 174413 (2006).

[132] T. Gottschall, K. P. Skokov, D. Benke, M. E. Gruner, and O. Gutfleisch, Phys. Rev. B **93**, 184431 (2016).

[133] W. Ito, Y. Imano, R. Kainuma, Y. Sutou, K. Oikawa, and K. Ishida, Metall. Mater. Trans. A **38**, 759 (2007).

[134] V. Recarte, J. I. Pérez-Landazábal, S. Kustov, and E. Cesari, J. Appl. Phys. **107**, 053501 (2010).

[135] J. Enkovaara, A. Ayuela, J. Jalkanen, L. Nordström, and R. M. Nieminen, Phys. Rev. B **67**, 054417 (2003).

[136] M. K. Chattopadhyay, S. B. Roy, and P. Chaddah, Phys. Rev. B **72**, 180401 (2005).

[137] W. Ito, K. Ito, R. Y. Umetsu, R. Kainuma, K. Koyama, K. Watanabe, A. Fujita, K. Oikawa, K. Ishida, and T. Kanomata, Appl. Phys. Lett. **92**, 021908 (2008).

[138] J. I. Pérez-Landazábal, V. Recarte, V. Sánchez-Alarcos, C. Gómez-Polo, S. Kustov, and E. Cesari, J. Appl. Phys. **109**, 093515 (2011).

[139] T. Fukuda, T. Kakeshita, and Y. Lee, Acta Mater. **81**, 121 (2014).

[140] J. Monroe, J. Raymond, X. Xu, M. Nagasako, R. Kainuma, Y. I. Chumlyakov, R. Arroyave, and I. Karaman, Acta Mater. **101**, 107 (2015).

[141] P. J. Shamberger and F. S. Ohuchi, Phys. Rev. B **79**, 144407 (2009).

[142] B. Kaeswurm, V. Franco, K. P. Skokov, and O. Gutfleisch, J. Mag. Mag. Mater. **406**, 259 (2016).

[143] T. Gottschall, K. P. Skokov, R. Burriel, and O. Gutfleisch, Acta Mater. **107**, 1 (2016).

[144] K. P. Skokov, K.-H. Müller, J. D. Moore, J. Liu, A. Y. Karpenkov, M. Krautz, and O. Gutfleisch, J. Alloys Compd. **552**, 310 (2013).

[145] J. Liu, J. Moore, K. Skokov, M. Krautz, K. Löwe, A. Barcza, M. Katter, and O. Gutfleisch, Scripta Mater. **67**, 584 (2012).

[146] I. Titov, M. Acet, M. Farle, D. González-Alonso, L. Mañosa, A. Planes, and T. Krenke, J. Appl. Phys. **112**, 073914 (2012).

[147] F. Casanova, A. Labarta, X. Batlle, E. Vives, J. Marcos, L. Mañosa, and A. Planes, Eur. Phys. J. B **40**, 427 (2004).

[148] M. D. Kuz'min, K. P. Skokov, D. Y. Karpenkov, J. D. Moore, M. Richter, and O. Gutfleisch, Appl. Phys. Lett. **99**, 012501 (2011).

[149] X. Xu, T. Kihara, M. Tokunaga, A. Matsuo, W. Ito, R. Y. Umetsu, K. Kindo, and R. Kainuma, Appl. Phys. Lett. **103**, 122406 (2013).

[150] J. D. Moore, D. Klemm, D. Lindackers, S. Grasemann, R. Träger, J. Eckert, L. Löber, S. Scudino, M. Katter, A. Barcza, K. P. Skokov, and O. Gutfleisch, J. Appl. Phys. **114**, 043907 (2013).

[151] B. Pulko, J. Tušek, J. D. Moore, B. Weise, K. Skokov, O. Mityashkin, A. Kitanovski, C. Favero, P. Fajfar, O. Gutfleisch, A. Waske, and A. Poredoš, J. Mag. Mag. Mater. **375**, 65 (2015).

[152] I. A. Radulov, K. P. Skokov, D. Y. Karpenkov, T. Braun, and O. Gutfleisch, IEEE Trans. Magn. **51**, 1 (2015).

[153] M. D. Kuz'min, Appl. Phys. Lett. **90**, 251916 (2007).

[154] N. Teichert, D. Kucza, O. Yildirim, E. Yuzuak, I. Dincer, A. Behler, B. Weise, L. Helmich, A. Boehnke, S. Klimova, A. Waske, Y. Elerman, and A. Hütten, Phys. Rev. B **91**, 184405 (2015).

[155] T. Krenke, X. Moya, S. Aksoy, M. Acet, P. Entel, L. Mañosa, A. Planes, Y. Elerman, A. Yücel, and E. Wassermann, J. Mag. Mag. Mater. **310**, 2788 (2007).

[156] J. Liu, M. Krautz, K. P. Skokov, T. G. Woodcock, and O. Gutfleisch, Acta Mater. **59**, 3602 (2011).

[157] B. Li, W. J. Ren, Q. Zhang, X. K. Lv, X. G. Liu, H. Meng, J. Li, D. Li, and Z. D. Zhang, Appl. Phys. Lett. **95**, 172506 (2009).

[158] A. Waske, L. Giebeler, B. Weise, A. Funk, M. Hinterstein, M. Herklotz, K. Skokov, S. Fähler, O. Gutfleisch, and J. Eckert, Phys. Status Solidi RRL **9**, 136 (2015).

[159] L. Mañosa, D. González-Alonso, A. Planes, M. Barrio, J.-L. Tamarit, I. S. Titov, M. Acet, A. Bhattacharyya, and S. Majumdar, Nat. Commun. **2**, 595 (2011).

[160] N. Scheerbaum, D. Hinz, O. Gutfleisch, K.-H. Müller, and L. Schultz, Acta Mater. **55**, 2707 (2007).

[161] F. Guillou, G. Porcari, H. Yibole, N. van Dijk, and E. Brück, Adv. Mater. **26**, 2671 (2014).

[162] N. H. Dung, L. Zhang, Z. Q. Ou, and E. Brück, Scripta Mater. **67**, 975 (2012).

[163] N. H. Dung, L. Zhang, Z. Q. Ou, L. Zhao, L. van Eijck, A. M. Mulders, M. Avdeev, E. Suard, N. H. van Dijk, and E. Brück, Phys. Rev. B **86**, 045134 (2012).

[164] S. Glöser, L. T. Espinoza, C. Gandenberger, and M. Faulstich, Resour. Policy **44**, 35 (2015).

[165] V. Khovaylo, M. Lyange, K. Skokov, O. Gutfleisch, R. Chatterjee, X. Xu, and R. Kainuma, Materials Science Forum Vols. **738-739**, 446 (2013).

[166] H. Xuan, F. Chen, P. Han, D. Wang, and Y. Du, Intermetallics **47**, 31 (2014).

[167] T. Krenke, E. Duman, M. Acet, X. Moya, L. Mañosa, and A. Planes, J. Appl. Phys. **102**, 033903 (2007).

[168] D. Cong, S. Roth, and L. Schultz, Acta Mater. **60**, 5335 (2012).

[169] P. W. Egolf, A. Kitanovski, M. Diebold, C. Gonin, and D. Vuarnoz, J. Mag. Mag. Mater **321**, 758 (2009).

[170] Y. Song, K. P. Bhatti, V. Srivastava, C. Leighton, and R. D. James, Energy Environ. Sci. **6**, 1315 (2013).

[171] T. Christiaanse and E. Brück, Metall. Mater. Trans. E **1**, 36 (2014).

[172] R. Sobczak, Monatshefte für Chemie / Chemical Monthly **109**, 455 (1978).

[173] P. J. Webster, K. R. A. Ziebeck, S. L. Town, and M. S. Peak, Philos. Mag. B **49**, 295 (1984).

[174] R. Coll, L. Escoda, J. Saurina, J. L. Sánchez-Llamazares, B. Hernando, and J. J. Suñol, J. Therm. Anal. Calorim. **99**, 905 (2009).

[175] J. Sharma and K. Suresh, J. Alloys Compd. **620**, 329 (2015).

[176] J. L. Sánchez Llamazares, T. Sanchez, J. D. Santos, M. J. Pérez, M. L. Sanchez, B. Hernando, L. Escoda, J. J. Suñol, and R. Varga, Appl. Phys. Lett. **92**, 012513 (2008).

[177] J. Ren, H. Li, S. Feng, Q. Zhai, J. Fu, Z. Luo, and H. Zheng, Intermetallics **65**, 10 (2015).

[178] V. V. Sokolovskiy, V. D. Buchelnikov, M. A. Zagrebin, A. Grünebohm, and P. Entel, Phys. Procedia **75**, 1381 (2015).

[179] M. Khan, J. Brock, and I. Sugerman, Phys. Rev. B **93**, 054419 (2016).

[180] M. Khan, I. Dubenko, S. Stadler, J. Jung, S. S. Stoyko, A. Mar, A. Quetz, T. Samanta, N. Ali, and K. H. Chow, Appl. Phys. Lett. **102**, 112402 (2013).

[181] C. Chluba, W. Ge, R. Lima de Miranda, J. Strobel, L. Kienle, E. Quandt, and M. Wuttig, Science **348**, 1004 (2015).

[182] K. Buschow, P. van Engen, and R. Jongebreur, J. Magn. Magn. Mater. **38**, 1 (1983).

[183] E. I. Shreder, A. D. Svyazhin, and K. A. Fomina, Phys. Met. Metallogr. **113**, 146 (2012).

[184] M. Yin, P. Nash, and S. Chen, Intermetallics **57**, 34 (2015).

Curriculum vitea

Name	**Tino Gottschall**
Date and place of birth	30 June 1987, Dessau, Germany
Citizenship	German
Research interests	• Preparation and advanced characterization of new Heusler compounds for magnetic refrigeration • Development of a magnetocaloric demonstrator device • Modelling of transformation mechanisms in materials with first-order magnetostructural transitions
Education	
07.2012 - 07.2016	**Ph.D. in material science** TU Darmstadt, Germany On the magnetocaloric properties of Heusler compounds: Reversible, time- and size-dependent effects of the martensitic phase transition Supervisor: Professor Oliver Gutfleisch
10.2007 - 06.2012	**Diploma in physics** TU Dresden, Germany Untersuchung des magnetokalorischen Effektes in Ni-Mn basierten Heusler-Legierungen Supervisor: Professor Oliver Gutfleisch
06.2006	**Abitur** Gymnasium Philanthropinum Dessau, Germany

Conferences

- DPG Frühjahrstagung 2016 - Regensburg 03.2016 - talk
- Intermag 2016 - San Diego 01.2016 - talk
- Delft Days 2015 - Delft 11.2015 - poster
- Intermag 2015 - Beijing 05.2015 - talk
- DPG Frühjahrstagung 2012 - Berlin 03.2015 - poster
- MSE 2014 - Darmstadt 09.2014 - talk
- Thermag 2014 - Victoria 07.09.2014 - 2 talks
- Intermag 2014 - Dresden 05.2014 - talk and poster
- DPG Frühjahrstagung 2014 - Dresden 04.2014 - talk
- MMM Conference - Denver 11.2013 - talk
- Delft Days of Magnetocalorics - Delft 10.2013 - poster
- JEMS - Rhodos 08.2013 - talk
- Intermag - Chicago 01.2013 - poster
- Materials Day - Bochum 11.2012 - invited talk
- MSE 2012 - Darmstadt 09.2012 - poster
- DPG Frühjahrstagung 2012 - Berlin 03.2012 - talk

Own publications and patents

Peer-reviewed publications

O. Gutfleisch, **T. Gottschall**, M. Fries, D. Benke, I. Radulov, K. P. Skokov, H. Wende, M. Gruner, M. Acet, P. Entel and M. Farle, *Mastering hysteresis in magnetocaloric materials*, Phil. Trans. R. Soc. A **374**, 20150308 (2016)

T. Gottschall, K. P. Skokov, D. Benke, M. E. Gruner, and O. Gutfleisch, *Contradictory role of the magnetic contribution in inverse magnetocaloric Heusler materials*, Phys. Rev. B **93**, 184431 (2016)

T. Gottschall, K. P. Skokov, F. Scheibel, M. Acet, M. Ghorbani-Zavareh, Y. Skourski, J. Wosnitza, M. Farle, and O. Gutfleisch, *Dynamical Effects of the Martensitic Transition in Magnetocaloric Heusler Alloys from Direct ΔT_{ad} Measurements under Different Magnetic-Field-Sweep Rates*, Phys. Rev. Applied **5**, 024013 (2016)

T. Gottschall, K. P. Skokov, R. Burriel, and O. Gutfleisch, *On the S(T) diagram of magnetocaloric materials with first-order transition: Kinetic and cyclic effects of Heusler alloys*, Acta Mater. **107**, 1-8 (2016)

V. Franco, **T. Gottschall**, K. P. Skokov, and O. Gutfleisch, *FORC analysis of magnetocaloric Heusler-type alloys*, IEEE Magn. Lett. **6**, 1 (2016)

T. Gottschall, K. P. Skokov, B. Frincu, and O. Gutfleisch, *Large reversible magnetocaloric effect in Ni-Mn-In-Co*, Appl. Phys. Lett. **106**, 021901, 1-4 (2015)

I. A. Radulov, K. P.Skokov, D. Yu. Karpenkov, **T. Gottschall**, and O. Gutfleisch, *On the preparation of La(Fe,Mn,Si)$_{13}H_x$ polymer-composites with optimized magnetocaloric properties*, J. Mag. Mag. Mater. **396**, 228-236 (2015)

M. Krautz, A. Funk, K. P. Skokov, **T. Gottschall**, J. Eckert, O. Gutfleisch, and A. Waske, *A new type of La(Fe,Si)$_{13}$-based magnetocaloric composite with amorphous metallic matrix*, Scripta Mater. **95**, 50-53 (2015)

F. Scheibel, **T. Gottschall**, K. P. Skokov, O. Gutfleisch, M. Ghorbani-Zavareh, Y. Skourski, J. Wosnitza, Ö. Cakýr, M. Farle, and M. Acet, *Dependence of the inverse magnetocaloric effect on the field-change rate in Mn_3GaC and its relationship to the kinetics of the phase transition*, Appl. Phys. Lett. **117**, 233902, 1-6 (2015)

J. Döntgen, J. Rudolph, **T. Gottschall**, O. Gutfleisch, S. Salomon, A. Ludwig, and D. Hägele, *Temperature dependent low-field measurements of the magnetocaloric ΔT with sub-mK resolution in small volume and thin film samples*, Appl. Phys. Lett. **106**, 032408, 1-4 (2015)

K. P. Skokov, D. Yu. Karpenkov, M. D. Kuz'min, I. A. Radulov, **T. Gottschall**, B. Kaeswurm, M. Fries, and O. Gutfleisch, *Heat exchangers made of polymer-bonded $La(Fe,Si)_{13}$*, J. Appl. Phys. **115**, 17A941, 1-3 (2014)

M. Krautz, K. P. Skokov, **T. Gottschall**, C. S. Teixeira, A. Waske, J. Liu, L. Schultz, and O. Gutfleisch, *Systematic investigation of Mn substituted $La(Fe,Si)_{13}$ alloys and their hydrides for room-temperature magnetocaloric application*, J. Alloys Compd. **598**, 27-32 (2014)

D. Comtesse, M. Gruner, M. Ogura, V. V. Sokolovskiy, V. D. Buchelnikov, A. Grünebohm, R. Arróyave, N. Singh, **T. Gottschall**, O. Gutfleisch, V. A. Chernenko, F. Albertini, S. Fähler, and P. Entel, *First-principles calculation of the instability leading to giant inverse magnetocaloric effects*, Phys. Rev. B **89**, 184403, 1-6 (2014)

J. Liu, **T. Gottschall**, K. P. Skokov, J. D. Moore, and O. Gutfleisch, *Giant magnetocaloric effect driven by structural transitions*, Nat. Mater. **11**, 620-626 (2012)

Patent applications

Deutsche Patentanmeldung 10 2015 119 103.2 "Verfahren zum Herstellen eines magnetokalorischen Pulvers und Verbundmaterial mit einem magnetokalorischen Pulver", 6. November 2015

Deutsche Patentanmeldung 10 2016 110 385.3 "Kühlvorrichtung und ein Verfahren zum Kühlen", 6. Juni 2016

Appendix

Table 5.1: Part 1: Overview of the prepared and investigated compounds except for Ni-Mn-In-(Co) and Ni-Mn-Sn-(Co). The stoichiometry and the heat treatment are specified. A single-phase material is described by yes (y), in the case of secondary phases by no (n) and if the phase purity is not studied by -. If a martensitic transition is observed, the austenite-start temperature A_s is given. Materials showing no transformation are indicated by no (n) and if the transition character is not investigated by -. Some alloys undergo an antiferromagnetic-to-ferromagnetic transition, which is specified by AFM-FM.

Material	Treatment	Single-phase	Transformation
$Mn_{50.0}Ni_{40.5}Co_{2.0}Sn_{7.5}$	900°C - 24h - wq	y	-
$Mn_{50}Ni_{40}Co_2Sn_8$	900°C - 24h - wq	y	-
$Mn_{50}Ni_{41}Sn_9$	900°C - 24h - wq	y	A_s = 300 K
$Fe_{50}Ni_{25}Al_{25}$	as-cast	n	n
$Ni_{50}Fe_{30}Al_{20}$	1000°C - 24h - wq	n	n
$Ni_{50}Fe_{32}Al_{18}$	1000°C - 24h - wq	n	n
$Ni_{50}Fe_{34}Al_{16}$	1000°C - 24h - wq	n	n
$Ni_{50}Fe_{30}Al_{20}$	as-cast	n	n
$Ni_{50}Fe_{32}Al_{18}$	as-cast	n	n
$Ni_{50}Fe_{32}Al_{18}$	as-cast	n	n
$Ni_{52}Fe_{20}Ga_{23}Al_2Co_3$	900°C - 24h - wq	n	n
$Ni_{52}Fe_{20}Ga_{23}Al_3Co_2$	900°C - 24h - wq	n	A_s = 220 K
$Ni_{52}Fe_{20}Ga_{23}Al_5$	900°C - 24h - wq	y	A_s = 230 K
$Ni_{52}Fe_{20}Ga_{23}Al_2Co_3$	as-cast	n	-
$Ni_{52}Fe_{20}Ga_{23}Al_3Co_2$	as-cast	y	A_s = 250 K
$Ni_{52}Fe_{20}Ga_{23}Al_5$	as-cast	y	-
$Ni_{50}Fe_{22}Ga_{28}$	900°C - 24h - wq	y	n
$Ni_{50}Fe_{23}Ga_{27}$	900°C - 24h - wq	y	-
$Ni_{50}Fe_{24}Ga_{26}$	900°C - 24h - wq	n	-
$Ni_{54}Fe_{22}Ga_{24}$	900°C - 24h - wq	n	n
$Ni_{54}Fe_{20}Ga_{26}$	900°C - 24h - wq	n	A_s = 280 K
$Ni_{54}Fe_{21}Ga_{25}$	900°C - 24h - wq	n	A_s = 280 K
$Ni_{50}Fe_{25}Ga_{25}$	as-cast	n	-
$Ni_{54}Fe_{22}Ga_{24}$	as-cast	n	-
$Ni_{54}Fe_{20}Ga_{26}$	as-cast	n	-
$Ni_{54}Fe_{21}Ga_{25}$	as-cast	n	-

Table 5.2: Part 2: Overview of the prepared and investigated compounds except for Ni-Mn-In-(Co) and Ni-Mn-Sn-(Co). The stoichiometry and the heat treatment are specified. A single-phase material is described by yes (y), in the case of secondary phases by no (n) and if the phase purity is not studied by -. If a martensitic transition is observed, the austenite-start temperature A_s is given. Materials showing no transformation are indicated by no (n) and if the transition character is not investigated by -. Some alloys undergo an antiferromagnetic-to-ferromagnetic transition, which is specified by AFM-FM.

Material	Treatment	Single-phase	Transformation
$Ni_{45}Mn_{32}In_{13}Cr_5Co_5$	as-cast	n	-
$Ni_{50}Mn_{34,5}Fe_2In_{13,5}$	as-cast	n	-
$Ni_{50}Mn_{34}Fe_4In_{12}$	as-cast	n	-
$Ni_{50}Mn_{34,5}Fe_2In_{13,5}$	as-cast	y	A_s = 220 K
$Ni_{50}Mn_{33,5}Fe_2In_{14,5}$	as-cast	y	n
$Ni_{50}Cr_{35,5}In_{14,5}$	as-cast	n	-
$Ni_{50}Mn_{35,5}In_{12,5}Mg_2$	as-cast	-	A_s = 430 K
$Ni_{50}Mn_{26}Cr_{15}In_9$	as-cast	-	n
$Ni_{50}Mn_{28,5}Cr_{10}In_{11,5}$	as-cast	-	n
$Ni_{50}Mn_{28}Cr_{10}In_{12}$	900°C - 24h - wq	n	A_s = 230 K
$Ni_{50}Mn_{29,5}Cr_8In_{12,5}$	900°C - 24h - wq	n	A_s = 310 K
$Ni_{50}Mn_{31}Cr_6In_{13}$	900°C - 24h - wq	n	A_s = 335 K
$Ni_{50}Mn_{32,5}Cr_4In_{13,5}$	900°C - 24h - wq	n	A_s = 370 K
$Ni_{50}Mn_{34}Cr_2In_{14}$	900°C - 24h - wq	y	A_s = 390 K
$Fe_{50}Mn_{25}Ga_{25}$	900°C - 24h - wq	n	n
$Ni_{50}Mn_{25}Bi_{25}$	900°C - 24h - wq	-	n
$Ni_{50}Mn_{36,5}Si_{13,5}$	as-cast	-	n
$Ni_{50}Mn_{36,5}Si_{13,5}$	as-cast	-	n
$Co_{50}Mn_{38}Ge_{12}$	900°C - 24h - wq	-	AFM-FM at 190 K
$Co_{50}Mn_{39}Ge_{11}$	900°C - 24h - wq	-	AFM-FM at 190 K
$Co_{50}Mn_{40}Ge_{10}$	900°C - 24h - wq	-	AFM-FM at 190 K
$Co_{50}Mn_{25}Si_{25}$	900°C - 24h - wq	-	n
$Co_{50}Mn_{35}Si_{15}$	900°C - 24h - wq	-	AFM-FM at 190 K
$Co_{50}Mn_{36}Si_{14}$	900°C - 24h - wq	-	AFM-FM at 190 K
$Co_{50}Mn_{37}Si_{13}$	900°C - 24h - wq	-	AFM-FM at 190 K

Acknowledgments

I thank **Prof. Dr. Oliver Gutfleisch** especially for supervising me in my Ph.D. and in general for giving me the opportunity to join his work group in 2010 as a student worker and later as a Diploma student. For me it was an exceptional time in which I realized my fascination with magnetism.

Furthermore, I want to thank **Prof. Dr. Heiko Wende**, who kindly agreed to be a referee for my doctoral thesis.

My special thanks go to **Dr. Konstantin P. Skokov**. He always took the time to discuss, guide and assisted in complicated measurements.

I want to thank all members and former members of the group "**Funktionale Materialien**" for the wonderful and diverse time in Darmstadt. It was a great pleasure to work together with all of you.

My thanks go to **DPG - SPP1599 - Ferroic cooling** for funding my thesis and especially to all project partners of the project for all the productive discussions and the successful cooperation.

I thank **Franziska Scheibel**, **Prof. i.R. Dr. Mehmet Acet** and **Prof. Dr. Michael Farle** from the University of Duisburg-Essen for our joint ΔT_{ad} measurements.

Furthermore, I thank **Dr. Yuri Skourski**, **Mahdiyeh Ghorbani Zavareh** and **Prof. Dr. Jochen Wosnitza** of the Helmholtz-Zentrum Dresden-Rossendorf for giving me the opportunity to do the pulsed-field measurements of the adiabatic temperature change in your institute.

My thanks go to **Prof. Dr. Ramon Burriel** of the University of Zaragoza for the fruitful cooperation and experiments we did together.

I am thankful to **Dr. Markus E. Gruner** for all the fruitful discussions we had which led us to a very nice joint publication

I want to thank **Andreas Taubel**, **Dimitri Benke** and **Alrun Günther** for prove-reading my thesis.

Last but not least, I want to thank my **family** and **friends**, but especially my wife for giving me motivation and assistance particularly in difficult times.